165
12.16.80
9 #C

#1

Dr. 2144

R706

GA-A15859
UC-77

MASTER

POSTIRRADIATION EXAMINATION OF CAPSULES GF-1, GF-2, AND GF-3

by

W. J. KOVACS, R. BLANCHARD, and M. L. POINTUD

Prepared under
Contract DE-AT03-76ET35300
for the San Francisco Operations Office
Department of Energy

DATE PUBLISHED: SEPTEMBER 1980

GENERAL ATOMIC COMPANY

Printed in the United States of America
Available from
National Technical Information Service
U.S. Department of Commerce
5285 Port Royal Road
Springfield, Virginia 22161
Price Code: Printed Copy A11; Microfiche A01

GA-A15859
UC-77

POSTIRRADIATION EXAMINATION OF CAPSULES GF-1, GF-2, AND GF-3

by

W. J. KOVACS, R. BLANCHARD,* and M. L. POINTUD*

Prepared under
Contract DE-AT03-76ET35300
for the San Francisco Operations Office
Department of Energy

*Commissariat a l'Energie Atomique, Saclay, France

GENERAL ATOMIC PROJECT 6400
DATE PUBLISHED: SEPTEMBER 1980

GENERAL ATOMIC COMPANY

THIS PAGE

WAS INTENTIONALLY

LEFT BLANK

ABSTRACT

The GF-1, GF-2, and GF-3 capsule tests were irradiated in the Siloe reactor at Grenoble, France between October 31, 1973 and July 25, 1975. High-enriched uranium (HEU) mixed oxide $(8Th,U)O_2$ fissile and ThO_2 fertile particles were tested over the following exposure conditions:

1. 3.8 to 11.0×10^{25} n/m^2 $(E > 29\ fJ)_{HTGR}$.
2. 960° to 1120°C time volume average temperature.
3. Mixed oxide $(8Th,U)O_2$ burnup between 5.3 and 11.4% FIMA and ThO_2 burnup between 1.1 and 3.6% FIMA.

Postirradiation examination of HTGR fuel rods in capsules GF-1, GF-2, and GF-3 showed acceptable structural integrity and irradiation-induced dimensional changes that were consistent with model predictions. Pressure vessel failure levels between different TRISO-coated $(8Th,U))O_2$ fissile particle types showed that the 400-μm-diameter kernel design was more conservative than the 500-μm-diameter designs. High OPyC failure levels (1.6% to 83%) on TRISO-coated fissile particles were attributed to inferior pyrocarbon microstructures, which resulted in high irradiation-induced internal stresses and premature failure. Furthermore, empirical data showed that undesirable OPyC microstructures could be avoided with current HTGR specification requirements, namely, OPyC microporosity >13 ml/kg OPyC and active coating gas ratios during deposition >0.25.

The fraction of as-manufactured defective SiC layers on fissile fuel determined by a mercury intrusion/radiographic technique was between 2.3% and 11.8%, which was approximately two orders of magnitude greater than the fraction determined by the standard burn-leach technique. The results imply

that localized microfissures in SiC layers are not always detectible with a burn-leach determination.

No amoeba migration or lanthanide fission product - SiC attack was observed in the fissile and fertile particles, and these results are consistent with fuel performance models.

CONTENTS

ABSTRACT iii

1. INTRODUCTION 1-1

   Reference 1-2

2. OBJECTIVES 2-1

3. COATED PARTICLES 3-1

   3.1. General Atomic Reference Fuel Samples 3-1

      3.1.1. Description 3-1

      3.1.2. Fabrication 3-2

      3.1.3. Properties 3-3

   3.2. General Atomic Advanced Fuel Samples 3-3

   3.3. Fuel Rods 3-3

      3.3.1. Description 3-3

      3.3.2. Fabrication 3-3

   3.4. CEA Fuel Samples 3-4

      3.4.1. Fissile Particles 3-4

      3.4.2. Fertile Particles 3-4

      3.4.3. Properties 3-4

      3.4.4. Fuel Rods 3-4

      3.4.5. Properties 3-5

   References 3-5

4. DESCRIPTION OF IRRADIATION 4-1

   4.1. Irradiation Facilities 4-1

      4.1.1. Thermal Measurements and Calculations 4-1

      4.1.2. Neutron Fluence Calculations 4-4

      4.1.3. Heavy Metal Burnup Calculations 4-7

      4.1.4. Fission Gas Release Measurements 4-8

   References 4-10

5. POSTIRRADIATION EXAMINATION 5-1
5.1. Fuel Sample Unloading 5-1
5.2. Fuel Rod Visual Examination 5-1
5.3. Loose Particle Visual Examination 5-2
5.3.1. Pressure Vessel Failure 5-2
5.3.2. OPyC Failure 5-3
5.4. Fuel Rod Dimensional Change 5-5
5.5. Fuel Rod Thermal Conductivity Measurements 5-9
5.6. Fission Gas Release Measurements 5-10
5.6.1. Postirradiation Fission Gas Release Measurements. 5-10
5.6.2. Determination of Fuel Failure Levels 5-11
5.7. Determination of Fuel Failure by Fuel Rod Disintegration. 5-15
5.8. Structural Evaluation 5-17
5.8.1. Fuel Rod and Matrix Structure 5-17
5.8.2. Fissile and Inert Particles 5-19
5.8.3. Fertile Particles 5-29
5.8.4. Advanced Fuel Particle Concepts 5-31
References 5-36
6. DISCUSSION 6-1
6.1. Coated Particle Irradiation Performance 6-1
6.1.1. Fissile Particles 6-1
6.1.2. Thermochemical Stability 6-5
6.1.3. Fertile Particles 6-7
6.1.4. Advanced Fuel Particles 6-8
References 6-9
7. CONCLUSIONS 7-1
7.1. Fuel Rods 7-1
7.2. TRISO-Coated Particle Design 7-2
7.3. Thermochemical Stability 7-4
7.4. Development Fuels 7-4
APPENDIX

TABLES

2-1. Objectives of different fuel rod types 2-2

3-1. Summary description of GA-coated particles 3-6

3-2. Fabrication coating parameters for GA-coated particles 3-7

3-3. Properties of GA total coated particles 3-8

3-4. Summary description of advanced fuel unbonded particles and bonded particle rings 3-9

3-5. Summary description of GA fuel rods 3-10

3-6. Properties of CEA total coated particles 3-11

3-7. Fabrication coating parameters for CEA-coated particles . . . 3-12

3-8. Summary description of CEA-coated particles 3-13

3-9. Summary description of fuel rods 3-20

4-1. Summary description of irradiation conditions 4-11

4-2. Thermal properties used in calculation of GF-1, GF-2, and GF-3 capsule temperatures 4-12

4-3. Irradiation temperatures 4-13

5-1. Results of visual examination of unbonded fissile and fertile particles tested in capsule GF-1 5-39

5-2. Results of visual examination of unbonded fissile and fertile particles tested in capsule GF-2 5-40

5-3. Results of visual examination of unbonded fissile and fertile particles tested in capsule GF-3 5-41

5-4. Summary of visually determined unbonded particle failures . . 5-42

5-5. TRISO-coated loose particle OPyC property and process characteristics 5-43

5-6. Fuel rod dimensional change data 5-44

5-7. Thermal conductivity measurements on irradiated GF-1 and GF-2 fuel rods 5-45

5-8. Comparative evaluation of EOL Kr-85m R/B measurements 5-46

5-9. Kr-85m R/B measurements on laser-failed, TRISO-coated particles 5-47

5-10. Calculated fissile particle failure based on Kr-85m R/B early in life 5-48

5-11. Calculated fissile and fertile particle failures based on Kr-85m R/B at end-of-life 5-49

5-12. Determination of fuel particle failure levels by electrochemical disintegration of fuel rods 5-50
5-13. Metallographic and microradiographic examination of fuel particles 5-51
5-14. Range of V_{matrix} values 5-52
5-15. Comparative evaluation of OPyC failure levels determined visually for unbonded particles and metallographically for particles tested in fuel rods 5-52
5-16. Fission product distributions in TRISO-coated UC_2 fuel 5-53
5-17. OPyC failure in TRISO-coated fuel 5-54
5-18. Summary of defective SiC layers in fissile particles 5-55
5-19. Summary of visual examination for advanced fuels 5-56
5-20. Gamma spectrometry measurements defining migration of metallic fission products in BISO-coated doped and undoped fuel 5-57
6-1. Comparative evaluation of calculated and observed in-pile pressure vessel failure early in life 6-11
6-2. Thermal exposure conditions 6-12
A-1. Fission gas release results for isotopes of Kr and Xe in capsule GF-1 . . . . A-1
A-2. Fission gas release results for isotopes of Kr and Xe in capsule GF-2 . . . . A-5
A-3. Fission gas release results for isotopes of Kr and Xe in capsule GF-3 . . . . A-9

FIGURES

4-1. Schematic diagram of TUMULT G device and Siloe reactor core penetrations 4-14
4-2. Schematic diagram of irradiation capsules GF-1 and GF-2 . . . 4-15
4-3. Schematic diagram of irradiation capsule GF-3 4-16
4-4. Axial flux profiles for position 47G in Siloe reactor 4-17
4-5. Axial flux profiles for position 45G in Siloe reactor 4-18
4-6. Ni/SiC attack observed in TRISO-coated fuel tested in CORAIL IV A and B 4-19
4-7. Fast and thermal axial fluence profiles for capsule GF-1 . . . 4-20
4-8. Fast and thermal axial fluence profiles for capsule GF-2 . . . 4-21

4-9. Fast and thermal axial fluence profiles for capsule GF-3 . . . 4-22
4-10. Irradiation history of GF-1, cell 1 4-23
4-11. Irradiation history of GF-1, cell 2 4-24
4-12. Irradiation history of GF-1, cell 3 4-25
4-13. Irradiation history of GF-1, cell 4 4-26
4-14. Irradiation history of GF-2, cell 1 4-27
4-15. Irradiation history of GF-2, cell 2 4-28
4-16. Irradiation history of GF-2, cell 3 4-29
4-17. Irradiation history of GF-2, cell 4 4-30
4-18. Irradiation history of GF-3, cell 1 4-31
4-19. Irradiation history of GF-3, cell 2 4-32
4-20. Irradiation history of GF-3, cell 3 4-33
4-21. Irradiation history of GF-3, cell 4 4-34
4-22. Capsule GF-1 Kr-85m R/B measurements during irradiation . . . 4-35
4-23. Capsule GF-2 Kr-85m R/B measurements during irradiation . . . 4-36
4-24. Capsule GF-3 Kr-85m R/B measurements during irradiation . . . 4-37
4-25. Capsule GF-1 Kr-85 measurements during irradiation 4-38
4-26. Capsule GF-2 Kr-85 measurements during irradiation 4-39
4-27. Capsule GF-3 Kr-85 measurements during irradiation 4-40
5-1. Neutron radiographs of individual cells in capsule GF-2 . . . 5-58
5-2. Neutron radiographs of individual cells in capsule GF-3 . . . 5-59
5-3. Disassembly apparatus used for capsules GF-1, GF-2, and GF-3 . 5-60
5-4. Fuel rod compact No. 1 irradiated in GF-1 5-61
5-5. Fuel rod compact No. 2 irradiated in GF-1 5-62
5-6. Fuel rod compact No. 3 irradiated in GF-1 5-63
5-7. Fuel rod compact No. 4 irradiated in GF-1 5-64
5-8. Fuel rod compact No. 5 irradiated in GF-1 5-65
5-9. Fuel rod compact No. 6 irradiated in GF-1 5-65
5-10. Fuel rod compact No. 1 irradiated in GF-2 5-66
5-11. Fuel rod compact No. 2 irradiated in GF-2 5-66
5-12. Fuel rod compact No. 3 irradiated in GF-2 5-67
5-13. Fuel rod compact No. 4 irradiated in GF-2 5-67
5-14. Fuel rod compact No. 5 irradiated in GF-2 5-68

5-15. Fuel rod compact No. 6 irradiated in GF-2 5-68
5-16. Fuel rod compact No. 1 irradiated in GF-3 5-69
5-17. Fuel rod compact No. 2 irradiated in GF-3 5-70
5-18. Fuel rod compact No. 3 irradiated in GF-3 5-71
5-19. Fuel rod compact No. 4 irradiated in GF-3 5-72
5-20. Fuel rod compact No. 5 irradiated in GF-3 5-73
5-21. Fuel rod compact No. 6 irradiated in GF-3 5-74
5-22. TRISO-coated (8Th,U)O_2 loose particle batch 6155-02-020-1 irradiated in capsule GF-1 5-75
5-23. Correlation between OPyC failure and fluence for TRISO-coated loose particle batch 6155-00-010 5-76
5-24. Predicted and measured irradiation-induced volumetric changes versus fluence 5-77
5-25. Predicted and measured irradiation-induced axial dimensional changes versus fluence 5-78
5-26. Predicted and measured irradiation-induced diametral dimensional changes versus fluence 5-79
5-27. Irradiation-induced volumetric changes of matrix phase . . . 5-80
5-28. Predicted and measured strain anisotrophy versus fluence . . 5-81
5-29. Reirradiation and measurement of R/B gaseous release at 600°C for fuel rods in GF-1 5-82
5-30. Reirradiation and measurement of R/B gaseous release at 600°C for fuel rods in GF-2 5-83
5-31. Kr-85m R/B versus burnup for laser-failed (8Th,U)O_2 and ThO_2 fuel particles 5-84
5-32. Diametral photomicrograph of a type a fuel rod after irradiation in capsule GF-2 5-85
5-33. Longitudinal photomicrograph of a type b fuel rod after irradiation in capsule GF-3 5-86
5-34. Diametral photomicrograph of a type b' fuel rod after irradiation in capsule GF-1 5-87
5-35. Longitudinal photomicrograph of a type b' fuel rod after irradiation in capsule GF-1 5-88
5-36. Diametral photomicrograph of a type c fuel rod after irradiation in capsule GF-3 5-89
5-37. Diametral photomicrograph of a type d fuel rod after irradiation in capsule GF-2 5-90
5-38. Diametral photomicrograph of a type e fuel rod after irradiation in capsule GF-1 5-91

5-39. Longitudinal photomicrograph of a type e fuel rod after irradiation in capsule GF-1 5-92

5-40. Longitudinal photomicrograph of a type f' fuel rod after irradiation in capsule GF-3 5-93

5-41. Representative metallographic cross section of matrix and shim material in a GA type a fuel rod 5-94

5-42. Representative metallographic cross section of matrix and shim material in a GA type b' fuel rod 5-94

5-43. Representative metallographic cross section of CERCA natural type matrix in CEA type e fuel rod 5-95

5-44. Representative metallographic cross section of CERCA artificial type matrix in CEA type f' fuel rod 5-95

5-45. Representative photomicrographs of TRISO (8Th,U)O_2 particles (6155-01-020) from type e fuel rod 237 irradiated in capsule GF-1 5-96

5-46. Representative photomicrograph of TRISO (8Th,U)O_2 particles (6155-01-020) from type e fuel rod 237 irradiated in capsule GF-1 5-97

5-47. Representative photomicrographs of TRISO (8Th,U)O_2 particles (6155-00-030) from type a fuel rod (7161-003-01-4) irradiated in capsule GF-1 5-97

5-48. Representative photomicrographs of TRISO (8Th,U)O_2 particles (6155-02-030) from type b' fuel rod (7161-003-03-5) irradiated in capsule GF-1 5-98

5-49. Representative photomicrographs of TRISO (8Th,U)O_2 particles (6155-02-030) from a type b' fuel rod (7161-003-03-5) irradiated in capsule GF-1 5-99

5-50. Representative photomicrographs of TRISO (8Th,U)O_2 particles (6155-02-030) from a type b' fuel rod (7161-003-03-5) irradiated in capsule GF-1 5-100

5-51. Representative photomicrographs of TRISO (8Th,U)O_2 particles (MG 178) from type f' fuel rod 817 irradiated in capsule GF-3 5-101

5-52. Representative photomicrograph of TRISO (8Th,U)O_2 particles (MG 178) from type f' fuel rod 817 irradiated in capsule GF-3 5-102

5-53. Representative photomicrographs of TRISO (8Th,U)O_2 particles (6155-01-030) from type b fuel rod (7161-003-02-04) irradiated in capsule GF-3 5-103

5-54. Representative photomicrographs of TRISO (8Th,U)O_2 particles (6155-01-030) from type c fuel rod (7161-003-04-4) irradiated in capsule GF-3 5-104

5-55. Representative photomicrograph of TRISO (8Th,U)O$_2$ particles (6155-01-030) from type c fuel rod (7161-003-04-4) irradiated in capsule GF-3 5-105

5-56. Representative photomicrographs of TRISO inert particles (6351-01-020) from type b' fuel rod (7161-003-03-5) irradiated in capsule GF-1 5-105

5-57. Representative photomicrograph of unbonded TRISO UC$_2$ particles (6151-00-010) irradiated in capsule GF-1 5-106

5-58. Representative photomicrographs of unbonded TRISO UC$_2$ particles (6151-00-010) irradiated in capsule GF-1 5-107

5-59. Representative photomicrographs of unbonded TRISO UC$_2$ particles (6151-00-010) irradiated in capsule GF-1 5-108

5-60. Representative photomicrographs of unbonded TRISO UC$_2$ particles (6151-00-010) irradiated in capsule GF-1 5-109

5-61. Representative photomicrographs of unbonded TRISO UC$_2$ particles (6151-00-010) irradiated in capsule GF-1 5-110

5-62. Representative photomicrographs of unbonded TRISO UC$_2$ particles (6151-00-010) irradiated in capsule GF-1 5-111

5-63. Representative photomicrograph of unbonded TRISO UC$_2$ particles (6151-00-010) irradiated in capsule GF-3 5-112

5-64. Back-scattering electron image defining Nd, La, Ce, and Pr distributions in TRISO-coated UC$_2$ (6151-00-010) irradiated in capsule GF-1 5-113

5-65. Back-scattering electron image defining U, Si, Cs, Ba, and Pd distributions in TRISO-coated UC$_2$ (6151-00-010) irradiated in capsule GF-1 5-114

5-66. Representative photomicrographs of unbonded TRISO (8Th,U)O$_2$ particles (6151-01-020) irradiated in capsule GF-1 5-115

5-57. Representative photomicrographs of unbonded TRISO (8Th,U)O$_2$ particles (6151-01-020) irradiated in capsule GF-1 5-116

5-68. Representative photomicrograph of unbonded TRISO (8Th,U)O$_2$ particle (6151-01-020) irradiated in capsule GF-1 5-117

5-69. Representative photomicrograph of unbonded BISO (8Th,U)O$_2$ particles (6445-00-010) irradiated in capsule GF-3 5-118

5-70. Representative photomicrographs of unbonded TRISO (8Th,U)O$_2$ particles (MG 178) irradiated in capsule GF-3 5-119

5-71. Representative photomicrographs of unbonded TRISO (8Th,U)O$_2$ particles (MG 178) irradiated in capsule GF-3 5-120

5-72. Representative photomicrographs of unbonded TRISO (8Th,U)O$_2$ particles (MG 199) irradiated in capsule GF-3 5-121

5-73. Representative photomicrographs of unbonded TRISO (8Th,U)O_2 particles (MG 199) irradiated in capsule GF-3 5-122

5-74. Comparative evaluation of OPyC failure versus microporosity 5-123

5-75. Contact microradiographs of TRISO-coated fissile fuel impregnated with Hg at 69 MPa 5-124

5-76. Contact microradiograph of a TRISO-coated fissile particle from batch 6155-01-020 5-125

5-77. OPyC microporosity versus the volume fraction of active coating gases 5-126

5-78. Scanning electron microscope photographs of unirradiated OPyC layer on TRISO-coated fissile batch 6155-00-020 5-127

5-79. Microradiographs of burned-back, TRISO-coated fissile particles subjected to Hg intrusion at 69 MPa 5-128

5-80. Fraction Cs-137 release versus heat treat time at 1600°C for as-manufactured TRISO-coated (8Th,U)O_2 fuel 5-129

5-81. Fraction Cs-137 release versus heat treat time at 1600°C for as-manufactured BISO-coated (8Th,U)O_2 5-130

5-82. Representative photomicrographs of BISO ThO_2 particles (6542-02-036) from type e fuel rod 237 irradiated in capsule GF-1 5-131

5-83. Representative photomicrographs of BISO ThO_2 particles (6542-02-036) from type e fuel rod 237 irradiated in capsule GF-1 5-132

5-84. Representative photomicrographs of BISO ThO_2 particles (6542-02-036) from type a fuel rod 7161-003-01-5 irradiated in capsule GF-1 5-133

5-85. Representative photomicrographs of BISO ThO_2 particles (6542-02-036) from type b' fuel rod 7161-003-03-5 irradiated in capsule GF-1 5-134

5-86. Representative photomicrographs of BISO ThO_2 particles (MG 156) from type f' fuel rod 817 irradiated in capsule GF-3 5-135

5-87. Representative photomicrographs of BISO ThO_2 particles (6542-02-036) from type b fuel rod 7161-003-02-4 irradiated in capsule GF-3 5-136

5-88. Representative photomicrograph of unbonded BISO ThO_2 particles (6542-02-036-1) irradiated in capsule GF-1 5-137

5-89. Representative photomicrograph of unbonded BISO ThO_2 particles (6542-02-036-1) irradiated in capsule GF-1 5-138

5-90. Representative photomicrographs of unbonded BISO (8Th,U)O_2 particles (6111-107E) irradiated in capsule GF-1 5-139

5-91. Back-scattering electron image defining C, Al, Si, Cs, and Ba distributions in BISO-coated (8Th,U)O_2, batch 611-105E irradiated in capsule GF-3 5-140

5-92. Back-scattering electron image defining Th, Cs, Rb, and S distributions in BISO-coated (8Th,U)O_2, batch 6445-00-010 irradiated in capsule GF-1 5-141

5-93. Representative photomicrographs of unbonded ZrC-TRISO-coated (8Th,U)O_2 particles irradiated in capsule GF-1 5-142

5-94. Representative photomicrographs of unbonded BISO (8Th,U)O_2 particles (6171-115E), 30% Si dopant) irradiated in capsule GF-3 5-143

5-95. Representative photomicrograph of unbonded BISO (8Th,U)O_2 particles (6171-107E, 25% Si dopant) irradiated in capsule GF-3 5-144

5-96. Representative photomicrograph of unbonded BISO (8Th,U)O_2 particles (6171-105E, 19% Si-doped OPyC layer) irradiated in capsule GF-2 5-144

6-1. Predicted pressure vessel failure fraction 6-13

6-2. Comparative evaluation of calculated and observed fissile particle pressure vessel failure 6-14

6-3. Rate of change of SiC thickness 6-15

1. INTRODUCTION

A cooperative program between General Atomic Company (GA) and the French Commissariat a l'Energie Atomique (CEA) was instituted in 1973 for qualifying the CEA and its industrial partners to manufacture and market high-temperature gas-cooled reactor (HTGR) fuel based on technology licensed from GA. The program also was designed to contribute significantly to the HTGR fuel development already under way at GA.

The GF-1, GF-2, and GF-3 capsule tests irradiated in the Siloe reactor at Grenoble, France were the first in a series of instrumented irradiation tests planned under the cooperative GA/CEA program. The GF-1, GF-2, and GF-3 capsule tests were irradiated between October 31, 1973 and July 25, 1975. High-enriched uranium (HEU) mixed oxide $(8Th,U)O_2$ fissile particles and ThO_2 fertile particles were tested in GF-1, GF-2, and GF-3 because at the time of program inception they were candidate fuel types for use in French HTGRs and for future HTGRs in the U.S. Approximately 75% of the irradiation test space in the GF-1, GF-2, and GF-3 capsules was occupied by GA samples with the remaining 25% occupied by CEA samples. Each capsule contained four individual cells. The four cells were continuously monitored for surface temperatures of fuel samples and periodically purged for measurement of fission gas release, which is related to monitoring in-pile fuel failure. The range of irradiation conditions for the three capsules is summarized as follows:

1. A fast fluence exposure between 3.8 to 11×10^{25} n/m^2 $(E > 29\ fJ)_{HTGR}$.

2. A time volume average fuel rod temperature between 960° and 1120°C with loose particle samples between 985° and 1095°C.

3. A burnup for mixed oxide (8Th,U)O_2 between 5.3 and 11.4% FIMA and for ThO_2 between 1.1 and 3.6% FIMA.

The purpose of this report is to describe in detail the GF-1, GF-2, and GF-3 experiments, the results of postirradiation examination (PIE), and the analysis of results relative to fuel material properties and performance. Emphasis is placed on how particle performance for the oxide fuel systems tested in GF-1, GF-2, and GF-3 supports current OPyC and SiC specification requirements. A synopsis of the GF-1, GF-2, and GF-3 irradiation tests was given in Ref. 1-1; the intent of this report is to provide a more comprehensive discussion of the results.

REFERENCE

1-1. Blanchard, R., and M. L. Pointud, "Rapport de Synthèse des Irradiations GF-1, GF-2, and GF-3," CEA Report DMG DR 34/78, November 16, 1978 (also General Atomic unpublished data).

2. OBJECTIVES

The objectives of the GF-1, GF-2, and GF-3 capsules are listed below in order of decreasing priority.

1. Serve as a qualification test for irradiation performance of TRISO-coated HEU $(8Th,U)O_2$ fissile fuel and BISO-coated ThO_2 fertile fuel.

2. Extend the empirical data base on TRISO- and BISO-coated fuels used to support generic HTGR property limits; i.e., use TRISO particle performance experience from the GF capsules to support the reference TRISO-coated UC_2 and ThO_2 fuel systems.

3. Evaluate alternate methods for inhibiting metallic fission product release and improving high-temperature stability of coated fuel particles, i.e., dopants in kernels and/or coatings.

4. Provide a comparative test to qualify CEA procedures and materials relative to GA in order to establish a basis for French HTGR technology.

Table 2-1* summarizes the different fuel rod types tested in capsules GF-1, GF-2, and GF-3 and also gives a brief description of the objectives for each type.

---

*Tables appear at the end of each section.

TABLE 2-1
OBJECTIVES OF DIFFERENT FUEL ROD TYPES TESTED IN CAPSULES GF-1, GF-2, AND GF-3

Fuel Rod Type	Coated Particle Type		Purpose
	Fissile	Fertile	
a	TRISO	BISO	Test fissile TRISO particles with oxide kernels and the potential performance improvement associated with a smaller kernel diameter (400 μm) compared to the reference 500-μm-diameter design.
b	TRISO	BISO	Test fissile TRISO particles with oxide kernels and the potential performance improvement associated with increasing the thickness of the buffer layer to 100 μm on the reference kernel diameter (500 μm).
b'	TRISO	BISO	Test fissile TRISO particles that have increased heavy metal loading density
c	TRISO	TRISO	Test a total TRISO system having oxide kernels and demonstrate a higher retention of fission products compared to a TRISO/BISO fuel system.
d	BISO	BISO	Test a total BISO system for comparative purposes with TRISO/BISO and TRISO/TRISO fuel systems.
e and e'	TRISO	BISO	Test the CERCA matrix containing two types of graphite (natural and artificial) and containing GA particles.
f and f'	TRISO	BISO	Test rods made by CEA that contain CERCA matrix and CEA-fabricated particles.

3. COATED PARTICLES

3.1. GENERAL ATOMIC REFERENCE FUEL SAMPLES

3.1.1. Description

Fissile and fertile coated particles with both TRISO and BISO designs were tested in the GF capsules. One of the fissile particle samples contained reference large high-temperature gas-cooled reactor (LHTGR) HEU uranium carbide kernels while the remaining fissile particle samples contained HEU mixed (8Th,U)O_2 kernels. All fertile particles had thorium oxide kernels. One batch of TRISO-coated particles containing carbon resin kernels was used in the fuel rods as inert particles. All kernels and coated particles were fabricated at GA according to the Fuel Materials Branch specifications (Ref. 3-1).

3.1.1.1. Fissile Particles. The (8Th,U)O_2 fissile particles were TRISO coated with the exception of one BISO-coated batch. In addition, a single batch of TRISO-coated, 200-μm diameter UC_2 [VSM (drop melting)] was tested; however, this fuel type was only tested as loose particles. The (8Th,U)O_2 kernels were either 400 μm or 500 μm in diameter. The 400-μm kernels were coated with a conservative TRISO design in order to provide high assurance of low particle failure fractions. TRISO-coated fuel with 500-μm kernels was based on the following design considerations:

1. A conservatively designed TRISO coating with a predicted end-of-life pressure vessel failure of 0.5% (Ref. 3-1).

2. A high heavy metal density TRISO coating design with a predicted end-of-life pressure vessel failure of 5% (Ref. 3-1).

Core design economics favor a TRISO particle design with a high heavy metal loading; consequently, large kernel diameters and thin TRISO coating layers are desirable, provided fuel performance and fuel fabrication requirements are met. The 500-μm-diameter, TRISO-coated (8Th,U)O_2 fuel particles were directed at establishing an acceptable upper limit to high heavy metal density TRISO design. BISO-coated (8Th,U)O_2 particles were also irradiated as part of a long-range program to develop fuel for axially zoned cores where metallic fission product release from BISO coated fuel could be limited by restricting use of these particles to cooler regions.

3.1.1.2. Fertile Particles. All fertile particles contained 500 μm kernels, with the majority of the samples being ThO_2 BISO-coated particles, i.e., the candidate reference HTGR fertile fuel (Ref. 3-2). One ThO_2 BISO sample was obtained by separating it from the parent batch using a gradient density column. This technique ensured that the particles would have a constant total coated particle density. In addition, one batch of TRISO-coated ThO_2 kernels was tested to define potential improvements in metallic fission product retention compared to the BISO particle design.

3.1.1.3. Inert Particles. The TRISO-coated inert particles are contained in the 200- to 300-μm carbon resin kernels.

3.1.2. Fabrication

All oxide kernels were made by a gel-supported precipitation technique. The VSM process was used to manufacture the UC_2 kernels. Inert carbon kernels were processed from cation exchange resin beads. After kernel fabrication particle coatings were deposited in a 127-mm fluidized bed coater. The TRISO coatings were fabricated with buffer from propylene, SiC from methyltrichlorosilane, and PyC from propylene. The BISO coatings were fabricated with buffer and PyC from propylene.

3.1.3. Properties

Summary descriptions of the kernel and coated particle properties are presented in Tables 3-1, 3-2, and 3-3. Fabrication coating parameters are given in Table 3-2.

3.2. GENERAL ATOMIC ADVANCED FUEL SAMPLES

Thirty-four batches representing four types of advanced coated particles were tested in the GF capsules. Particles were tested as unbonded samples and in bonded particle rings. The properties and number of particles being tested are given in Table 3-4.

3.3. FUEL RODS

3.3.1. Description

Five fuel rod types were made for the GF capsules and designated a, b, b', c, and d. Each rod type contains different batch combinations of fissile and fertile particles and graphite shim particles (impregnated 1099 isotropic graphite powder, Great Lakes Carbon Corporation). The basic raw materials used in manufacturing the matrix for rod injection consisted of pitch binder (A240 petroleum pitch, Ashland Oil Company), additives (octadecanol and polystyrene), and graphite flour (6353 natural flake graphite flour, Asbury Graphite Mills). A general description of fuel rod types irradiated in each capsule is given in Table 3-5.

3.3.2. Fabrication

Fuel rods for GF-1, GF-2, and GF-3 capsules were manufactured by near-reference HTGR and FSV processes according to Fuel Materials Branch specifications (documented in Ref. 3-1). The rods were approximately 15.73 mm in diameter by 50 mm in length and consisted of fissile, fertile, and inert coated particles; shim particles; and matrix. All rods contained 25 vol %

of shim particles, which is representative of highly shimmed rods in an HTGR plant design. Varying amounts of TRISO-coated inert particles were added to the rods to maintain a random close-packed particle array and meet the fuel particle and shim loading requirements. Green fuel rods were carbonized in-place or in a packed bed to 1000°C in nitrogen. All rods were high fired to 1800°C in argon.

3.4. CEA FUEL SAMPLES

3.4.1. Fissile Particles

Two batches of TRISO-coated and one batch of BISO-coated $(8Th,U)O_2$ fissile fuel particles were fabricated by CEA DMG at Grenoble. The kernel diameters ranged between 468 and 518 μm with other coating thicknesses comparable to GA-fabricated particles.

3.4.2. Fertile Particles

Two batches each of TRISO- and BISO-coated ThO_2 fuel having kernel diameters between 490 and 509 μm were fabricated by CEA DMG at Grenoble.

3.4.3. Properties

A summary description of kernel and coated particle properties is presented in Tables 3-6, 3-7, and 3-8.

3.4.4. Fuel Rods

Four fuel rods were fabricated by CEA at Saclay using the CERCA process, i.e., hot pressing a mixture of matrix and fuel particles into a cylindrical compact at ~200°C. Two rods designated e and f contained natural graphite in the matrix and the other rods (e' and f') contained artificial graphite.

3.4.5. Properties

A summary description of CEA-fabricated fuel rods is presented in Table 3-9.

REFERENCES

3-1. Young, C. A., D. P. Harmon, and C. Moreau, "Dossier No. 3 (Part 1) Preirradiation Report: GAC Fuel Materials for GF-1, GF-2, and GF-3 Irradiation Capsules," General Atomic unpublished data, December 15, 1974.

3-2. "HTGR Fuel Product Specification," General Atomic unpublished data, August 1979.

TABLE 3-1
SUMMARY DESCRIPTION OF GA-COATED PARTICLES IRRADIATED IN CAPSULES GF-1, GF-2, AND GF-3

Sample Data Retrieval Number	Kernel[a]		Coatings													Capsule Tested in (GF-)
				Buffer		IPyC			SiC			OPyC				
	Type	Diameter (μm)	Type	Thickness (μm)	Density (Mg/m^3)	Thickness (μm)	Density (Mg/m^3)	OPTAF[b]	Thickness (μm)	Density (Mg/m^3)	Fraction Defective[c] SiC	Thickness (μm)	Density (Mg/m^3)	Microporosity[d] (ml/kg OPyC)	OPTAF	
6151-00-010	UC_2	199	TRISO	97	1.18	35	1.94	1.19	31	3.20	(e)	44	1.80	6.77	1.11	1,3
6155-00-010	$(8Th,U)O_2$	403	TRISO	80	1.22	32	1.88	1.22	32	3.22	(e)	36	1.78	6.41	1.13	2,3
6155-00-020	$(8Th,U)O_2$	397	TRISO	78	1.15	27	1.92	1.11	31	3.22	(e)	41	1.76	7.51	1.14	1,3
6155-00-030	$(8Th,U)O_2$	410	TRISO	79	1.19	30	1.90	1.18	28	3.22	0.074	39	1.78	9.42	1.08	1,2
6155-01-010	$(8Th,U)O_2$	512	TRISO	100	1.22	30	1.96	1.20	27	3.22	(e)	40	1.78	9.19	1.13	2,3
6155-01-020	$(8Th,U)O_2$	502	TRISO	106	1.24	32	1.93	1.17	34	3.22	(e)	42	1.81	9.32	1.07	1,3
6155-01-030	$(8Th,U)O_2$	506	TRISO	103	1.23	31	1.95	1.24	27	3.21	0.089[f]	40	1.79	12.34	1.11	1,2
6155-02-010	$(8Th,U)O_2$	504	TRISO	77	1.13	26	1.94	1.25	28	3.21	(e)	40	1.81	9.36	1.13	2,3
6155-02-020	$(8Th,U)O_2$	505	TRISO	80	1.18	32	(g)	1.20	29	3.22	(e)	41	1.82	9.40	1.13	1,3
6155-02-030	$(8Th,U)O_2$	493	TRISO	79	1.16	29	1.94	1.22	30	3.22	0.068	39	1.87	12.93	1.11	1,3
6445-00-010	$(8Th,U)O_2$	513	BISO	90	1.17	(h)	(h)	(h)	(h)	(h)	(h)	90	1.83	(i)	1.12	1,2,3
6252-00-020	ThO_2	512	TRISO	74	1.16	27	1.84	1.25	31	3.21	(e)	42	1.81	15.30	1.24	2,3
6542-02-036	ThO_2	481	BISO	79	1.18	(h)	(h)	(h)	(h)	(h)	(h)	74	1.89	12.03	1.12	1,2,3
6542-02-037	ThO_2	474	BISO	73	1.18	(b)	(h)	(h)	(h)	(h)	(h)	80	1.89	12.42	1.12	3
6351-01-020	C	210-297	TRISO	(e)	(e)	29	1.76	1.09	29	3.22	(e)	36	1.75	9.08	1.12	1,2,3

(a) Uranium is approximately 93.15% enriched U-235.

(b) Optical anisotropy factor, relative units.

(c) Determined by X-radiographic evaluation of burned-back particles intruded with Hg at 69 MPa for 2 min.

(d) Mercury intrusion at 69 MPa.

(e) Not determined.

(f) Average of two separate measurements.

(g) Not determined, density estimated to be approximately 1.90 to 1.95 Mg/m^3.

(h) Not applicable.

(i) Not determined.

TABLE 3-2
FABRICATION COATING PARAMETERS FOR GA-COATED PARTICLES

Sample Data Retrieval Number	Fuel Type	Buffer Mean Coating Rate[a] (μm/min)	Inner Isotropic Mean Coating Rate[a] (μm/min)	SiC Mean Coating Rate[a] (μm/min)	Outer Isotropic Mean Coating Rate[a] (μm/min)	Outer Isotropic Active Coating Gas Volume Fraction[b] (C/C + L + D)
6151-00-010	Fissile TRISO	4.85	1.17	0.19	1.47	0.13
6155-00-010	Fissile TRISO	20.1	4.57	0.48	2.25	0.11
6155-00-020	Fissile TRISO	26.0	3.60	0.54	2.83	0.11
6155-01-010	Fissile TRISO	22.2	3.75	0.53	3.08	0.11
6155-01-020	Fissile TRISO	24.9	4.57	0.48	3.36	0.11
6155-02-010	Fissile TRISO	23.4	3.47	0.56	3.33	0.11
6155-02-020	Fissile TRISO	24.6	4.27	0.55	3.42	0.11
6445-00-010	Fissile BISO	33.3	(c)	(c)	8.57	0.22
6252-00-020	Fertile TRISO	24.0	7.14	0.13	4.24	0.13
6542-02-036	Fertile BISO	18.0	(c)	(c)	2.16	0.13
6542-02-037	Fertile BISO	18.0	(c)	(c)	2.16	0.13
6351-01-020	Inert TRISO	(d)	1.38	0.14	1.06	0.17

(a) Determined from measured coating rate.

(b) C = active coating gas flow rate ($C_2H_2 + C_3H_6$), L = levitation gas flow rate (Ar or He or N_2), and D = diluent gas rate (Ar or He or N_2 or H_2).

(c) Not applicable.

(d) Not determined.

TABLE 3-3
PROPERTIES OF GA TOTAL COATED PARTICLES IRRADIATED IN CAPSULES GF-1, GF-2, AND GF-3

Sample Data Retrieval Number	Mean Diameter (μm)	Particle Density(a) (Mg/m^3)	Fraction Defective: Coated Particles(b)	Fraction Defective: SiC(c)	Exposed Heavy Metal: Hydrolysis Test $\left(\frac{\text{g heavy metal}}{\text{g heavy metal}}\right)$	Exposed Heavy Metal: Leach Test: U (g U/g U)	Exposed Heavy Metal: Leach Test: Th (g Th/g Th)	Fission Gas Release(d)	Where Used(e)
6151-00-010	595	2.28	(f)	3×10^{-4}	(g)	$<10^{-7}$	$<10^{-7}$	4×10^{-7}	U
6151-00-010	713	3.31	(f)	5×10^{-4}	4×10^{-6}	1×10^{-7}	$<10^{-7}$	4×10^{-7}	U
6155-00-020	695	3.24	(f)	3×10^{-6}	$<6 \times 10^{-7}$	3×10^{-6}	3×10^{-6}	2×10^{-6}	U
6155-00-030(h)	728	3.34	(f)	7×10^{-4}	$<7 \times 10^{-7}$	$<10^{-7}$	6×10^{-6}	6×10^{-7}	a
6155-01-010	888	3.32	(f)	6×10^{-5}	$<6 \times 10^{-7}$	7×10^{-7}	$<10^{-7}$	1×10^{-6}	U
6155-01-020	885	3.34	(f)	9×10^{-6}	7×10^{-5}	6×10^{-7}	$<10^{-7}$	6×10^{-7}	U
6155-01-030(h)	884	3.33	7×10^{-4}	3×10^{-5}	7×10^{-4}	$<10^{-7}$	3×10^{-6}	2×10^{-7}	b,c
6155-02-010	831	3.72	8×10^{-4}	2×10^{-4}	$<6 \times 10^{-7}$	7×10^{-7}	1×10^{-6}	6×10^{-6}	U
6155-02-020	840	3.69	(f)	3×10^{-4}	$<6 \times 10^{-7}$	6×10^{-7}	1×10^{-6}	8×10^{-5}	U
6155-02-030(h)	812	3.74	(f)	8×10^{-4}	$<6 \times 10^{-7}$	7×10^{-6}	4×10^{-6}	3×10^{-7}	b'
6445-00-010	870	3.21	(f)	(i)	$<6 \times 10^{-7}$	$<10^{-7}$	$<10^{-7}$	6×10^{-8}	U,d
6252-00-020	833	3.77	(f)	3×10^{-4}	9×10^{-7}	(i)	$<10^{-7}$	(i)	U,c
6542-02-036	786	3.54	(f)	(i)	9×10^{-6}	(i)	8×10^{-5}	(i)	U,a,b,b',d
6542-02-037	768	3.54	(f)	(i)	9×10^{-6}	(i)	8×10^{-5}	(i)	U
6351-01-020	573	1.83	(f)	(i)	(i)	(i)	(i)	(i)	a,b,b',c,d

(a) Measured by air pycnometer.

(b) Determined by microscopic examination of particle batch radiograph.

(c) Determined by burn-leach test.

(d) Release rate/birth rate of Kr-85m at 1100°C.

(e) U denotes unbonded particle sample; a, b, b', c, d denote fuel rod types.

(f) No failures observed.

(g) Not determined.

(h) Composite of above two batches (i.e., -010 and -020).

(i) Not applicable.

TABLE 3-4

SUMMARY DESCRIPTION OF ADVANCED FUEL UNBONDED COATED PARTICLES AND BONDED PARTICLE RINGS TESTED IN GF-1, GF-2, AND GF-3

Description	Sample No.	Number of Particles			Kernel			Type	Coatings							
									Buffer		Inner PyC		ZrC		Outer PyC	
		GF-1	GF-2	GF-3	Type	Diam. (μm)	Density (gm/cc)		Thickness (μm)	Density (gm/cc)	Thickness (μm)	Density (gm/cc)	Thickness (μm)	Density (gm/cc)	Thickness (μm)	Density (gm/cc)
Doped Kernels	4-9-2 6111-107E	600	240	120	(2Al, 4Si, 8Th,U) O_2	500	9.357	BISO	89	1.11	-	-	-	-	88	1.820
	4-18-1 6111-71E	360	120	60	(8Th,U) O_2	500	9.917	BISO	94	1.04	-	-	-	-	88	1.789
	4-19-2 6111-101E	360	120	60	(.5 Si, 8Th,U) O_2	500	9.357	BISO	98	1.14	-	-	-	-	85	1.804
	4-19-1 6111-95E	360	120	60	(2 Si, 8Th,U) O_2	500	8.758	BISO	92	1.06	-	-	-	-	86	1.804
	4-18-2 6111-93E	360	240	60	(4 Si, 8Th,U) O_2	500	7.822	BISO	91	1.04	-	-	-	-	83	1.802
	4-10-1 6111-111E	360	120	60	(.5 Al, 8Th,U) O_2	500	9.99	BISO	105	1.12	-	-	-	-	95	1.823
	4-5-2 6111-109E	360	120	60	(2 Al, 8Th,U) O_2	500	9.75	BISO	93	1.12	-	-	-	-	94	1.823
	4-5-1 6111-103E	360	240	60	(4 Al, 8Th,U) O_2	500	9.06	BISO	95	1.08	-	-	-	-	88	1.812
	4-12-1 6111-117E	360	120	60	(.5Al,1Si, 8Th,U) O_2	500	5.27	BISO	93	1.05	-	-	-	-	96	1.817
	4-12-3 6111-105E	360	120	60	(2Al, 2Si, 8Th,U) O_2	500	8.38	BISO	95	1.04	-	-	-	-	84.3	1.817
	4-13-1 6111-99E	360	120	60	(2Al, 1Si, 8Th,U) O_2	500	8.72	BISO	96	1.13	-	-	-	-	100	1.799
Doped Kernels	4-12-2 6111-113E	360	240	60	(4Al, 4Si, 8Th,U) O_2	500	7.26	BISO	95	1.09	-	-	-	-	91	1.814
FRD Series Si BISO	6171-105E	-	240	120	(8Th,U) O_2	400	9.70	Silicon BISO (19% Si)	97	1.21	17	1.864	-	-	84	2.149
	6171-107E	-	240	120	(8Th,U) O_2	400	9.70	Silicon BISO (25% Si)	97	1.21	17	1.864	-	-	81	2.195
	6171-115E	-	240	120	(8Th,U) O_2	400	9.70	Silicon BISO (39% Si)	97	1.21	17	1.864	-	-	78	2.321
	6171-117E	-	240	120	(8Th,U) O_2	400	9.70	Silicon BISO (47.5% Si)	97	1.21	17	1.864	-	-	85	2.481
Si BISO	6171-119E	-	240	120	(8Th,U) O_2	400	9.70	Silicon BISO (40% Si)	97	1.21	17	1.864	-	-	61	2.417
LTI BISO	6171-67E	-	150	45	(8Th,U) O_2	400	9.70	BISO	97	1.21	-	-	-	-	80	1.784
	6171-65E	-	150	45	(8Th,U) O_2	400	9.70	BISO	97	1.21	-	-	-	-	81	1.847
	6171-41E	-	150	45	(8Th,U) O_2	400	9.70	BISO	97	1.21	-	-	-	-	87.3	1.936
HTI BISO	6222-19E	-	150	45	(8Th,U) O_2	400	9.70	BISO	97	1.21	-	-	-	-	87	1.718
	6222-25E	-	150	45	(8Th,U) O_2	400	9.70	BISO	97	1.21	-	-	-	-	76	1.583
ZrC TRISO Particles	6171-15E	120	-	-	UC_2	200	10.99	TRISO	120	1.0(a)	-	-	46	6.2(a)	64	1.8(a)
	6171-17E	120	-	-	(8Th,U) O_2	400	9.70	TRISO	84	1.0(a)	-	-	52	6.2(a)	75	1.8(a)
	6111-145E	120	-	-	(8Th,U) O_2	400	9.70	TRISO	110	.97	13	1.8(a)	45	6.2(a)	85	1.8(a)
	6111-147E	120	-	-	UC_2	200	10.99	TRISO	102	.98(a)	8	1.8(a)	45	6.2(a)	50	1.778
ZrC TRISO Particles for Bonded Rings	6171-15E	24	24	-	(8Th,U) O_2	400	9.70	TRISO	84	1.0(a)	-	-	52	6.2(a)	75	1.8(a)
	6171-17E	36	36	-	UC_2	200	10.99	TRISO	120	1.0(a)	-	-	46	6.2(a)	64	1.8(a)
	6111-145E	24	24	-	(8Th,U) O_2	400	9.70	TRISO	110	.97	13	1.8(a)	45	6.2(a)	85	1.8(a)
	6111-147E	36	36	-	UC_2	200	10.99	TRISO	102	.98(a)	8	1.8(a)	45	6.2(a)	50	1.778
													SiC			
OPTAF Series	6111-13 (1/64 in.)	9	-	8	Al_2O_3	1/64 in.	3.95	TRISO	-	-	36	1.782	30	3.2	31	1.975
	6111-13 (1 mm)	4	-	5	Al_2O_3	1 mm	3.95	TRISO	-	-	29	1.828	30	3.2	35	1.972
	6111-9 (1/64 in.)	10	-	10	Al_2O_3	1/64 in.	3.95	TRISO	-	-	36	1.782	30	3.2	43.7	1.942
	6111-9 (1 mm)	5	-	5	Al_2O_3	1 mm	3.95	TRISO	-	-	29	1.828	30	3.2	60	1.941
	6111-3 (1/64 in.)	4	-	4	Al_2O_3	1/64 in.	3.95	TRISO	-	-	36	1.782	30	3.2	36	1.959
	6111-3 (1 mm)	1	-	1	Al_2O_3	1 mm	3.95	TRISO	-	-	29	1.828	30	3.2	49	1.953
	6041-137 (1/64 in.)	4	-	4	Al_2O_3	1/64 in.	3.95	TRISO	-	-	36	1.782	30	3.2	27	1.965
OPTAF Series	6041-137 (1 mm)	1	-	1	Al_2O_3	1 mm	3.95	TRISO	-	-	29	1.828	30	3.2	23	1.981

(a) estimated

TABLE 3-5

SUMMARY DESCRIPTION OF GA FUEL RODS IRRADIATED IN CAPSULES GF-1, GF-2, AND GF-3[(a)]

		Coated Particles				Matrix[(c)]			Green Rod Dimensions (µm)									
		Fissile		Fertile			Pitch Coke[(e)]					Fuel Loading Uniformity[(g)]			Exposed Heavy Metal[(i)]	Defective SiC Coatings[(j)]		
Rod Type[(b)]	Data Retrieval Number 7161-003-	Type	Data Retrieval Number	Type	Data Retrieval Number	Macro-Porosity[(d)] (%)	Yield (%)	Apparent Density (Mg/m^3)	Diameter	Length	Particle Packing[(f)] (%)	U	Th	Fission Gas Release[(h)]	$\left(\frac{\text{g heavy metal}}{\text{g heavy metal}}\right)$	U (g U/g U)	Th (g Th/g Th)	Primary Variables
										GF-1 Capsule								
a	01-4	$(Th,U)O_2$ TRISO	6155-00-030	ThO_2 BISO	6542-02-036	35	32	0.13	1.573	5.016	58	1.01	1.02	1×10^{-5}	2×10^{-4} $<6 \times 10^{-7}$	(k)	(l)	Conservative, 400 µm kernel, TRISO fissile
a	01-5	$(Th,U)O_2$ TRISO	6155-00-030	ThO_2 BISO	6542-02-036	35	33	0.13	1.573	4.991	58	1.01	1.06	3×10^{-6}	2×10^{-4} $<5 \times 10^{-7}$	(k)	(l)	Conservative, 400 µm kernel, TRISO fissile
b	02-5	$(Th,U)O_2$ TRISO	6155-01-030	ThO_2 BISO	6542-02-036	33	32	0.13	1.573	5.018	57	1.07	1.02	2×10^{-6}	$<5 \times 10^{-7}$	(k)	(l)	Conservative, 500 µm kernel, TRISO fissile
b'	03-5	$(Th,U)O_2$ TRISO	6155-02-030	ThO_2 BISO	6542-02-036	34	35	0.14	1.573	5.040	57	1.09	1.06	2×10^{-6}	5×10^{-4}	(k)	(l)	Less conservative, 500 µm kernel, TRISO fissile
										GF-2 Capsule								
a	01-6	$(Th,U)O_2$ TRISO	6155-00-030	ThO_2 BISO	6542-02-036	35	34	0.13	1.573	5.031	57	1.01	1.08	2×10^{-6}	2×10^{-4} $<5 \times 10^{-7}$	(k)	(l)	Conservative, 400 µm kernel, TRISO fissile
a (packed bed)	08-4	$(Th,U)O_2$ TRISO	6155-00-030	ThO_2 BISO	6542-02-036	31	25	0.10	1.573	4.994	57	1.02	1.07	3×10^{-6}	$<1 \times 10^{-6}$	(k)	(l)	Conservative, 400 µm kernel, TRISO fissile
c	04-6	$(Th,U)O_2$ TRISO	6155-01-030	ThO_2 TRISO	6252-00-020	31	31	0.11	1.573	4.983	58	1.07	1.04	2×10^{-6}	$<1 \times 10^{-6}$	8×10^{-4}	2×10^{-3}	Conservative, TRISO fissile, 500 µm kernel, TRISO fertile
c	04-7	$(Th,U)O_2$ TRISO	6155-01-030	ThO_2 TRISO	6252-00-020	31	32	0.12	1.573	5.003	57	1.01	1.03	1×10^{-6}	$<1 \times 10^{-6}$	8×10^{-4}	2×10^{-3}	Conservative, TRISO fissile, 500 µm kernel, TRISO fertile
d	05-4	$(Th,U)O_2$ BISO	6445-00-010	ThO_2 BISO	6542-02-036	37	32	0.12	1.573	4.969	57	1.07	1.04	8×10^{-7}	$<1 \times 10^{-6}$	(l)	(l)	500 µm kernel, BISO fissile
d	05-5	$(Th,U)O_2$ BISO	6445-00-010	ThO_2 BISO	6542-02-036	37	31	0.12	1.573	4.971	58	1.03	1.03	1×10^{-6}	$<1 \times 10^{-6}$	(l)	(l)	500 µm kernel, BISO fissile
										GF-3 Capsule								
b	02-4	$(Th,U)O_2$ TRISO	6155-01-030	ThC_2 BISO	6542-02-036	33	33	0.13	1.573	4.984	58	1.11	1.05	3×10^{-6}	$<6 \times 10^{-7}$	(k)	(l)	Conservative, 500 µm kernel, TRISO fissile
b'	03-4	$(Th,U)O_2$ TRISO	6155-02-030	ThC_2 BISO	6542-02-036	34	34	0.13	1.573	5.011	57	1.07	1.04	3×10^{-7}	6×10^{-4}	(k)	(l)	Less conservative, 500 µm kernel, TRISO fissile
c	04-4	$(Th,U)O_2$ TRISO	6155-01-030	ThC_2 TRISO	6252-00-020	31	32	0.12	1.574	4.957	58	1.02	1.04	1×10^{-6}	$<1 \times 10^{-6}$	8×10^{-4}	2×10^{-3}	Conservative, TRISO fissile, 500 µm kernel, TRISO fertile
c	04-5	$(Th,U)O_2$ TRISO	6155-01-030	ThC_2 TRISO	6252-00-020	31	30	0.11	1.573	4.971	58	1.05	1.07	1×10^{-6}	$<1 \times 10^{-6}$	8×10^{-4}	2×10^{-3}	Conservative, TRISO fissile, 500 µm kernel, TRISO fertile

(a) Required fuel loadings are 0.130 g of U-235 and 4.371 g of Th-232 per rod. Each rod contains 25 vol % 1099 impregnated shim (F0125) and TRISO-coated carbon inert particles (6351-01-020).

(b) All rods cured-in-place except where noted.

(c) Fuel rod matrix has A-240 pitch for the binder, 6353 natural flake graphite for the filler, and SC011 as an additive.

(d) Determined from metallographic cross section of a companion fired rod from same batch.

(e) Calculated from green and fired fuel rod weights and nominal particle weights.

(f) Calculated from fired rod and nominal particle parameters.

(g) Ratio of maximum gamma count rate to mean count rate determined from gamma counting both ends of rod.

(h) Release rate/birth rate of Kr-85m at 1100°C.

(i) Determined by hydrolysis test. < sign denotes value below the detectability of the apparatus. A correction factor to account for total conversion of ThO_2 to ThC_2 has been applied to rods having detectable contamination. Measurements made on one or two companion rods. Mean value given if two numbers were similar; both values given if numbers differ by orders of magnitude.

(j) Determined by burn-leach test; measurement made on companion rod from same batch.

(k) Not determined.

(l) Not applicable.

TABLE 3-6
PROPERTIES OF CEA TOTAL COATED PARTICLES IRRADIATED IN CAPSULES GF-2 AND GF-3

Particle Batch No.	Mean Diameter(a) (μm)	Particle Density(b)	Mean Particle Weight(c) (mg)	Surface Contamination		Faceting (MIFI)(d)	Crushing Force (kg)	Where Used	
				Acid Leach (ppm/ particle)	Activity (μ Ci)			Capsule	Test Type(e)
MG 156	821	3.14	0.905	Th = 6 U = 5	1.5 x 10^{-8}	3.96	2.2	GF-2,-3	U,f
MG 165	857	3.13	1.024	Th = 1 U = 1	1 x 10^{-8}	3.76	2.3	GF-2	U
MG 175	864	3.13	1.021	Th = 1.3 U ≤ 0.5	5.9 x 10^{-8}	3.82	2.3	GF-2,-3	U
MG 178	885	3.19	1.155	(f)	35 x 10^{-8}	3.88	2.2	GF-2,-3	U,f
MG 197	845	2.88	0.898	Th = 7 U = 4	2.3 x 10^{-8}	2.92	(f)	GF-2,-3	U
MG 199	822	3.11	0.882	Th = 1.1 U = 0.5	0.5 x 10^{-8}	2.76	(f)	GF-2,-3	U
MG 207	810	3.29	0.881	Th = 8 U = 3	10 x 10^{-8}	3.65	1.9	GF-3	U

(a) Measured by radiography.

(b) Density by Archimedes' pressure.

(c) By weight after coating.

(d) MIFI = index of variation in form between 1 for the poor form and 4 for the spherical form.

(e) U denotes unbonded particle sample; f denotes CEA fuel rod type.

(f) Not determined.

TABLE 3-7
FABRICATION COATING PARAMETERS FOR CEA-COATED PARTICLES

Particle Batch Number	Fuel Type	Buffer Mean Coating Rate (μm/min)	Seal Coat Mean Coating Rate (μm/min)	Inner Isotropic Mean Coating Rate (μm/min)	SiC Mean Coating Rate (μm/min)	Outer Isotropic Mean Coating Rate (μm/min)	Outer Isotropic Active Coating Gas Volume Fraction[(b)] (C/C + L + D)
MG 156	Fertile BISO	11.5	11.5	(a)	(a)	2.22	0.3
MG 165	Fertile TRISO	10.8	10.8	2.54	0.17	2.22	
MG 175	Fertile TRISO	11.79	11.79	2.52	0.40	2.25	
MG 173	Fissile TRISO	14.0	14.0	2.80	0.20	2.35	
MG 197	Fissile BISO	11.7	11.7	(a)	(a)	2.18	
MG 199	Fissile TRISO	11.8	11.8	2.7	0.42	2.25	
MG 207	Fertile BISO	15.1	15.1	(a)	(a)	4.5	

(a) Not applicable.

(b) C = volume of C_3H_6, L = volume of inert levitation gas Ar, and D = volume of H_2 diluent gas.

TABLE 3-8
SUMMARY DESCRIPTION OF CEA-COATED PARTICLES IRRADIATED IN CAPSULES GF-2 AND GF-3

Particle Batch No.	Kernel		Coatings											Capsule Tested in (GF-)
				Buffer		IPyC			SiC		OPyC			
	Type	Diameter (μm)	Type	Thickness[a] (μm)	Density (Mg/m^3)	Thickness (μm)	Density (Mg/m^3)	DAR[b] (Optical Anisotropy)	Thickness (μm)	Density (Mg/m^3)	Thickness (μm)	Density[c] (Mg/m^3)	DAR (Optical Anisotropy)	
MG 156	ThO_2	490	BISO	85	1.13	(d)	(d)	(d)	(d)	(d)	80	1.90	1.010	2,3
MG 155	ThO_2	490	TRISO	89	1.21	30	1.93	1.022	22	3.185	40	1.86	1.016	2
MG 175	ThO_2	490	TRISO	92	1.12	27	1.95	1.022	26	3.195	39	1.85	1.018	2,3
MG 178	$(8Th,U)O_2$	518	TRISO	93	1.09	29	1.95	1.028	25	3.195	40	1.88	1.016	2,3
MG 197	$(8Th,U)O_2$	477	BISO	97	1.11	(d)	(d)	(d)	(d)	(d)	87	1.85	1.014	2,3
MG 199	$(8Th,U)O_2$	468	TRISO	90	1.11	27	1.87	1.022	24	3.195	37	1.85	1.020	2,3
MG 207	ThO_2	509	BISO	84	1.08	(d)	(d)	(d)	(d)	(d)	72	1.92	1.014	3

(a) Mean by radiography and photodensitometry.

(b) DAR (window diameter = 15 μm); DAR $\approx$ OPTAF and $BAF_0 \approx 0.27 \times OPTAF + 0.733$, where OPTAF is optical anisotropy factor and BAF_0 is Bacon anistropy factor determined by Seibersdorf device using 25 μm spot diameter.

(c) By flotation.

(d) Not applicable.

TABLE 3-9
SUMMARY DESCRIPTION OF FUEL RODS IRRADIATED IN CAPSULES GF-1 AND GF-3

Fuel Rod		Irradiated In		Particle Loadings Per Rod								Volume Fraction (Fissile + Fertile)	Inert		Matrix		Total Uranium Per Rod (g)	Total Thorium Per Rod (g)	Rod Dimensions (mm)				Rod Weight (g)
				Fissile				Fertile											Diameter				
Type	Number	Capsule	Cell	Type	Number	Weight (g)	No. of Particles	Type	Number	Weight (g)	No. of Particles		Weight (g)	No. of Particles	Type (CERCA)	Density (Mg/m^3)			Top	Middle	Bottom	Height	
e	237	GF-1	1	(8Th,U)O$_2$ TRISO	6155-01-020	2.68	2371	ThO$_2$ BISO	6542-01-036	6.62	7937	0.27	1.355	7527	LCL 8102 Natural	1.6	0.140	4.873	15.82	15.81	15.80	50.41	20.843
e'	239	GF-1	1	(8Th,U)O$_2$ TRISO	6155-01-020	2.68	2371	ThO$_2$ BISO	6542-01-036	6.62	7937	0.27	1.355	7527	LCL 8418 Artificial	1.6	0.140	4.873	15.84	15.83	15.83	50.40	20.820
f	815	GF-3	1	(8Th,U)O$_2$ TRISO	MG 178	2.587	2240	ThO$_2$ BISO	MG 156	7.165	7917	0.307	0.589	3272	LCL 8102 Natural	1.6	0.1345	4.908	15.80	15.81	15.80	50.38	20.460
f'	817	GF-3	1	(8Th,U)O$_2$ TRISO	MG 178	2.587	2240	ThO$_2$ BISO	MG 156	7.165	7917	0.307	0.589	3272	LCL 8418 Artificial	1.4	0.1345	4.908	15.76	15.76	15.77	50.09	19.048

4. DESCRIPTION OF IRRADIATION

4.1. IRRADIATION FACILITIES

The GF-1, GF-2, and GF-3 capsules were irradiated in a TUMULT G device. TUMULT G occupied one-quarter of the available core penetrations in the Siloe reactor (Grenoble, France) and consisted of four independent cylindrical compartments each ~100 mm long with a maximum usable diameter of 15.76 mm. Figure 4-1* is a schematic diagram showing the individual components of the TUMULT G device and the specific Siloe core locations for GF-1, GF-2, and GF-3. The temperature in each of the individual cells was monitored by a tungsten-sheathed Chromel/Alumel (C/A) thermocouple and regulated by a common Ne-He gas mixture. Figures 4-2 and 4-3 are schematic diagrams showing the fuel rod and loose particle cell arrangements in the TUMULT G device for irradiation capsules GF-1, GF-2, and GF-3. The flux dosimeters used for these capsules were Cu, CuO, and VCo alloys; the measured thermal and fast flux axial profiles for Siloe core locations 45G and 47G are shown in Figs. 4-4 and 4-5, respectively. Table 4-1 provides a summary description of the irradiation test conditions for capsules GF-1, GF-2, and GF-3. A brief description of the thermal and neutron fluence calculations is presented in the following sections; more detailed information is included in Ref. 4-1.

4.1.1. Thermal Measurements and Calculations

Thermal analysis of capsules GF-1, GF-2, and GF-3 was based on in-pile temperature measurements using C/A thermocouples and computer codes that described heat fluxes and thermal resistances. This procedure enables fuel temperatures to be calculated as a function of capsule position and time during irradiation. The controlling thermocouples were located at the inner containment wall and in the graphite bodies adjacent to the fuel compacts

---

*Figures appear at the end of each section.

(Fig. 4-2). These measured temperatures were below 1100°C and were monitored with C/A thermocouples in an Inconel sheath. The Inconel sheath was covered with a deposit of tungsten in order to avoid diffusion of the nickel into the graphite. This was essential to prevent premature failure of TRISO-coated fuel by Ni/SiC attack (Fig. 4-6). The C/A thermocouples are stable during irradiation and are not affected by alloy composition changes caused by transmutation (Ref. 4-3); consequently, no irradiation correction factors are required. Material thermal properties used in the calculation of GF-1, GF-2, and GF-3 temperatures are listed in Table 4-2. It should be noted in this table that the fuel rod thermal conductivity undergoes a 30% reduction during irradiation. This has been substantiated by actual measurements on irradiated rods (see Section 5.5). In addition to temperature measurements, the following equations were used to relate measured temperatures to calculated fuel temperatures:

$$T_s - T_i = (T_s - T_c)/10 \qquad (4\text{-}1)$$

$$T_s - T_c = 1.11 \times (T_i - T_c) \quad , \qquad (4\text{-}2)$$

where T_s = surface temperature of fuel compact,

T_i = measured graphite temperature,

T_c = measured container wall temperature (controlled to ≤750°C to maintain design fuel temperature).

These equations were established empirically by using a simulated mockup of the GF-1, GF-2, and GF-3 capsule design with electrical heaters serving as the heat source (Ref. 4-1). These equations served to account for the geometry and complicated heat fluxes in the system; consequently, a simplified one-dimensional heat flux thermal calculation was possible for relating measured temperatures to calculated temperatures and powers. The temperature at the fuel rod axis (T_a) is calculated as:

$$T_a = T_s + \Delta T_{(k)} \quad , \tag{4-3}$$

where $\Delta T_{(k)}$ is the calculated fuel rod radial temperature drop for a given power level. The calculated mean fuel surface and axial centerline temperatures for each cycle of capsules GF-1, GF-2, and GF-3 are shown in Section 4.1.2 (Figs. 4-10 through 4-21). As a point of reference, the fuel rod volume average temperature ($T_{\bar{v}}$) is:

$$T_{\bar{v}} = 1/V \int_o^{r_o} (T_a - br^2) \times 2\pi \times dr = (T_a - T_s)/2 \tag{4-4}$$

where V = volume of fuel rod,

r_o = radius of fuel rod,

$b = (T_a - T_s)/r_o^2$.

The corresponding time-volume average temperature is defined as:

$$T_{\bar{v},t} = 1/t \int_o^t T_{\bar{v}}(t)dt \quad , \tag{4-5}$$

where t is the irradiation time. Average temperatures are calculated in a like manner for the center of the fuel rod ($T_{a,\bar{t}}$) and for the surface ($T_{s,\bar{t}}$) of the fuel rod. These time-averaged temperatures for each of the irradiation cells in capsules GF-1, GF-2, and GF-3 are listed in Table 4-3. The 2σ uncertainty band on reported temperatures in capsules GF-1, GF-2, and GF-3 is estimated at ~100°C. This accounts for uncertainties associated with fuel rod thermal conductivity, fuel heat generation rate (fission and gamma), and fuel rod/graphite radial gap widths. A more detailed discussion of thermal analysis uncertainties in irradiation capsule tests is presented in Ref. 4-4.

4.1.2. Neutron Fluence Calculations

Neutron fluence in the Siloe reactor is measured in terms of graphite damage units, which are then transposed to equivalent HTGR ($E > 29$ fJ) fluence units. The neutron-induced lattice displacement rate in graphite depends on the probability of a neutron reaction occurring, $\sigma_S(E)$, and the number of lattice displacements resulting from each reaction, $p(E)$. Therefore, a displacement cross section can be defined as:

$$\sigma_D(E) = \sigma_S(E)p(E) \quad ,$$

where $\sigma_D(E)$ = displacement cross section; the displacement rate per unit neutron flux of energy E,

$\sigma_S(E)$ = neutron reaction cross section,

$p(E)$ = displacement weighing function.

The displacement cross section is a material-dependent parameter. Neutron reaction cross sections are available from sources such as ENDF/B* libraries. The displacement weighting functions are derived from physics considerations that account for neutron energy levels and atomic bonding energies. The displacement weighting function most widely used for interpretation of graphite irradiation results was developed by Thompson and Wright (Ref. 4-5). The displacement rate for a material at a given flux position in the reactor is

$$D = \int_0^\infty \sigma_D(E)\phi(E)dE \quad , \tag{4-6}$$

where D is the displacement rate and $\phi(E)$ is the neutron flux at energy E. The above expression is valid provided the energy dependence of neutron flux does not change during irradiation. Furthermore, a convenient

---

*ENDF is the Evaluated Nuclear Data File and is the national reference set of evaluated cross section data.

simplification for graphite is to select a limiting energy (E_L) value of 29 fJ (0.18 MeV); i.e., σ_D for $E > E_L$ is equal to $\sigma_D(\bar{E}_L)$. This means graphite has a constant displacement cross section for energies >29 fJ.

The equivalent HTGR fluence for damage in graphite is defined as follows:

$$\Phi(E_L)_{HTGR} = \frac{\int_0^\infty \int_{t_1}^{t_2} \sigma_D(E)\phi(E,t)dEdt}{\int_0^\infty \sigma_D(E)\phi(E)_{HTGR}dE \Big/ \int_{E_L}^\infty \phi(E)_{HTGR}dE} \quad , \tag{4-7}$$

$$\Phi(E_L)_{HTGR} = \frac{\text{total displacements}}{\bar{\sigma}(E_L)_{HTGR}} \quad , \tag{4-8}$$

where
$\bar{\sigma}_{HTGR}$ = effective displacement cross section for an HTGR spectrum above energy E_L,
$\phi(E,t)$ = neutron flux in the irradiation test (Siloe or HTGR flux),
$\Phi(E_L)_{HTGR}$ = equivalent HTGR fluence for damage in graphite for energy above E_L,
$t_2 - t_1$ = extent of irradiation test.

Physically, $\Phi(E_L)_{HTGR}$ is the neutron fluence above energy E_L in an HTGR that is required to produce the number of displacements which occurred in a particular irradiation test.

Other displacement damage characteristics have been defined for use in comparison of damage in graphite. The "equivalent fission fluence for damage in graphite" Φ_G is defined as follows:

$$\Phi_G = \frac{\displaystyle\int_{t_1}^{t_2} \int_0^{\infty} \sigma_D(E)\sigma(E,t)dEdt}{\displaystyle\int_0^{\infty} \sigma_D(E)\chi(E)dE \Big/ \int_0^{\infty} \chi(E)dE} \quad , \tag{4-9}$$

or

$$\Phi_G = \frac{\text{total displacements}}{\bar{\sigma}_x} \quad , \tag{4-10}$$

where $t_2 - t_1$ = duration of the irradiation test,

$\bar{\sigma}_x$ = fission spectrum average cross section [$\chi(E)$ is the neutron fission spectrum],

$\phi(E,t)$ = neutron flux in the irradiation test (Siloe or HTGR flux).

Physically, Φ_G is the fluence required in a fission spectrum to produce the number of displacements that occurred in a particular irradiation test.

Using Φ_G as an equivalent basis for comparison, the Siloe and HTGR reactor spectra have the following fluence equivalence (Ref. 4-3):

$$\Phi(E > 161 \text{ fJ})_{Siloe} \times 2 = \Phi_G \quad , \tag{4-11}$$

$$\Phi(E > 29 \text{ fJ})_{HTGR} \times 1.25 = \Phi_G \quad . \tag{4-12}$$

These equations imply the following fluence equivalence:

$$\Phi(E > 161 \text{ fJ})_{Siloe} \times 1.6 = \Phi(E > 29 \text{ fJ})_{HTGR} \quad . \tag{4-13}$$

Figures 4-4 and 4-5 are plots of the axial profiles for thermal and fast flux measured for the Siloe reactor. The flux dosimeters used were Cu, CuO, and VCo alloys. Equation 4-13 was used to convert a measured Siloe fluence (E > 161 fJ) to a corresponding HTGR fluence (E > 29 fJ). The corresponding fast and thermal axial fluence profiles for capsules GF-1, GF-2, and GF-3 are plotted in Figs. 4-7, 4-8, and 4-9. In addition, plots of the equivalent HTGR fast fluence versus irradiation time for capsules GF-1, GF-2, and GF-3 are shown in Figs. 4-10 through 4-21.

4.1.3. Heavy Metal Burnup Calculations

Heavy metal burnup is a measure of the total fissions that have occurred in a fuel sample during irradiation, and it is proportional to the amount of fission products generated. The heavy metal burnup of each fuel sample irradiated in GF-1, GF-2, and GF-3 was calculated using the APPOLLO computer code, a code that subdivides thermal and epithermal neutron energy levels into 99 separate groups.

Required inputs are reactor power history, average thermal fluences, initial uranium and thorium loadings, macroscopic cross sections, and fission yields. Isotopic fission yields were obtained from a compilation of Meek and Rider (Ref. 4-6). The cross sections used in the program were normalized relative to the thermal fluence measured by cobalt dosimetry (refer to Section 4.1.2) and are listed below:

	Fission Cross Section (barns)	Capture Cross Section (barns)
U-235	606	129
U-233	695	72
Th-232	--	22

The APPOLLO code was used to calculate the burnup for both U-235 and thorium (U-233) at the end of irradiation. However, because of the complexity and computer run time, a simplified calculation was performed to determine burnups at the end of each irradiation cycle. This simplified code was used to provide a basis for noble fission gas release [rate of release/rate of birth (R/B)] measurements during each cycle. The simplified code was capable of calculating isotopic concentrations and burnups to within ±5% of the more exact APPOLLO calculations.

4.1.4. Fission Gas Release Measurements

The inert sweep gas (Ne/He) used to control fuel temperatures in each cell was sampled every 10 days to monitor fission gas release from fuel specimens during irradiation. Six short-lived gaseous fission product isotopes (Kr-85m, Kr-87, Kr-88m, Kr-89, Xe-137, and Xe-138) were measured. These isotopes were of primary interest because they constitute the main source of gaseous activity released from failed fuel, thereby affording a direct means of determining fuel performance during irradiation. The R/B determinations were made by allowing equilibration of gaseous activity through a standard tube prior to sampling. After equilibration, a gas sample was withdrawn into an evacuated vial and gamma counted using a Ge(Li) detector coupled with a multichannel analyzer. A standard decay time was used to permit transport of the gas samples to the counting room. The daughter product, Rb-89, was used for determining the yield of the short-lived Kr-89 isotope, and the longer-lived isotopes (Kr-85m, Kr-87, Kr-88m, Xe-137, and Xe-138) were counted directly. Absolute quantities of all isotopes were calculated to determine the amount of gas released at the surface of the samples. This was accomplished by knowing the flow rates of the sweep gas from each cell to the sampling station. In-pile fission gas release measurements provide a direct measure of fuel performance. Specifically, gas release due to exposed U and/or Th contamination and gas release due to fuel failure are measured. The following equation defines individual contributors to R/B:

$$R/B = \left[\frac{(U_c \cdot F_{U-235} \cdot Y_{U-235}) + (T_c \cdot F_{U-233} \cdot Y_{U-233})}{(F_{U-235} \cdot Y_{U-235}) + (F_{U-233} \cdot Y_{U-233})}\right]_{\text{contamination}}$$

$$+ \left[\frac{(X_{\text{fissile}} \cdot R_{\text{fissile}} \cdot F_{U-235} \cdot Y_{U-235}) + (X_{\text{fertile}} \cdot R_{\text{fertile}} \cdot F_{U-233} \cdot Y_{U-233})}{(F_{U-235} \cdot Y_{U-235}) + (F_{U-233} \cdot Y_{U-233})}\right]_{\substack{\text{fuel}\\ \text{failure}}} , \tag{4-14}$$

where R/B = total release per birth,

U_c = beginning-of-life uranium contamination measured by TRIGA,

T_c = beginning-of-life thorium contamination measured on companion rods using LINAC or thorium hydrolysis test,

F_{U-235} = fissions from U-235,

F_{U-233} = fissions from U-233,

Y_{U-235} = yield of a particular isotope per U-235 fission (Y_{U-235} for Kr-85m = 0.013),

Y_{U-233} = yield of a particular isotope per U-233 fission (Y_{U-233} for Kr-85m = 0.022),

$X_{fissile}$ = fissile particle failure fraction,

$X_{fertile}$ = fertile particle failure fraction,

$R_{fissile}$ = fractional release of a certain isotope per failed TRISO particle,

$R_{fertile}$ = fractional release of a certain isotope per failed BISO particle.

The following points are worth noting regarding Eq. 4-14 and in-pile R/B measurements:

1. At the beginning-of-life and in the absence of fuel failure, the contamination term dominates R/B measurements.

2. At beginning-of-life the fraction of fissions in fissile fuel is much greater than in fertile fuel ($F_{U-235} > F_{U-233}$); this reverses at end-of-life ($F_{U-233} > F_{U-235}$). This implies that either fissile contamination and/or failure dominates the R/B measurement during the early part of irradiation, and fertile contamination and/or failure dominates R/B near end-of-life.

3. Short-lived isotopes, such as Kr-85m, are a measure of instantaneous fission gas release and do not account for time-dependent diffusive release. However, long-lived isotopes such as Kr-85 account for the cumulative time-dependent diffusive release of gases occurring in surface contamination or in failed fuel.

The resulting in-pile R/B measurements for Kr-85m and Kr-85 are plotted in Figs. 4-22 through 4-27 for GF-1, GF-2, and GF-3. Loose particle cell measurements are not included in these figures because of the wide variety of fuel types tested in each cell and the inability to correlate R/B release with a particular fuel type. In addition, in-pile R/B measurements on the long-lived isotopes Kr-87, Kr-88, Xe-133, Xe-135m, and Xr-138 are included in Appendix A.

REFERENCES

4-1. Gentil, J., et al., "Irradiation de Combustible Capsules GF-1, GF-2, and GF-3, Dossier No. 2," CEA Report PI/SEDTI 1321-73/JG/PV, August 22, 1973 (also General Atomic unpublished data).

4-2. Janvier, J. C., and R. Blanchard, "Postirradiation Examination of CORAIL IV A and B," CEA Compte Rendu DMG 29/74, April 24, 1974 (also General Atomic unpublished data).

4-3. Sandefur, N. L., J. S. Steibel, and R. J. Grenda, "EMF Drift of Chromel/Alumel and W-3% Re/W-25% Re Thermocouples Measured In-Pile to High Neutron Exposures," USAEC Report Gulf-GA-A12501, General Atomic Company, May 24, 1973.

4-4. Scott, C. B., D. P. Harmon, and J. F. Holzgraf, "Postirradiation Examination of Capsules P13R and P13S," General Atomic Report GA-A13827, October 8, 1976.

4-5. Thompson, M. W., and S. B. Wright, "A New Damage Function for Predicting the Effect of Reactor Irradiations on Graphite in Different Neutron Spectra," J. Nucl. Mater. 16, 146 (1965).

4-6. Meek, M. E., and B. F. Rider, "Compilation of Fission Product Yields," General Electric Company, Vallecitos Nuclear Center, Report NEDO-12154/71 NED 41, January 1972.

TABLE 4-1
SUMMARY DESCRIPTION OF IRRADIATION CONDITIONS FOR CAPSULES GF-1, GF-2, AND GF-3

Capsule	Cell	Fuel Description[(a)]	Mean Temperature[(b)] (°C)[(a)]	Maximum Cell Fluence (10^{25} n/m^2) (E > 29 fJ)$_{HTGR}$	Mean Fluence (10^{25} n/m^2) (E > 29 fJ)$_{HTGR}$	Kernel Burnup (% FIMA)		Date Irradiation Began	Date Irradiation Ended	Length of Irradiation (h)	Siloe Position	General Operating Conditions
						Fissile (8Th,U)O$_2$	Fertile ThO$_2$					
GF-1	4	Loose particles and coupons	1149	--	4.4	7.10	1.10	10/31/73	9/24/74	5130 (10 cycles)	45D	Functioned well. Some thermocouples failed because of the reaction between the thermocouple well and the tungsten deposit.
	3	2 rods (types b and b')	1248 to 1311	--	6.4	9.35	1.10					
	2	2 rods (type a)	1252 to 1350	6.9	6.7	9.70	2.40					
	1	2 rods (types e and e'	1149 to 1216	--	5.2	8.53	1.67					
GF-2	4	Loose particles	1183 to 707[(c)]	--	3.7	5.29	0.51	1/3/74	12/19/74	4784 (10 cycles)	45G and 47D	Irradiation terminated prematurely following expulsion of cell 2 contents into gas tube.
	3	2 rods (type c)	1024 to 1024	--	4.5	7.40	1.17					
	2	2 rods (type a)	1033 to 1084	5.1	5.0	7.59	1.25					
	1	2 rods (type d)	1011 to 988	--	3.8	6.48	0.81					
GF-3	4	2 rods (type c)	1165 to 1199	--	6.6	9.02	1.97	1/31/74	7/25/75	8714 (17 cycles)	47G	Functioned very well although some thermocouples failed.
	3	Loose particles and coupons	1028	--	9.4	11.07	3.43					
	2	2 rods (types b and b')	1043 to 1120	10.2	9.8	11.40	3.55					
	1	2 rods (types f and f')	1027 to 1074	--	7.4	9.53	2.24					

(a) Refer to Section 2 for a description of rod types and loose particle cells.
(b) The two values given correspond to the beginning and end of irradiation and are based on calculations that assume a 30% reduction in fuel rod thermal conductivity.
(c) The temperature in cell 4 of GF-2 decreased.

TABLE 4-2
THERMAL PROPERTIES USED IN CALCULATION OF GF-1, GF-2, AND GF-3 CAPSULE TEMPERATURES

	Thermal Property		
Capsule Component	Thermal Conductivity[a] (W/cm-°C)	Thermal Dilatation (°C^{-1})	Emissivity
Fuel rod compacts	0.104, 0.073[b]	5×10^{-6}	1
Graphite sleeve	0.45	5×10^{-6}	1
Inner containment	$(0.139 + 0.18 \times 10-2 \times T)$	$(16 + 0.4 \times 10^{-2} \times T) \times 10^{-6}$	0.6
Bridge to primary containment	$(0.233 - 0.227 \times 10^{-3} \times T + 0.568 \times 10^{-6} \times T^2)$	$(10.5 + 0.3 \times 10^{-2} \times T) \times 10^{-6}$	0.4
Helium	$(1.47 + 3.35 \times 10^{-3} \times T - 0.56 \times 10^{-6} \times T^2) \times 10^{-3}$	--	--
Neon	$(0.5 + 0.8 \times 10^{-3} \times T) \times 10^{-3}$	--	--

[a] T defines temperature dependence in °C.

[b] End-of-life fuel rod thermal conductivity (30% reduction from initial preirradiation value.

TABLE 4-3
IRRADIATION TEMPERATURES OF CAPSULES GF-1, GF-2, AND GF-3

Capsule	Cell	Fuel Description	Fuel Centerline Temperature (°C)			Volume Average Temperature (°C)			Fuel Service Temperature (°C)			Average Fuel Surface Temperature Gradient (°C/cm)
			Maximum	Time Average	EOL	Maximum	Time Average	EOL	Maximum	Time Average	EOL	
GF-1	1	Type e, e' rods	1215	1150	1150	1145	1080	1075	1080	1015	1000	135
	2	Type a rods	1270	1250	1270	1190	1170	1180	1115	1085	1085	165
	3	Type b, b' rods	1275	1250	1235	1205	1170	1150	1130	1090	1060	160
	4	Loose particles	1160	1110	1090	1140	1095	1070	1120	1075	1040	35
GF-2	1	Type d rods	1090	1010	950	1030	960	900	970	905	855	105
	2	Type a rods	1065	1035	1035	990	970	975	920	905	915	130
	3	Type c rods	1055	1025	1010	980	960	955	910	900	900	125
	4	Loose particles	1185	1000	715	1170	985	690	1145	965	670	35
GF-3	1	Type f, f' rods	1050	1030	1030	995	975	975	940	920	920	110
	2	Type b, b' rods	1070	1045	1060	1000	975	990	925	910	920	135
	3	Loose particles	1075	1030	1030	1050	1000	1005	1020	975	970	55
	4	Type c rods	1200	1165	1160	1155	1120	1115	1110	1080	1070	85

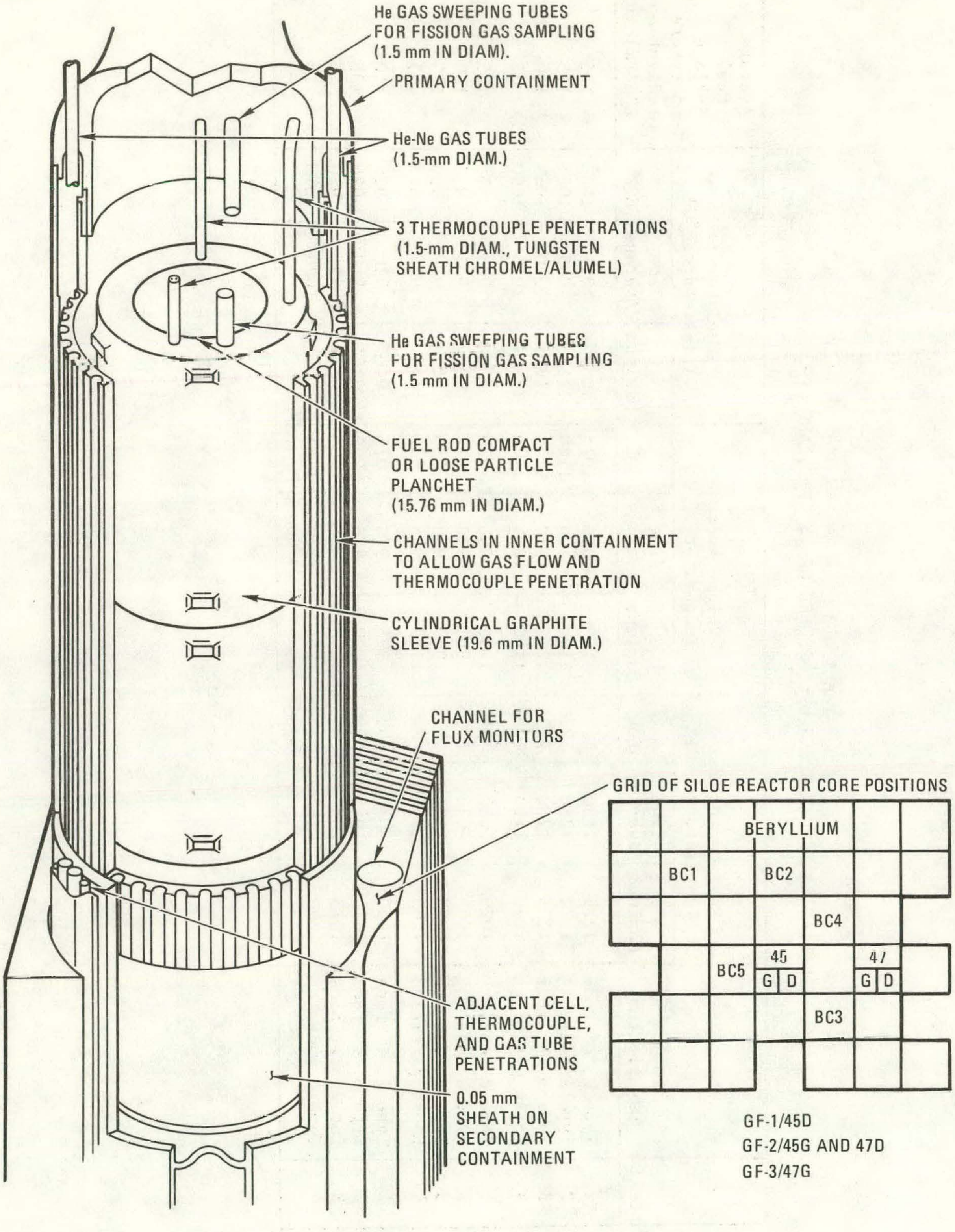

Fig. 4-1. Schematic diagram of TUMULT G device and Siloe reactor core penetrations

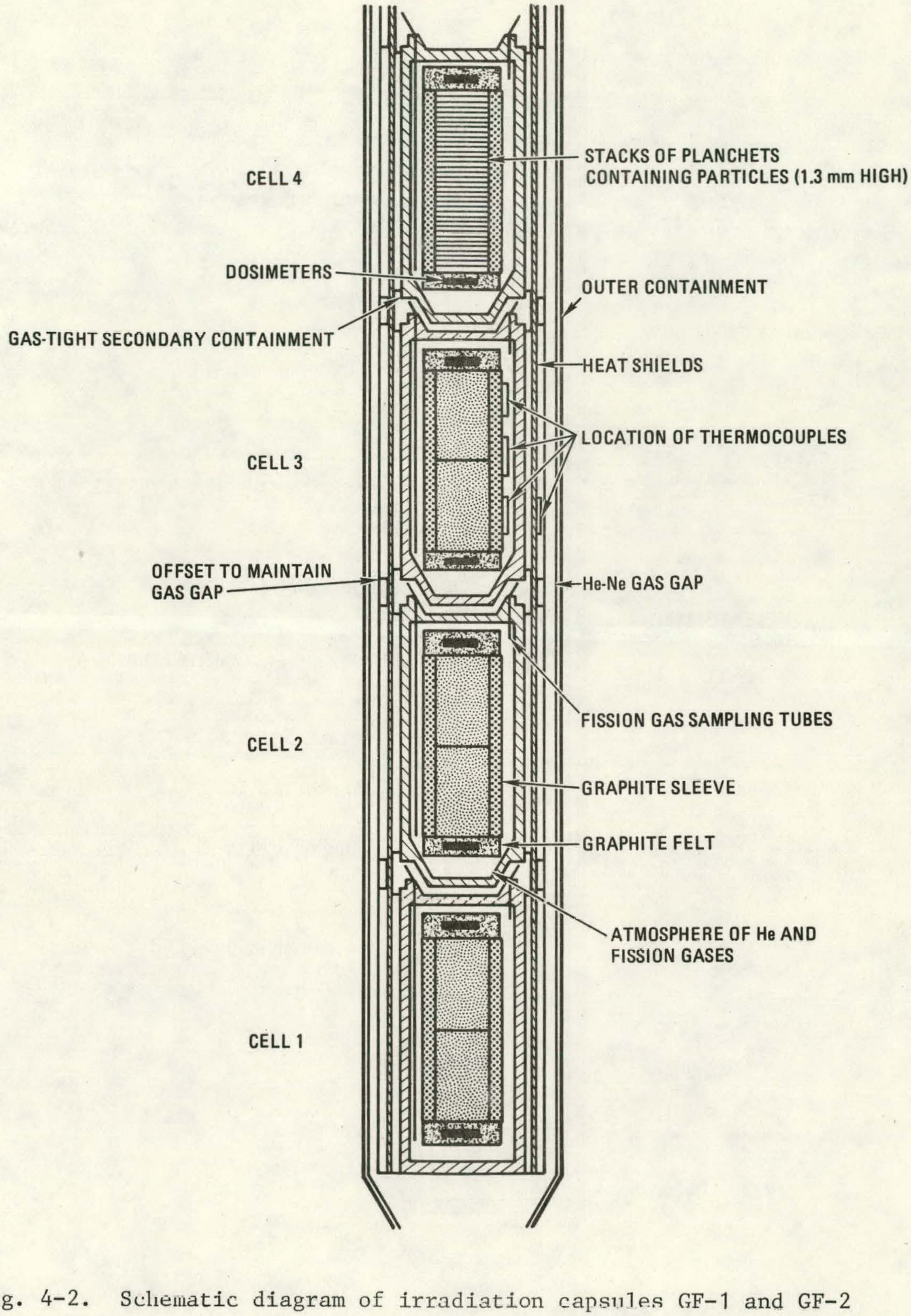

Fig. 4-2. Schematic diagram of irradiation capsules GF-1 and GF-2

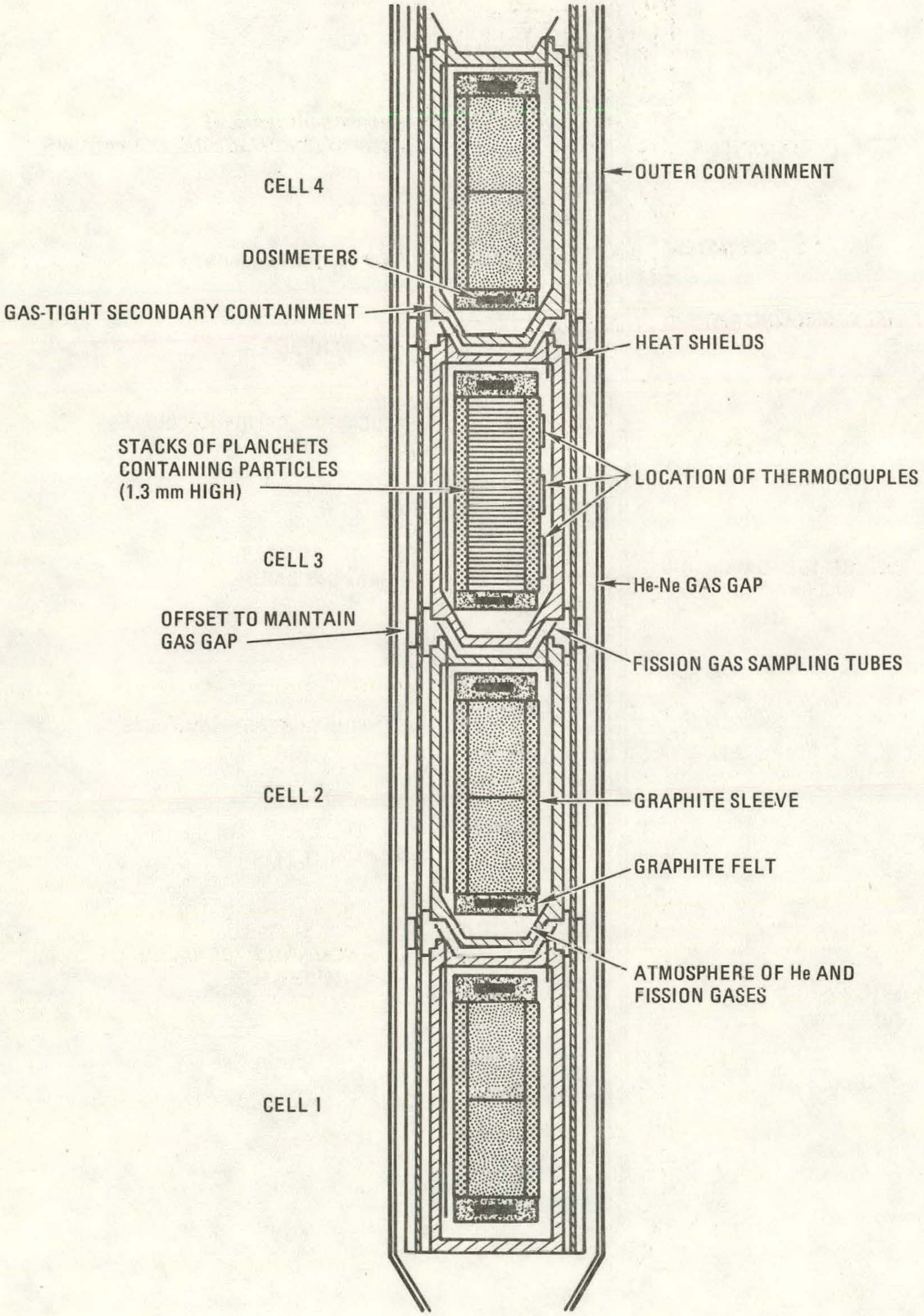

Fig. 4-3. Schematic diagram of irradiation capsule GF-3

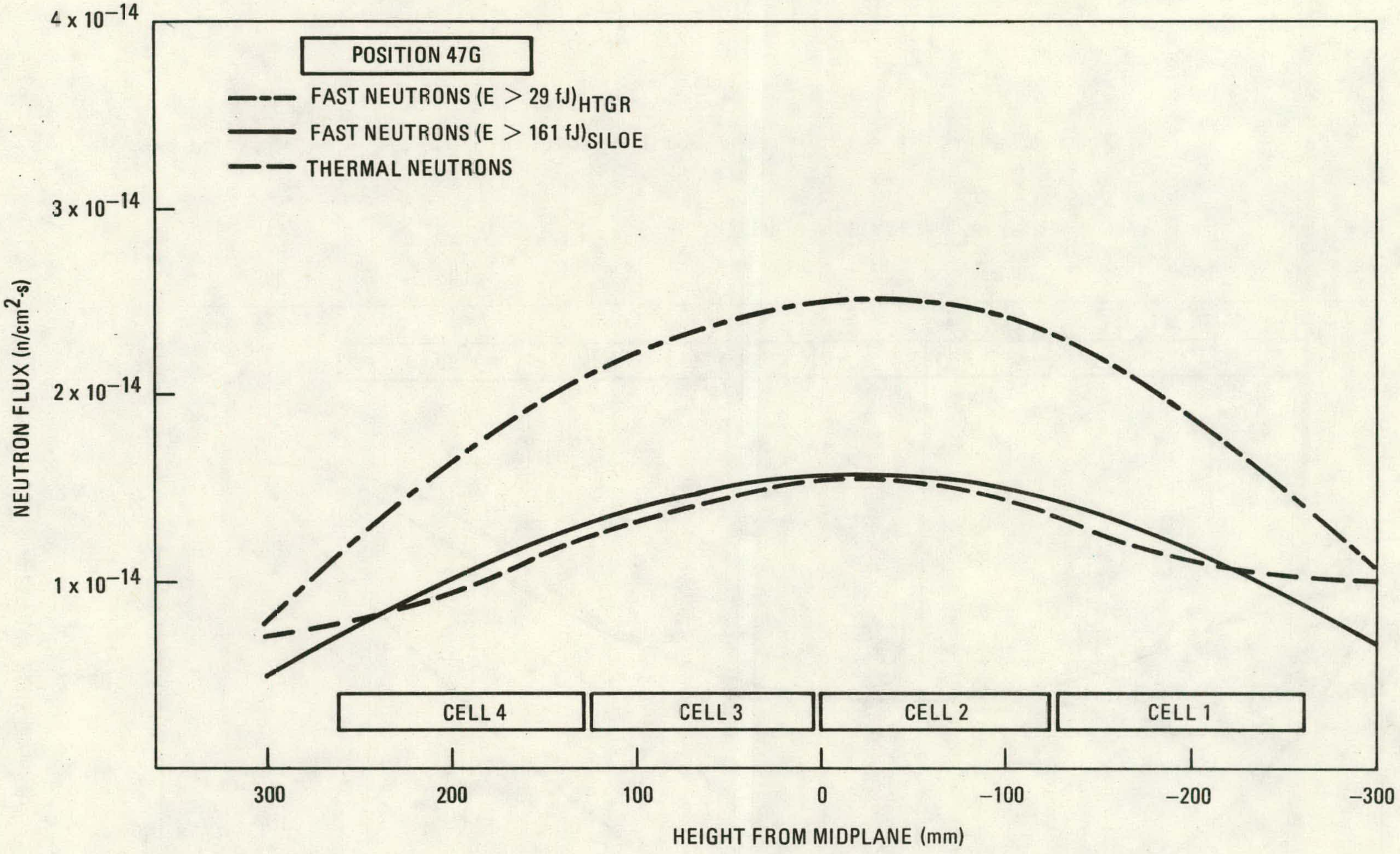

Fig. 4-4. Axial flux profiles for position 47G in Siloe reactor

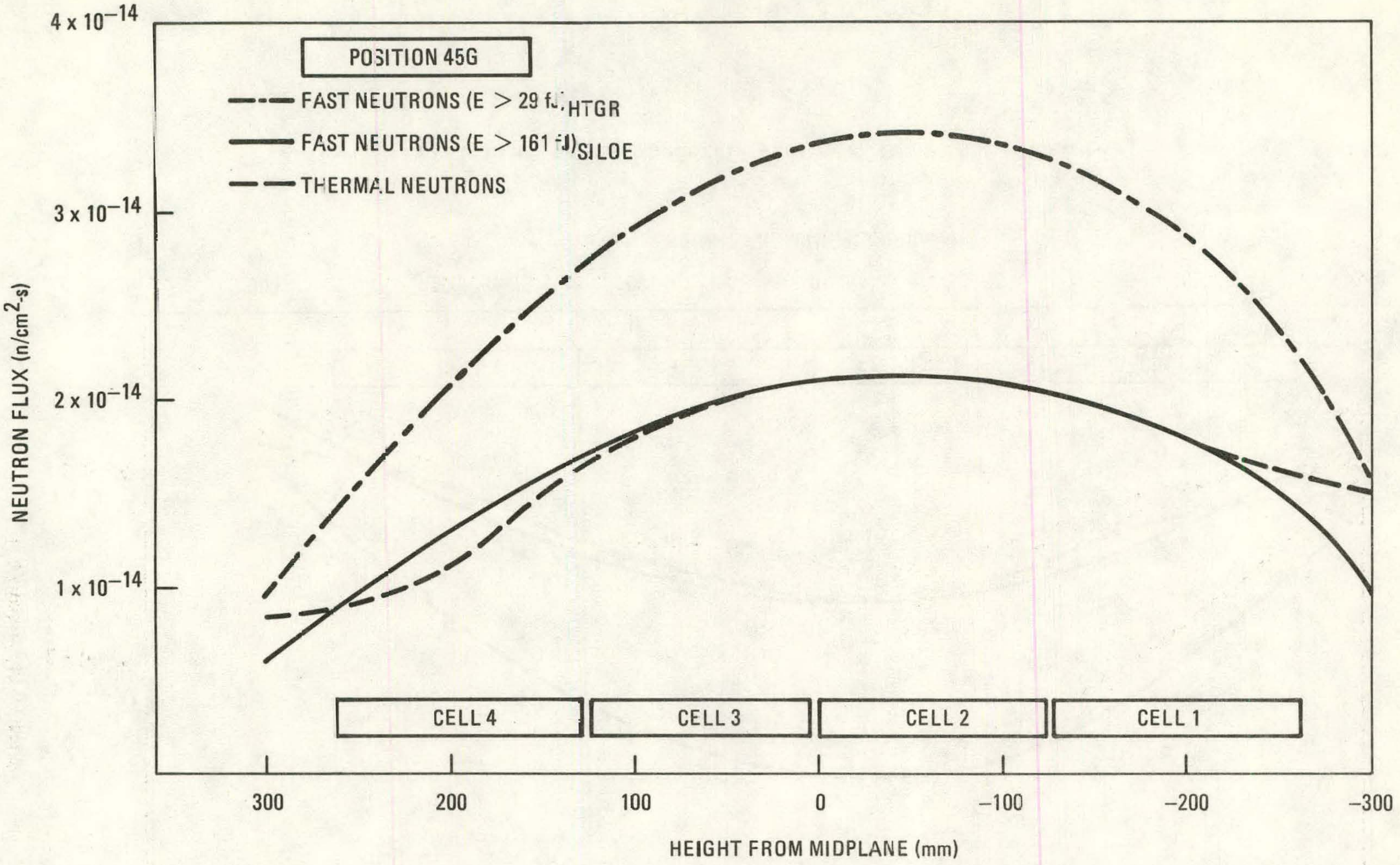

Fig. 4-5. Axial flux profiles for position 45G in Siloe reactor

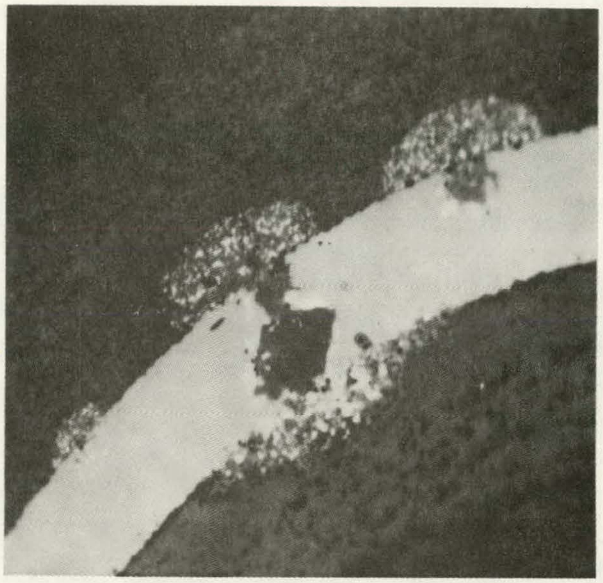
(N79077-1)

Ni/SiC ATTACK BROACHING INTEGRITY OF SiC LAYER

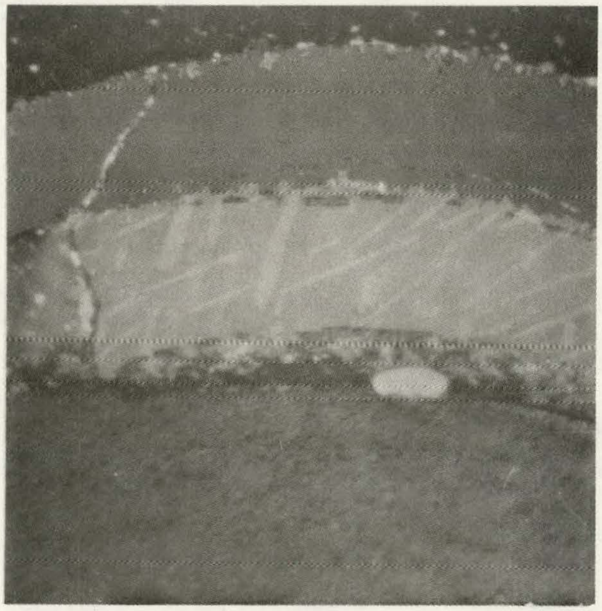
(N79077-2)

POLARIZED LIGHT SHOWING NiSi PRECIPITATES IN SiC LAYER

Fig. 4-6. Ni/SiC attack observed in TRISO-coated fuel tested in CORAIL IV A and B; irradiated for 9 months between 1150° and 1250°C (Ref. 4-2)

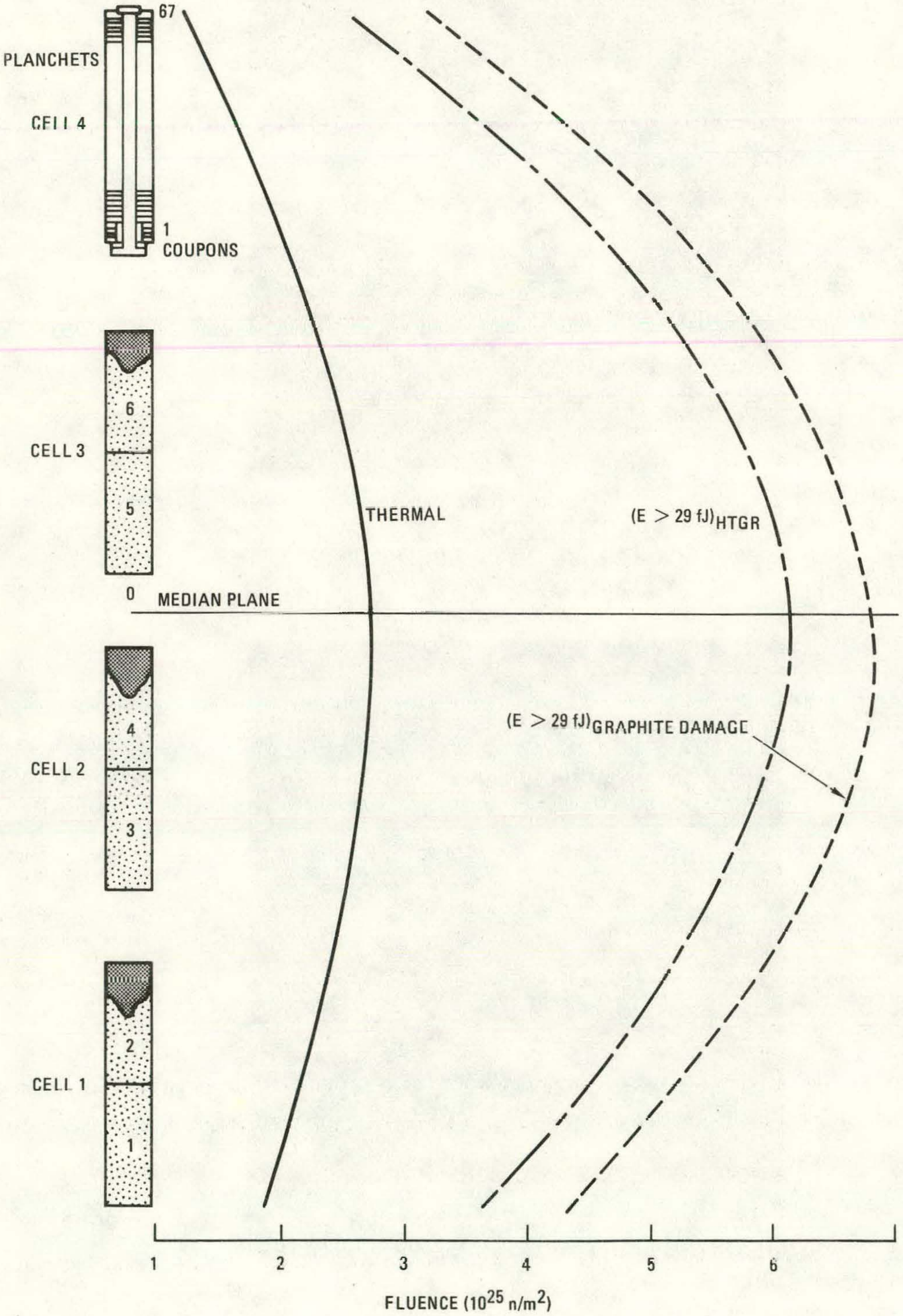

Fig. 4-7. Fast and thermal axial fluence profiles for capsule GF-1

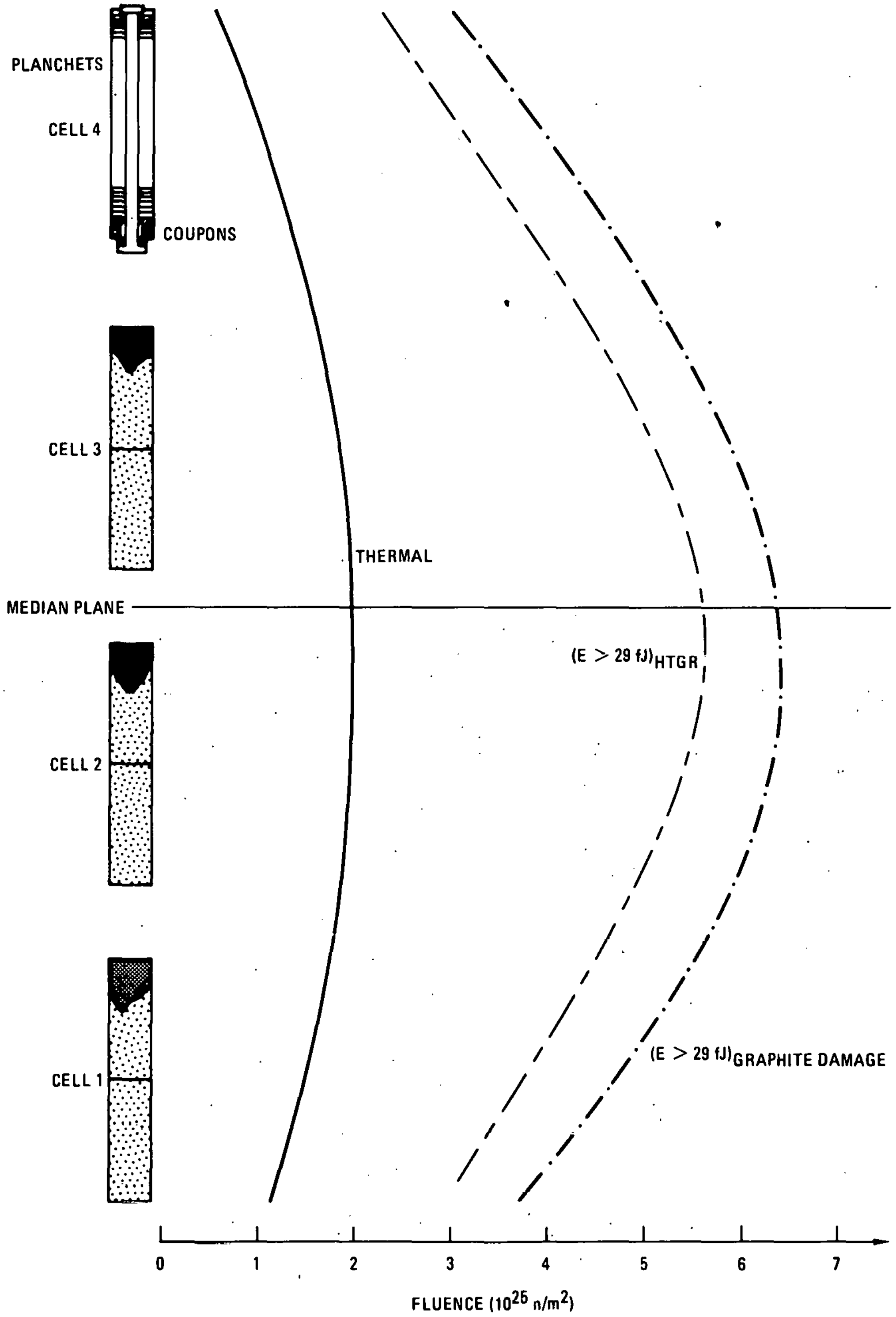

Fig. 4-8. Fast and thermal axial fluence profiles for capsule GF-2

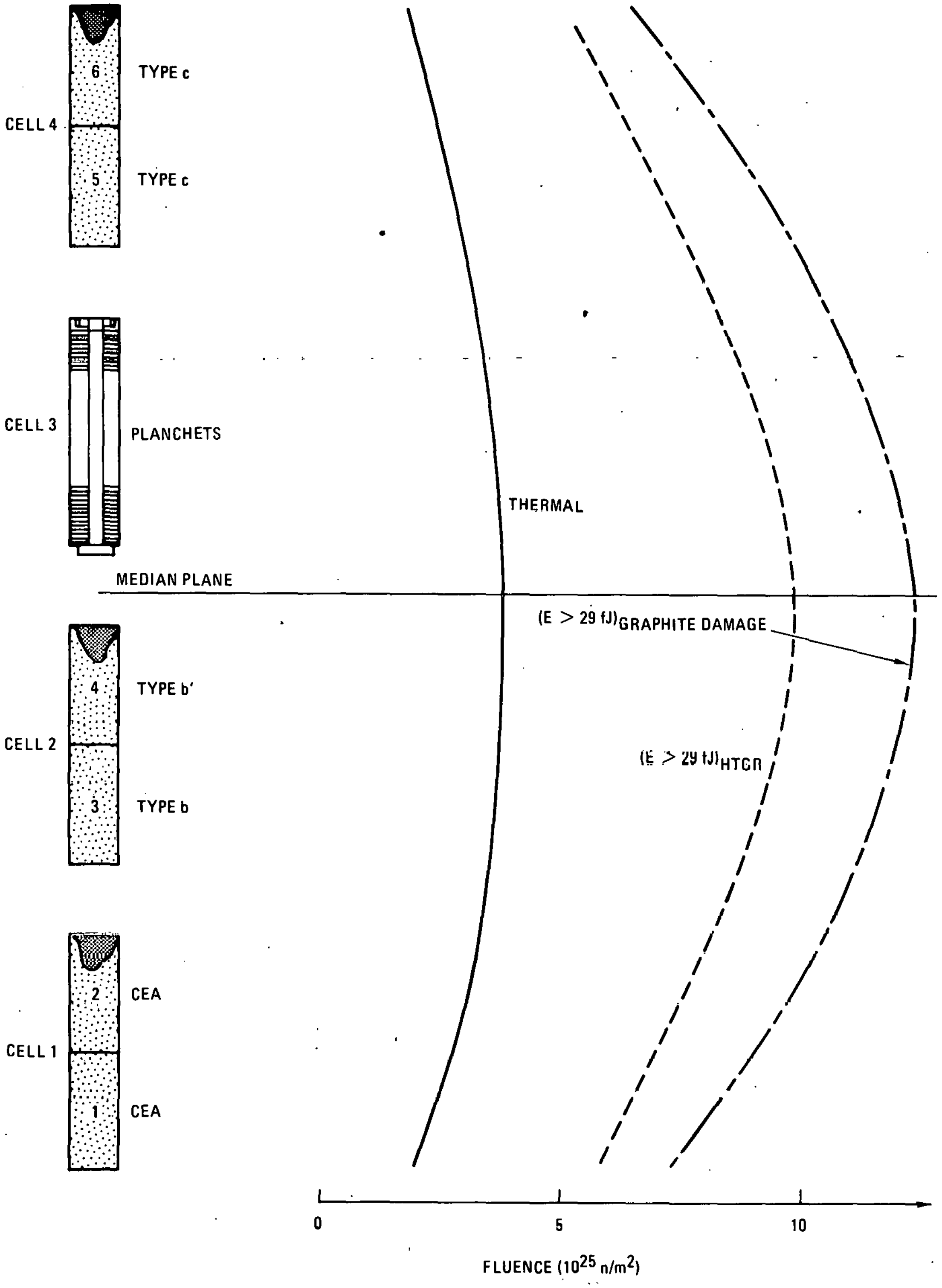

Fig. 4-9. Fast and thermal axial fluence profiles for capsule GF-3

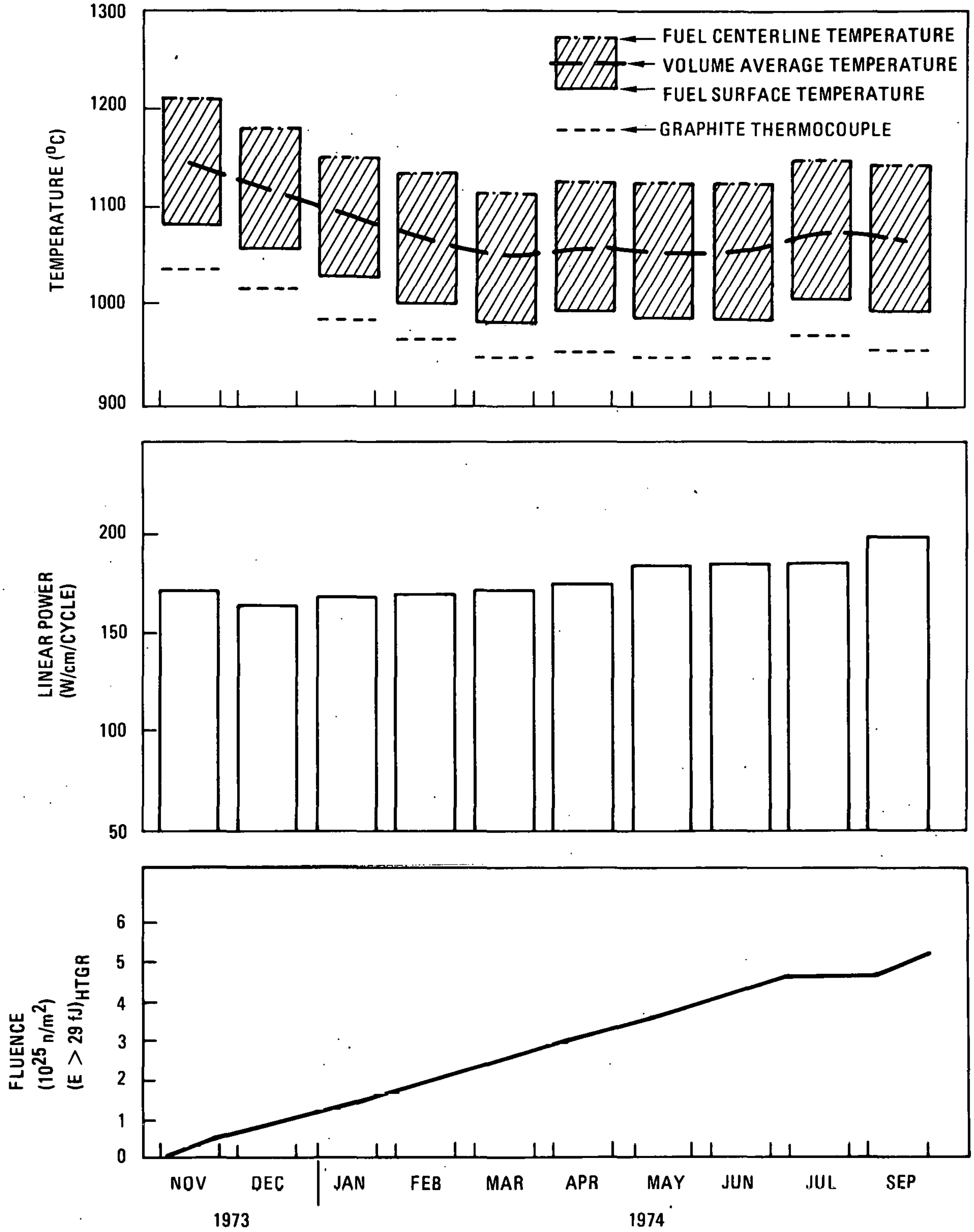

Fig. 4-10. Irradiation history of GF-1, cell 1

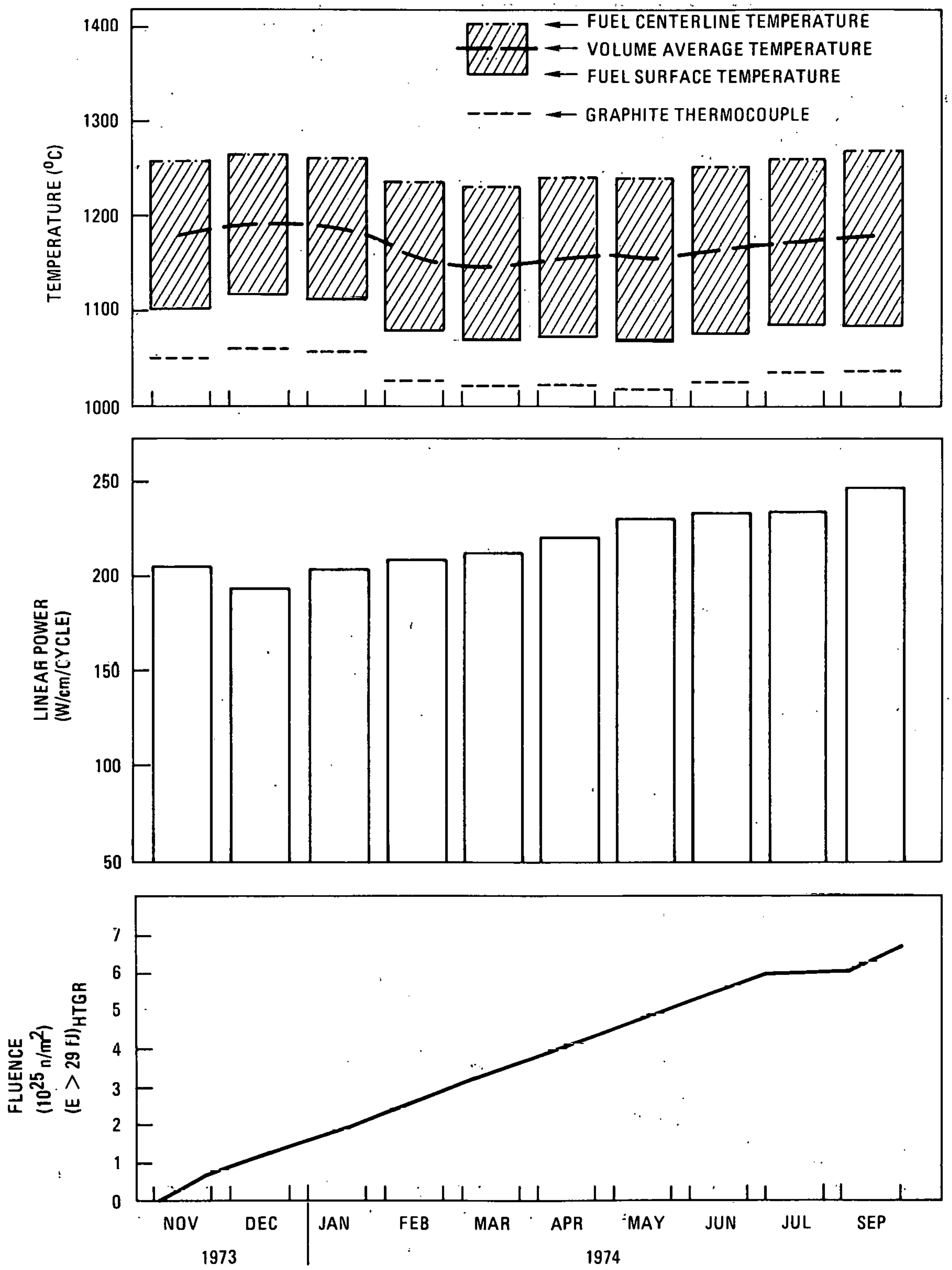

Fig. 4-11. Irradiation history of GF-1, cell 2

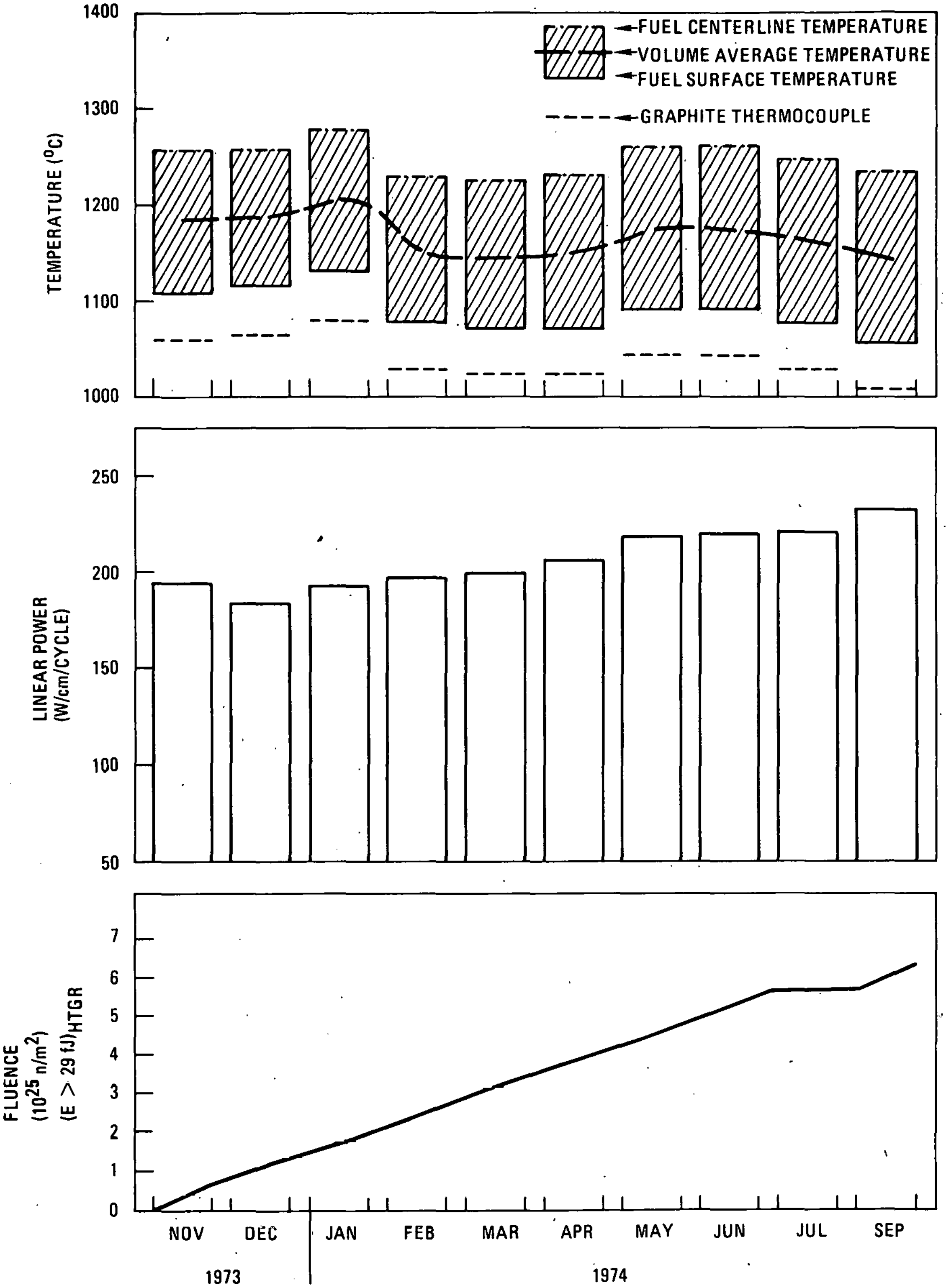

Fig. 4-12. Irradiation history of GF-1, cell 3

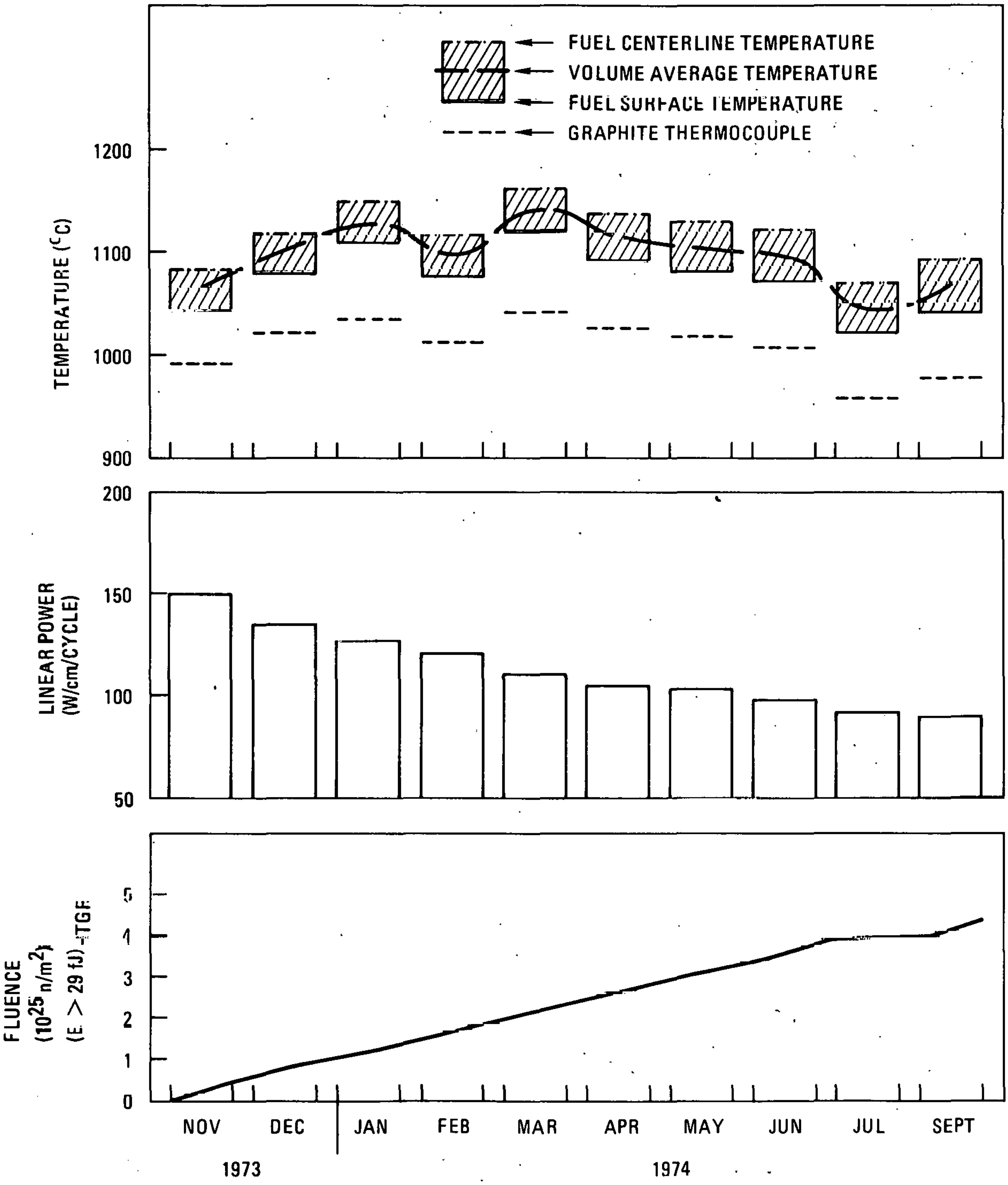

Fig. 4-13. Irradiation history of GF-1, cell 4

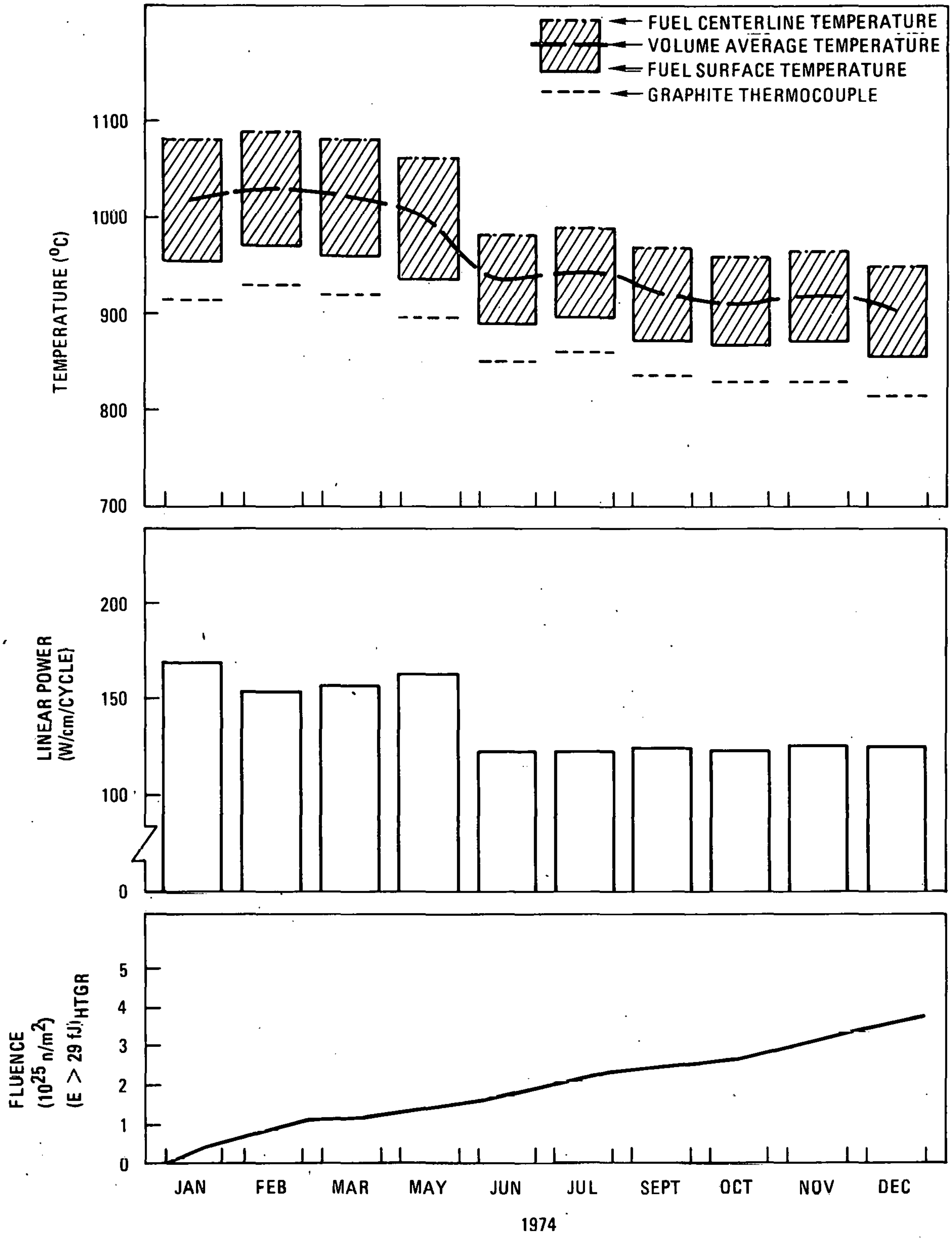

Fig. 4-14. Irradiation history of GF-2, cell 1

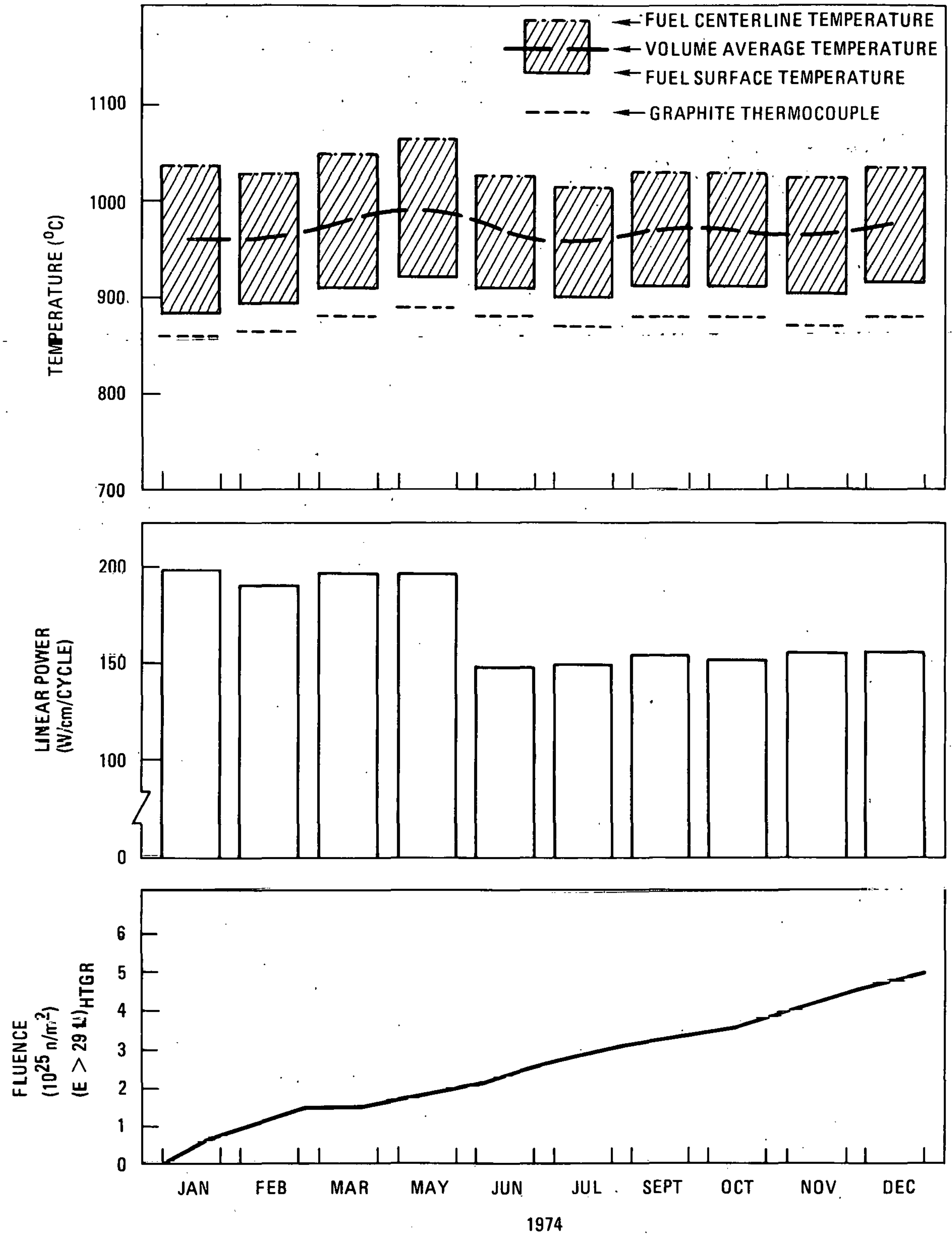

Fig. 4-15. Irradiation history of GF-2, cell 2

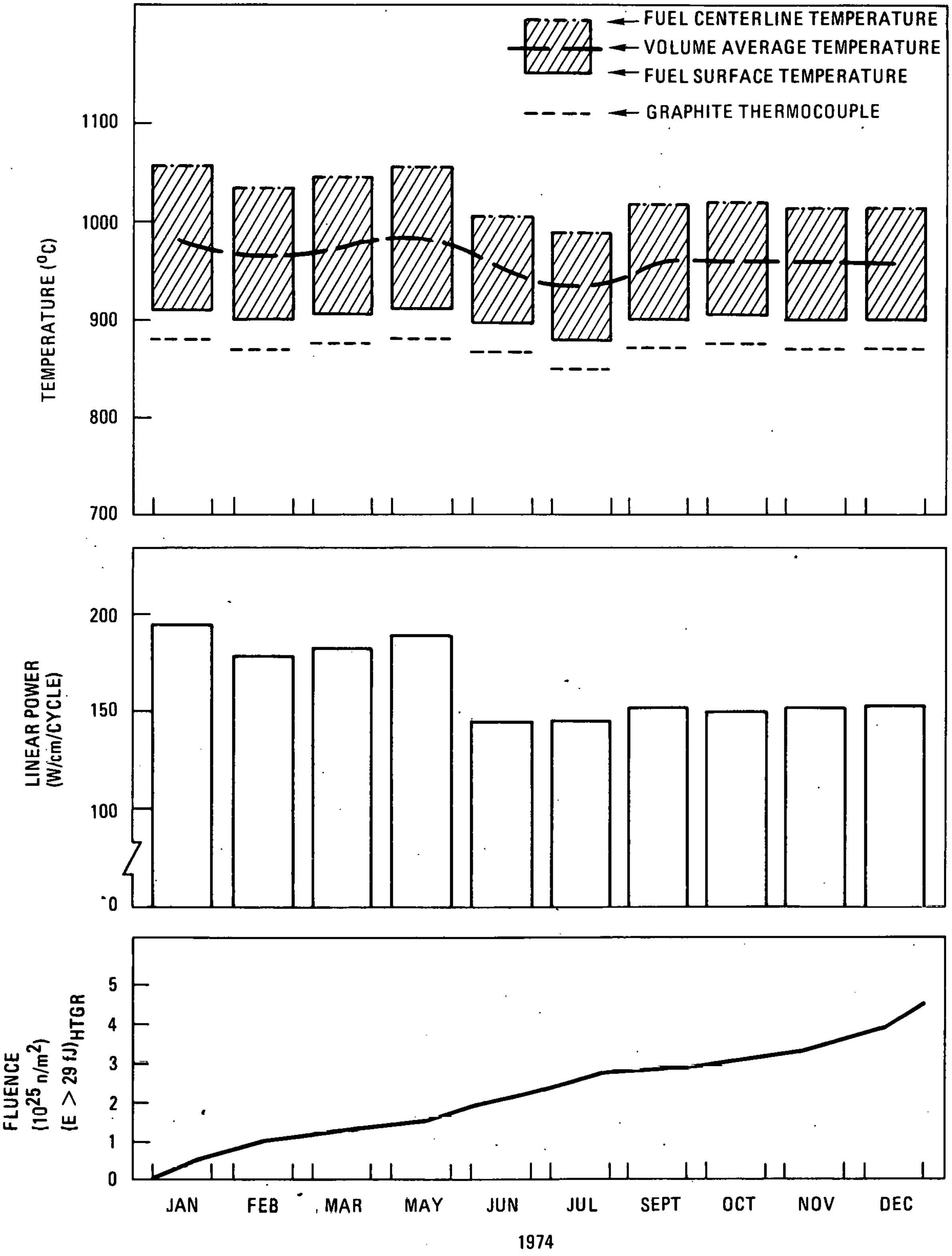

Fig. 4-16. Irradiation history of GF-2, cell 3

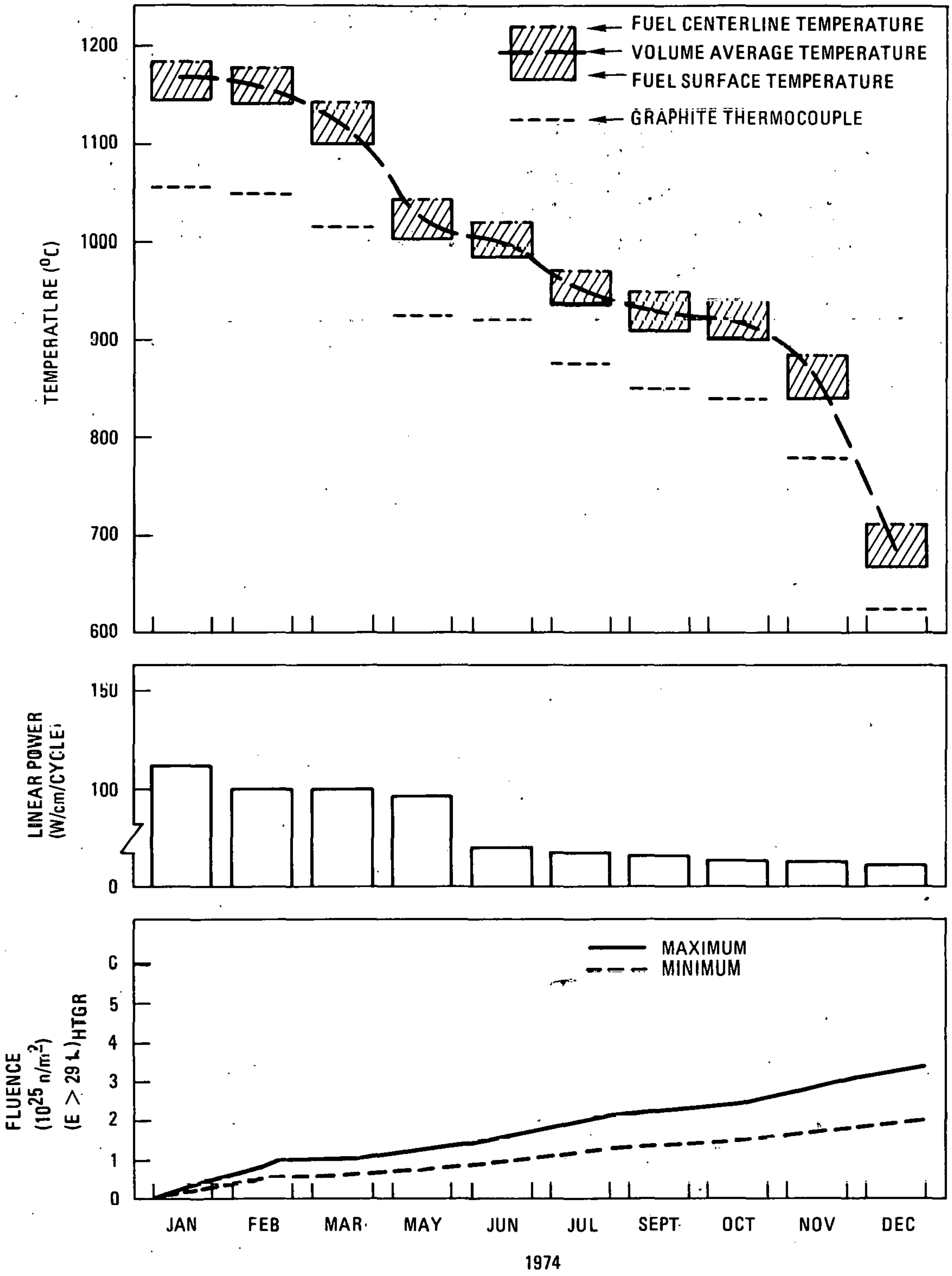

Fig. 4-17. Irradiation history of GF-2, cell 4

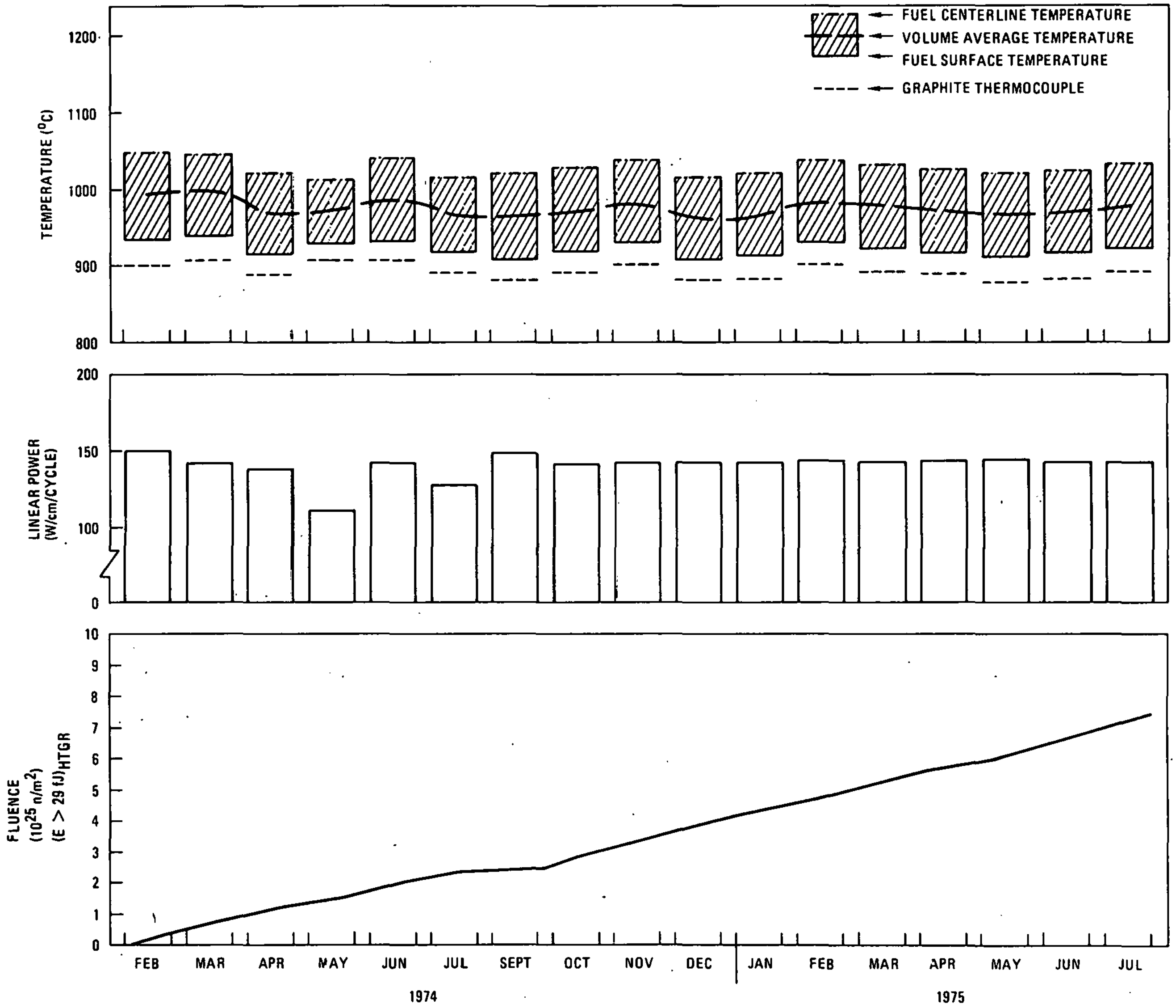

Fig. 4-18. Irradiation history of GF-3, cell 1

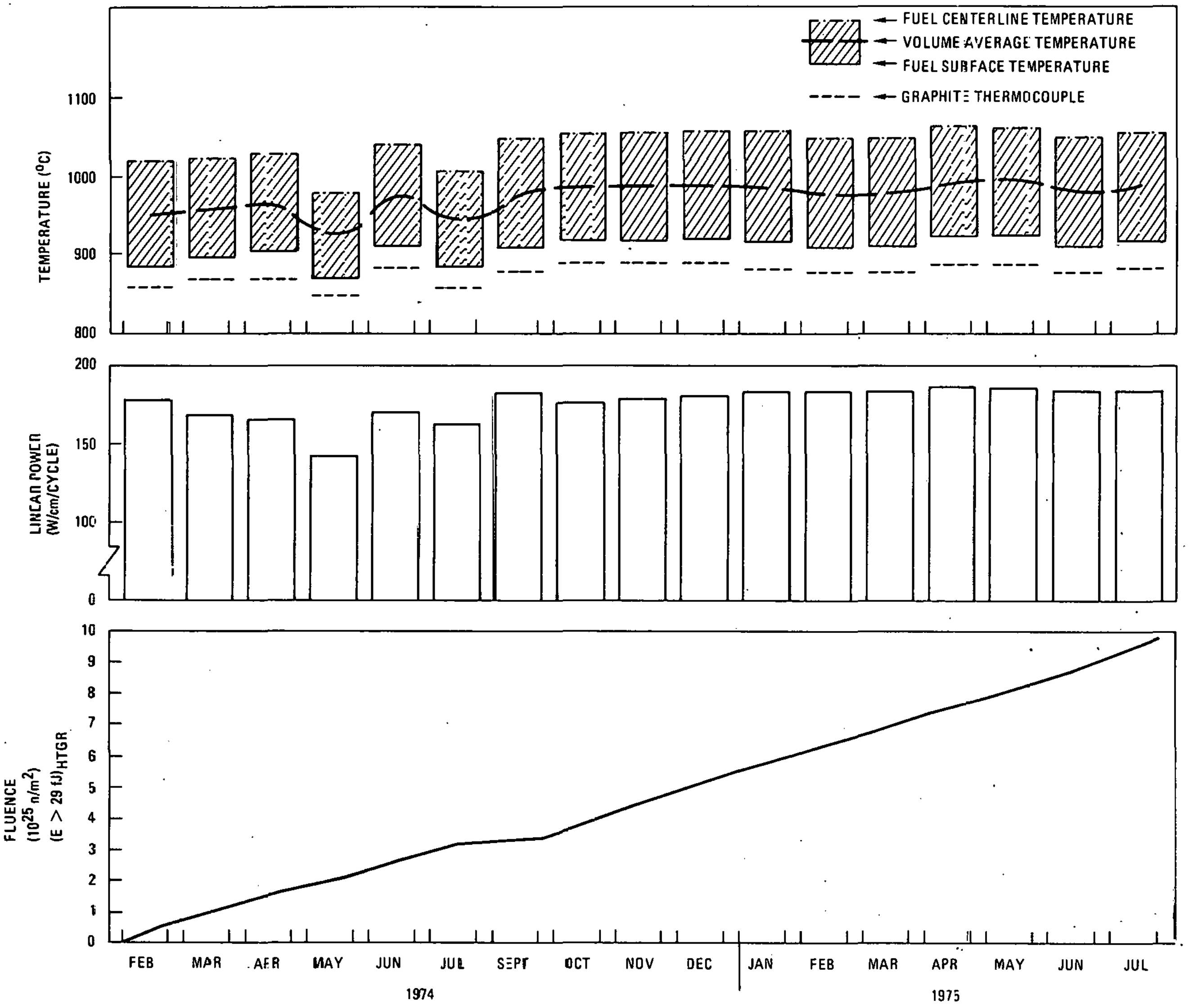

Fig. 4-19. Irradiation history of GF-3, cell 2

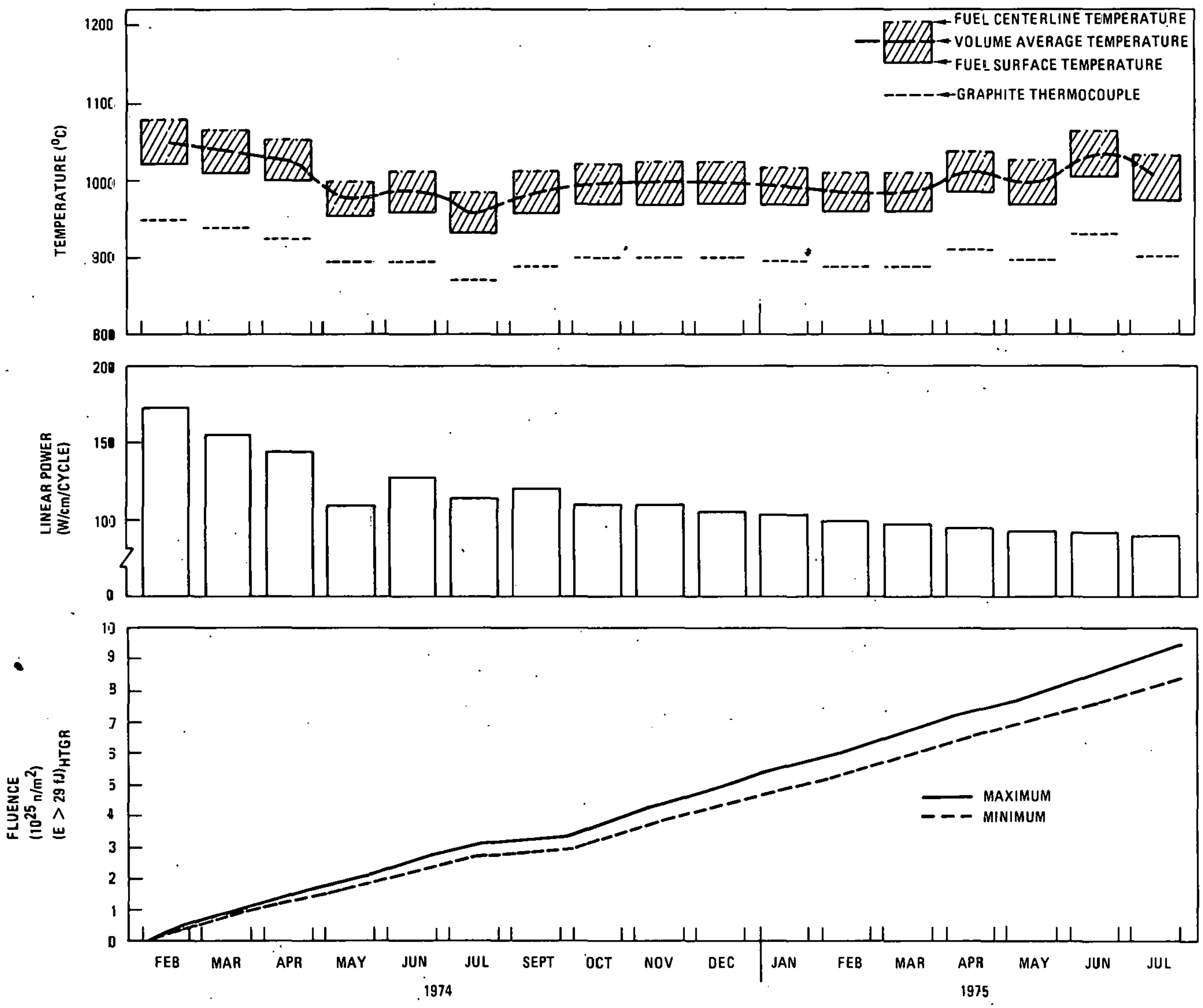

Fig. 4-20. Irradiation history of GF-3, cell 3

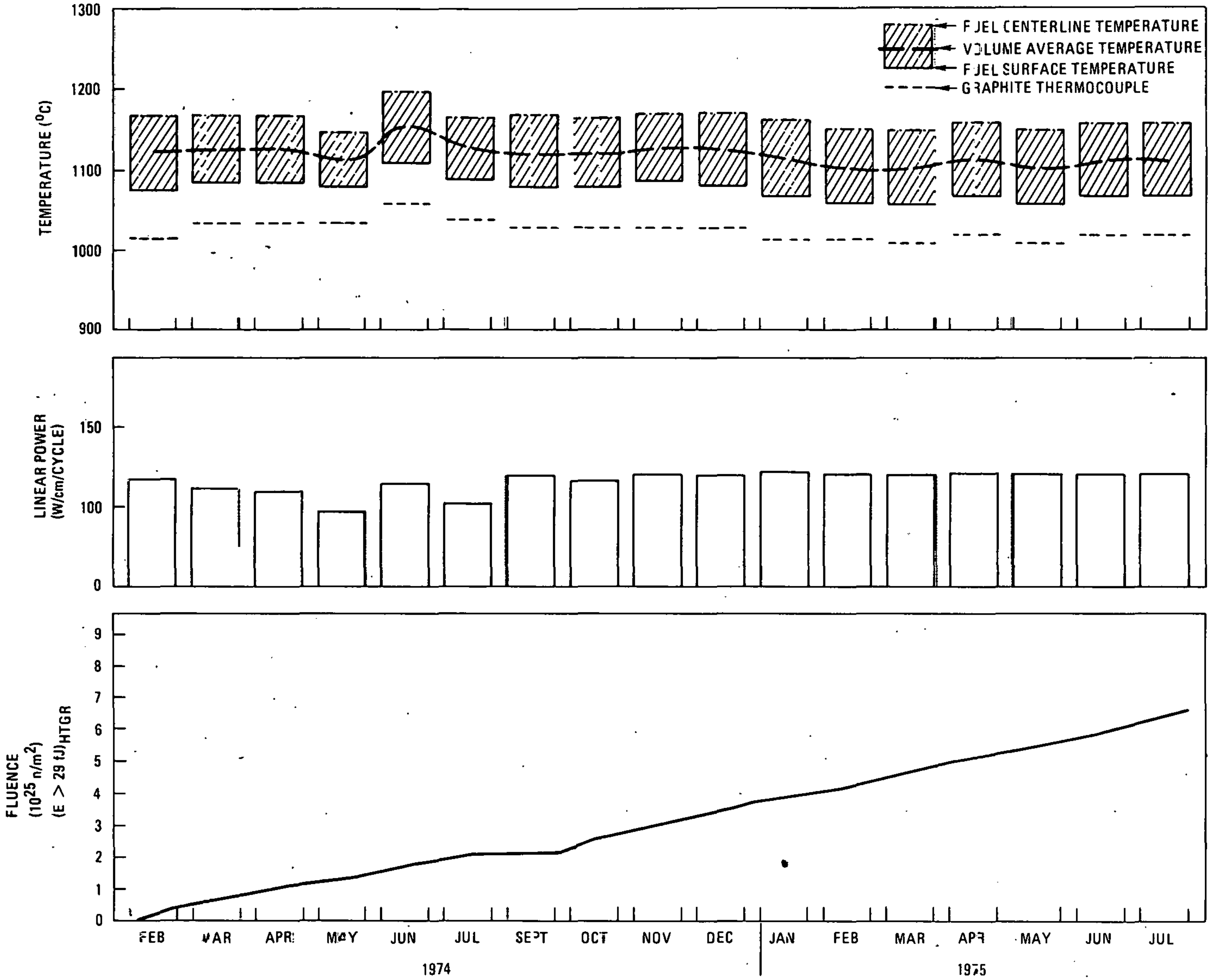

Fig. 4-21. Irradiation history of GF-3, cell 4

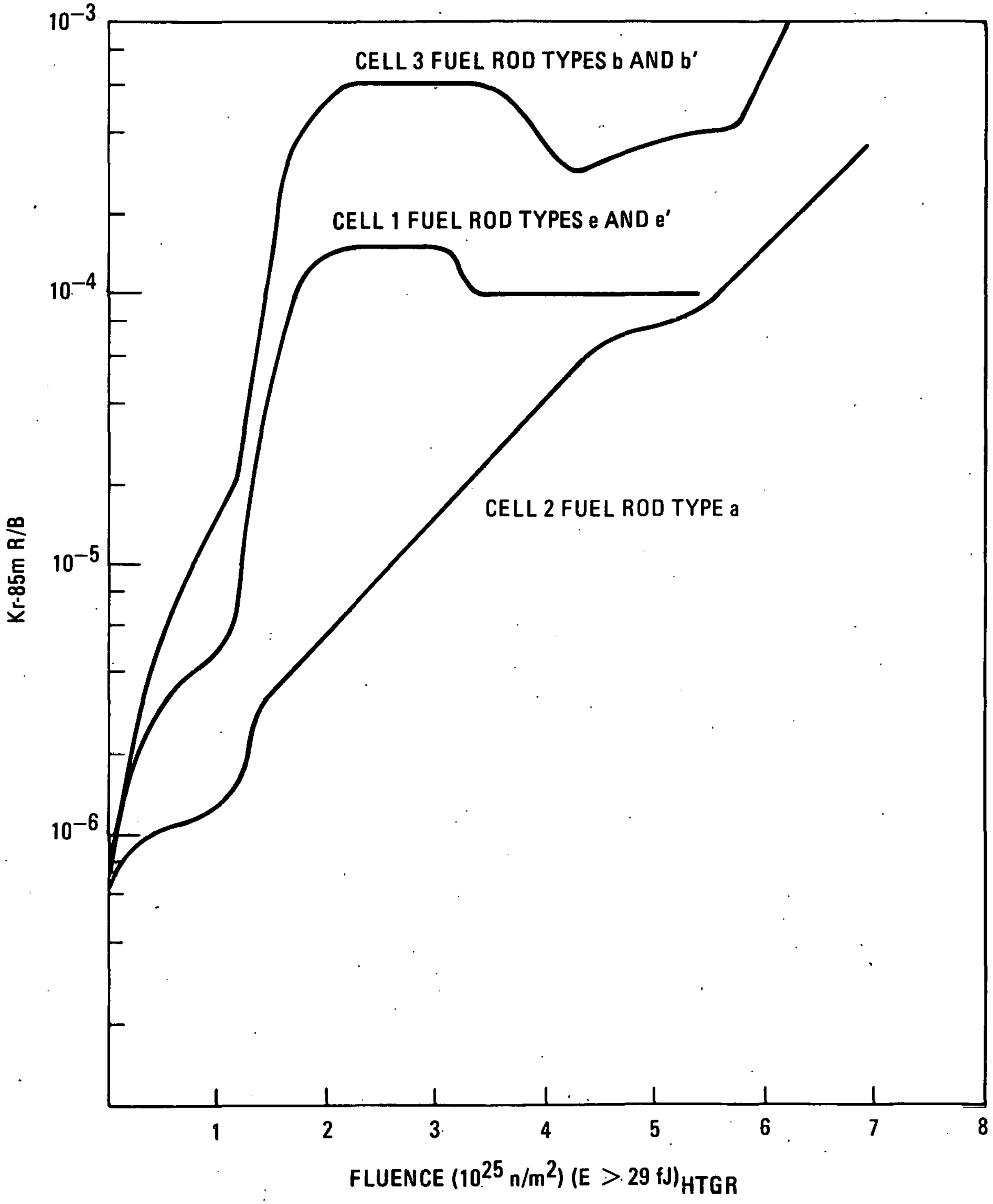

Fig. 4-22. Capsule GF-1 Kr-85m R/B measurements during irradiation

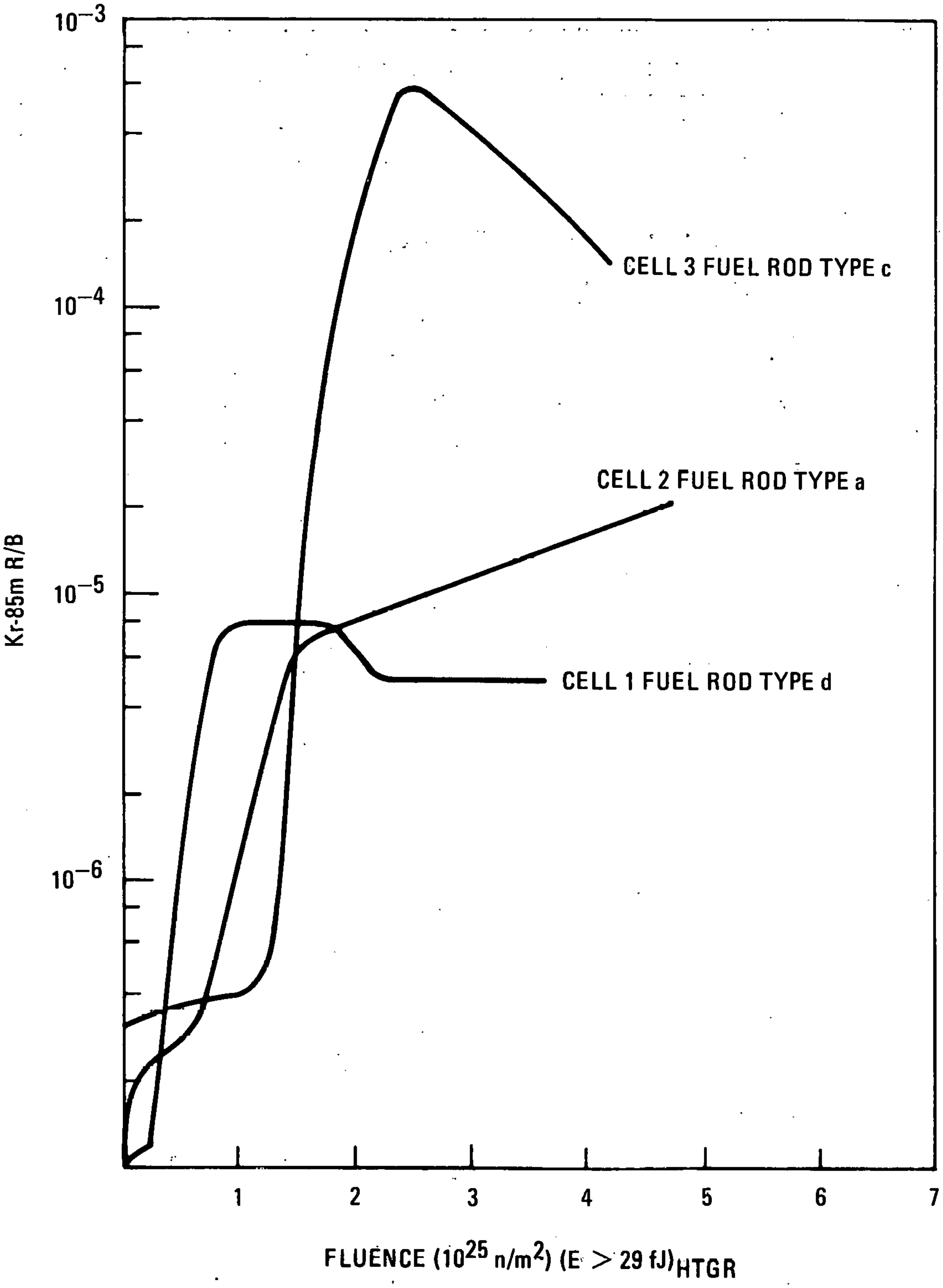

Fig. 4-23: Capsule GF-2 Kr-85m R/B measurements during irradiation

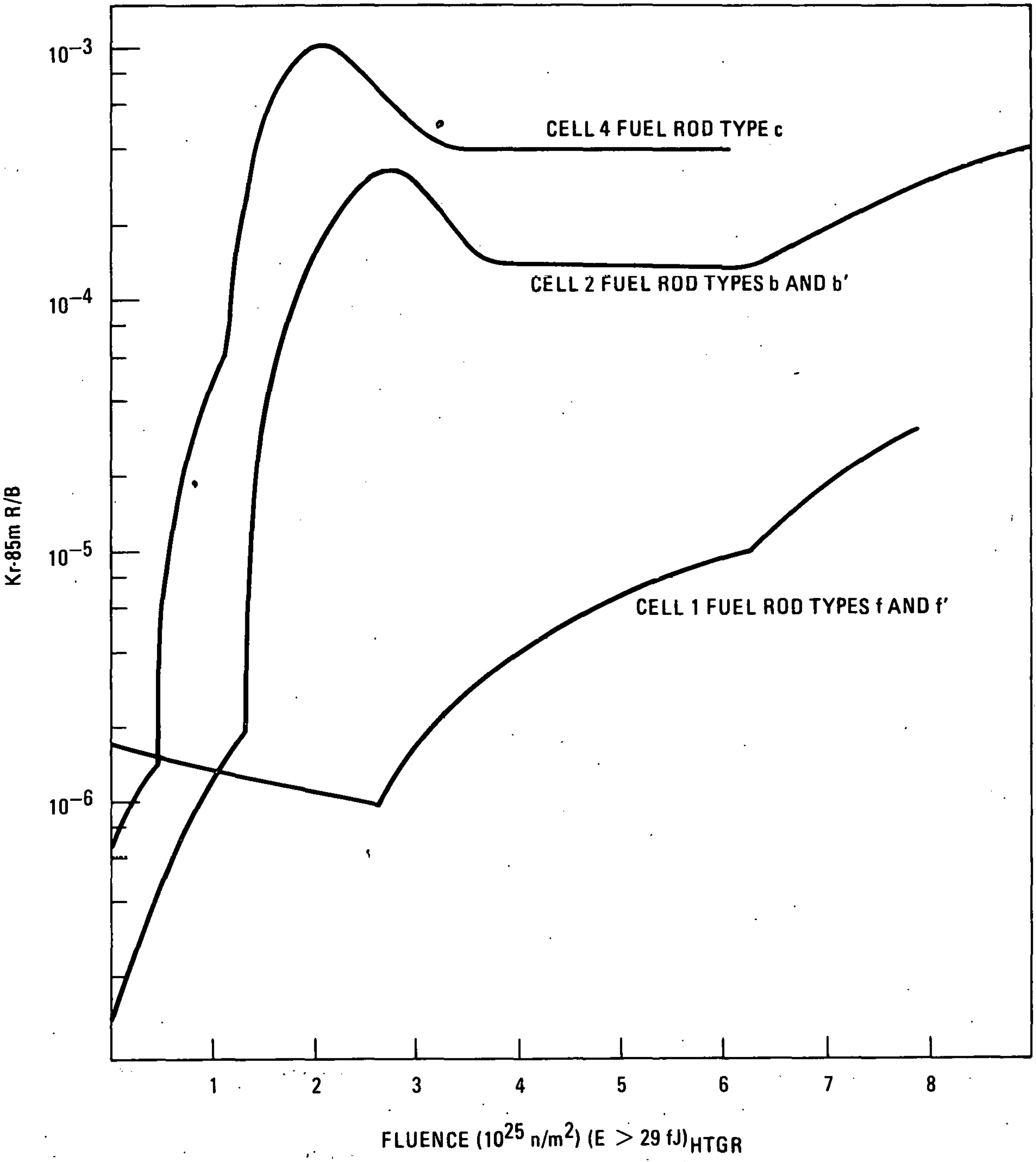

Fig. 4-24. Capsule GF-3 Kr-85m R/B measurements during irradiation

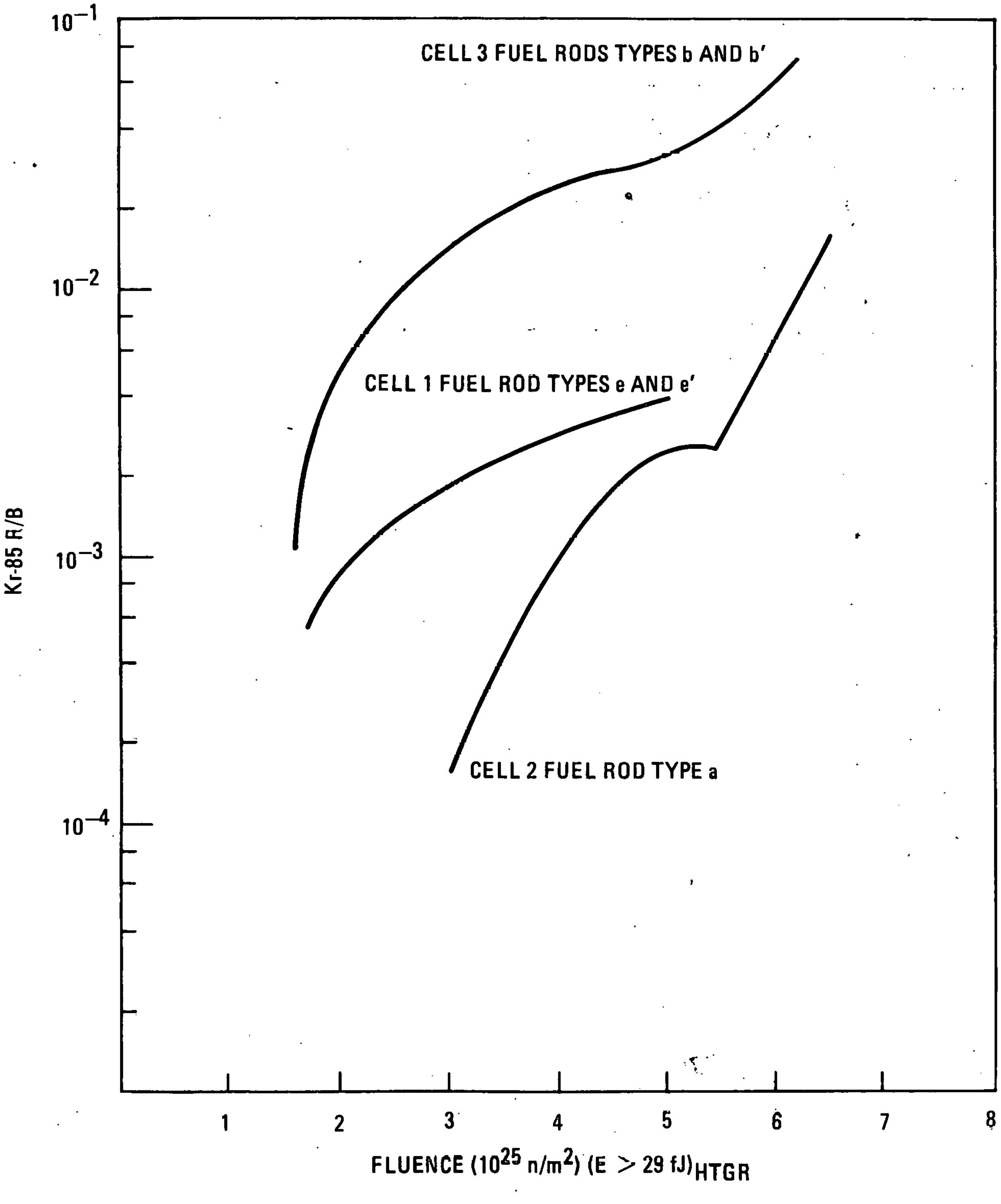

Fig. 4-25. Capsule GF-1 Kr-85 measurements during irradiation

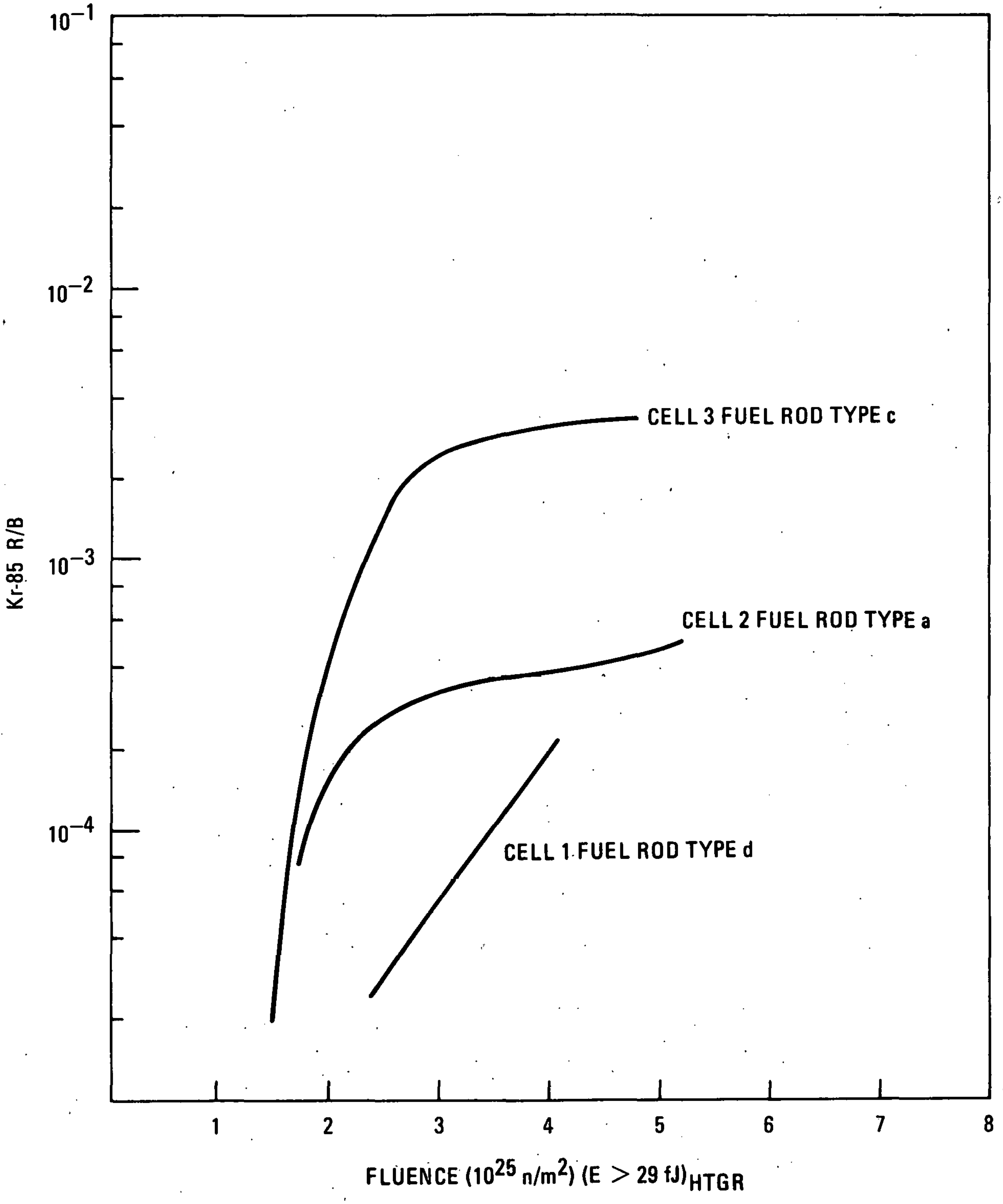

Fig. 4-26. Capsule GF-2 Kr-85 measurements during irradiation

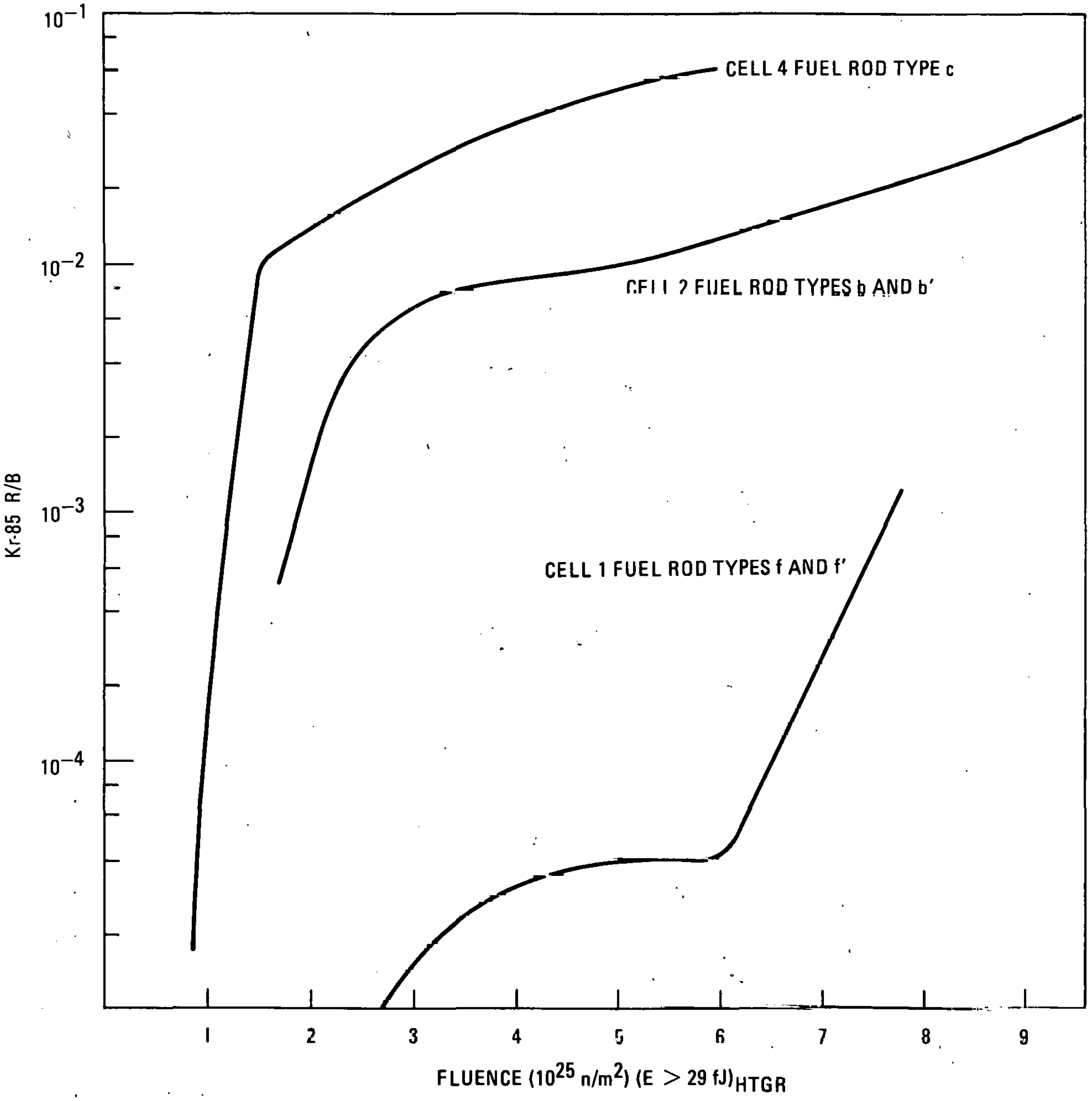

Fig. 4-27. Capsule GF-3 Kr-85 measurements during irradiation

5. POSTIRRADIATION EXAMINATION

5.1. FUEL SAMPLE UNLOADING

GF-1, GF-2, and GF-3 fuel rod compacts were contained in graphite crucibles, and the loose particle and ring samples were contained in graphite planchets. As shown in Fig. 4-1, the test samples were housed in a TUMULT G device having an inner and outer containment. During capsule disassembly, the outer containment between cells was cut and each cell was separated individually. Neutron radiographs of individual cells in GF-2 and GF-3 are shown in Figs. 5-1 and 5-2. The apparatus used for the disassembly of fuel rods and loose particle planchets is shown in Fig. 5-3.

5.2. FUEL ROD VISUAL EXAMINATION

After disassembly, the general irradiation performance and integrity of the loose particle samples and fuel rod compacts were assessed by visual examination. The criteria for judging fuel rod integrity after irradiation are that fuel rods remain intact with minimal cracking and experience negligible particle debonding. The examination was conducted with a stereomicroscope at a magnification range of approximately 10X to 20X (Refs. 5-1 through 5-3). Photographs of each of the irradiated rods are shown in Figs. 5-4 through 5-21. In general, all rods exhibited good to excellent structural integrity with no irradiation-induced fractures evident. The GA rods, which were fabricated by matrix injection, exhibited superficial microcracks on the surface and were fragile; also, there was a tendency for the rod ends to chip or crumble, further accentuating the microcracks (Figs. 5-9, 5-12, 5-13, and 5-21). In contrast, CEA rods fabricated with the CERCA process using natural graphite exhibited exceptional surface appearance and structural integrity (to Figs. 5-5 and 5-17).

5.3. LOOSE PARTICLE VISUAL EXAMINATION

Each particle sample from GF-1, GF-2, and GF-3 was examined visually (stereomicroscope at ~10X) and a measure of the OPyC coating integrity and pressure vessel failure was determined by counting the number of particles with defective coatings. The irradiation parameters and the results of the visual examination of each particle batch are given in Tables 5-1 through 5-3. It should be noted that an accurate assessment of pressure vessel failure (failed SiC and OPyC layers) is difficult in some TRISO-coated batches because of the adherence of a partially failed OPyC coating over the SiC substrate. Consequently, localized failures in the SiC layer could be obscured. The stereomicroscope photograph in Fig. 5-22 illustrates visual characterization of OPyC and pressure vessel failures in loose particle batch 6155-02-020. Visual results are summarized in Table 5-4 for the reference-type fuel systems:

1. TRISO-coated $(8Th,U)O_2$.
2. TRISO-coated UC_2.
3. TRISO-coated ThO_2.
4. BISO-coated $(8Th,U)O_2$.
5. BISO-coated ThO_2.

Advanced fuel particle systems (Al- and Si-doped kernels, ZrC TRISO fuels, and Si-doped OPyC layers) were not irradiated in fuel compacts and do not constitute reference HTGR fuel systems. These developmental fuels are discussed in detail in Section 5.8.4, including a summary of the visual results.

5.3.1. Pressure Vessel Failure

Pressure vessel failure in TRISO-coated $(8Th,U)O_2$ ranged between 0 and 2.3% in capsules GF-1 and GF-3 (Table 5-4). No pressure vessel failure was observed in GF-2. This trend correlates with the progressive increase in

FIMA from GF-2 (5.3% FIMA) to GF-1 (7.1% FIMA) to GF-3 (11.1% FIMA). The increase in FIMA leads to a corresponding increase in fission gas pressure and higher tensile stresses in the load-bearing SiC layers. However, the visually observed pressure vessel failure in these fuel types is greater than the target design value, i.e., an end-of-life failure of <0.5% (refer to Section 3.1.1.1) for reference 400-μm (8Th,U)O_2 fuel. In addition, the visually observed loose particle failures in TRISO-coated (8Th,U)O_2 fuels are confirmed by the high Kr-85m R/B release measurements in cells containing fuel rods made with these fissile particles. Specificially, type b and b' fuel rods containing fissile batch 6155-02-020 exhibited high Kr-85m R/B releases early in life (Figs. 4-22 and 4-24). The excessive failure in these fuel types is attributed to defective SiC layers (refer to Section 5.8.2.4) and premature OPyC failure (refer to Section 5.8.2.3). In contrast, no pressure vessel failure was observed in TRISO-coated ThO_2 fuel irradiated to 3.4% FIMA and 1000°C in GF-3. The pressure vessel failure in TRISO-coated UC_2 was 0.25% for fuel irradiated at 1095°C to a burnup of 50% FIMA. This level of visual failure is consistent with the current design value for UC_2, i.e., <0.5% at 1250°C and 78% FIMA (Ref. 5-6).

Table 5-4 shows that pressure vessel failure in BISO-coated, 500-μm-diameter (8Th,U)O_2 kernels was <0.3% under the range of exposure conditions experienced in GF-1, GF-2, and GF-3. This is less than the pressure vessel failures observed in TRISO-coated (8Th,U)O_2 kernels with 500-μm-diameter kernels subjected to the same exposure conditions. This discrepancy could be rationalized on the basis of a permeable BISO coating layer, which would result in a decrease in the internal fission gas pressure.

5.3.2. OPyC Failure

Table 5-4 shows the OPyC failure on TRISO-coated (8Th,U)O_2, ThO_2, and UC_2 kernels ranged from 0 to 63.2%. The morphology of OPyC failures is generally characterized as "rose petal," i.e., equidistant cracks emanating from a common point followed by peeling back of the pyrocarbon layer due to

OPyC densification (Fig. 5-22). The following general conclusions are evident from the visual observations on OPyC failure:

1. OPyC failure in the same particle batches irradiated in GF-1 and GF-3 was comparable. This implies that OPyC failure is insensitive to differences in fluence and temperature exposure conditions in these capsules:

   GF-1 - 5.6 to 6.4 x 10^{25} n/m^2 (E > 29 fJ)$_{HTGR}$ and volume average temperature of 1095°C

   GF-3 - 8.8 to 10.2 x 10^{25} n/m^2 (E > 29 fJ)$_{HTGR}$ and volume average temperature of 1000°C

2. OPyC failure in GF-2 appears in general to be greater than failure observed for the same batches irradiated in GF-1 and GF-3. The exposure conditions for GF-2 appear to be less severe:

   GF-2 - 1.9 to 4.0 x 10^{25} n/m^2 (E > 29 fJ)$_{HTGR}$ and volume average temperature of 985°C

The GF-2 results imply that OPyC failures occur early in life at fluences <2.8 x 10^{25} n/m^2 (E > 29 fJ)$_{HTGR}$. This observation is consistent with a much larger base of empirical data (Ref. 5-7). In addition, the volume-time average temperature for GF-2 during the first three irradiation cycles was ~1145°C compared to volume-time average temperatures of ~1100°C for GF-1 and ~1040°C for GF-3 (refer to Figs. 4-13, 4-17, and 4-20). Furthermore, during the third cycle (March 1974) of GF-3 operation, a temperature excursion of ~200°C occurred, which subjected the loose particles to ~1400°C. This temperature excursion and the high volume average temperature during the initial part of irradiation are considered to be the primary reasons for the higher OPyC failures in TRISO-coated particle batches irradiated in GF-2 in comparison with companion batches irradiated in GF-1 and GF-3. The impact of temperature on OPyC failures has been documented for other capsules (Ref. 5-8), and the general trend appears to be a marked increase in OPyC failure between 1000° and 1350°C for a given fast fluence exposure.

A further remark concerning OPyC failure is that, in general, Tables 5-1 through 5-3 indicate that OPyC failure occurs in early life at fluence levels $<2.8 \times 10^{25}$ n/m^2 ($E > 29$ fJ)$_{HTGR}$. However, one batch (6155-00-010) exhibited a correlation between OPyC failure and fluence. This correlation, which is summarized in Fig. 5-23, shows OPyC failure increasing linearly with fluence. It is probable that this batch had different OPyC structural properties compared to other batches, which enabled it to reach higher fluences before exhibiting >20% OPyC failures. The explanation for premature OPyC failures on TRISO-coated loose particles irradiated in GF-1, GF-2, and GF-3 is related to the deposition conditions and structural properties of the pyrocarbon layer, which are summarized in Table 5-5. All of the OPyC properties in this table with the exception of active coating gas ratio and microporosity were within the required specification ranges defined in Ref. 5-9. All of the OPyC layers on TRISO-coated fuel that exhibited failure levels >1.3% had OPyC microporosities $\lesssim$10 ml/kg OPyC. These relatively low microporosities (current specification limit $\geq$13 ml/kg OPyC) are related to deposition conditions with dilute active coating gas concentrations, i.e., <25 vol % C_2H_2 plus C_3H_6 in total coating gas. A more detailed discussion in Section 5.8.2.3 shows that these deposition conditions lead to low microporosities and an OPyC structure that undergoes anisotropic dimensional changes during irradiation. It is inferred that the resulting irradiation-induced stresses in these structures are sufficient to cause premature OPyC failure.

5.4. FUEL ROD DIMENSIONAL CHANGE

Postirradiation fuel rod dimensional change measurements were made using a calibrated dial gauge micrometer that had an accuracy of $\pm 10^{-4}$ mm. Three diametral measurements were made on each fuel rod, i.e., one on each end and one in the middle. In addition, one length measurement was made on each fuel rod. The averages of each set of diameter and length measurements, before and after irradiation, were used to calculate the percent dimensional change due to irradiation. In addition, the volumetric dimensional change of fuel rods was calculated on the basis of a cylindrical fuel rod geometry as follows:

$$\Delta V/V = 2\Delta D/D + \Delta L/L \quad , \qquad (5\text{-}1)$$

where $\Delta V/V$, $\Delta D/D$, and $\Delta L/L$ are incremental volume, diameter, and length changes, respectively, due to irradiation. Table 5-6 lists values for $\Delta V/V$, $\Delta D/D$, and $\Delta L/L$ along with irradiation exposure conditions for each fuel rod tested in capsules GF-1, GF-2, and GF-3. Table 5-6 also lists fuel rod anisotropy, which is arbitrarily defined as $\Delta L/L - \Delta D/D$. The volumetric, length, and diametral changes versus fast fluence for GF-1, GF-2, and GF-3 fuel rods are plotted in Figs. 5-24 through 5-26. These figures show separate plots for measured and predicted volumetric and dimensional changes for rods containing either all TRISO-coated fuel or TRISO/BISO-coated fuel.

Fuel rod volumetric and dimensional changes were predicted using the model described in Ref. 5-10. The model assumes that the fuel rod structure consists of a point-to-point contact of the particle phases with an interconnecting matrix network through the interstitial voids. Initially, based on limited experimental evidence, it was assumed that irradiation-induced matrix shrinkage was always greater than the shrinkage of the close-packed fuel particles, so that the bulk volume change of a fuel rod was determined by the dimensional change of particles (Ref. 5-11). This led to the conclusion that the fuel rods always exhibited isotropic dimensional change and the matrix phase did not contribute to fuel rod dimensional change; i.e., it continued to shrink into the interstitial volume. However, recent experimental evidence (Ref. 5-10) indicated that shrinkage of the matrix with respect to the particles cannot be assumed to operate over the entire range of temperature and fluence conditions. Consequently, the matrix must be accounted for in a general description of fuel rod dimensional changes. The general model accounts for the volume fraction and irradiation-induced volumetric changes of all components in a fuel rod, i.e., fuel particles, shim, matrix, and porosity. Reference 5-10 defines the volumetric changes for each of the fuel rod components in GF-1, GF-2, and GF-3 fuel rods. Specific attention is directed toward the matrix behavior in these rods. Figure 5-27 is a plot of the volumetric change of the matrix versus fast fluence, which describes matrix behavior in GF-1, GF-2, and GF-3 fuel rods. The point to be noted is that the matrix phase undergoes volumetric expansion for fast fluences greater than ~5 x 10^{25} n/m^2 $(E > 29\ fJ)_{HTGR}$. This matrix behavior is particularly evident in GF-1, GF-2, and GF-3 fuel rods fabricated with all TRISO-coated fuel as shown in Fig. 5-24, which shows measured volumetric expansion at ~6 x 10^{25} n/m^2 $(E > 29\ fJ)_{HTGR}$. These rod types contain TRISO-coated fuel, shim, and matrix. The TRISO-coated fuel and shim particles undergo a maximum volumetric contraction of -3% to -4% for fast fluences between 3 and 9 x 10^{25} n/m^2 at temperatures of 1100°C or less. Consequently, the matrix phase is the only component in these fuel rods types that can account for fuel rod expansion.

Two other points are also worth noting in Fig. 5-24:

1. Measured volumetric changes are less than predicted values at fast fluences greater than ~4 x 10^{25} n/m^2 $(E > 29\ fJ)_{HTGR}$.

2. Fuel rods containing TRISO/BISO-coated fuel particles exhibit a greater volumetric contraction compared to rods containing all TRISO fuel.

Regarding item 1 above, the model described in Ref. 5-10 assumes that during matrix expansion the matrix can expand into void volume previously created as a result of differential volumetric changes between the matrix and particles. However, as also stated in Ref. 5-10, it is possible that the matrix can creep during irradiation to accommodate differential volumetric contractions. Under this condition voids would not be created and the fuel rod would exhibit an expansion comparable to that of the matrix phase. This appears to be the case when a comparison is made between the volumetric expansion in Fig. 5-24 of fuel rods containing TRISO-coated fuel (Fig. 24) with matrix expansion (Fig. 5-27). Consequently, the model defined in Ref. 5-10 may have to be modified to account for matrix creep as more empirical data are developed.

Item 2 above is explained on the basis of BISO-coated fuel particles exhibiting volumetric contractions of ~18% at fluences between 6 and 8×10^{25} n/m^2 (E > 29 fJ)$_{HTGR}$ (Ref. 5-10). The relatively large volumetric contractions of BISO-coated particles compared to TRISO-coated particles accounts for the correspondingly larger volumetric changes in fuel rods shown in Fig. 5-24. This same trend is evident in the length and diametral changes plotted in Figs. 5-25 and 5-26.

Predicted diameter and length dimensional changes in GF-1, GF-2, and GF-3 fuel rods are defined on the following basis:

$$\Delta L/L = 1/3\ (\Delta V/V + 2 \cdot \Delta\varepsilon) \qquad (5\text{-}2)$$

$$\Delta D/D = 1/3\ (\Delta V/V - \Delta\varepsilon) \quad , \qquad (5\text{-}3)$$

where $\Delta L/L$, $\Delta D/D$, and $\Delta V/V$ are length, diameter, and volume changes respectively, and $\Delta\varepsilon$ is strain anisotropy, which is defined as ($\Delta L/L - \Delta D/D$). If a fuel rod exhibits isotropic behavior, $\Delta\varepsilon = 0$ and Eqs. 5-2 and 5-3 reduce to $\Delta L/L = \Delta D/D = 1/3\ \Delta V/V$. However, fuel rods containing matrix and shim particles exhibit anisotropic behavior, which is described by the $\Delta\varepsilon$ versus fast fluence relationship plotted in Fig. 5-28. This relationship combined with predicted volumetric fuel rod changes was used with Eqs. 5-2 and 5-3 to predict length and diameter changes in Figs. 5-25 and 5-26. The solid line in Fig. 5-28 is the expected strain anisotropy for GF-1, GF-2, and GF-3 fuel rods based on an empirical model (Ref. 5-10). The strain anisotropy data observed for GF-1, GF-2, and GF-3 fuel rods are superimposed in this figure. In general, the GF capsule data are bounded by the 90%

confidence bounds of the model. Figure 5-28 also shows that fuel rod strain anisotropy exhibits the following characteristics:

1. A positive correlation with fast fluence exposure, i.e., a progressive increase in strain anisotropy.

2. A preferential bias between diametral and length changes, with $\Delta\epsilon$ being consistently greater than unity with the exception of one data point.

These observations may be rationalized on the basis of systematic preferential alignment of anisotropic components within a fuel rod. The most plausible explanation for the strain anisotropy trends evident in Fig. 5-28 is that the preferred alignment of graphite shim and/or filler particle basal planes perpendicular to the rod axial direction resulted in expansion or less shrinkage in the axial direction compared with the radial direction. This has been partially substantiated by empirical results presented in Ref. 5-10.

5.5. FUEL ROD THERMAL CONDUCTIVITY MEASUREMENTS

The relative thermal conductivities of two GF-1 and three GF-2 rods were measured after irradiation at three temperatures: 600°, 700°, and 800°C. No measurements were made on GF-3 rods because of difficulties associated with rod fragmentation. The relative thermal conductivity measurements were converted to absolute values by comparing all measurements to graphite standards of known thermal conductivities. The measurement technique is referred to as a "LECI" thermal conductivity measurement and is documented in Refs. 5-12 and 5-13. The implicit assumption in applying this technique is that differences in thermal conductivity between the sample and the standard do not result in significant changes in the response of thermal flux meters in the apparatus. This condition is not generally met; consequently, large uncertainties in the reported thermal conductivities exist. Table 5-7 summarizes GF-1 and GF-2 fuel rod thermal conductivity measurements. The general trends evident from this table are summarized as follows:

1. Before irradiation the thermal conductivities of fuel rods fabricated by the CEA CERCA process were 55% to 105% greater than those for GA matrix injected rods. After irradiation to fluences $>5.0 \times 10^{25}$ n/m^2 $(E > 29\ \mathrm{fJ})_{HTGR}$, this difference was reduced from 27% to 61%.

2. Fuel rod thermal conductivities after irradiation (for GA rods) ranged from 42% to 64% of the preirradiated conductivity. These data indicate that this reduction in conductivity occurs early in life, i.e., at fluences of $\sim 4 \times 10^{25}$ n/m^2 $(E > 29\ \mathrm{fJ})_{HTGR}$.

A further point worth noting is that the friable character of irradiated fuel rods (surface microcracks) made it impossible to obtain plane or parallel surfaces on samples that were needed for the measuring device. This experimental difficulty, combined with the inaccuracies associated with a comparative standard measurement in the LECI technique, resulted in large uncertainties (estimated at 25% to 50%) in the reported thermal conductivities in Table 5-7. The estimated uncertainties are based on the magnitude of the corrections needed to calibrate "LECI" thermal conductivity measurements against known standards.

5.6. FISSION GAS RELEASE MEASUREMENTS

5.6.1. Postirradiation Fission Gas Release Measurements

The failure fraction of fuel particles can be determined for a sample of particles from knowledge of the R/B ratio of a given isotope and the fractional release for a failed particle, $(R/B)_f$. In order to characterize the failure fraction in capsules GF-1 and GF-2, fuel rods were individually subjected to neutron activation after removal from the fuel element. The reirradiation was carried out at 600°C, where the activities of Kr-85m, Kr-87, Kr-88, Kr-89, Xe-137, and Xe-138 were measured and converted to R/B values (Ref. 5-12).

Figures 5-29 and 5-30 are plots of R/B versus isotope half-life for GF-1 and GF-2 fuel rods reirradiated at 600°C. The isotopes half-lives are bounded by Kr-85m (4.48 hours) and Kr-89 (3.16 minutes). The progressive decrease in R/B with decreasing half-life is related to the rapid decay of the isotope prior to diffusive release through the coatings (refer to Section 4.1.3). GF-3 fuel rods were not reirradiated after irradiation.

The reirradiation Kr-85m R/B measurements at 600°C when corrected for temperature are generally consistent with in-pile EOL measurements (Table 5-8). Table 5-8 shows that the reirradiated EOL temperature corrected values and the in-pile EOL values are typically within a factor of two. This is considered to be a good agreement based on uncertainties associated with (1) fission gas release measurements, and (2) R/B temperature correction values.

5.6.2. Determination of Fuel Failure Levels

Fuel particle failure levels for each fuel rod type can be determined from in-pile or postirradiation fission gas release measurements provided the following information is defined:

1. Heavy metal (U and Th) contamination that is present outside of the coatings. This is defined at the preirradiation state and is termed as manufacturing contamination.

2. The fractional release of fission gases from failed fuel particles, $(R/B)_f$.

The determination of a failure fraction from the R/B data depends upon defining the dependence of $(R/B)_f$ on critical irradiation conditions. In order to empirically establish a value for $(R/B)_f$ for failed fuel, laser-failed particles with burnups between 3 and 9% FIMA were subjected to neutron activation at 600°, 1050°, and 1230°C (Ref. 5-12). Kr-85m R/B measurements for these laser-failed particles are listed in Table 5-9. The fraction of short-lived gaseous isotopes released from failed fuel depends principally on the following:

1. Kernel structure, e.g., oxide versus carbide and porous versus dense.

2. Temperature.

3. Type of failed coating (complete rupture, fine fissures, or coating permeability).

Figure 5-31 is a plot of the Kr-85m R/B measurements listed in Table 5-9 versus kernel burnup. This figure shows that for a given temperature, Kr-85m R/B increases markedly with kernel burnups in the range of 0 to 10% FIMA. The consistency of these data with current fission gas release models (Refs. 5-14, 5-15) is shown by a comparison of the 1050°C measurements with the dashed curve in Fig. 5-31. Also, the figure shows a logarithm increase in Kr-85m R/B with temperature for a given burnup. These data on fission gas release from laser-failed particles can be combined with in-pile Kr-85m R/B measurements to deduce early-in-life fissile particle failure levels and EOL fissile plus fertile particle failure levels.

Equation 4-14 defines the relationship between measured R/B, isotope yield, fraction of U-235 and U-233 fissions, U and Th contamination, and the fraction of fissile and fertile particle failures. Equation 4-14 can be simplified to the following approximation early in life:

$$(R/B)_{\sim BOL} \approx X_{fissile} \times R_{fissile} \quad , \qquad (5\text{-}4)$$

where $X_{fissile}$ = fissile particle failure fraction,

$R_{fissile}$ = fractional release of gaseous isotope from failed fissile particle (dependent on kernel burnup and failure geometry).

This approximation is valid provided the following conditions are met:

1. The fraction of fissions in the fissile fuel is approximately one; i.e., early in life minimal U-233 is bred from Th, and the U-235 in the fissile fuel is predominantly responsible for the birth of gaseous isotopes.

2. The contribution to R/B is predominantly due to fuel failure; consequently, contributions due to heavy metal contamination may be neglected.

The fraction of fissions occurring in fissile fuel tested in GF-1, GF-2, and GF-3 varies linearly from 1 at BOL to ~0.4 at a fluence of 9.8×10^{25} n/m^2 (E > 29 fJ)$_{HTGR}$ (Refs. 5-16 through 5-18). Referring to Figs. 4-22, 4-23, and 4-24, the Kr-85m values increased rapidly for some cells to near peak values for relatively low fluences [~2.5×10^{25} n/m^2 (E > 29 fJ)$_{HTGR}$]. This rapid increase in Kr-85m R/B at low exposures implies that fuel failure is predominantly fissile. A good approximation of fissile failure early in life is obtained by applying Eq. 5-4 at a fluence of 2.5×10^{25} n/m^2 (E > 29 fJ)$_{HTGR}$. At this exposure level, the fraction of fissions in fissile fuel is ~0.85 and Eq. 5-4 is a reasonable approximation to Eq. 4-14. Table 5-10 lists calculated fissile particle failures at a fluence of 2.5×10^{25} n/m^2 (E > 29 fJ)$_{HTGR}$ and shows that fissile failures ranged from <0.13% for types a, d, f, and f' to 1.5% to 8.6% for types b, b', c, and e. Also, it should be noted that the same fissile particles were present in fuel rod types b and c and that all but one cell exhibiting high R/B release contained one of these fuel rod types. Fuel rod type c exhibited the largest failure level in GF-2 cell 3 (8.6%). The explanation for the relatively large fissile failure early in life (discussed fully in Section 6.1.1.3) is related to premature OPyC failure and defective SiC layers.

Fuel failure at EOL can be approximated by the following equation:

$$(R/B)_{EOL} \simeq X\,(R_{fissile} \cdot \bar{F}_{fissile} + R_{fertile} \cdot \bar{F}_{fertile}) \quad , \qquad (5\text{-}5)$$

where X = fissile and fertile particle failure fraction,

$R_{fissile}$, $R_{fertile}$ = fractional release of gaseous isotope from failed fissile and fertile fuel respectively,

$F_{fissile}$, $F_{fertile}$ = fraction of fissions in fissile and fertile fuel respectively,

Equation 5-5 is a valid approximation to Eq. 4-14 provided the following conditions are met:

1. Equal fissile and fertile particle failure fractions.
2. Contribution to R/B is predominantly due to fuel failure; consequently, contributions due to heavy metal contamination may be neglected.
3. Equivalent gaseous isotope yields in fissile and fertile particles. This is a good approximation considering the fissile fuel is $(8Th,U)O_2$.

The calculated fuel failure fractions based on Kr-85m R/B at EOL using Eq. 5-5 and the above assumptions range between 0.07% and 7.38% (Table 5-11). It should be emphasized that the EOL calculations of fuel failure are more uncertain than the early-in-life predictions of fissile fuel failure listed in Table 5-10. This is a consequence of having to assume equal fissile and fertile particle failure fractions at EOL. Without this assumption there is an infinite number of allowable fissile and fertile particle failure fractions that would satisfy a given Kr-85m R/B measurement (Eq. 4-14). Furthermore, additional evidence is presented in Sections 5.7 and 5.8.2.1 (metallography and fuel rod disintegration) which supports the contention that fuel failure predominantly occurs in fissile particles.

These observations imply that the EOL fertile particle failures calculated from in-pile Kr-85m R/B (Table 5-11) are an overestimate of actual fertile particle failures.

A further point to be emphasized is the lack of a systematic trend in pressure vessel failure levels between different fissile particle types. The rod and fissile particle types are as follows:

	TRISO-Coated $(8Th,U)O_2$	
	Kernel Diameter (μm)	Buffer Thickness (μm)
Rod type a	400	80
Rod types b and c	500	100
Rod type b'	500	80

The above particle designs suggest that for equivalent exposure conditions, fissile particle pressure vessel failure should progressively increase when comparing type a rods to type b or c rods and to type b' rods. This is a consequence of the progressive increase in fission gas pressure due to increased kernel diameters with no compensating increase in buffer void volume. Referring to Table 5-10, early-in-life fissile particle failure levels show that the 400-μm-diameter kernel tested in type a rods exhibited pressure vessel failures between 0.05% and 0.13%. This is substantially less than the 3.0% to 8.6% failure range observed for 500-μm-diameter kernels tested in b, b', and c rods. A similar comparison of end-of-life fissile particle failure levels in Table 5-11 shows that type a rods exhibited particle failures between 0.24% and 2.17% compared to a failure range of 1.70% to 7.4% for type b, b', and c rods. Consequently, these data suggest that the 400-μm-diameter $(8Th,U)O_2$ kernel is a more conservative design compared to the 500-μm-diameter kernel designs.

5.7. DETERMINATION OF FUEL FAILURE BY FUEL ROD DISINTEGRATION

The previous section discussed fuel failure levels as determined by fission gas release measurements. In order to further support these failure determinations, a chemical fuel rod disintegration technique was selectively applied to one rod from GF-1 and one from GF-2 (Ref. 5-12). However, only two rods were used because the technique is destructive. Additionally, the technique has certain disadvantages as follows:

1. Long fuel rod dissolution times are required in the hot cell using equipment that is resistant to corrosive vapor.

2. The fuel rod is destroyed; however, fuel particles can be used for subsequent applications.

3. There is a potential risk of attacking intact BISO coatings when when selectively disintegrating carbonaceous matrix in fuel rods.

Experience has shown that the risk associated with failing intact OPyC layers can be avoided by limiting the time of attack; however, this must be balanced against the assurance that all thorium from exposed particles is dissolved. A schematic diagram of the disintegration technique, together with the results for each of the two fuel rods measured, is shown in Table 5-12. The results from electrochemical disintegration show high fissile particle failure (4% to 31%) in batch 6155-01-030 and low fertile particle failure (<1%) in batches 6542-02-036 and 6252-00-020. A comparison of the electrochemical and Kr-85m R/B determined failure levels shows excellent agreement for rod IVA in GF-3 (4% versus 3.8%) and poor agreement for rod IIIA in GF-1 (31% versus 7.4%). An electrochemically determined fissile particle failure of 31% in rod IIIA of GF-1 cannot be rationalized with respect to the 4% failure level determined on the same fissile particle batch (6155-01-030), which was exposed to comparable irradiation conditions (Table 5-12). It can only be suggested that the fuel particles in rod IIIA of GF-1 were damaged after irradiation during unloading and handling.

5.8. STRUCTURAL EVALUATION

A metallographic and electron microprobe examination was performed on 8 fuel rods and 17 loose particle samples irradiated in capsules GF-1, GF-2, and GF-3. The objective of this phase of the PIE was to: (1) evaluate irradiation-induced changes in the fuel particle coating and fuel kernel microstructure; (2) characterize fission product distributions in fuel particles; and (3) characterize the structure and integrity of the carbonaceous fuel rod matrix. Table 5-13 lists the different fuel rod types and loose particle batches evaluated.

5.8.1. Fuel Rod and Matrix Structure

Representative metallographic cross sections for the different fuel rod types are shown in Figs. 5-32 through 5-40.

General Atomic fuel rods (types a, b, b', c, and d) containing shim particles and fabricated by matrix injection have a different structural appearance than CEA rods (types e, e', f, and f') fabricated by the CERCA process. These structural differences are highlighted as follows:

1. Metallographic cross sections of GA rods (Figs. 5-32 through 5-37) show four predominant fuel rod components (fuel particles, graphite shim, matrix, and macroporosity*). The spherical particles are either TRISO-coated fissile or fertile fuel and the shim is a near-isotropic equiaxed graphite particle nominally 800 mm in diameter. Matrix and macroporosity phases are interconnecting and distinguished as a mottled (black and white) area, and a light grey phase is the metallographic mount resin that has impregnated the preexisting voids. The macroporosity range for GA-fabricated rods is 25% to 52%.

---

*Macroporosity is defined as void in the matrix phase that is >50 μm in extent and microporosity is defined as void that is <50 μm in extent.

2. Metallographic cross sections of CEA rods (Figs. 5-38 through 5-40) show only two predominant components (fuel particles and matrix). No shim was used in CEA rods and the matrix phase has no apparent macroporosity. It is probable that the improved structural appearance and integrity of CEA rods compared to GA rods (Section 5.2) is a result of minimal macroporosity. Figures 5-41 through 5-44 are representative metallographic cross sections of the matrix and shim particle in CEA- and GA-fabricated fuel rods. These illustrations indicate that microporosity is typically 50% in GA rods and 13% to 37% in CEA rods.

The improved structural integrity of CEA rods compared to GA rods can be rationalized on the basis of an increased volume fraction of matrix ($\bar{V}_{\text{matrix}}$) in fired rods; namely, $\bar{V}_{\text{matrix}}$ is defined as:

$$\bar{V}_{\text{matrix}} = (1 - \bar{V}_{\text{macroporosity}}) \times (1 - \bar{V}_{\text{microporosity}}) \quad ,$$

where $$V_{\text{matrix}} = \frac{\text{volume coke plus filler}}{\text{volume coke plus filler plus porosity}} \quad ,$$

$V_{\text{macroporosity}}$ = volume fraction of porosity in matrix >50 μm in extent,

$V_{\text{microporosity}}$ = volume fraction of porosity in matrix <50 μm in extent.

Table 5-14 summarizes the range of V_{matrix} values for CEA- and GA-fabricated rods. CEA rods have a V_{matrix} value approximately two and one-half times greater than GA rods; consequently, there is considerably more coke binder and less porosity, which results in improved structural integrity.

5.8.2. Fissile and Inert Particles

5.8.2.1. Metallographic Evaluation. Referemces 5-19 through 5-21 provide a detailed description of the metallographic evaluation of GF-1, GF-2, and GF-3 fuel particles. Representative metallographic cross sections of fissile and inert particles after irradiation are shown in Figs. 5-45 through 5-63. No coating failure was observed that could be attributed to thermochemical effects such as kernel migration (amoeba effect) or fission product attack. However, a number of the photographs (Figs. 5-45, 5-46, 5-47, 5-48, 5-50, 5-53, 5-54, and 5-55) show characteristic irradiation-induced OPyC failure. The fact that failure is irradiation induced and not an artifact of polishing damage is based on the following metallographic observations:

1. Impregnation of the grey mount resin into the failed region of the OPyC layer implies that failure occurred prior to metallographic polishing.

2. Large void openings in failed OPyC layers are characteristic of premature OPyC failure at $\lesssim 3.0 \times 10^{25}$ n/m^2 (E > 29 fJ)$_{HTGR}$, which is followed by densification of the failed OPyC layer on the SiC substrate.

In general the OPyC failure levels observed metallographically in fuel rods are consistent with those observed in the loose particle tests (Table 5-15). Table 5-15 shows a comparative evaluation for three different fissile batches of visually and metallographically determined OPyC failures. Differences in OPyC failures for a given fissile batch are attributed to either differences in exposure conditions (temperature and fluence) and/or statistical uncertainties associated with limited particle counts (typically $\lesssim$100 and $\lesssim$36 for visual and metallographic evaluations, respectively). No metallographic evidence was observed showing matrix - OPyC coating interactions; consequently, it is reasonable to expect comparable OPyC failure levels for fissile particles tested in the unbonded (loose particle) and bonded (fuel rod) state.

No metallographic determination of SiC layer failures was made because of the inherent brittleness of this layer and the tendency for cracking during polishing (Ref. 5-22). Furthermore, since this layer is dimensionally stable during irradiation, there is no tendency for localized irradiation-induced failures to enlarge in a manner similar to OPyC failures and consequently become distinguishable from polishing artifacts. No catastrophic SiC failure was observed metallographically in any of the fissile particle batches. This implies that the SiC failure that did occur as evidenced by the high Kr-85m R/B values early in life (Section 5.6) is most probably a localized crack in the SiC layer. Such localized cracks are consistent with manufacturing defects determined by a mercury intrusion/radiographic evaluation (Section 5.8.2.4).

Two additional structural features that were characterized during the metallographic evaluation were IPyC cracks and the tendency for IPyC shrinkage away from the SiC layer. The range of irradiation-induced IPyC cracks was between 0% for CEA lot MG 198 (irradiated in GF-3, rod IB) to 60% for lot 6155-01-030 (irradiated in GF-3, rod IIIB). A representative photomicrograph of IPyC cracking is shown in Figs. 5-48 and 5-50. No systematic trend was observed between IPyC cracking and rod lot variables or irradiation conditions. The tendency for IPyC/SiC layer separation is also variable and ranges from 0 to ~36%. Figure 5-54 is a representative photomicrograph of IPyC/SiC layer separation. Though unsubstantiated, it would appear that IPyC coating conditions and properties that favor pyrocarbon crystallite anisotropy are more likely to produce conditions favoring IPyC cracking or IPyC/SiC separation. The optical anisotropy of the separated IPyC layer in Fig. 5-54 is evident under polarized light. The IPyC/SiC separation is attributed to an increased rate of IPyC densification during irradiation and higher internal stresses in this layer.

It should be emphasized that the generic TRISO-coated particle design basis for the IPyC layer is related exclusively to the permeability of this layer to gaseous chlorine products during SiC deposition (Ref. 5-7). Specifically, reaction products formed between H_2 and methyltrichlorosilane during SiC deposition can diffuse through a permeable IPyC layer, react with the kernel, and cause excessive heavy metal dispersion. The original intent of the IPyC layer was to protect the SiC from chemical reactions with the kernel during irradiation, as well as to provide added structural support to the composite TRISO coating. It has been observed in high-burnup, high-temperature irradiations of UC_2 TRISO particles that the IPyC is an effective sink for some of the highly mobile fission products (lanthanides). Interactions with these fission products, however, degrade the coating structurally to a degree where it appears no longer to provide any mechanical support to the composite layer pressure vessel. This is clearly evident in Fig. 5-60, which shows a high density of lanthanide fission products at the outer perimeter of the IPyC layer. Figure 5-60 also shows IPyC-SiC separation and the corresponding lack of any mechanical support that the IPyC layer might provide to the SiC layer. Therefore, when setting property limits for this coating, its role in containing fission gas pressure has not been considered, and emphasis has been placed upon manufacturing process requirements related to keeping Cl_2 from the methyltrichlorosilane decomposition out of the buffer during SiC deposition.

The fissile particle kernel types for CF-1, GF-2, and GF-3 were $(8Th,U)O_2$ and UC_2. The mixed oxide fuel was fabricated by either a sol-gel process (GA fuel) or an AVS process (CEA fuel). UC_2 fuel was fabricated by a high-temperature sphere-forming process (patented as VSM). The structural appearance of the $(8Th,U)O_2$ kernels after irradiation was characterized by fission gas bubbles dispersed evenly throughout the kernel (Figs. 5-45 through 5-55). A comparative evaluation of the different $(8Th,U)O_2$ kernel structures indicates that larger gas bubble formations are favored in those structures irradiated to higher burnups and/or at higher operating temperatures (Figs. 5-48 and 5-53).

This observation is consistent with an increased rate of bubble coalescence due to increased bubble concentrations at higher burnups and increased migration rates at higher temperatures. In addition, occasional kernel cracking was observed (Figs. 5-46 and 5-48) and appeared to be more pronounced in AVS kernels compared to sol-gel fabricated kernels. Metallography revealed no metallic fission product concentrations in the kernel or in the buffer and IPyC layers. Consequently, the mixed oxide fissile kernels appear to be highly retentive of metallic fission products and suppress the potential for metallic fission product - SiC attack. A final structural observation is that no kernel migration (amoeba effect) was observed in any of the $(8Th,U)O_2$ kernels. In addition to the TRISO-coated $(8Th,U)O_2$ fuel, a single batch (6445-00-010) of BISO-coated $(8Th,U)O_2$ fuel was tested as loose particles. The visual examination indicated that this fuel exhibited <0.3% pressure vessel failure; this is substantiated by metallographic evaluation, which showed no OPyC failure (see Fig. 5-69, Section 5.8.2.2). It should also be noted that the kernel structures in the batch are comparable to the structures observed for TRISO-coated $(8Th,U)O_2$ fuel. However, the BISO coating may be permeable to gaseous fission products, which would reduce internal fission gas pressure and the tendency for pressure vessel failure. Although speculative, this is partially substantiated by gaseous CO_2 permeability measurements made at CEA on BISO OPyC coatings with properties comparable to batch 6445-00-010. Specifically, Ref. 5-23 showed that BISO coatings on ThO_2 and $(8Th,U)O_2$ had measured CO_2 permeabilities at room temperature between 0.4 and 5.0×10^{-11} cm^2/s. The possibility exists that noble fission gases could readily diffuse through BISO coatings at higher temperatures.

The UC_2 VSM kernel structures showed segregation into a fuel phase and regions of rejected carbon (Figs. 5-61 and 5-63). The kernels were irregular in shape and the high-carbon regions appeared optically anisotropic when viewed under polarized light. These structural observations on UC_2 kernels are consistent with irradiation capsules P13R and P13S test results on reference-type UC_2 fuel irradiated at temperatures between 1000° and 1100°C

(Ref. 5-8). The UC_2 kernels also showed extensive migration of metallic fission products into the IPyC layer and adjacent to the SiC interface (Fig. 5-59). This is particularly clear in a polarized light metallographic cross section (Fig. 5-59), which shows the optically active metallic fission products deposited uniformly around the IPyC-SiC interface. The metallic fission products in the IPyC layer and at the IPyC-SiC interface are lanthanides. In addition, localized pockets ($\lesssim 5$ μm in extent) of palladium were also present at the SiC interface (see Section 5.8.2.2 for a detailed discussion). In general, it appears that metallic fission product migration in UC_2 fuel is less in the GF-3 loose particle tests than in the GF-1 tests. This is a consequence of ~100°C lower operating temperature for GF-3 compared to GF-1 (1095° versus 1000°C). In no case was metallic fission product - SiC attack observed. In addition, no kernel migration (amoeba effect) was observed in UC_2 fuel.

5.8.2.2. Electron Microprobe Evaluation. A detailed electron microprobe evaluation was performed to characterize metallic fission product distributions in the BISO-coated $(8Th,U)O_2$ fuel and reference-type TRISO-coated UC_2 fuel (Ref. 5-24). The UC_2 fuel (batch 6151-00-010) was irradiated as loose particles in position 40 of capsule GF-1. The exposure conditions were 1095°C, 3.7×10^{25} n/m^2 $(E > 29\ fJ)_{HTGR}$, and ~55% FIMA. Electron microprobe characterization of this fuel concentrated on the following structural features observed during the metallographic evaluation:

1. Presence of a dense anisotropic carbon zone at the perimeter of the fuel kernel (Fig. 5-63).

2. Presence in the IPyC layer of a zone that appeared white and was confined to one side of the kernel (Figs. 5-58 and 5-59).

Table 5-15 summarizes the electron microprobe results for different structural regions in the TRISO-coated UC_2 fuel. In addition to the fission product distributions defined in Table 5-16, palladium is also present in the form of a fine ring at the IPyC-SiC interface. The results from this phase of the investigation are summarized as follows:

1. The region at the UC_2 kernel perimeter contains a large number of metallic fission products; however, the lanthanide group elements have a substantially reduced concentration (0.1 to 1 wt %) compared to the "white region" in the IPyC layer, which contains ~2 wt % each of La, Ce, Pr, and Nd (Table 5-16).

2. Under exposure conditions of 1095°C, 3.6×10^{25} n/m^2 (E > 29 fJ)$_{HTGR}$, and 55% FIMA in UC_2, the SiC layer is highly retentive of Cs, Ba, La, Ce, Pr, and Pd (Figs. 5-64 and 5-65).

A detailed electron microprobe evaluation of a BISO-coated $(8Th,U)O_2$ fuel (batch 6445-00-010) was performed to define a basis for comparing the effectiveness of different kernel dopants (Al or Si) on metallic fission product retention. A back-scattered electron density image defining the distribution of Cs, Rb, S, and Th in the BISO-coated particle is shown in Section 5.8.4.2 (Fig. 5-92). This fuel was irradiated in GF-1 to 2.7×10^{25} n/m^2 (E > 29 fJ)$_{HTGR}$, 7.1% FIMA, and 1095°C. This figure shows that Cs is distributed in an unusual way in the buffer coating; namely, Cs is found in a localized phase containing S and Rb. The Cs content in these localized reigons is ~20 wt %. Furthermore, instability during electron measurements of the metallic fission products implies that these localized regions contain oxygen.

The presence of Rb and Cs is reasonable since these are two alkaline metals with similar chemical properties; however, it is difficult to rationalize the pressure of sulfur. In addition to localized Cs concentrations in the buffer layer, Cs was detected in the OPyC layer and surrounding matrix at concentrations of ~1000 ppm. Barium and strontium were not found in the buffer or OPyC coatings but were detected in small quantities in the kernel where they were homogeneously distributed.

5.8.2.3. OPyC Characterization on TRISO-Coated Fissile Fuel. Metallographic and loose particle visual examinations of TRISO-coated fissile fuel in GF-1, GF-2, and GF-3 showed high OPyC failure levels (1.3% to 83% (Tables 5-4 and 5-15). These high OPyC failure levels are consistent with the empirical correlation established in Ref. 5-7, which shows that the probability of OPyC failure increases significantly as OPyC microporosity decreases below ~15 ml/kg OPyC layer (Fig. 5-74). Figure 5-74 shows a relatively narrow transition region between 7 and 15 ml/kg OPyC bounded by the GF-1, GF-2, and GF-3 loose particle fissile tests. The microporosity plotted on the abscissa in Fig. 5-74 is a measure of the total interconnecting porosity that is accessible to mercury intrusion at 69 MPa.

Additional investigations showed that there is considerable variability of OPyC microporosities among particles coated from the same parent batch. This variability is shown in Fig. 5-75 and appears to increase as the average microporosity increases. Furthermore, the fraction of OPyC layers in a batch with low microporosities, i.e., mercury intruded into <9% of OPyC coating thickness, correlates well with the OPyC failure fraction. Figure 5-76 is a visual standard of the minimum degree of OPyC microporosity required for acceptable OPyC performance. The fraction of OPyC layers in GF-1, GF-2, and GF-3 fissile particles with microporosities less than the standard in Fig. 5-76 were calculated. These low OPyC microporosity fractions are compared to the OPyC failure fraction ranges observed in GF-1, GF-2, and GF-3 (Table 5-17). The comparison in Table 5-17 shows that the level of OPyC failures is closely correlated with the percent of layers with low microporosities; however, there is no apparent correlation with either optical anisotropy or mean coating rate. Originally, it was thought (Ref. 5-7) that optical anisotrophies ≲1.040 and coating rates between 2.5 and 8.0 μm/ min were sufficient controls to assure acceptable OPyC performance during irradiation. However, the OPyC failures in GF-1, GF-2, and GF-3 fissile particles are in conflict with this. A further evaluation of coating conditions for TRISO-coated fissile fuel in GF-1, GF-2, and GF-3 shows that for GA-fabricated fuel particles, the OPyC layers were deposited under relatively dilute concentrations of active coating gases. Namely, the ratio of the volume of C_2H_2 plus C_3H_6 to the total volume of coating gases was 0.11. Currently, process specifications for TRISO-coated OPyC layers require that the actual coating gas ratio be >0.25 (Ref. 5-7). This is a consequence of the strong positive correlation between OPyC microporosity and the volume fraction of active coating gases shown in Fig. 5-77.

The underlying problem is to determine which inherent structural features in the shadowed region of Fig. 5-77 contributed to premature irradiation-induced OPyC failure. When considering the deposition process, the volume fraction of hydrocarbon gases (C_2H_2 and C_3H_6) in the total coating gas and the coating temperature determine the relative amounts of pyrocarbon crystallite nucleation and growth in the vapor phase and on the levitated particle bed substrate. This in turn controls the structure of the pyrocarbon layers. Reference 5-25 provides a detailed discussion of structural variations in pyrolytic carbons in terms of different deposition conditions and presents supporting data (transmission electron microscopy) that are consistent with the empirical observations presented in Fig. 5-77. Specifically, oriented pyrocarbon crystallites within conical growth features are expected as the deposition coating rate or the hydrocarbon concentration is reduced. The crystallites in the conical growth features show a strong tendency for orientation of the carbon layer planes parallel to the surface of the substrate. No intergrowth feature pores are present because the cones impinge uniformly on one another, and the crystallites tend to lie with the layer planes perpendicular to the axis of the conical growth feature. Consequently, the interconnecting microporosity for these types of structures is expected to be low. As the deposition coating rate and hydrocarbon gas concentration are increased, the growth features progress from conical to spherical and intergrowth pores develop, which result in higher measured microporosities. In addition, the preferred orientation of the pyrocarbon crystallites between different spherical growth features is disposed randomly, which results in a more isotropic structure.

The inferior irradiation performance of pyrocarbon structures deposited under low hydrocarbon gas concentrations (<0.25) and/or with low microporosities (<13 ml/kg OPyC) is attributed to excessive orientation of pyrocarbon crystallites. This anisotropy leads to a differential between irradiation-induced strains parallel and perpendicular to the substrate surface, which in turn results in higher irradiation-induced stresses. These structural changes are supported by CEA scanning electron microscope examination of OPyC layers on TRISO-coated fissile fuel in GF-1, GF-2, and GF-3 (Ref. 5-12).

The unirradiated pyrocarbon was characterized as an agglomeration of carbon spheroids with the crystallite layers in each spheroid parallel to the spheroid surface. These structural features are shown in Fig. 5-78. This type of structure can be considered macroscopically isotropic since the spheroids are randomly oriented. However, during irradiation individual crystallites begin coalescing into relatively large turbostratic structures with a preferred orientation, i.e., crystallite layers that are parallel to the surface of the deposit. Furthermore, preliminary results tend to indicate that the degree of preferred orientation is proportional to the concentration of spheroids in the unirradiated structure (Ref. 5-12). The degree of anisotropy in the OPyC layers in GF-1, GF-2, and GF-3 fissile particles has been measured optically and shown to increase from a DAR of 1.02 in the unirradiated state to 1.07 for irradiated fuel (Ref. 5-12).

5.8.2.4. <u>SiC Characterization on TRISO-Coated Fissile Fuel.</u> The metallographic evaluation of TRISO-coated fissile particles tested in GF-1, GF-2, and GF-3 did not show SiC failure levels consistent with the in-pile Kr-85m R/B measurements (refer to Section 5.6.1). Furthermore, classical pressure vessel failure is not expected in fissile particles early in life when burnup exposures are less than 50% of peak design values. These considerations prompted a further characterization of the unirradiated fissile particles, which concentrated on detecting localized flaws in the SiC layers of as-manufactured fuel particles. The two techniques used to detect flaws were:

1. Radiographic evaluation of burned-back TRISO-coated particles that were subjected to mercury intrusion at 69 MPa.

2. Measurements of diffusive cesium release on burned-back particles that were activated in the GA TRIGA installation.

The first technique relies on the high hydrostatic pressure to force mercury into microcracks that may be present in defective SiC layers. Once the mercury has intruded into the IPyC and buffer layers, it is readily apparent during a radiograph evaluation. Figure 5-79 is a microradiograph showing defective SiC layers in batches 6155-01-030 and 6155-02-030. Figure 5-79 shows that one of the defective SiC layers has allowed complete mercury intrusion while the other shows localized intrusion. SiC is considered defective when mercury at 69 MPa intrudes into the IPyC layer.

The second technique used to determine the level of defective SiC layers was based on diffusive cesium release. Briefly stated, this technique involved activating a sample (300 to 500 particles) of GF-1, GF-2, and GF-3 fissile particles in TRIGA to produce a Cs-137 inventory of $\sim 10^{15}$ atoms per sample. The samples were then isothermally heat treated at 1600°C for varying times up to 900 hours, and the diffusive Cs-137 released from the particles was measured for each heat-treat time. Also BISO-coated fissile batch 6445-00-010 was included in this study to define a relative basis for Cs-137 release under these heat-treat conditions. Specifically, BISO coatings are permeable to Cs at 1600°C, and a progressive increase in Cs release will occur with heat-treat time. Figures 5-80 and 5-81 are plots of the cumulative Cs-137 release versus time at 1600°C for fissile fuel tested in GF-1, GF-2, and GF-3. Figure 5-81 shows that the BISO batch (6445-00-010) released all the Cs-137 at 900 hours. This implies that an effective SiC defect fraction for TRISO-coated fuel can be determined by defining the fractional Cs-137 release for a 900-hour heat treatment at 1600°C.

Table 5-18 summarizes the fraction defective SiC layers in GF-1, GF-2, and GF-3 fissile particles determined by radiographic evaluation after mercury intrusion, by the fraction Cs-137 released, and by the standard burn-leach technique. Table 5-18 shows that the level of defective SiC layers determined radiographically is approximately two orders of magnitude greater than the burn-leach values. This could be reconciled on the basis that fine microcracks are relatively inaccessible to a leach solution and/or that only a small fraction of the fuel is leachable through these microfissures. Furthermore, the level of defective SiC layers determined radiographically is between a factor of two to an order of magnitude greater than the defective SiC fraction determined by Cs-137 release. This discrepancy could be attributed to the partial retention of Cs by SiC layers that are locally defective; i.e., microfissures in SiC provided a restricted diffusive path compared to large breaches in the SiC layers.

5.8.3. Fertile Particles

5.8.3.1. Metallographic Evaluation. Metallographic cross sections of representative fertile particles irradiated in GF-1, GF-2, and GF-3 are shown in Figs. 5-82 through 5-89. Two batches of GA-fabricated ThO_2 fertile particles were irradiated in GF-1, GF-2, and GF-3 fuel rods, namely, one batch of BISO-coated ThO_2 (6542-02-036) and one batch of TRISO-coated ThO_2 (6252-00-020). The CEA fertile fuel consisted of two batches of BISO-coated ThO_2 (lots MG 156 and MG 207). The quantitative coating failure analysis done on the fertile particles has a high level of uncertainty because of the limited number of particles ($\lesssim$36) observed metallographically for each batch.

TRISO-coated fertile batch 6252-00-020 exhibited an average OPyC failure of 13.8% determined visually; this is generally consistent with the level of metallographically observed failures. The OPyC microporosity in batch 6252-00-020 is 15 ml/kg OPyC layer; however, the active coating gas ratio during deposition was 0.13, which is outside the specification range. Consequently, the high irradiation-induced failure in this batch is expected and consistent with the empirical correlation presented for fissile fuel (refer to Section 5.8.2.3). The OPyC specification is designed to reject batches that are either coated with an active coating gas ratio <0.25 or have an OPyC microporosity <13 ml/kg OPyC (Fig. 5-77). No OPyC failure was observed metallographically in BISO-coated fuel with the exception of batch 6542-02-036. Figures 5-83 and 5-85 show typical microcracks observed in the OPyC layers of this batch. The level of OPyC failure detected in this batch metallographically was 5%; in contrast, no OPyC failure was detected in this batch visually. However, microcracks of this size would be difficult to observe during visual examination. Batch 6542-02-037, which was density separated from the same parent batch as 6542-02-036, showed 2.3% OPyC failure determined visually. Consequently, visual and metallographic observations imply that BISO-coated particles from batches 6542-02-036 and -037 are susceptible to 0 to ~5% pressure vessel failure when exposed to the following conditions: ~3.4 % FIM, 9.4 to 9.6 x 10^{25} n/m^2 (E > 29 fJ)$_{HTGR}$, and 975° to 1000°C.

The buffer coating layers in the fertile fuel increased in density during irradiation and also appeared slightly active optically under polarized light (Fig. 5-86). However, this degree of anisotropy did not result in excessive buffer cracking nor did it appear detrimental to the mechanical integrity of the BISO-coated particle during irradiation.

Irradiation-induced changes in the ThO_2 fuel kernel microstructure in GF-1, GF-2, and GF-3 show the following structural features:

1. At burnups $\lesssim$3.6% FIMA an equiaxed kernel gain structure (~20 mm in diameter), which is readily visible under polarized light (Fig. 5-82). This type of grain structure appears to be susceptible to intergranular cracking during irradiation or subsequent polishing (Figs. 5-84 and 5-87).

2. Homogeneously distributed fine fission gas porosity (Figs. 5-82 and 5-86).

These structural features are consistent with other irradiation experience on ThO_2 (Ref. 5-8).

5.8.4. Advanced Fuel Particle Concepts

Thirty different batches of HTGR-type fuel particles were tested to evaluate the following concepts:

1. Improved metallic fission product retention by using aluminum and silicon dopants in the kernel.
2. Irradiation performance of TRISO-coated particle design using ZrC instead of SiC.
3. BISO-coated $(8Th,U)O_2$ with OPyC layers deposited with a homogeneous distribution of finely dispersed silicon.
4. Irradiation stability of TRISO-coated OPyC layers versus optical anisotropy.

Particles in category 4 were not evaluated during the PIE of capsules GF-1, GF-2, and GF-3; consequently, only the other particle types will be discussed. This section summarizes the visual, metallographic, and metallic fission product characterization for fuel types in categories 1, 2, and 3.

5.8.4.1. Visual Examination of Advanced Fuel Particles. Table 5-19 summarizes the visual results of advanced fuel particles. The first 12 batches in this table are BISO-coated $(8Th,U)O_2$ kernels with different Al and Si kernel dopant concentrations. In general, it appears that these particles are more susceptible to pressure vessel failure as the concentration of kernel dopants increases (refer to GF-1 and GF-2 trends). Furthermore, it should be noted that these particles exhibited zero pressure vessel failure when tested in capsule GF-3. This could be attributed to reduced operating temperatures early in life where rapid pyrocarbon densification occurs and the probability of OPyC failure is greatest. The time-averaged temperature of GF-3 was 1000°C, while the average temperature of GF-1 was 1095°C. Also, during the first part of irradiation (up to 2 x 10^{25} n/m^2 (E > 29 fJ)$_{HTGR}$, GF-2 had an average temperature of ~1075°C.

The next set of four batches in Table 5-19 relates to TRISO-coated $(8Th,U)O_2$ and UC_2 fuel with ZrC layers. A detailed evaluation of these batches is presented in Ref. 5-26. Batch 6171-15E had a ZrC layer deposited on the UC_2 kernel and exhibited 4.6% pressure vessel failure. However, this failure is not unexpected since there is no void volume inside the ZrC layer for accommodation of fission gas pressure. The other batch, (6171-17E), with a ZrC-coated $(8Th,U)O_2$ kernel, did not exhibit any pressure vessel failure; however, the burnup in this batch was 7.1% FIMA as compared to ~60% FIMA for UC_2 in batch 6171-15E. The other two ZrC TRISO-coated batches, which had a buffer layer between the kernel and ZrC layer, showed no pressure vessel failure. The last five batches of BISO-coated $(8Th,U)O_2$, with varying silicon concentrations in the OPyC layer, showed excellent performance. Only one failure was observed in the batch with the highest Si concentration (47.5 wt %).

5.8.4.2. Metallographic Examination of Advanced Fuel Particles. BISO-BISO-coated $(8Th,U)O_2$ particles with doped kernels had a characteristic structural apppearance at the buffer-kernel interface. Figure 5-90 shows a dense, irregular-shaped band around the kernel perimeter. Electron microprobe characterization has shown that this band is essentially comprised of carbon that is depleted in Al and Si dopants and also contains small amounts of fission products. The dense carbon band becomes more pronounced as the concentrations of Si and Al increase. Furthermore, it appears that as the kernel dopant concentration increases, there is a greater tendency for radial fissures to develop in the buffer layer during irradiation. This carbon band is not active optically under polarized light (Fig. 5-90).

Metallic fission product distribution for these fuel types (notably Cs, Sr, and Ba) were evaluated by electron microprobe and gamma spectroscopy. The kernel compositions evaluated by electron microprobe were:

$(8Th,U)O_2$ + 2Al + 1Si (GF-1 and GF-3)

$(8Th,U)O_2$ + 2Al + 2Si (GF-3)

$(8Th,U)O_2$ + 4Al + 4Si (GF-1)

$(8Th,U)O_2$ [GF-1 reference standard without dopants (refer to Section 5.8.2.2)]

Conclusions from this part of the investigation are fully documented in Refs. 5-27 and 5-28 and are summarized as follows:

1. Al and Si dopants are confined to the kernel and do not migrate into the coating layers (Fig. 5-91).

2. A dense carbon-rich band develops at the buffer-kernel interface, which contains a small concentration of fission products but is depleted of Al and Si (Fig. 5-91).

3. Fission products in the kernel generally are associated with Si and to a lesser extent with Al. In addition, comparison of fission product distributions in the same batch [$(8Th,U)O_2$ + 2Al + 1Si] tested in GF-1 and GF-3 indicates that temperature plays a significant role. Specifically, fission products were associated with Si and Al in GF-1, which operated at 1095°C, but not in GF-3, which operated at 1000°C.

4. Zones rich in Si and fission products are characterized by a Si/Al ratio of ~3, which is consistent with feldspar structures (aluminum silicates containing either group 1 or 2 metallic elements).

5. The presence of sulfur in the undoped reference standard (Fig. 5-92) is unexplained and complicates a direct comparison as to the effectiveness of Al and Si kernel dopants.

In addition to electron microprobe characterization, gamma spectroscopy was performed on the kernel and coating layers. This investigation is documented in Ref. 5-29; briefly stated, it involves determining the amount of isotopes that are gamma emitters for both the kernel and coating layers. The following three batches irradiated in GF-1 were evaluated with this technique:

6111-71E	$(8Th,U)O_2$ (reference standard without dopants)
6111-101E	$(8Th,U)O_2$ + 0.5Si
6111-111E	$(8Th,U)O_2$ + 0.5Si

Table 5-20 lists for the above batches the mean content of Pa-233, Ru-103, Zr-95, Cs-134, and Cs-137 determined in the buffer and OPyC coating layers. The results from this table indicate that, in general, Si and Al dopants added separately to $(8Th,U)O_2$ kernels do not appear to be effective in retarding metallic fission product migration. An exception is evident in the case of Ru-103 migration in the kernel containing 0.5Al, where migration is reduced by a factor of 3 to 4 compared to the other batches.

Figure 5-93 is a representative series of metallographic cross sections of four batches of fuel utilizing ZrC coating layers. This figure shows cracked ZrC layers for those batches with the ZrC deposited directly on a UC_2 or $(8Th,U)O_2$ kernel substrate. This is attributed to recoil damage and/or insufficient void volume to accommodate internal fission gas pressure. In contrast, Fig. 5-93 shows that the structural integrity of the ZrC layer is maintained when it occupies the normal SiC position in a TRISO-coated particle design. The good mechanical integrity of these particle designs was confirmed by the visual examination (Table 5-19). Furthermore, electron microprobe analysis of fuel batches 6111-147E and 6111-145E showed that the ZrC layer was an effective barrier to Cs and lanthanide fission product migration into the OPyC layer. In addition, no reaction zone was apparent between the ZrC and metallic fission products. Metallic fission product migration outside the ZrC layer was observed in those batches (6171-15E and 6171-17E) that had the ZrC deposited directly on the kernel substrate; however, fission product migration in these systems is attributed to fissures in the ZrC layer.

Representative metallographic cross sections of BISO-coated (8Th,U)O_2 fuel particles with Si-doped OPyC layers are shown in Figs. 5-94 through 96. These figures clearly show the laminated structural appearance of the OPyC layer; namely, the concentric ring striations in the OPyC layers are regions of high Si concentrations. Polarized light accentuates this structural feature (Fig. 5-94). In addition, Fig. 5-94 shows an intense white band at the buffer-kernel interface, which corresponds to the metallic fission product recoil zone. Fission product distributions were characterized by electron microprobe analysis on the following two batches irradiated in GF-3:

6171-115E	(39 wt % Si in OPyC layer)
6171-105E	(19 wt % Si in OPyC layer)

These results indicated that the mixed PyC + SiC coating was an excellent barrier to fission products, except in the case where the buffer coating contained chlorine. The chlorine may be introduced into the buffer coating during fabrication if the high-density seal coating surrounding the buffer coating is not tight. It has been confirmed that this seal coating layer was tight in the batch with 39% Si but not tight in the batch with 19% Si. In this last batch, the presence of chlorine in the buffer layer resulted in a systematic formation of localized metallic fission products along the inner surface of the OPyC layer and the presence of Cs (~1000 ppm) in the Si-doped OPyC layer.

REFERENCES

5-1. Moreau, C., R. Blanchard, and A. Gueguen, "Examens apres Irradiation GF-1," CEA Report DR 32/75, Dossier No. 5, Part 1, May 28, 1975 (also General Atomic unpublished data).

5-2. Blanchard, R., and J. Veau, "Demontage de la Capsule GF-1," CEA Report DR 42/75, June 30, 1975 (also General Atomic unpublished data).

5-3. Blanchard, R., A. Gueguen, and J. Veau, "GF-3 Examens apres Irradiation Demontage de la Capsule," CEA Report DR 9/76, Dossier No. 5, March 1, 1976 (also General Atomic unpublished data).

5-4. Blanchard, R., "Resultats de l'Examen Visuel des Particles Libres de GF-2," CEA Report DR 28/75, May 22, 1975 (also General Atomic unpublished data).

5-5. Blanchard, R., and A. Gueguen, "Resultats de l'Observation Visuelle des Particles Libres et des Mesures Dimensionnelles des Compacts de GF-3," CEA Report DR 5/76, Dossier No. 5, January 28, 1976 (also General Atomic unpublished data).

5-6. Smith, C. L., "Fuel Particle Behavior Under Normal and Transient Conditions," USAEC Report GA-A12971, General Atomic Company, October 1, 1974.

5-7. Kovacs, W. J., and D. P. Harmon, "Technical Support Document for Issue C of the HTGR Fuel Product Specification," General Atomic unpublished data, August 1979.

5-8. Scott, C. B., D. P. Harmon, and J. F. Holzgraf, "Postirradiation Examination of Capsules P13R and P13S," ERDA Report GA-A13827, General Atomic Company, October 8, 1976, p. 5-56.

5-9. "HTGR Fuel Product Specification," General Atomic unpublished data, December 16, 1974.

5-10. Kovacs, W. J., and D. P. Harmon, "Irradiation-Induced Dimensional Changes in HTGR Fuel Rods," General Atomic unpublished data, November 1979.

5-11. "Public Service Company of Colorado 330-MW(e) High-Temperature Gas-Cooled Reactor Research and Development Program Quarterly Progress Report for the Period Ending September 30, 1970," USAEC Report GA-A10313, General Atomic Company, October 30, 1970, p. 191.

5-12. Blanchard, R., and M. L. Pointud, "Rapport de Synthese des Irradiations GF-1, GF-2, GF-3," CEA Report DR 34/78, November 16, 1978 (also General Atomic unpublished data).

5-13. Rosset, P. J., et al., "Measure de la Vanation du Coefficient de Conductivite Thermique sur Materiaux Irradies," CEA Report SECS/LECI No. 278 (also General Atomic unpublished data).

5-14. "Fuel Design Data Manual," Issue C, General Atomic unpublished data, August 30, 1979.

5-15. "HTGR Generic Technology Program: Fuels and Core Development, Quarterly Progress Report for the Period Ending August 31, 1978, DOE Report GA-A15093, General Atomic Company, September 1978, p. 4-7.

5-16. Gentil, J., and E. Junod, "Irradiation de Combustible GF-1," CEA Report PI/EDTI 236/75, Dossier No. 4, June 5, 1975 (also General Atomic unpublished data).

5-17. Gentil, J., and E. Junod, "Irradiation de Combustible GF-2," CEA Report PI/EDTI 87/76, Dossier No. 4, March 3, 1976 (also General Atomic unpublished data).

5-18. Gentil, J., and E. Junod, "Irradiation de Combustible GF-3," CEA Report PI/EDTI 86/76, Dossier No. 4, March 6, 1976 (also General Atomic unpublished data).

5-19. Blanchard, R., et al., "Irradiation GF-1, Examens apres Irradiation (Metallographic)," CEA Report DR 68/75, Dossier No. 5, Partie 3, December 9, 1975 (also General Atomic unpublished data).

5-20. Blanchard, R., et al., "Examen Apres Irradiation de l'Experience GF-2, Microradiographic et Metallographic," CEA Report DR 6/76, Dossier No. 5, February 5, 1976 (also General Atomic unpublished data).

5-21. Blanchard, R., et al., "Examens Metallographiques et Microradiographiques du Combustible de GF-3," CEA Report DR 4/77, January 28, 1977 (also General Atomic unpublished data).

5-22. Scott, C. B., and D. P. Harmon, "Postirradiation Examination of Capsule F-30," General Atomic Report GA-A13208, April 1, 1975.

5-23. Court, M., "Gas Permeability of Irradiated Pyrocarbon Coatings," CEA Report DR 6/78, February 23, 1978 (also General Atomic unpublished data).

5-24. Morlevat, J. P., and M. Chaudet, "Irradiation GF-1 Examens apres Irradiation: Microanalyse Electronique," CEA Report DR 52/75, September 8, 1975 (also General Atomic unpublished data).

5-25. Kaae, J. L., "Implications of the Structure of Pyrolytic Carbons on the Deposition Mechanism," General Atomic Report GA-A14673, January 1978.

5-26. Reynolds, G., et al., "Irradiation Behavior of Experimental Fuel Particles Containing Chemically Vapor Deposited ZrC Coatings," J. Nucl. Mater. 62, 9 (1976).

5-27. Morlevat, J. P., and M. Chaudet, "Irradiation GF-1 Examens apres Irradiation: Microanalyse Electronique," CEA Report DMG DR 52/75, November 1975 (also General Atomic unpublished data).

5-28. Morlevat, J. P., and M. Chaudet, "Irradiation GF-3 Examens apres Irradiation: Microanalyse Electronique," CEA Report DMG DR 59/76, December 10, 1976 (also General Atomic unpublished data).

5-29. Blanchard, R., and M. Chevalier, "Determination du Coefficient de Partition de Broduits de Fission Entre Noyaux et Enbrobages. Noyaux d'Oxyde Mixte," CEA Report DMG 57/75, September 18, 1975 (also General Atomic unpublished data).

TABLE 5-1

RESULTS OF VISUAL EXAMINATION OF UNBONDED FISSILE AND FERTILE PARTICLES TESTED IN CAPSULE GF-1 (REF. 5-1) AT A TIME-VOLUME AVERAGE TEMPERATURE OF 1095°C

Sample Designation	Kernel Type[a]	Coating Type[b]	No. of Planchets	No. of Particles	Visual Failures (%)		Irradiated Particles Tested (in Fuel Rod or Coupon No.)	Planchet No.	Fluence (10^{25} n/m^2) (E > 29 fJ)$_{HTGR}$
					OPyC	PV[c]			
6155-01-020	MO	T	4	400	63.25	0	Compacts 1, 2, and 5	1,18,35,52	Max. = 4.4 Min. = 2.5 (d)
6155-00-020	MO	T	4	400	3.50	0	Compacts 3 and 4	2,19,36,53	
6155-02-020	MO	T	4	400	26.75	1.5	Compact 6	3,20,37,54	
6445-00-010	MO	B	4	400	0	0		4,21,38,55	
6542-02-036	ThO_2	B	4	400	0	0	Compacts 1 through 6	5,22,39,56	
6151-00-010	UC_2	T	4	400	1.75	0.25		6,23,40,57	
4-18-1-6111-71E	MO	B	2	202	0	0		8,25	
4-19-2-6111-101E	MO (0.5 Si)	B	3	303	0	0		9,26,60	
4-10-1-6111-111E	MO (0.5 Al)	B	3	202	0	0		28,45,62	
4-19-1-6111-95E	MO (2 Si)	B	3	303	0	0		10,43,61	
4-5-2-6111-109E	MO (2 Al)	B	3	404	0	0		12,46,63	
4-18-2-6111-93E	MO (4 Si)	B	3	303	0	17.50		11,27,44	
4-5-1-6111-103E	MO (4 Al)	B	3	303	0	0		13,29,47	
4-12-1-6111-117E	MO (0.5 Al, 1 Si)	B	3	303	0	0		30,48,64	
4-13-1-6111-99E	MO (2 Al, 1 Si)	B	3	303	0	0		31,50,65	
4-12-3-6111-105E	MO (2 Al, 2 Si)	B	3	303	0	1.65		14,49,68	
4-9-2-6111-107E	MO (2 Al, 4 Si)	B	5	505	0	57.43		7,24,41,42,58	
4-12-2-6111-113E	MO (4 Al, 4 Si)	B	3	303	0	25.70		15,51,66	
6111-147E	UC_2	T (ZrC)	1	164	0	0	Coupon 2	16	
6171-17E	UC_2	T (ZrC)	1	108	0	4.63	Coupon 4	34	
6171-15E	MO	T (ZrC)	1.5	97	0	0	Coupon 3	33,67	
6111-145E	MO	T (ZrC)	1.5	89	0	0	Coupon 1	32,67	
--	Saphire	--	1	37	0	0			

(a) MO refers to $(8Th,U)O_2$ with dopants indicated in parentheses.

(b) T refers to TRISO coating and B refers to BISO coating; ZrC TRISO coatings are indicated.

(c) Refers to pressure vessel failure (failed SiC and OPyC layers).

(d) Fluence for individual planchets calculated as $\psi = 2.5 + (\text{planchet No.})(0.02794)$.

TABLE 5-2
RESULTS OF VISUAL EXAMINATION OF UNBONDED FISSILE AND FERTILE PARTICLES TESTED IN CAPSULE GF-2 (REF. 5-4)
AT A TIME-VOLUME AVERAGE TEMPERATURE OF 985°C

Sample Designation	Kernel Type[a]	Coating Type[b]	No. of Planchets	No. of Particles	Visual Failures (%) PV[c]	Visual Failures (%) OPyC	Particles Tested in Fuel Rod Compact No.	Planchet No.	Fluence (10^{25} n/m^2) ($E > 29$ fJ)$_{HTGR}$
6155-01-010	MO	T	4	392	0	63.26		1,18,35,52	Max. = 3.7
6155-00-010	MO	T	4	393	0	8.91		2,19,36,53	Min. = 2.2
6155-02-010	MO	T	4	391	0	25.83		3,20,37,54	(d)
MG 178	MO	T	4	398	0	1.00		4,21,38,55	
MG 199	MO	T	4	395	0	2.79		6,23,40,57	
6171-41-E	MO	B	1	106	0	0		29	
6171-65-E	MO	B	1	106	0	0		25	
6171-67-E	MO	B	1	106	0	0		27	
MG 197	MO	B	4	396	0	0		14,30,34,64	
6252-00-020	ThO_2	T	4	393	0	19.85	5	5,22,39,56	
MG 155	ThO_2	T	3	299	0	1.0		17,51,56	
MG 175	ThO_2	T	3	299	0	0		32,58,57	
MG 156	ThO_2	B	4	397	0	0		15,31,33,59	
6111-71-E	MO	B	1	98	0	0		8	
6111-101-E	MO (0.5 Si)	B	1	99	0	0		26	
6111-111-E	MO (0.5 Al)	B	1	95	0	0		45	
6111-95-E	MO (2 Si)	B	1	97	0	0		43	
6111-109-E	MO (2 Al)	B	1	92	0	0		46	
6111-117-E	MO (0.5 Al + 1 Si)	B	1	97	0	0		48	
6111-99-E	MO (2 Al + 1 Si)	B	1	97	0	0		50	
6111-105-E	MO (2 Al + 1 Si)	B	1	98	0	0		49	
6111-103-E	MO (4 Al)	B	2	189	0	0		13,47	
6111-93-E	MO (4 Si)	B	2	198	33.84	0		11,44	
6111-113-E	MO (4 Al + 4 Si)	B	2	200	24	0		15,65	
6111-107-E	MO (2 Al + 4 Si)	B	2	198	65.15	0		7,42	
6171-105-E	MO	B (19% Si)	2	214	0	0		28,62	
6171-107-E	MO	B (25% Si)	2	213	0	0		10,61	
6171-115-E	MO	B (39% Si)	2	214	0	0		9,60	
6171-119-E	MO	B (40% Si)	2	213	0	0		12,63	
6171-117-E	MO	B (47.5% Si)	2	213	0	0.46		24,41	

(a) MO refers to $(3Th,U)O_2$ with dopants indicated in parentheses.

(b) T refers to TRISO coating and B refers to BISO coating; Si-doped BISO coatings are with Si concentrations in parentheses.

(c) Refers to pressure vessel failure (failed SiC and OPyC layers).

(d) Fluence for individual planchets calculated as $\psi = 2.2 + (\text{planchet No.})(0.02239)$.

TABLE 5-3

RESULTS OF VISUAL EXAMINATION OF UNBONDED FISSILE AND FERTILE PARTICLES TESTED IN CAPSULE GF-3 (REF. 5-5) AT A TIME-VOLUME AVERAGE TEMPERATURE OF 1000°C

	Kernel Type(a)	Coating Type(b)	No. of Planchets	No. of Particles	Visual Failures (%)		Planchet No.	Fluence (10^{25} n/m^2) (E > 29 fJ)$_{HTGR}$
					OPyC	PV(c)		
6155-01-020	MO	T	3	300	58.7	0.3	1,35,52	Max. = 9.8
6155-00-020	MO	T	3	300	2.0	0	2,19,53	Min. = 8.4
6155-00-010	MO	T	3	300	2.73	0.7	3,18,36	(d)
6155-01-010	MO	T	3	300	56.3	1.33	5,21,57	
6155-02-010	MO	T	3	300	14.3	0.3	15,34,58	
6155-02-020	MO	T	3	300	26.3	2.3	20,37,54	
MG 178	MO	T	5	503	0.7	0	7,26,48,63,71	
MG 199	MO	T	4	402	0	0	8,30,49,65	
6445-00-010	MO	B	3	299	0	0.3	4,38,55	
MG 197	MO	B	4	402	0	0	9,31,51,66	
6171-41-E	MO	B	1	45	0	0		
6171-67-E	MO	B	1/2	45	0	0		
6171-65-E	MO	B	1/2	45	0	0		
6222-19-E	MO	B	1	76	0	0		
6222-25-E	MO	B	1	76	0	0		
6171-105-E	MO	B (19% Si)	1	108	0	0	28	
6171-107-E	MO.	B (25% Si)	1	108	0	0	10	
6171-115-E	MO	B (39% Si)	1	108	0	0	60	
6171-119-E	MO	B (40% Si)	1	108	0	0	12	
6171-117-E	MO	B (47.5% Si)	1	108	0	0	24	
6171-71-E (Ref.)	MO	B	1/2	50	0	0		
6111-101-E	MO (0.5 Si)	B	1/2	51	0	0		
6111-111-E	MO (0.5 Al)	B	1/2	50	0	0		
6111-95-E	MO (2 Si)	B	1/2	50	0	0		
6111-109-E	MO (2 Al)	B	1/2	51	0	0		
6111-117-E	MO (0.5 Al + 1 Si)	B	1/2	50	0	0		
6111-99-E	MO (2 Al + 1 Si)	B	1/2	50	0	0		
6111-105-E	MO (2 Al + 2 Si)	B	1/2	50	0	0		
6111-103-E	MO (4 Al)	B	1/2	50	0	0		
6111-93-E	MO (4 Si)	B	1	86	0	0	27	
6111-113-E	MO (4 Al + 4 Si)	B	1/2	51	0	0		
6111-107E	MO (2 Al + 4 Si)	B	1	101	0	0	41	
6252-00-020	ThO_2	T	3	300	6.0	0	16,44,64	
MG 175	ThO_2	T	4	404	0.25	0	14,47,67,69	
6542-02-037	ThO_2	B	3	300	2.3	0	22,39,56	
MG 156	ThO_2	B	4	402	0	0	11,32,59,62	
MG 207	ThO_2	B	5	505	0	0	13,33,61,68,70	
6151-00-010	UC_2	T	3	300	1.3	0	6,23,40	

(a)MO refers to $(8Th,U)O_2$ with dopants indicated in parentheses.

(b)T refers to TRISO coating and B refers to BISO coating; Si-doped BISO coatings are indicated with Si concentrations in parentheses.

(c)Refers to pressure vessel failure (failed SiC + OPyC layer).

(d)Fluence for individual planchets calculated as $\psi = 8.4 + (\text{planchet No.})(0.01972)$.

TABLE 5-4
SUMMARY OF VISUALLY DETERMINED UNBONDED PARTICLE FAILURES OBSERVED IN GF-1, GF-2, and GF-3
(EXCLUDES DOPED KERNEL AND ZrC-TRISO FUEL TYPES)

Particle Type	Sample Designation	Fuel Failure (%)						GF-1 + GF-2 + GF-3		
		GF-1[(a)]		GF-2[(b)]		GF-3[(c)]		No. of Particles Irradiated	Total OPyC Failure (%)	Total PV[(d)] Failure (%)
		OPyC	PV[(c)]	OPyC	PV[(d)]	OPyC	PV[(d)]			
TRISO with mixed oxide kernel	6155-01-020	63.2	0	--	--	58.7	0.3	700	61.3	0.1
	6155-01-010	--	--	63.3	0	56.3	1.3	692	60.2	0.6
	6155-02-020	26.7	1.5	--	--	26.3	2.3	700	26.5	1.8
	6155-02-010	--	--	25.8	0	14.3	0.3	691	20.5	0.1
	6155-00-020	3.5	0	--	--	2.0	0	700	2.8	0
	6155-00-010	--	--	8.9	0	27.3	0.7	693	16.7	0.3
	MG 178	--	--	1.0	0	0.7	0	901	0.9	0
	MG 199	--	--	2.8	0	0	0	797	1.3	0
BISO with mixed oxide kernel	6445-00-010	0	0	--	--	0	0.3	693	0	0.14
	MG 197	--	--	0	0	0	0	796	0	0
TRISO with thorium kernel	6252-00-020	--	--	19.8	0	6.0	0	693	13.8	0
	MG 175	--	--	0	0	0.25	0	699	0.1	0
	MG 165	--	--	1.0	0	--	0	299	1.0	0
BISO with thorium kernel	6542-02-037	--	--	--	--	2.3	0	300	2.3	0
	6542-02-036	0	0	--	--	--	--	400	0	0
	MG 156	--	--	0	0	0	0	699	0	0
	MG 207	--	--	--	--	0	0	505	0	0
TRISO with UC_2 kernel	6151-00-010	1.75	0.25	--	--	1.3	0	700	1.6	0.14

(a) Irradiation exposure: 1095°C and 5.6 to 6.4 x 10^{25} n/m^2 (E > 29 fJ)$_{HTGR}$.

(b) Irradiation exposure: 985°C and 1.9 to 4.0 x 10^{25} n/m^2 (E > 29 fJ)$_{HTGR}$.

(c) Irradiation exposure: 1000°C and 8.8 to 10.2 x 10^{25} n/m^2 (E > 29 fJ)$_{HTGR}$.

(d) Refers to pressure vessel failure (failed OPyC and SiC layer).

TABLE 5-5
TRISO-COATED LOOSE PARTICLE OPyC PROPERTY AND PROCESS CHARACTERISTICS (EXCLUDES ADVANCED FUEL PARTICLE TYPES)

			OPyC Properties						Range of Irradiation Conditions		
Particle Batch No.	Particle Type	TRISO-Coated Particle Size (μm)	Thickness (μm)	Density (Mg/m^3)	Optical Anisotropy	Microporosity (ml/Mg)	Coating Rate (μm/min)	Active Coating Volume Fraction	Time-Volume Average Temperature (°C)	Fluence (10^{25} n/m^2) (E > 29 fJ)$_{HTGR}$	Range of Visually Determined OPyC Failure (%)
6155-00-010	(8Th,U)O_2	713	36	1.78	1.13	6.41	2.25	0.11	985-1000	(a)	8.9-27.3
6155-00-020	(8Th,U)O_2	695	41	1.76	1.14	7.51	2.83	0.11	1095-1000	(b)	3.5-2.0
6155-01-010	(8Th,U)O_2	888	40	1.78	1.13	9.19	3.08	0.11	985-1000	(a)	63.3-56.3
6155-01-020	(8Th,U)O_2	885	42	1.81	1.07	9.32	3.36	0.11	1095-1000	(b)	63.2-58.7
6155-02-010	(8Th,U)O_2	831	40	1.81	1.13	9.36	3.33	0.11	985-1000	(a)	25.8-14.3
6155-02-020	(8Th,U)O_2	840	41	1.82	1.13	9.40	3.42	0.11	1095-1000	(b)	26.7-26.3
6151-00-010	UC_2	595	44	1.80	1.11	6.77	1.47	0.13	1095-1000	(b)	1.75-1.3
6252-00-020	ThO_2	833	42	1.81	1.24	15.30	4.24	0.13	985-1000	(a)	19.8-6.0

(a) Ref. Tables 5-2 and 5-3.
(b) Ref. Tables 5-1 and 5-3.

TABLE 5-6
FUEL ROD DIMENSIONAL CHANGE DATA FOR CAPSULES GF-1, GF-2, AND GF-3

Capsule	Rod and Cell No.(a)	Fuel Rod: GA Data Retrieval Number (7161-003-)	Fuel Rod: Type	Irradiation Conditions: Time Volume Average Temperature (°C)	Irradiation Conditions: Fast Fluence (10^{25} n/m^2) $(E > 29\ fJ)_{HTGR}$	Dimensional Change: Diametral ($\Delta D/D_o$) (%) Measured	Dimensional Change: Diametral ($\Delta D/D_o$) (%) Predicted(a)	Dimensional Change: Axial ($\Delta L/L_o$) (%) Measured	Dimensional Change: Axial ($\Delta L/L_o$) (%) Predicted(a)	Volumetric ($\Delta V/V_o$) (%) Measured	Volumetric ($\Delta V/V_o$) (%) Predicted	Fuel Rod Anisotropy (Axial - Diamentral) ($\Delta L/L - \Delta D/D$) (%)
GF-1	1-1	(b)	e'	1080	4.7	-2.01	(c)	-0.86	(c)	-4.88	(c)	1.15
	1-2	(b)	e	1080	5.5	-1.73	(c)	-0.95	(c)	-4.41	(c)	0.78
	2-3	01-4	a	1170	6.4	-1.16	-1.52	-0.12	-0.65	-2.44	-3.7	1.04
	2-4	01-5	a	1170	6.7	-1.18	-1.52	-0.21	-0.65	-2.57	-3.7	0.97
	3-5	02-5	b	1170	6.5	-1.13	-1.48	-0.03	-0.63	-2.24	-3.6	1.10
	3-6	03-5	b'	1170	6.1	-1.45	-1.48	-0.37	-0.63	-3.27	-3.6	1.08
GF-2	1-1	05-5	d	960	3.4	-2.05	-2.18	-1.55	-1.55	-5.65	-5.9	0.50
	1-2	05-4	d	960	4.1	-2.15	-2.18	-1.70	-1.55	-6.00	-5.9	0.45
	2-3	01-6	a	970	4.9	-1.70	-1.84	-1.28	-1.11	-4.68	-4.8	0.42
	2-4	08-4	a	970	5.1	-1.43	-1.81	-1.53	-1.08	-4.39	-4.7	-0.10
	3-5	04-7	c	960	4.8	-0.94	-1.13	-0.52	-0.44	-2.40	-2.7	0.42
	3-6	04-6	c	960	4.3	-1.15	-1.13	-0.30	-0.44	-2.60	-2.7	0.85
GF-3	1-1	(b)	f	975	6.4	-1.30	(c)	-0.22	(c)	-2.82	(c)	1.08
	1-2	(b)	f'	975	7.7	-0.57	(c)	+0.80	(c)	-0.34	(c)	1.37
	2-3	02-4	b	975	9.4	0	-0.74	(d)	+0.39	(d)	-1.1	(d)
	2-4	03-4	b'	975	9.8	-0.32	-0.71	--	+0.42	--	-1.0	--
	4-5	04-5	c	1120	7.2	+0.22	-0.79	+3.44	+0.08	+3.88	-1.5	3.22
	4-6	04-4	c	1120	6.0	-0.10	-0.79	+1.24	+0.08	+1.04	-1.5	1.34

(a) Diametral strain (ϵ'_{rr}) = 1/3 ($\hat{V}_{FR}$ - 2 x $\Delta\epsilon$) and axial strain (ϵ'_{zz}) = 1/3 ($\hat{V}_{FR}$ - $\Delta\epsilon$), where $\hat{V}_{FR}$ is predicted volumetric change and $\Delta\epsilon$ is strain anisotropy ($\Delta\epsilon$ - 0.31 + 0.084 x ψ)(Ref. 5-10).

(b) CEA rods fabricated using CERCA process.

(c) Not determined.

(d) Rod inadvertently broken and axial length not measured (Fig. 5-19).

TABLE 5-7
THERMAL CONDUCTIVITY MEASUREMENTS ON IRRADIATED GF-1 AND GF-2 FUEL RODS

Capsule	Fuel Rod Number	Fuel Rod Type(a) (Particle Types)	Volume/Time Averaged Temperature (°C)	Fluence (10^{25} n/m^2) ($E > 29$ fJ)$_{HTGR}$	Thermal Conductivity W/cm-°C-s)(b)		
					Measured Temperature (°C)	Before Irradiation	After Irradiation
GF-1	IIB (No. 4)	a (TRISO/BISO)	1170	6.7	700	0.140	0.084
					800	0.134	(c)
					900	0.125	(c)
	IB (No. 2)	e, e' (TRISO/BISO)	1080	5.5	600	0.2348	0.0984
					700	0.2231	0.0954
					800	0.2131	0.0921
GF-2	IIIA (No. 5)	c (TRISO/TRISO)	960	4.8	600	0.147	0.0942
					700	0.140	0.0862
					800	0.132	0.0686
	IIA (No. 3)	a (TRISO/BISO)	970	4.9	600	0.150	0.0774
					700	0.140	0.0712
					800	0.134	0.0569
	IB (No. 2)	d (BISO/BISO)	960	4.1	600	0.130	0.0578
					700	0.124	0.0567
					800	0.115	0.0536

(a) Fuel rod types a, c, and d fabricated by GA matrix injection process and rod types e and e' by CEA CERCA process.

(b) LECI technique (Ref. 5-13).

(c) Measurements not made because of poor surface conditions.

TABLE 5-8
COMPARATIVE EVALUATION OF EOL Kr-85m R/B MEASUREMENTS FOR CAPSULES GF-1 AND GF-2

Capsule	Cell	Fuel Rod Type	Fast Fluence (10^{25} n/m^2) ($E > 29$ fJ)$_{HTGR}$	EOL Volume-Average Temperature[a] (°C)	TRIGA Fission Gas Release (R/B for Kr-85m)		
					Reirradiated EOL at 600°C[b]	Reirradiated Corrected for EOL Operating Temperature[c]	In-Pile EOL[d]
GF-1	1	e, e'	5.2	1075	$2.2 - 2.8 \times 10^{-5}$	1.6×10^{-6}	9×10^{-5}
	2	a	6.7	1130	$1.3 - 1.7 \times 10^{-4}$	9×10^{-4}	2.2×10^{-4}
	3	b, b"	6.4	1150	$0.7 - 1.6 \times 10^{-3}$	7.4×10^{-3}	1.1×10^{-3}
GF-2	1	d	3.8	900	$1.4 - 3.8 \times 10^{-6}$	9.4×10^{-6}	5×10^{-6}
	2	a	5.0	975	$6 - 8.5 \times 10^{-6}$	2.7×10^{-5}	1.1×10^{-5}
	3	c	4.5	955	$3.8 - 5 \times 10^{-5}$	1.7×10^{-4}	1.5×10^{-4}

(a)Refer to Table 4-3.

(b)Refer to Figs. 5-29 and 5-30.

(c)Based on normalized temperature correction factors defined in Ref. 5-14.

(d)Refer to Figs. 4-22 and 4-23.

TABLE 5-9
Kr-85m R/B MEASUREMENTS ON LASER-FAILED, TRISO-COATED PARTICLES

Description of Fuel	Fissile Particle Batch Designation	Burnup (% FIMA)	Kr-85m R/B		
			600°C	1050°C	1250°C
Mixed oxide $(8Th,U)O_2$ kernel, sol-gel	6155-01-030 6155-00-030 6155-02-030	0 5	3.5×10^{-4} 5×10^{-3}	1.4×10^{-3} 1.5×10^{-2}	7.5×10^{-3} 3×10^{-2}
Mixed oxide $(8Th,U)O_2$ kernel, AVS	MG 178	0 9	ND(a) ND(a)	1.2×10^{-2} 1.7×10^{-2}	ND(a) ND(a)
ThO_2 kernel, sol-gel	6542-02-036	0 3	ND(a)	$7 - 8 \times 10^{-3}$	ND(a)

(a) ND = not determined.

TABLE 5-10
CALCULATED FISSILE PARTICLE FAILURE BASED ON Kr-85m R/B EARLY IN LIFE [2.5×10^{25} n/m^2 ($E > 29$ fJ)$_{HTGR}$]

Capsule	Cell	Rod Type	Temperature, Burnup, and R/B at a Fluence of 2.5×10^{25} n/m^2 ($E > 29$ fJ)$_{HTGR}$			Kr-85m R/B per Laser-Failed Particle, $R_{fissile}$(c)	Calculated Fissile Particle Failure at 2.5×10^{25} n/m^2 ($E > 29$ fJ)$_{HTGR}$, $X_{fissile}$ (%)
			Volume Avg. Temperature(a) (°C)	Fissile Burnup (% FIMA)	In-Pile Kr-85m R/B(b)		
GF-1	1	e, e'	1055	3.7	1.5×10^{-4}	10^{-2}	1.50
	2	a	1160	3.6	8×10^{-6}	1.5×10^{-2}	0.05
	3	b, b'	1140	3.7	6×10^{-4}	1.5×10^{-2}	3.00
GF-2	1	d	920	4.3	5×10^{-6}	$\sim 7 \times 10^{-3}$	0.07
	2	a	960	3.8	9×10^{-6}	$\sim 7 \times 10^{-3}$	0.13
	3	c	930	4.1	6×10^{-4}	$\sim 7 \times 10^{-3}$	8.57
GF-3	1	f, f'	970	3.2	10^{-6}	$\sim 6 \times 10^{-3}$	0.02
	2	b, b'	970	3.5	3.4×10^{-4}	$\sim 6 \times 10^{-3}$	5.66
	4	c	1125	3.4	7.2×10^{-4}	1.4×10^{-2}	5.14

(a) Refer to Figs. 4-10 through 4-21.

(b) Refer to Figs. 4-22 through 4-24.

(c) Refer to Fig. 5-31.

(d) Based on the approximation that most fissions along with fuel failure occur in fissile fuel early in life and there is no heavy metal contamination (refer to Eq. 5-4).

TABLE 5-11
CALCULATED FISSILE AND FERTILE PARTICLE FAILURES BASED ON Kr-85m R/B AT END-OF-LIFE

Capsule	Cell	Rod Type	EOL Volume Avg. Temperature (°C)	EOL Fluence (10^{25} n/m^2) (E > 29 fJ)$_{HTGR}$	EOL Burnup (% FIMA)		In-Pile EOL Kr-85m R/B[a]	Kr-85m R/B per Laser-Failed Particle[b]		Calculated Fissile and Fertile Particle Failure at EOL,[c] $X_{fissile}$, $X_{fertile}$ (%)
					Fissile	Fertile		Fissile, $R_{fissile}$	Fertile, $R_{fertile}$	
GF-1	1	e	1075	5.2	8.5	1.7	9.5×10^{-5}	1.7×10^{-2}	7×10^{-3}	0.74
	2	a	1180	6.7	9.7	2.4	3.4×10^{-4}	2.1×10^{-2}	1.1×10^{-2}	2.17
	3	b, b'	1150	6.4	9.4	2.2	1.1×10^{-3}	2×10^{-2}	10^{-2}	7.38
GF-2	1	d	900	3.8	6.5	0.8	4.8×10^{-6}	9×10^{-3}	4×10^{-3}	0.07
	2	a	975	5.0	7.6	1.3	2×10^{-5}	1.1×10^{-2}	5×10^{-3}	0.24
	3	c	955	4.5	7.4	1.2	1.5×10^{-4}	1.1×10^{-2}	5×10^{-3}	1.70
GF-3	1	f, f'	975	7.4	9.5	2.2	3×10^{-5}	1.3×10^{-2}	6×10^{-3}	0.07
	2	b, b'	990	9.8	11.4	3.6	4.7×10^{-4}	1.5×10^{-2}	8×10^{-3}	4.57
	4	c	1115	6.6	9.0	2.0	4×10^{-4}	1.2×10^{-2}	9×10^{-3}	3.78

(a) Refer to Figs. 4-22, 4-23, and 4-24.

(b) Refer to Fig. 5-31.

(c) Based on assumption of equal fissile and fertile particle failure fracitons and no heavy metal contamination (refer to Eq. 5-5).

TABLE 5-12
DETERMINATION OF FUEL PARTICLE FAILURE LEVELS BY ELECTROCHEMICAL DISINTEGRATION OF FUEL RODS

Rod Designation	Rod IIIA (No.5) from GF-1	Rod IVA (No. 5) from GF-3
Type of fuel	Fissile particle Mixed oxide (8Th,U)O_2 TRISO Lot 6155-01-030	Fissile particle Mixed oxide (8Th,U)O_2 TRISO Lot 6155-00-030
	Fertile particle ThO_2 BISO Lot 6542-02-036	Fertile particle ThO_2 TRISO Lot 6252-00-020
	Fuel rod Type b	Fuel rod Type c
Irradiation conditions		
Temperature	1090°C (surface) - 1310°C (central)	1165°C (surface) - 1200°C (central)
Burnup	9.35% FIMA	9.02% FIMA
Schematic diagram of electrochemical disintegration technique for each fuel rod	Electrochemical disintegration ↓ U, Th fission products in solution ↓ Determination of activity of Nb-95 and Pr-144 in solution ↓ Comparison of the mean activity of one fissile and one fertile particle	Electrochemical disintegration ↓ U, Th fission products in solution ↙ ↘ Dose of U-236 to trace fissile particles → Determination of the number of ruptured fissile particles Dose of U-233 to trace thorium → Determination of the number of ruptured fertile particles
Fuel failure		
Fissile	31% (7.4%)[a]	4% (3.8%)[a]
Fertile	<1%	1%

[a] Based on EOL Kr-85m R/B measurements (Table 5-11).

TABLE 5-13
METALLOGRAPHIC (X) AND MICRORADIOGRAPHIC (O) EXAMINATION OF FUEL PARTICLES TESTED IN CAPSULES GF-1, GF-2, AND GF-3

Fuel Description	Type of Rod	Particle Batch (F = fissile, f = fertile)	GF-1	GF-2	GF-3
Particles in rods	a	F = 6155-00-030 f = 6542-02-036	X	X	
	b	F = 6155-01-030 f = 6542-02-036			X
	b'	F = 6155-02-030 f = 6542-02-036	X		
	c	F = 6155-01-030 f = 6252-00-020			X
	d	F = 6445-00-010 f = 6542-02-036		X	
	237[a]	F = 6155-01-020 f = 6542-02-036	X		
	239[b]	F = 6155-01-020 f = 6542-02-036			
	815[c]	F = MG 178 f = MG 156			X
	817[d]	F = MG 178 f = MG 156			
Loose particles	6542-02-036 - ThO_2 BISO		X O		
	6155-02-020 - $(8Th,U)O_2$ TRISO		X		
	6155-00-020 - $(8Th,U)O_2$ TRISO		O		
	6151-00-010 - UC_2 TRISO		X O		X O
	6445-00-010 - $(8Th,U)O_2$ BISO				X O
	6155-01-020 - $(8Th,U)O_2$ TRISO		O		
	MG 197 - $(8Th,U)O_2$ BISO			X	X O
	MG 199 - $(8Th,U)O_2$ TRISO			X O	X
	MG 178 - $(8Th,U)O_2$ TRISO			X O	X
	MG 165 - ThO_2 TRISO			O	
	MG 156 - ThO_2 BISO				X
	MG 207 - ThO_2 BISO				X O
	MG 175 - ThO_2 TRISO				X

(a) CEA matrix, natural graphite, GA particles.
(b) CEA matrix, artificial graphite, GA particles.
(c) CEA matrix, natural graphite, CEA particles.
(d) CEA matrix, artificial graphite, CEA particles.

TABLE 5-14
RANGE OF V_{MATRIX} VALUES

Rod Type	$\bar{V}_{macroporosity}$	$\bar{V}_{microporosity}$	$\bar{V}_{matrix}$
GA (a,b,b',c,d)	0.25 - 0.52	~20.5	0.24 - 0.38
CEA (e,e',f,f')	0	0.13 - 0.37	0.63 - 0.97

TABLE 5-15
COMPARATIVE EVALUATION OF OPyC FAILURE LEVELS DETERMINED VISUALLY FOR UNBONDED PARTICLES AND METALLOGRAPHICALLY FOR PARTICLES TESTED IN FUEL RODS

Batch Designation	Sample Description	Fluence (10^{25} n/m^2) ($E > 29$ fJ)$_{HTGR}$	Temperature (°C)	OPyC Failure (%)
6155-01-030	Loose particle fuel rod (GF-3, rod IIA)	4.0 9.8	985-1095 975	63.3 83.0
6155-02-030	Loose particle fuel rod (GF-1, rod IIIB)	4.0 6.7	985-1095 1170	26 78
6155-00-030	Loose particle fuel rod (GF-2, rod IIA)	4.0 5.0	985 970	27 36

TABLE 5-16
FISSION PRODUCT DISTRIBUTIONS IN TRISO-COATED UC_2 FUEL (BATCH 6151-00-010) IRRADIATED IN GF-1 AT 1095°C AND TO 4.2×10^{25} n/m^2 $(E > 29\ fJ)_{HTGR}$ and 60% FIMA

Element	Element Concentration at Indicated Location (wt %)			
	Outer Kernel Perimeter	Buffer Layer	IPyC Layer	White Zone in Metallographic Cross Section; Located in IPyC Layer on One Side of Kernel
Sr	0.5 - 1	0.2 - 0.4	0.5	
Y	0.2	0.2		
Zr	1	0.2		
Mo	1			
Te	Traces			
I	Traces			
Xe	0.5 - 1	0.3		
Cs	1 - 2	1 - 2	~1	0.2
Ba	0.5 - 0.8	0.5	<0.5	
La	$<10^3$ ppm			2
Ce	~1	0.2	0.1	>2
Pr	0.4	0.1		~2
Nd	1	0.2	0.1	>2
Sm				0.5 - 1

TABLE 5-17

OPyC FAILURE IN TRISO-COATED FISSILE FUEL TESTED IN GF-1, GF-2, AND GF-3 VERSUS FRACTION OF OPyC LAYERS WITH LOW MICROPOROSITIES

Particle Batch Designation	Capsule Tests[a]	Irradiation Conditions		OPyC Failure (%)	OPyC Properties			
		Temperature (°C)	Fluence ($10^{25} n/m^2$) $(E > 29 fJ)_{HTGR}$		Low Microporosity[b] (% < critical)	Mean Microporosity (ml/kg OPyC)	Mean Optical Anisotropy, BAF°[c]	Mean Coating Rate (um/min)
6155-00-010	2, 3	985-1000	3.7-9.4	8.9-27.3	30.0	6.4	1.033	2.3
6155-00-020	1, 3	1095-1000	4.4-9.4	3.5-2.0	1.9	7.5	1.027	2.8
6155-01-010	2, 3	985-1000	3.7-9.4	53.3-56.3	(d)	9.2	1.025	3.1
6155-01-020	1, 3	1095-1000	4.4-9.4	53.2-58.7	57.3	9.3	1.025	3.4
6155-02-010	2, 3	985-1000	3.7-9.4	25.8-14.3	5.8	9.4	1.022	3.3
6155-02-020	1, 3	1095-1000	4.4-9.4	26.7-26.3	26.8	9.4	1.021	3.4

(a) Loose particle tests.

(b) Percent of OPyC layers with microporosities less than that shown in Fig. 5-76.

(c) Bacon anistropy factor measured optically on Seibersdorf polarizing microscope (25-um spot size).

(d) Particles not distinctive enough to allow a determination of percent with intruded mercury ≤9% of OPyC thickness; however, sizable fractions of OPyC layers appeared to be in this region.

TABLE 5-18
SUMMARY OF DEFECTIVE SiC LAYERS IN FISSILE PARTICLES GF-1, GF-2, AND GF-3

Sample Description(a)	Particle Batch Data Retrieval Number	Radiographic Evaluation After Mercury Intrusion at 69 MPa		Fraction Defective SiC Determined by Fractional Cs-137 Released After 900 h at 1600°C(c)	Fraction Defective SiC Determined By Burn-Leach
		Number of Particles	Fraction Defective SiC(b)		
Loose particles	6155-00-030	1300	4.2×10^{-2}	6.5×10^{-3}	7.4×10^{-4}
Loose particles	6155-01-030	575	8.9×10^{-2}	1.1×10^{-3}	3×10^{-5}
Loose particles	6155-02-030	443	2.3×10^{-2}	1.3×10^{-2}	8×10^{-4}
Fuel rod 2082-4, type a	6155-00-030	811(a)	7.4×10^{-2}	5.8×10^{-3}	ND(d)
Fuel rod 2084-2, type b	6155-01-030	564(a)	6×10^{-2}	8.2×10^{-3}	ND
Fuel rod 2086-4 type b'	6155-02-030	660(a)	6.8×10^{-2}	3.5×10^{-2}	ND
Fuel rod 2117-1, type c	6155-01-030	290(a)	11.8×10^{-2}	ND	8×10^{-4}

(a) Fissile particles were obtained by burning rod and screening out desired size fraction.
(b) Representative SiC flaws are shown in Fig. 5-79.
(c) Refer to Fig. 5-80.
(d) ND = not determined.

TABLE 5-19
SUMMARY OF VISUAL EXAMINATION FOR ADVANCED FUEL PARTICLES

Lot No.	Particle and Kernel Type	Particle Concepts Tested	Visual Examination GF-1[(a)] No. of Particles	GF-1[(a)] PV Failure (%)	GF-2[(b)] No. of Particles	GF-2[(b)] PV Failure (%)	GF-3[(c)] No. of Particles	GF-3[(c)] PV Failure (%)	GF-1, -2 and -3 No. of Particles	GF-1, -2 and -3 PV Failure (%)
		Doped Kernels								
6111-71-E	BISO-coated	0	202	0	98	0	50	0	350	0
6111-101-E	$(8Th,U)O_2$	0.5 Si	303	0	99	0	51	0	453	0
6111-111-E		0.5 Al	202	0	95	0	50	0	347	0
6111-95-E		2 Si	303	0	97	0	50	0	450	0
6111-109-E		2 Al	404	0	92	0	51	0	547	0
6111-117-E		0.5 Al + 1 Si	303	0	97	0	50	0	450	0
6111-99-E		2 Al + 1 Si	303	0	97	0	50	0	450	0
6111-105-E		2 Al + 2 Si	303	1.65	98	0	50	0	451	1.1
6111-103-E		4 Al	303	0	189	0	50	0	542	0
6111-93-E		4 Si	303	17.5	198	33.8	86	0	587	20.4
6111-107-E		2 Al + 4 Si	303	25.7	198	65.1	101	0	602	34.4
6111-113-E		4 Al + 4 Si	505	57.4	200	24	51	0	756	44.7
6171-15-E	TRISO-coated UC_2	ZrC coated kernel	120	4.6					120	4.6
6171-17-E	$(8Th,U)O_2$	ZrC coated kernel	120	0					120	0
6111-145-E	$(8Th,U)O_2$	ZrC TRISO	120	0					120	0
6111-147-E	UC_2	ZrC TRISO	120	0					120	0
		Doped OPyC layer								
6171-105-E	BISO-coated	19 wt % Si			240	0	120	0	360	0
6171-107-E	$(8Th,U)O_2$	25 wt % Si			240	0	120	0	360	0
6171-115-E		39 wt % Si			240	0	120	0	360	0
6171-117-E		47.5 wt % Si			240	0.4	120	0	360	0.3
6171-119-E		40.5 wt % Si			240	0	120	0	360	0

(a) $2.5\text{-}4.4 \times 10^{25}$ n/m^2 (E > 29 fJ)$_{HTGR}$, 7.1% FIMA, and 1095°C.
(b) $2.2\text{-}3.7 \times 10^{25}$ n/m^2 (E > 29 fJ)$_{HTGR}$, 3.7% FIMA in $(8Th,U)O_2$/50 to 60% FIMA in UC_2, and 985°C.
(c) $8.4\text{-}9.8 \times 10^{25}$ n/m^2 (E > 29 fJ)$_{HTGR}$, 11.1% FIMA, and 1000°C.

TABLE 5-20
GAMMA SPECTROMETRY MEASUREMENTS DEFINING MIGRATION OF METALLIC FISSION PRODUCTS IN BISO-COATED DOPED AND UNDOPED $(8Th,U)O_2$ FUEL

Batch and Kernel Composition(a)	Mean Content of Buffer and OPyC Layer as a Percent of the Total Quantity				
	Pa-233	Ru-103	Zr-95	Cs-137	Cs-134
6111-71E $(8Th,U)O_2$ No dopant	0	5.8	1.9(b)	5.9	4.7
6111-101E $(8Th,U)O_2$ + 0.5 Si	0	5.5	1.9(b)	6.8	4.9
6111-111E $(8Th,U)O_2$ + 0.5 Al	0	1.5	1.5(b)	14.1	15.5

(a) Irradiated in capsule GF-1.

(b) Consistent with quantity associated with recoil into buffer layer.

TOP BOTTOM

CELL 4

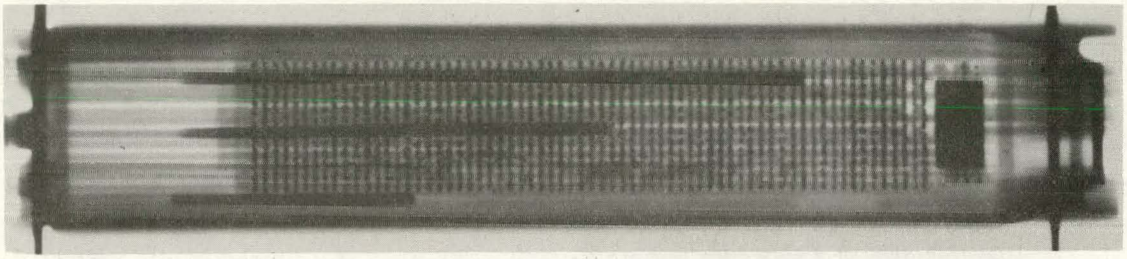

CELL 3

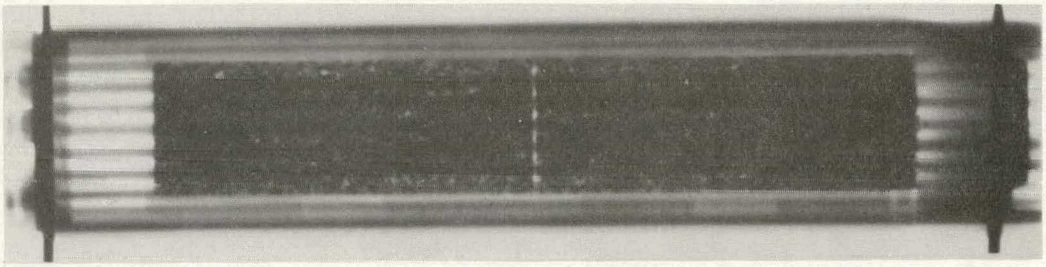

CELL 2

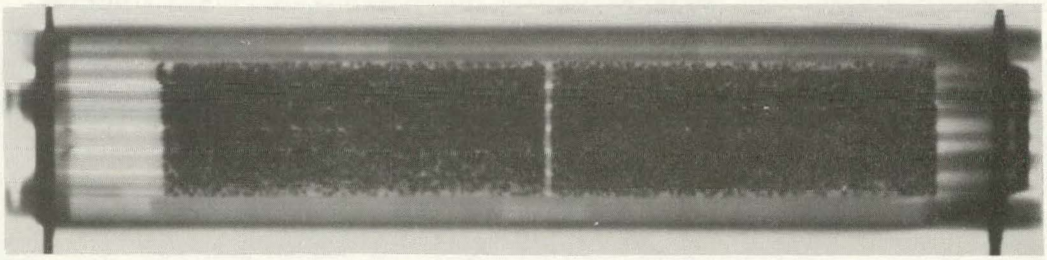

CELL 1

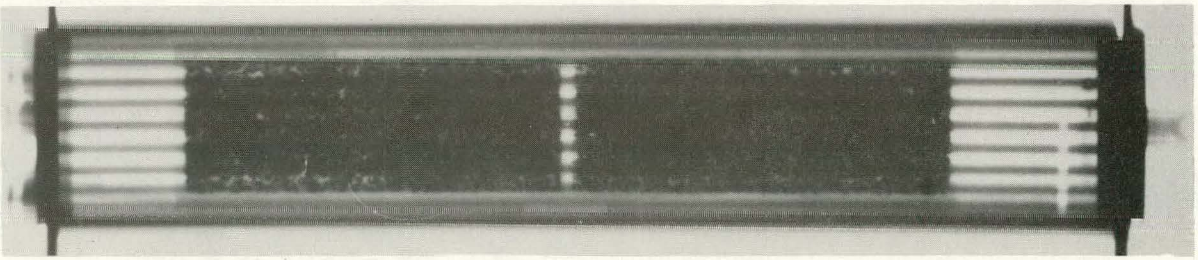

Fig. 5-1. Neutron radiographs of individual cells in capsule GF-2

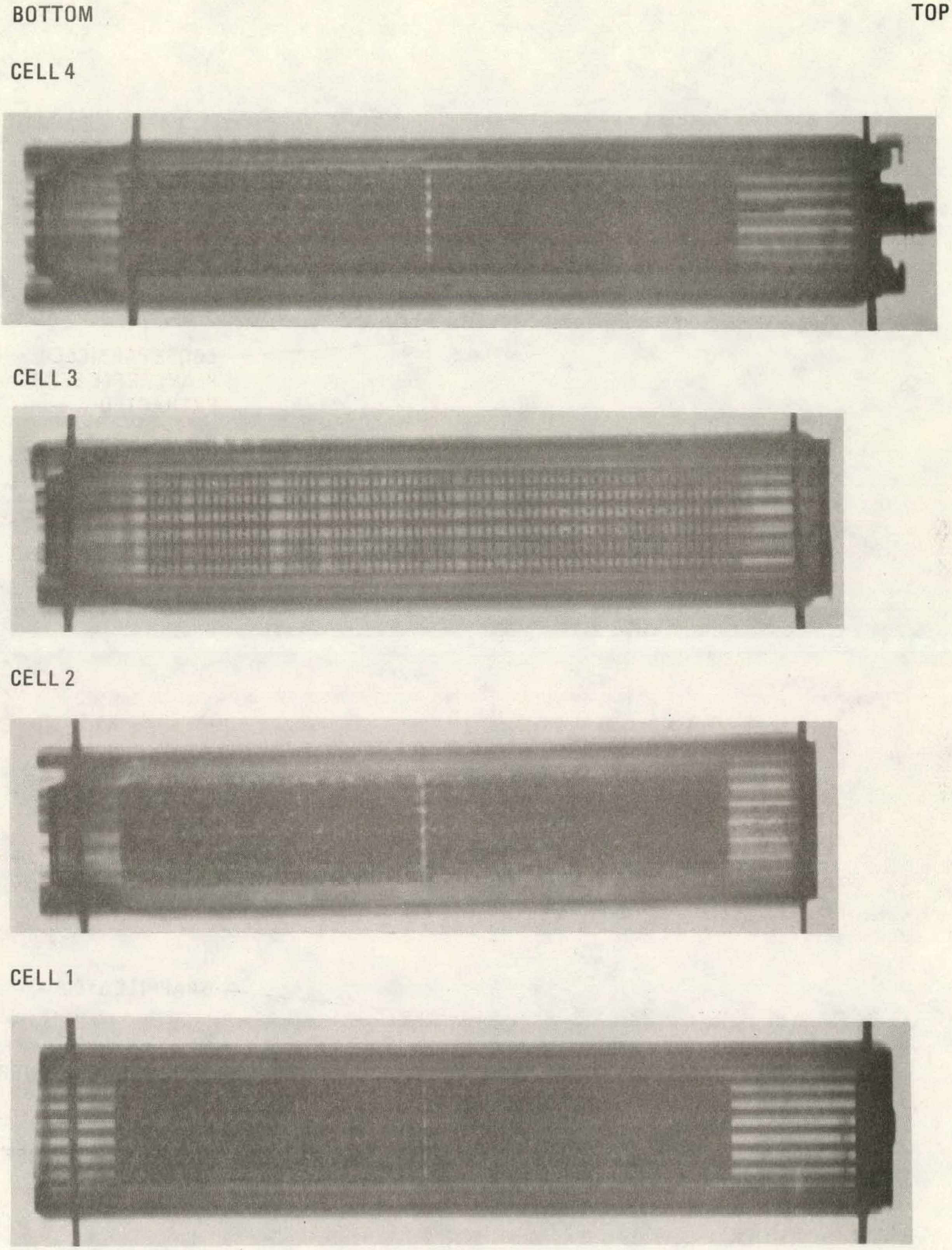

Fig. 5-2. Neutron radiographs of individual cells in capsule GF-3

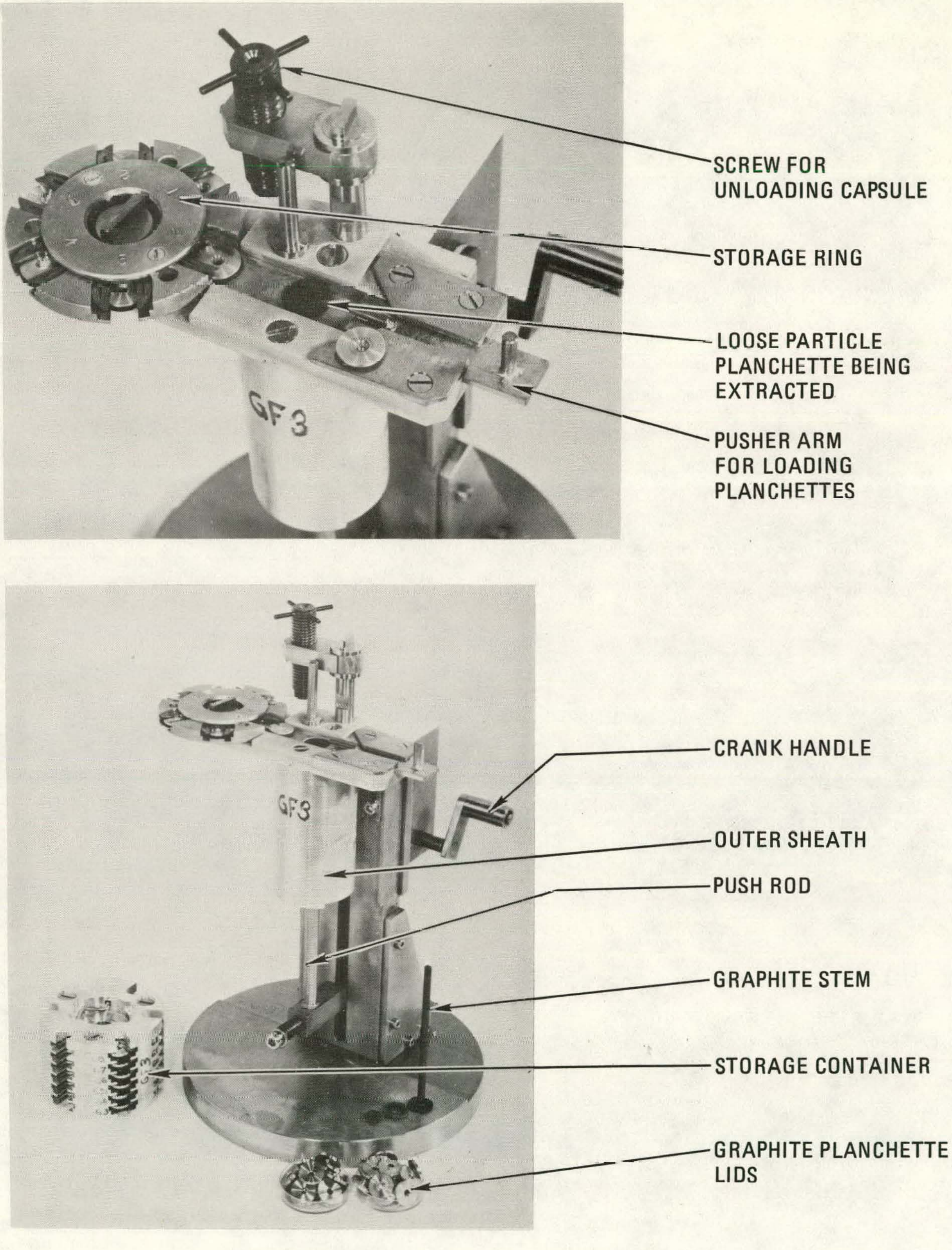

Fig. 5-3. Disassembly apparatus used for capsules GF-1, GF-2, and GF-3

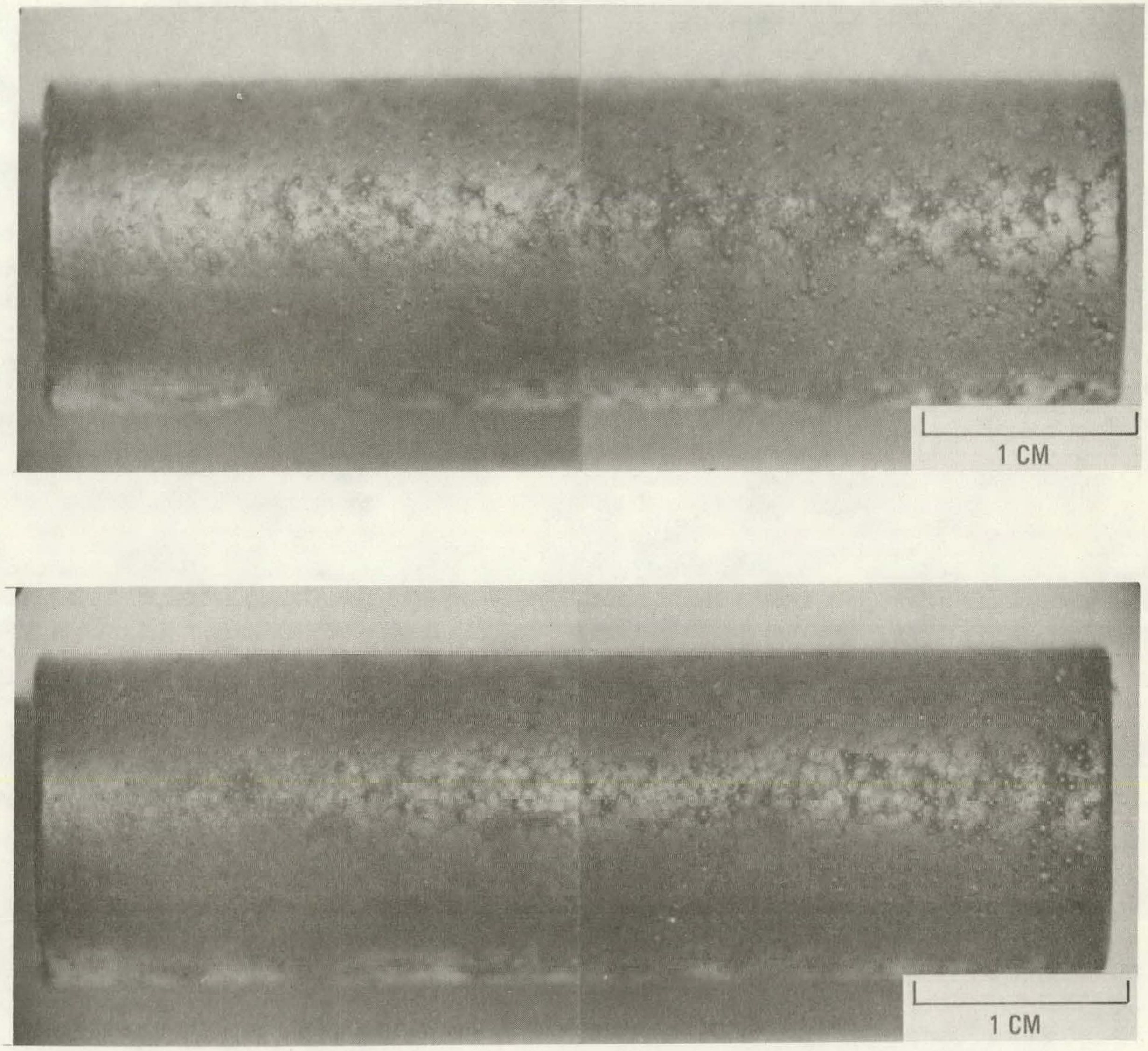

Fig. 5-4. Fuel rod compact No. 1 irradiated in GF-1 to 4.7×10^{25} n/m^2 $(E > 29\ \mathrm{fJ})_{\mathrm{HTGR}}$ and at 1080°C. This fuel rod is classified as type e' [TRISO $(8\mathrm{Th,U})\mathrm{O}_2$/BISO ThO_2] and was fabricated by CEA with the CERCA process using a synthetic graphite. (Two views at 180-deg rotation.)

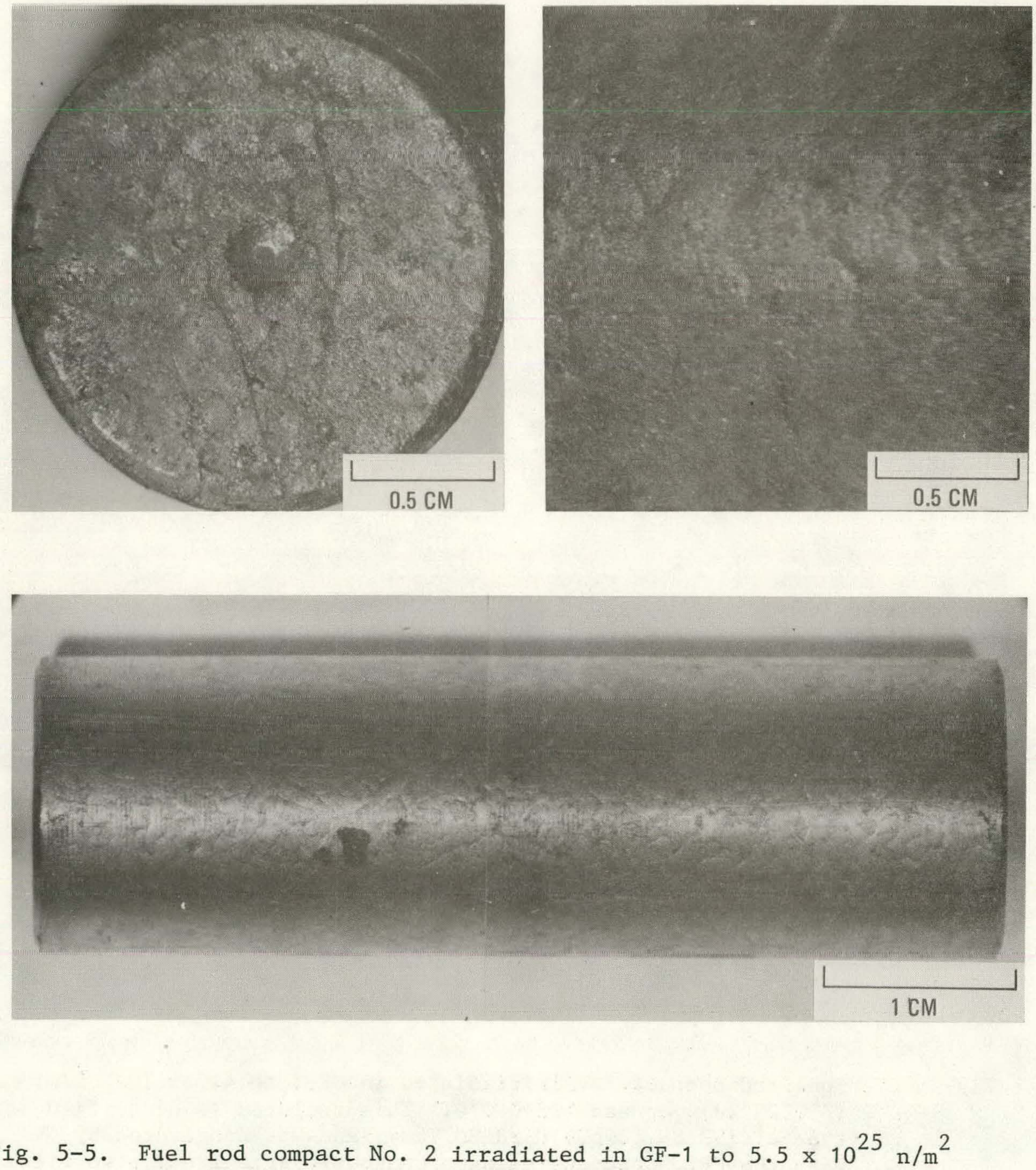

Fig. 5-5. Fuel rod compact No. 2 irradiated in GF-1 to 5.5 x 10^{25} n/m^2 (E > 29 fJ)$_{HTGR}$ and at 1080°C. This fuel rod is classified as type e [TRISO (8Th,U)O_2/BISO ThO_2] and was fabricated by CEA with the CERCA process using natural graphite. (Top and bottom views are end and axial orientations, respectively.)

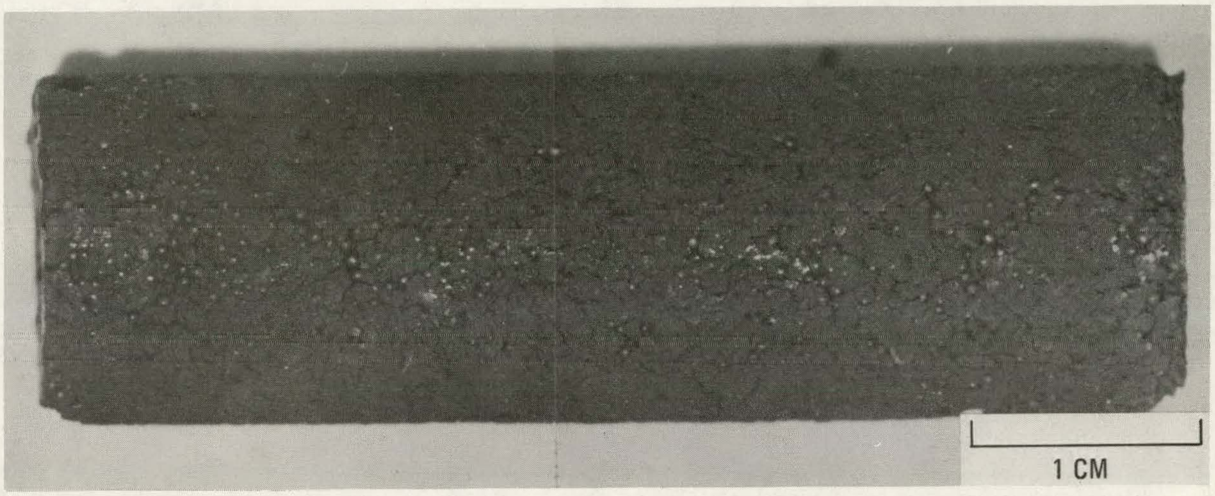

Fig. 5-6. Fuel rod compact No. 3 irradiated in GF-1 to 6.4×10^{25} n/m^2 ($E > 29$ fJ)$_{HTGR}$ and at 1170°C. Fuel rod is classified as type a [TRISO 400-μm-diameter $(8Th,U)O_2$/BISO ThO_2] and was fabricated by GA. (Axial view shown.)

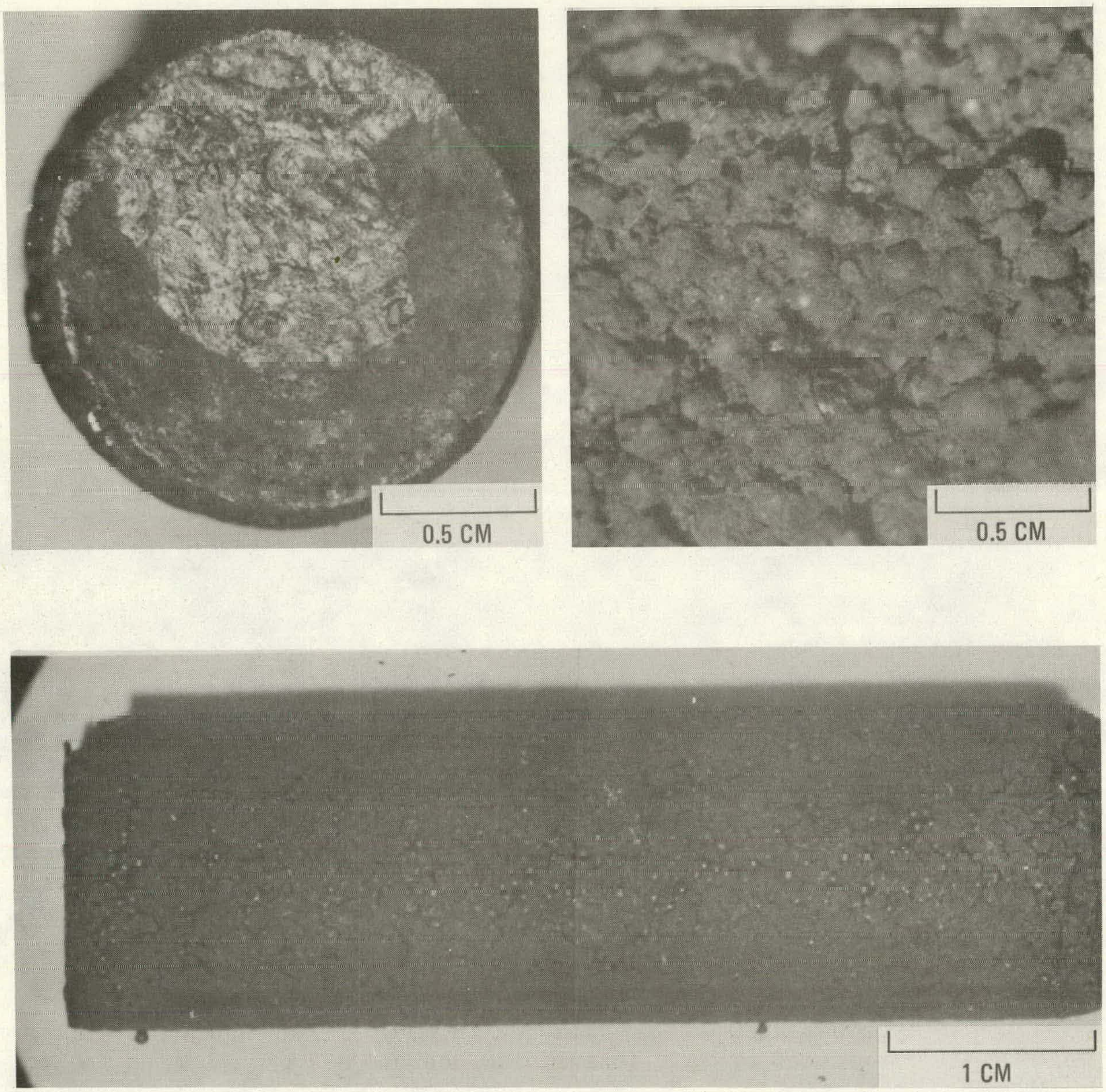

Fig. 5-7. Fuel rod compact No. 4 irradiated in GF-1 to 6.7×10^{25} n/m^2 (E > 29 fJ)$_{HTGR}$ and at 1170°C. This fuel rod is classified as type a [TRISO 400-μm-diameter (8Th,U)O_2/BISO ThO_2] and was fabricated by GA. (The top and bottom illustrations are end and axial views, respectively, and failed OPyC layers on surface particles are apparent in the top view.)

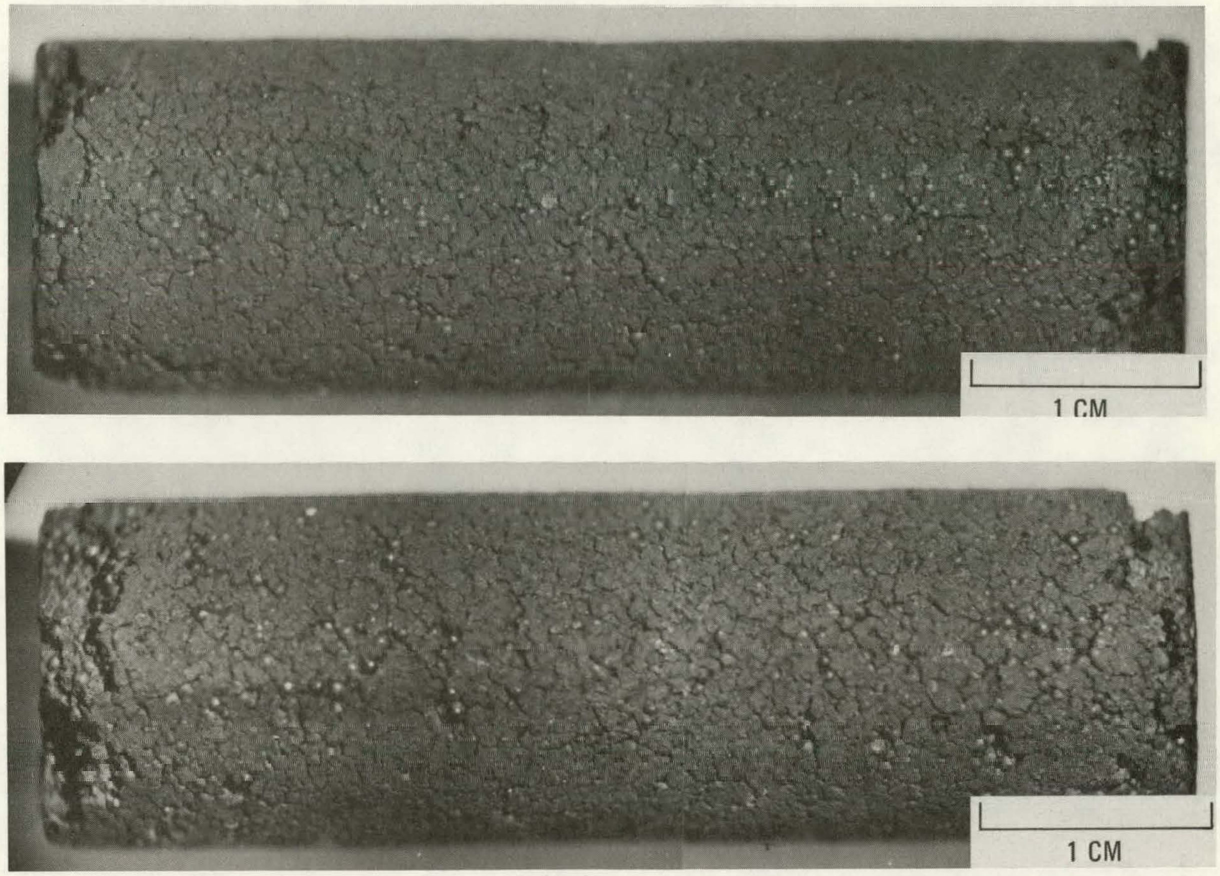

Fig. 5-8. Fuel rod compact No. 5 irradiated in GF-1 to 6.5×10^{25} n/m^2 $(E > 29\ \text{fJ})_{HTGR}$ and at 1170°C. This fuel rod is classified as type b [TRISO 500-μm-diameter $(8Th,U)O_2$, 100-μm buffer/BISO ThO_2] and was fabricated by GA. (Two views at 180-deg rotation.)

Fig. 5-9. Fuel rod compact No. 6 irradiated in GF-1 to 6.1×10^{25} n/m^2 $(E > 29\ \text{fJ})_{HTGR}$ and at 1170°C. This fuel rod is classified as type b' [TRISO 500-μm-diameter $(8Th,U)O_2$, 80-μm buffer/BISO ThO_2] and was fabricated at GA. (Axial view shown.) Note localized chipping and fuel particle spalling.

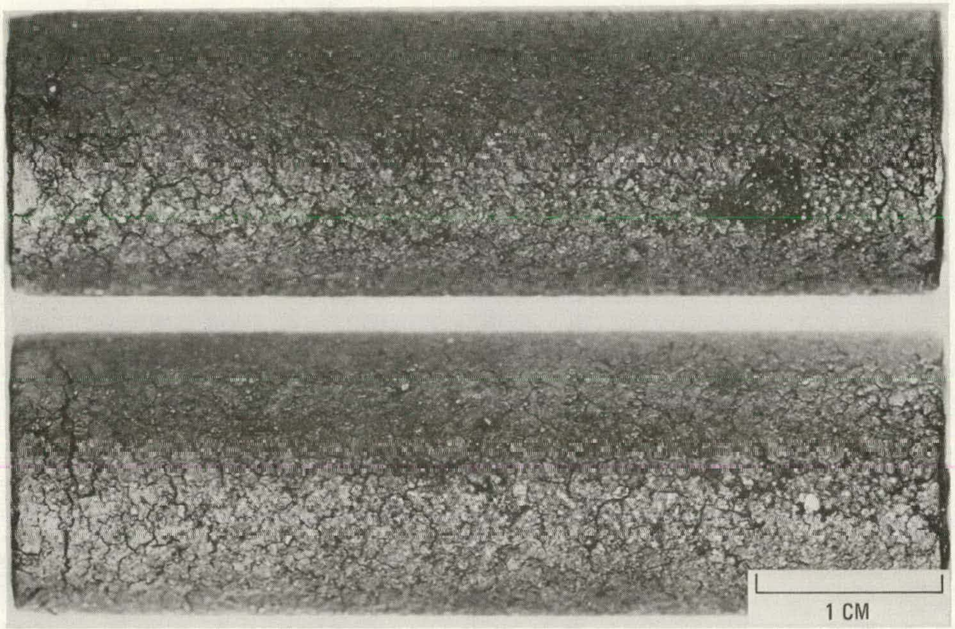

Fig. 5-10. Fuel rod compact No. 1 irradiated in GF-2 to 3.4×10^{25} n/m^2 $(E > 29\ fJ)_{HTGR}$ and at 1010°C. This fuel rod is classified as type d [BISO 500-μm-diameter $(8Th,U)O_2$/BISO ThO_2] and was fabricated at GA. (Two views at 180-deg rotation.) Note localized particle debonding in upper right section.

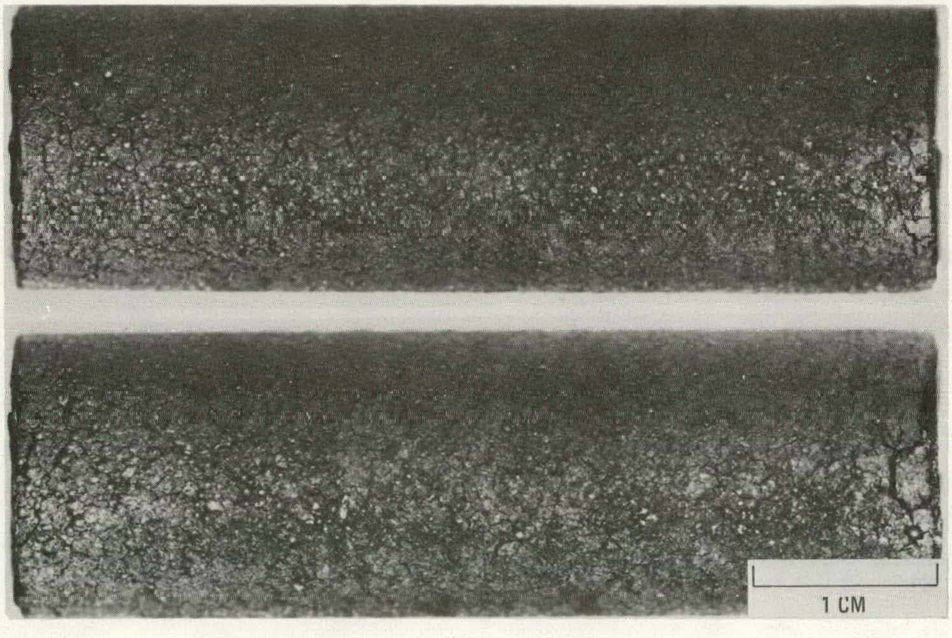

Fig. 5-11. Fuel rod compact No. 2 irradiated in GF-2 at 4.1×10^{25} n/m^2 $(E > 29\ fJ)_{HTGR}$ and at 1010°C. This fuel rod is classified as type d [BISO 500-μm-diameter $(8Th,U)O_2$/BISO ThO_2] and was fabricated at GA. (Two views at 180-deg rotation.)

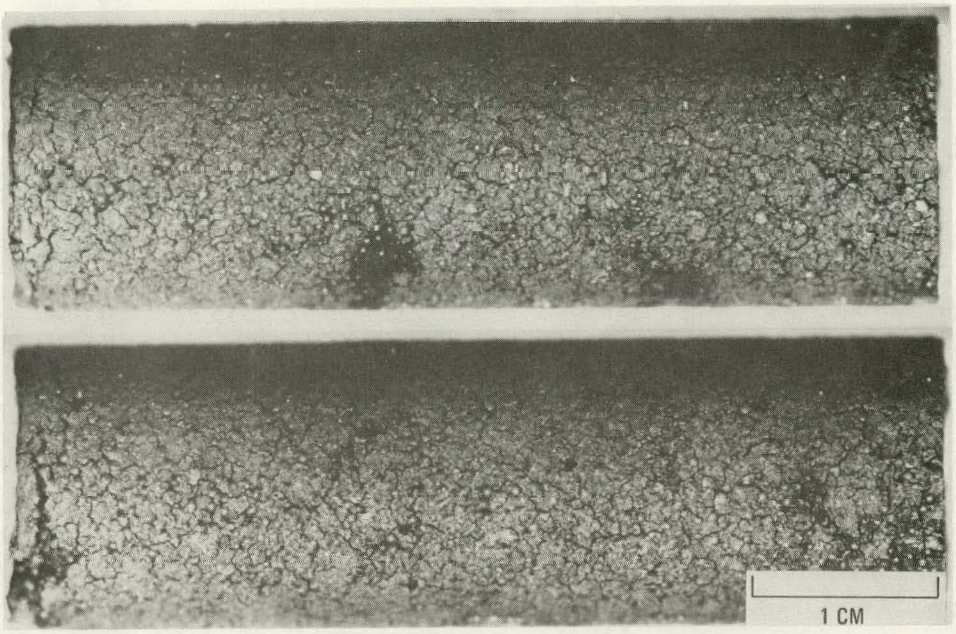

Fig. 5-12. Fuel rod compact No. 3 irradiated in GF-2 at 4.9×10^{25} n/m^2 $(E > 29\ \text{fJ})_{\text{HTGR}}$ and at 1035°C. This fuel rod is classified as type a [TRISO 400-μm-diameter $(8\text{Th},\text{U})\text{O}_2$/BISO ThO_2] and was fabricated at GA. (Two views at 180-deg rotation.) Note localized particle debonding in upper section.

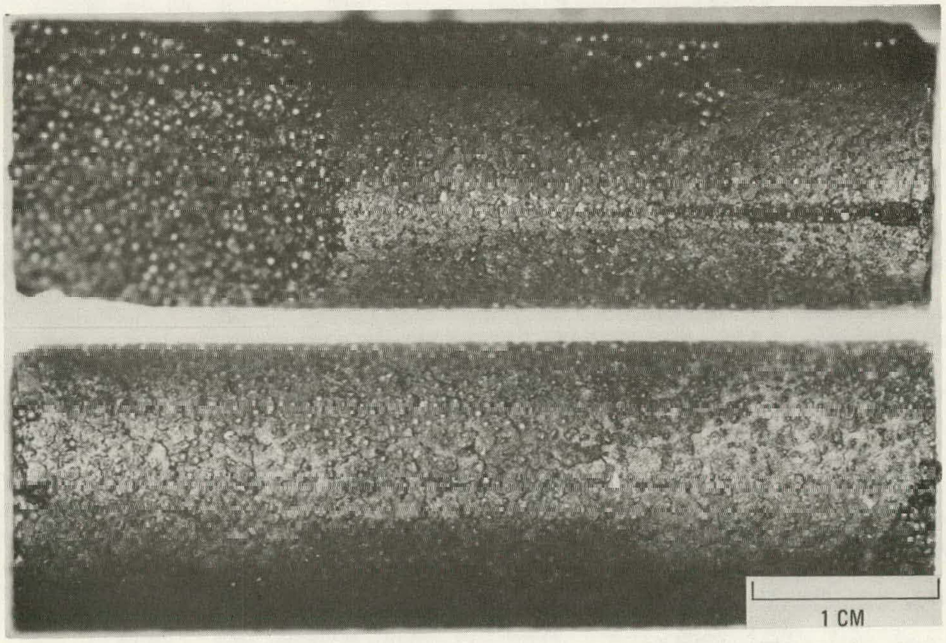

Fig. 5-13. Fuel rod compact No. 4 irradiated in GF-2 at 5.1×10^{25} n/m^2 $(E > 29\ \text{fJ})_{\text{HTGR}}$ and at 1035°C. This fuel rod is classified as type a [TRISO 400-μm-diameter $(8\text{Th},\text{U})\text{O}_2$/BISO ThO_2] and was fabricated by curing in an Al_2O_3 bed at GA. (Two views at 180-deg rotation.) Note extensive chipping and localized particle debonding in upper section.

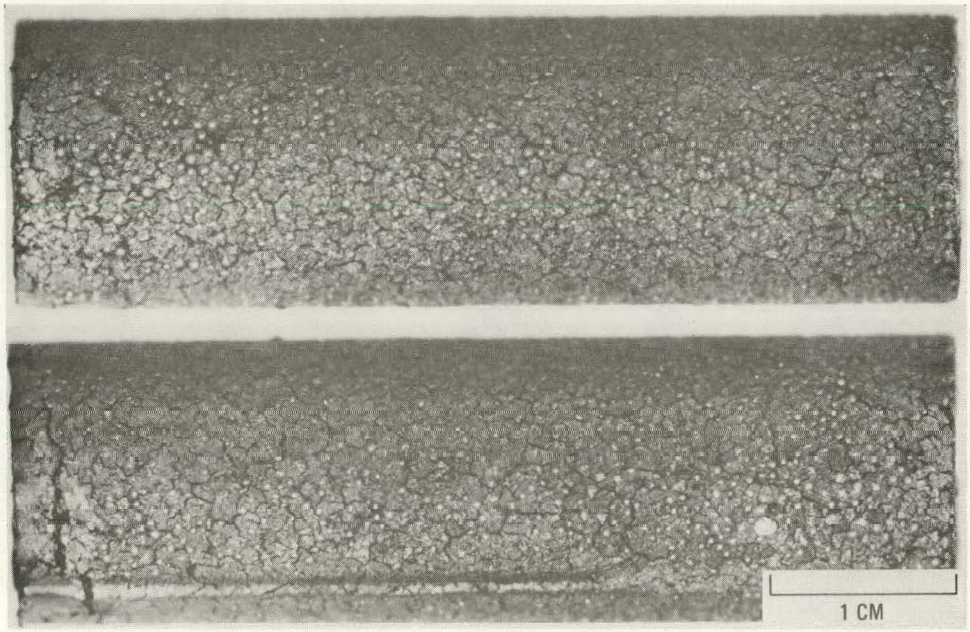

Fig. 5-14. Fuel rod compact No. 5 irradiated in GF-2 at 4.8×10^{25} n/m^2 (E > 29 fJ)$_{HTGR}$ and at 1025°C. This fuel rod is classified as type c [TRISO 500-μm-diameter (8Th,U)O_2, 100-μm buffer/TRISO ThO_2] and was fabricated at GA. (Two views at 180-deg rotation.)

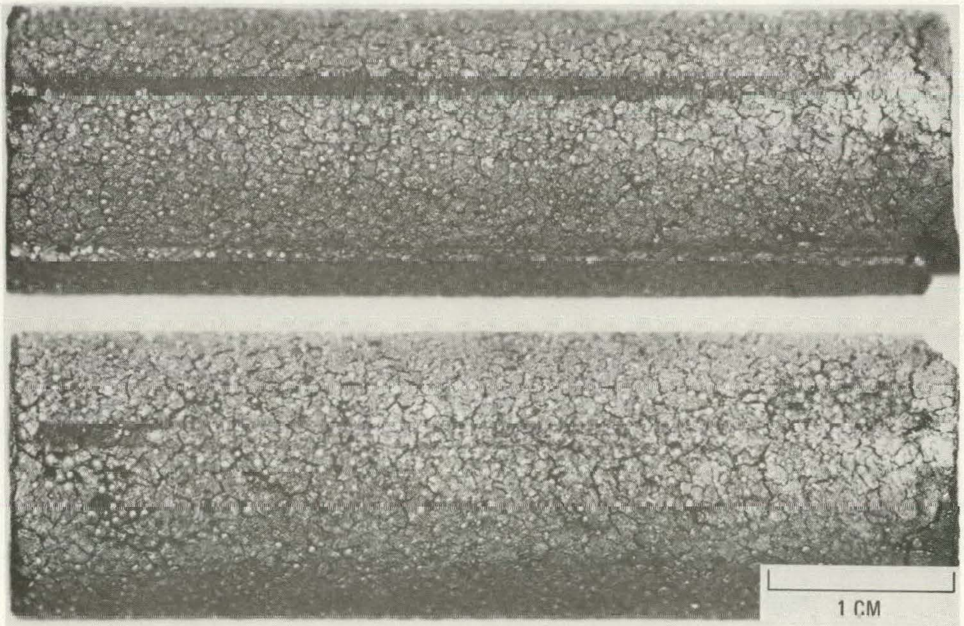

Fig. 5-15. Fuel rod compact No. 6 irradiated in GF-2 at 4.3×10^{25} n/m^2 (E > 29 fJ)$_{HTGR}$ and at 1025°C. This fuel rod is classified as type c [TRISO 500-μm-diameter (8Th,U)O_2, 100-μm buffer/TRISO ThO_2] and was fabricated at GA. (Two views at 180-deg rotation.)

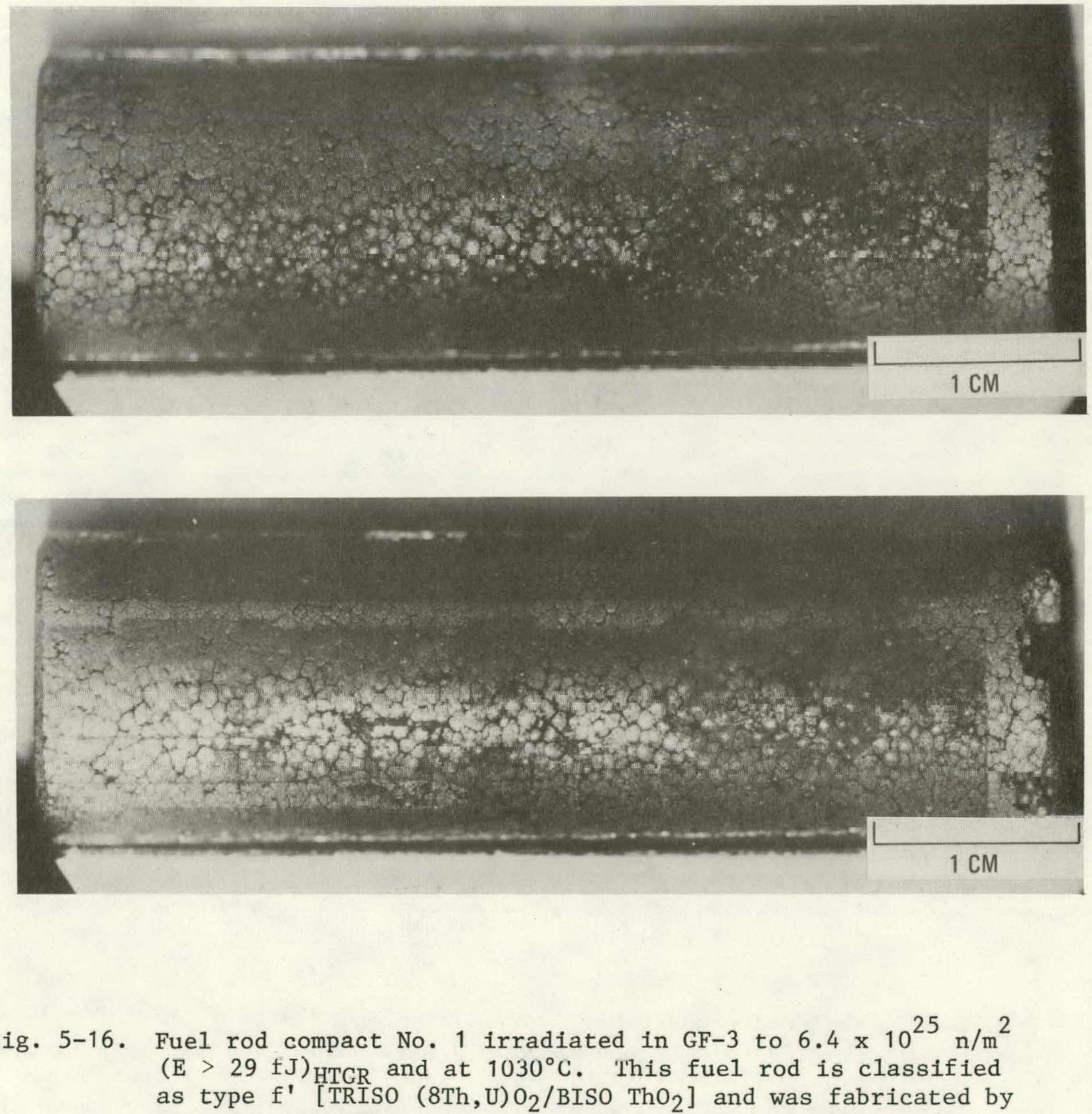

Fig. 5-16. Fuel rod compact No. 1 irradiated in GF-3 to 6.4×10^{25} n/m^2 $(E > 29\ fJ)_{HTGR}$ and at 1030°C. This fuel rod is classified as type f' [TRISO $(8Th,U)O_2$/BISO ThO_2] and was fabricated by CEA with the CERCA process using synthetic graphite. (Two views at 180-deg rotation.)

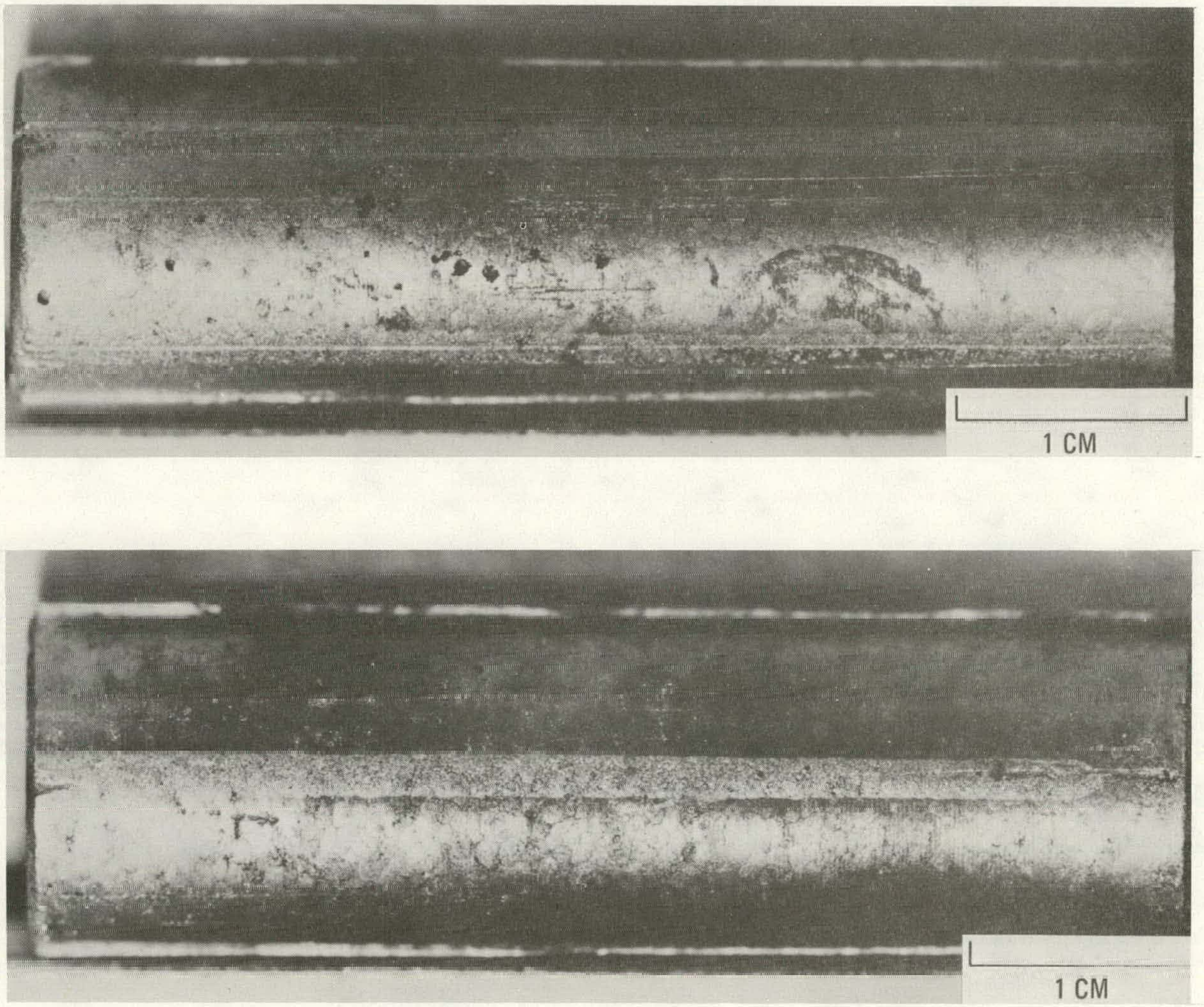

Fig. 5-17. Fuel rod compact No. 2 irradiated in GF-3 to 7.7×10^{25} n/m^2 ($E > 29$ fJ)$_{\mathrm{HTGR}}$ and at 1030°C. This fuel rod is classified as type f [TRISO $(8\mathrm{Th,U})\mathrm{O}_2$/BISO ThO_2] and was fabricated by CEA with the CERCA process using natural graphite. (Two views at 180-deg rotation.)

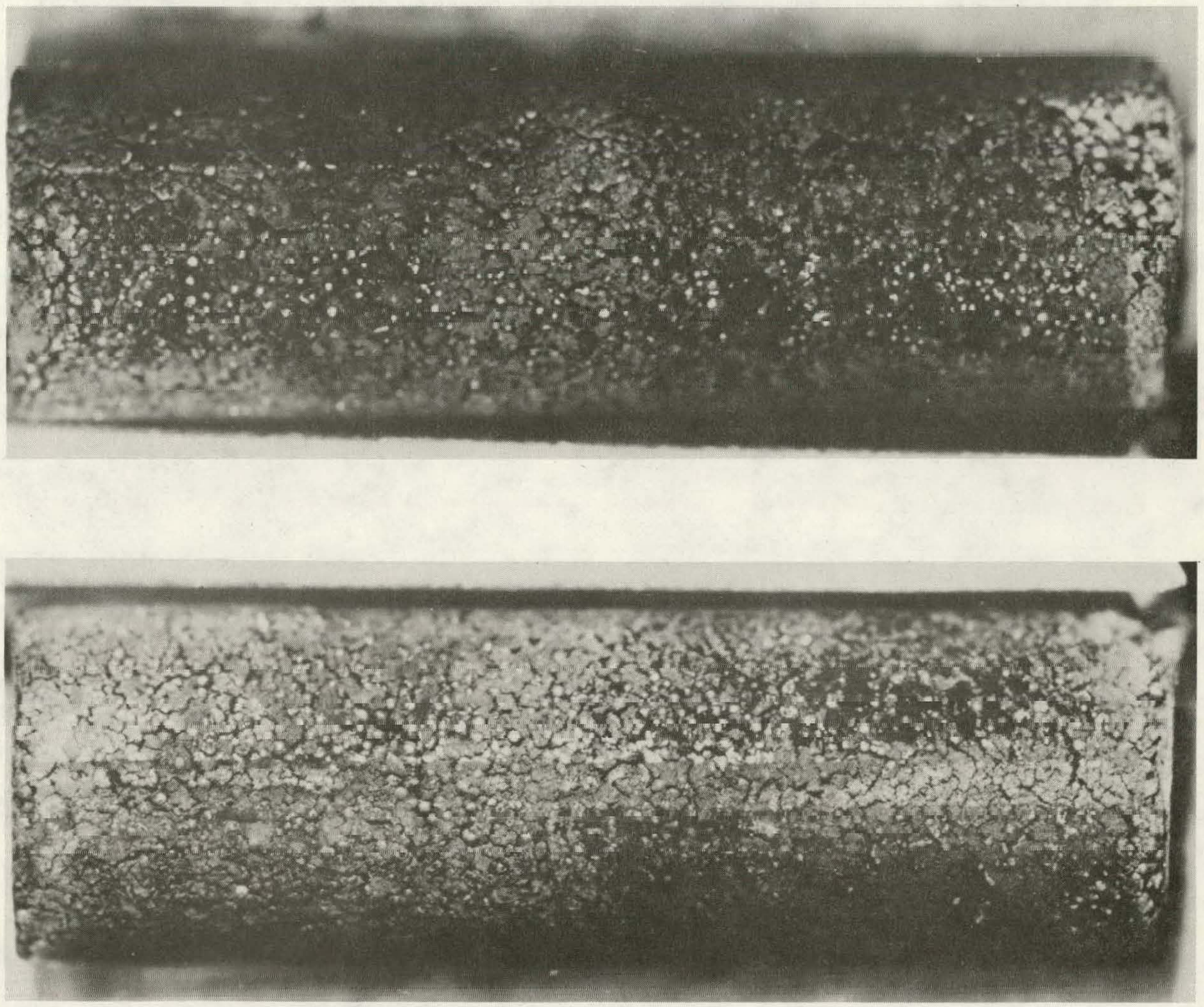

Fig. 5-18. Fuel rod compact No. 3 irradiated in GF-3 to 9.4×10^{25} n/m^2 $(E > 29\ fJ)_{HTGR}$ and at 1045°C. This fuel rod is classified as type b [TRISO 500-μm-diameter $(8Th,U)O_2$, 100-μm buffer/BISO ThO_2] and was fabricated by GA. (Two views at 180-deg rotation.)

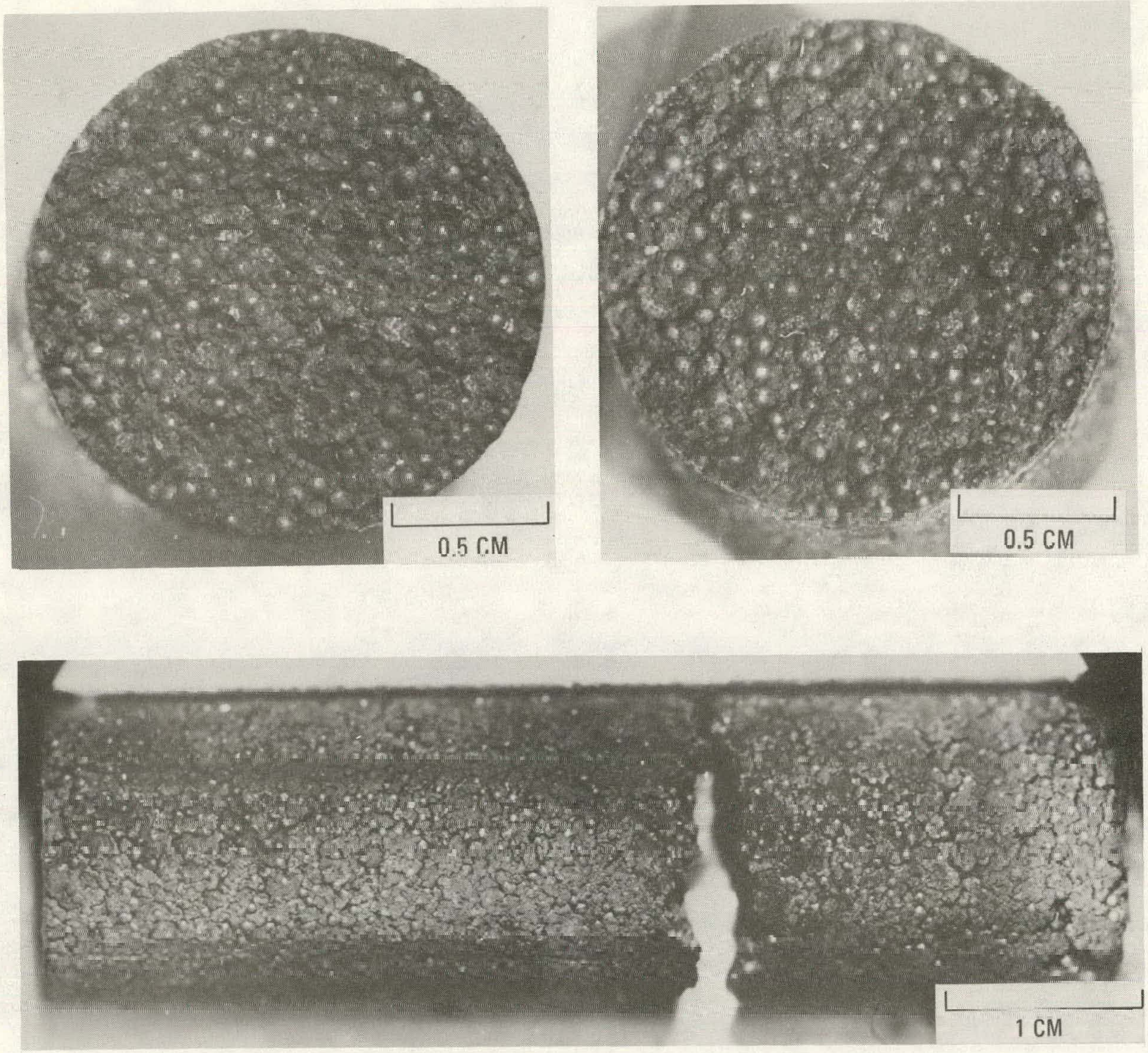

Fig. 5-19. Fuel rod compact No. 4 irradiated in GF-3 to 9.8×10^{25} n/m^2 $(E > 29\ fJ)_{HTGR}$ and at 1045°C. This fuel rod is classified as type b' [TRISO 500-μm-diameter $(8Th,U)O_2$, 80-μm buffer/BISO ThO_2] and was fabricated by GA. (Top and bottom illustrations are end views and axial views, respectively.) The fuel rod was inadvertently broken during capsule disassembly.

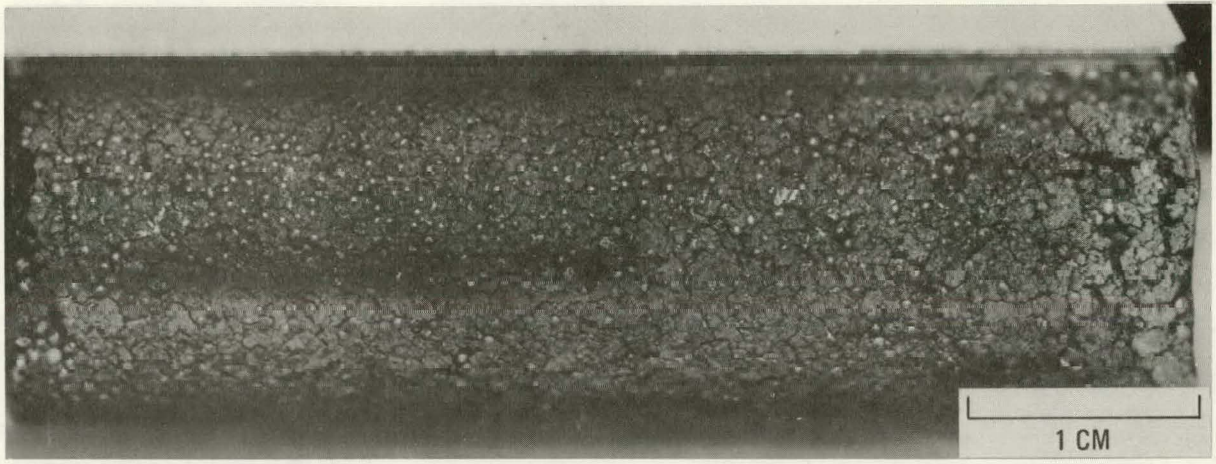

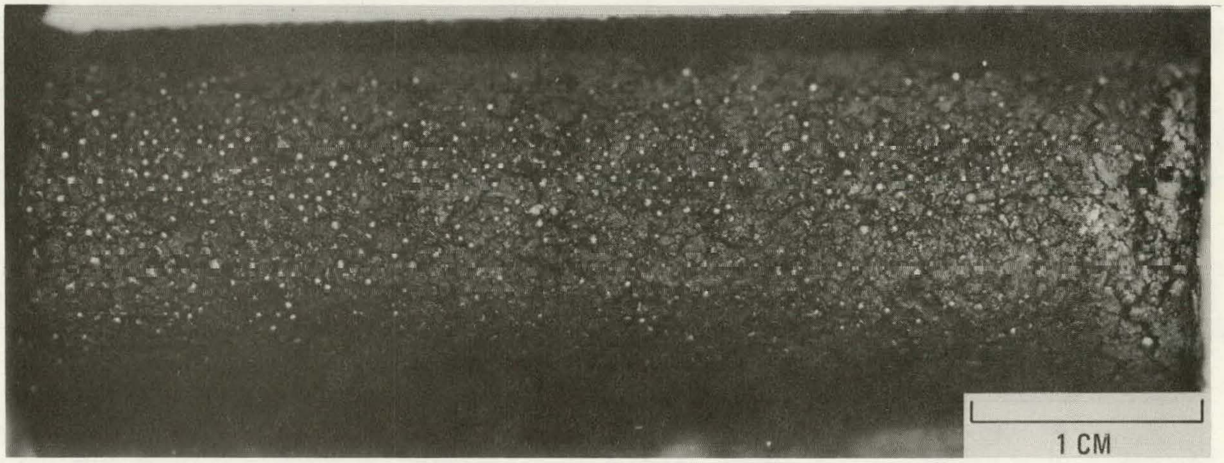

Fig. 5-20. Fuel rod compact No. 5 irradiated in GF-3 to 7.2×10^{25} n/m^2 ($E > 29$ fJ)$_{HTGR}$ and at 1165°C. This fuel rod is classified as type c [TRISO 500-μm-diameter $(8Th,U)O_2$, 100-μm buffer/TRISO ThO_2] and was fabricated by GA. (Two views at 180-deg rotation.)

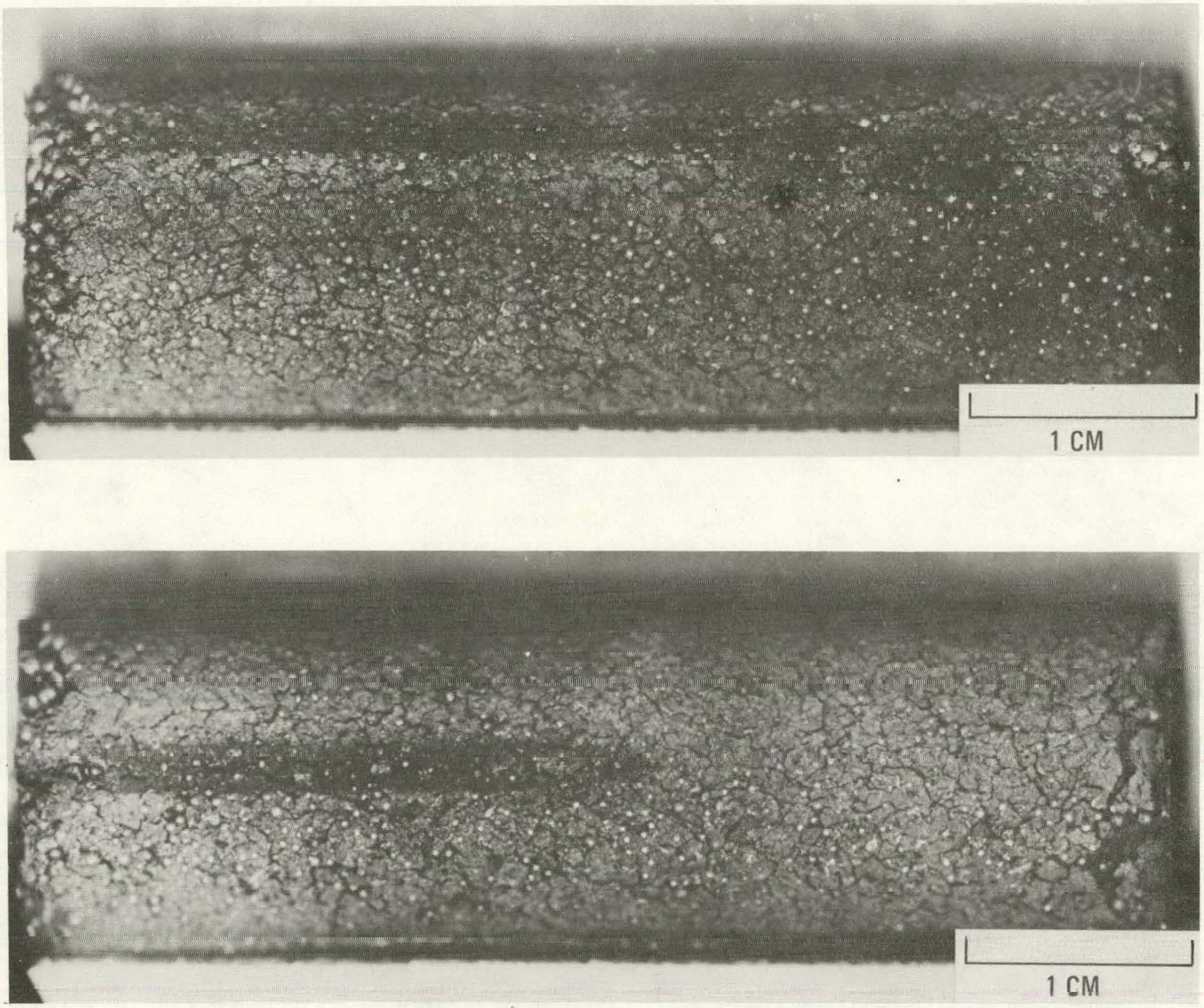

Fig. 5-21. Fuel rod compact No. 6 irradiated in GF-3 to 6.0 x 10^{25} n/m^2 (E > 29 fJ)$_{HTGR}$ and at 1165°C. This fuel rod is classified as type c [TRISO 500-μm-diameter (8Th,U)O_2, 100-μm buffer/ TRISO ThO_2] and was fabricated by GA. (Two views at 180-deg rotation.) Note localized chipping and particle debonding in upper section.

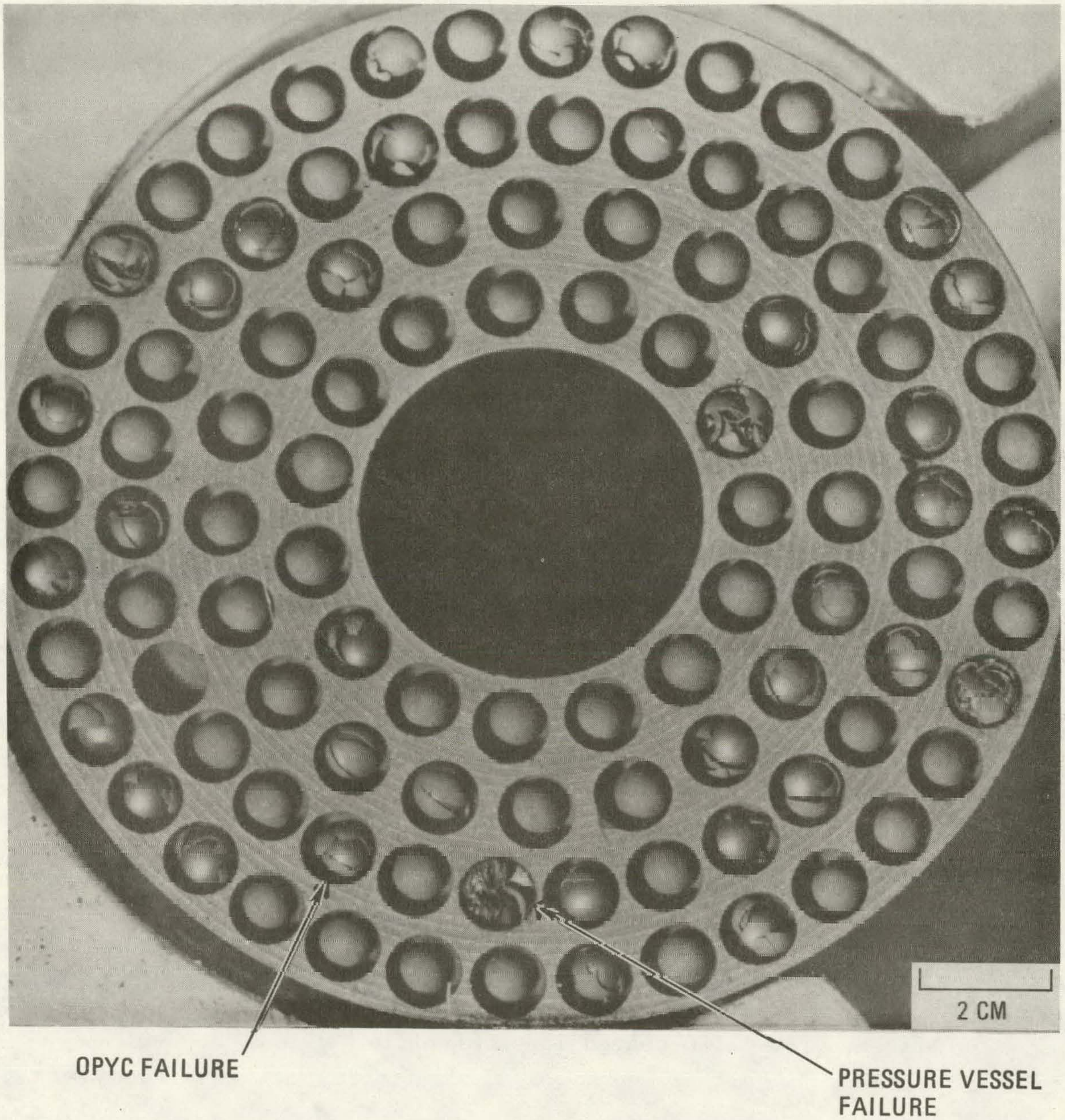

Fig. 5-22. TRISO-coated $(8Th,U)O_2$ loose particle batch 6155-02-020-1 irradiated in capsule GF-1 (planchet 13) to 4×10^{25} n/m^2 $(E > 29\ fJ)_{HTGR}$ and at a volume average temperature of 1095°C. This view illustrates the visual characterization of OPyC and pressure vessel failure.

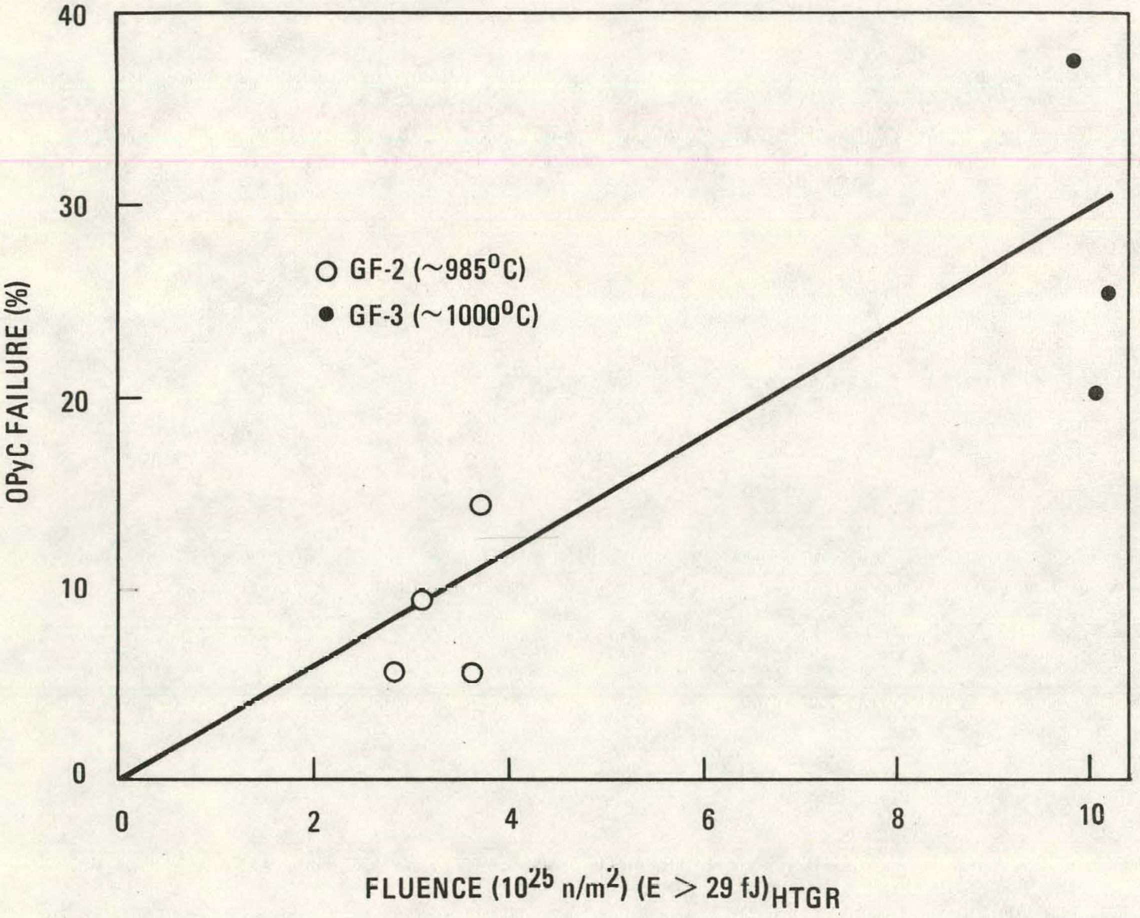

Fig. 5-23. Correlation between OPyC failure (determined visually) and fluence for TRISO-coated loose particle batch 6155-00-010

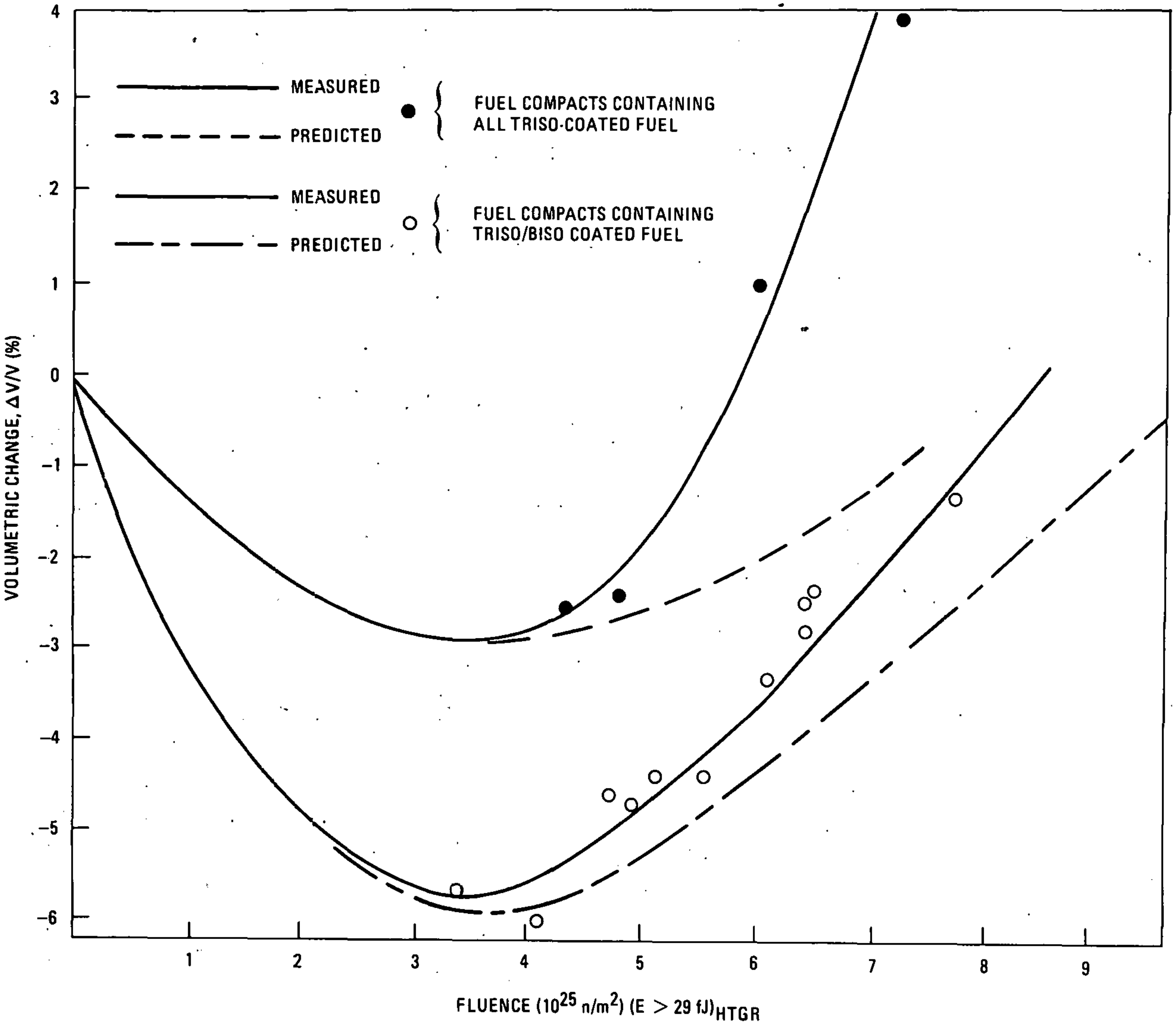

Fig. 5-24. Predicted and measured irradiation-induced volumetric changes versus fluence for GF-1, GF-2, and GF-3 fuel rod compacts

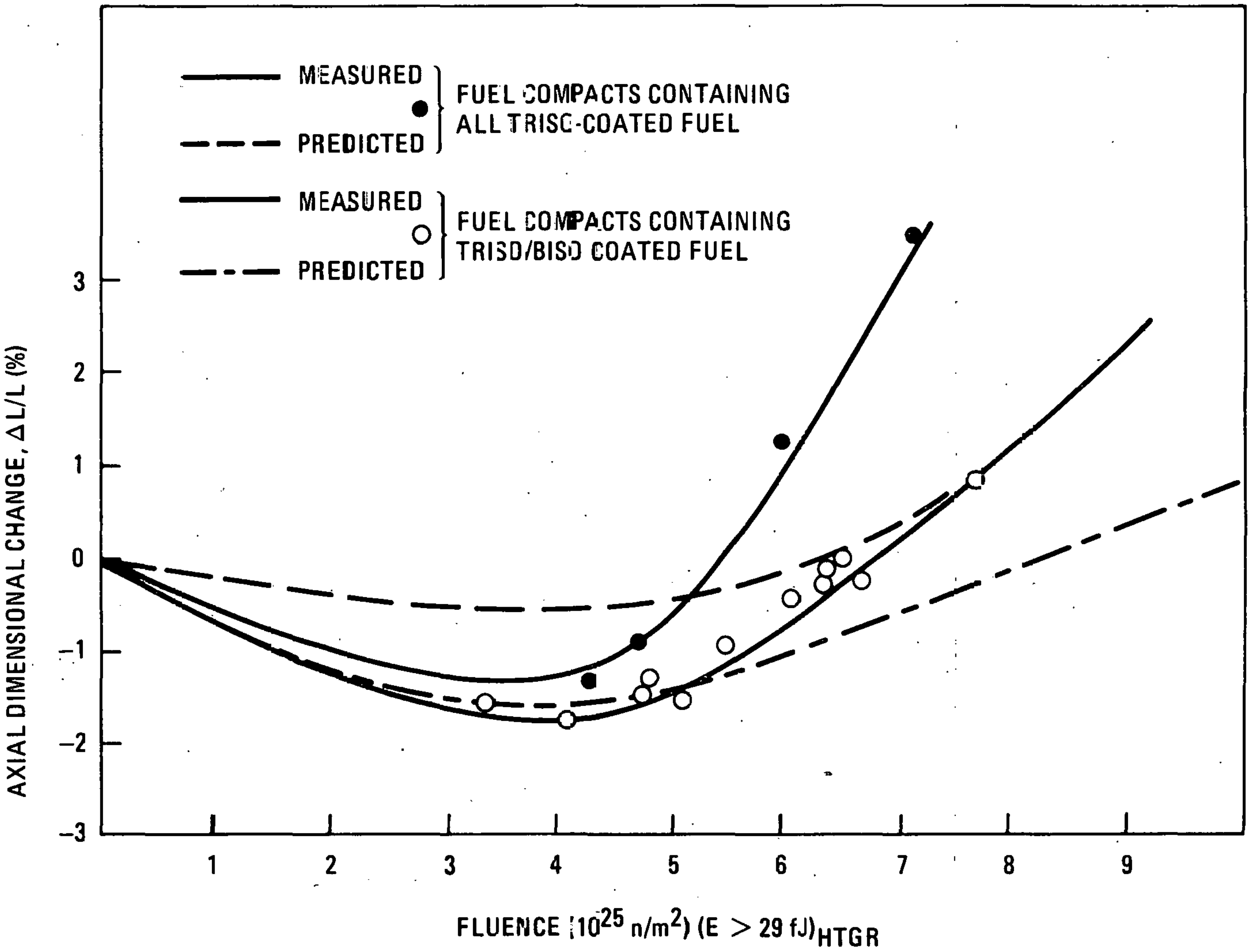

Fig. 5-25. Predicted and measured irradiation-induced axial dimensional changes versus fluence for GF-1, GF-2, and GF-3 fuel rod compacts

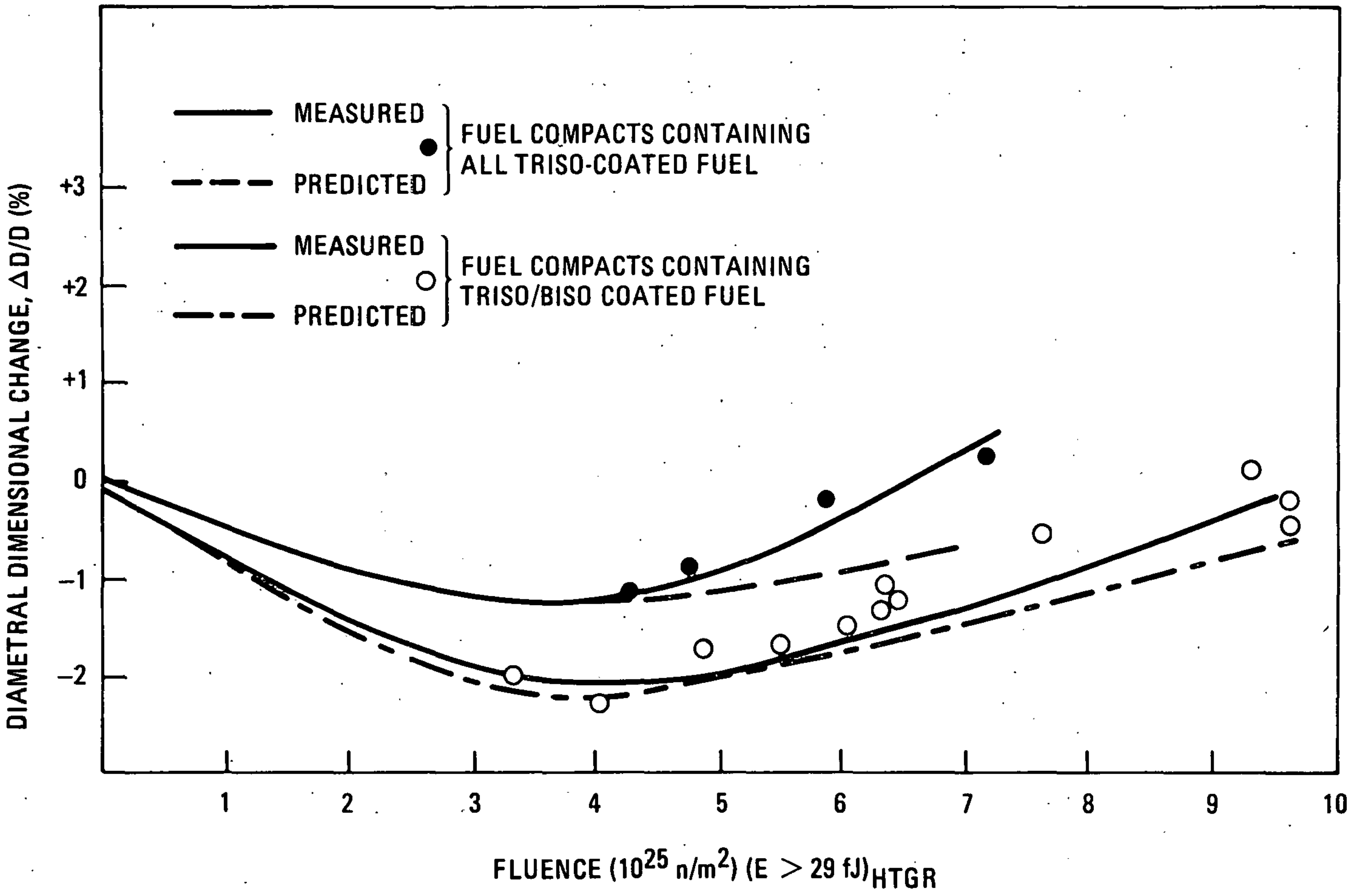

Fig. 5-26. Predicted and measured irradiation-induced diametral dimensional changes versus fluence for GF-1, GF-2, and GF-3 fuel rod compacts

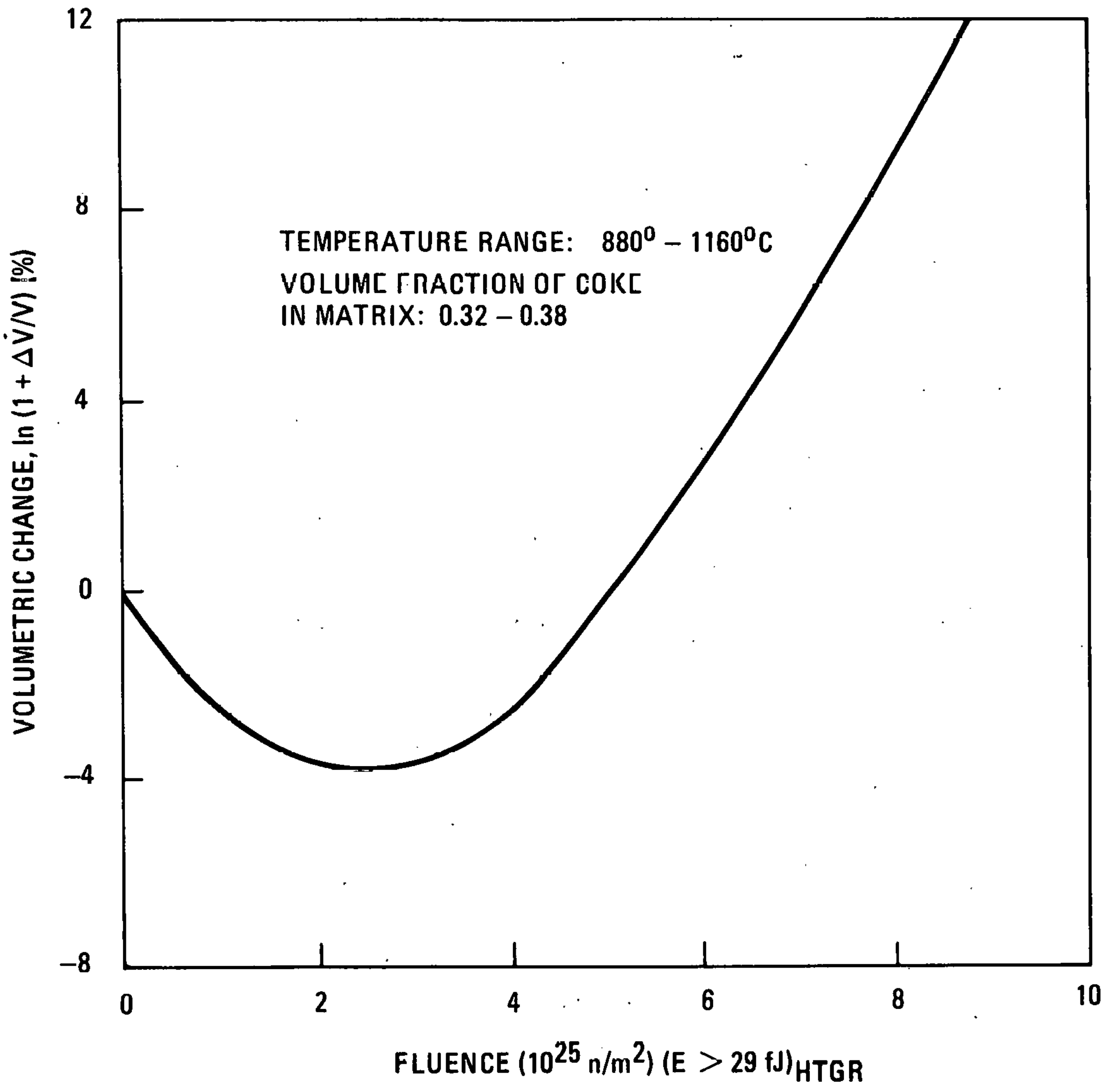

Fig. 5-27. Irradiation-induced volumetric changes of matrix phase used to predict GF-1, GF-2, and GF-3 fuel rod dimensional change behavior (Ref. 5-10.)

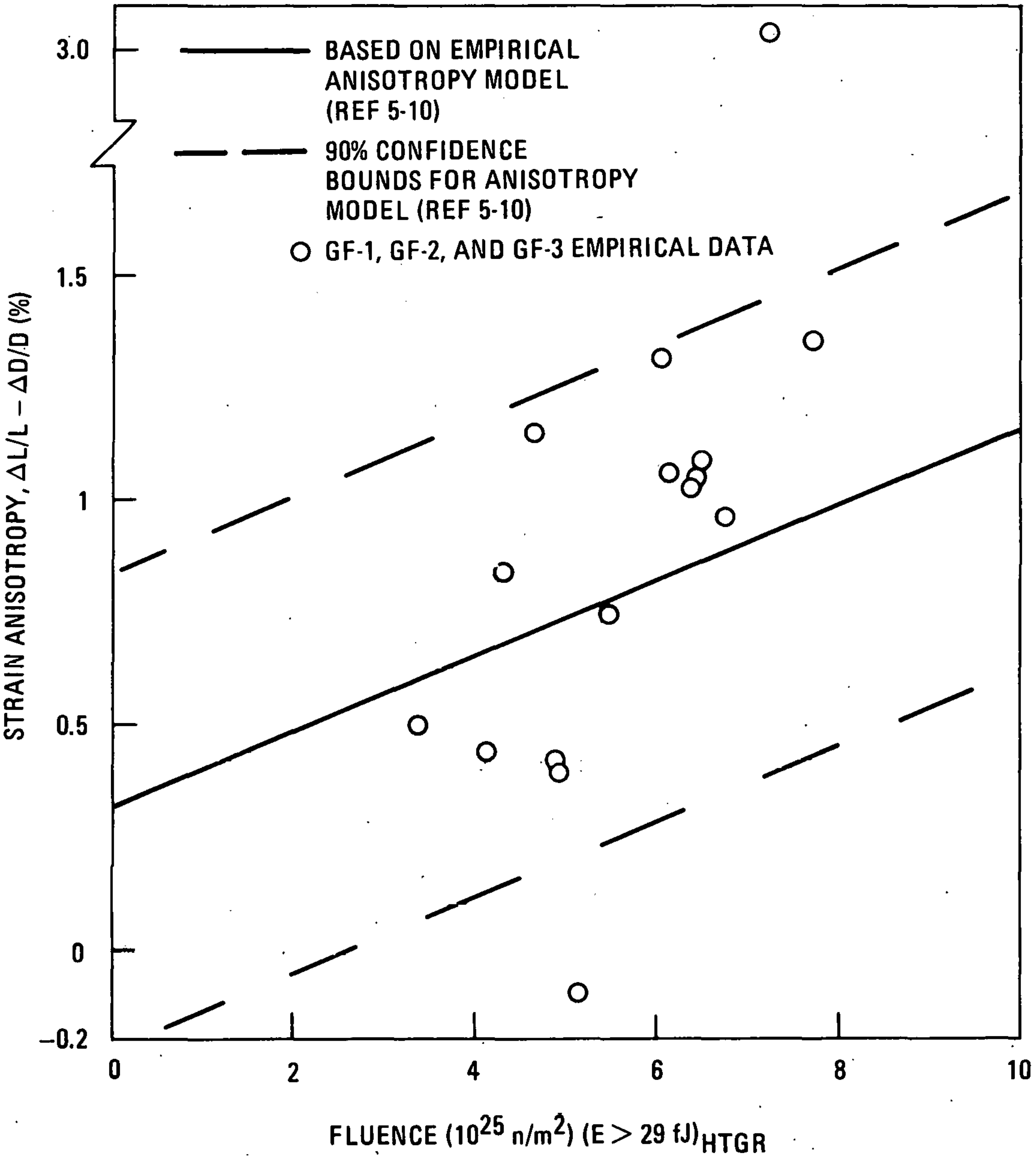

Fig. 5-28. Predicted and measured strain anisotrophy versus fluence for fuel compacts irradiated in GF-1, GF-2, and GF-3

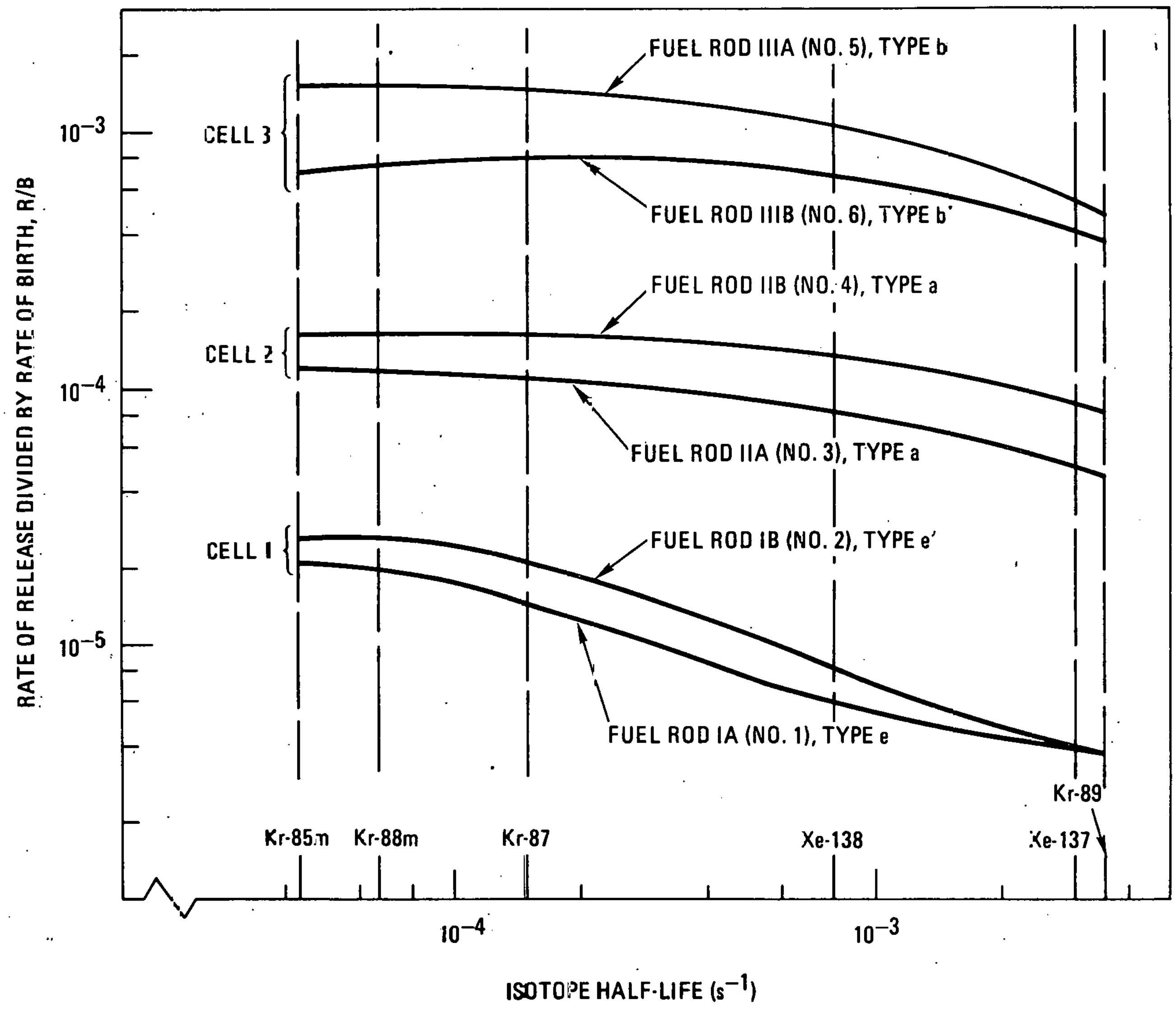

Fig. 5-29. Reirradiation and measurement of R/B gaseous release at 600°C for fuel rods in GF-1

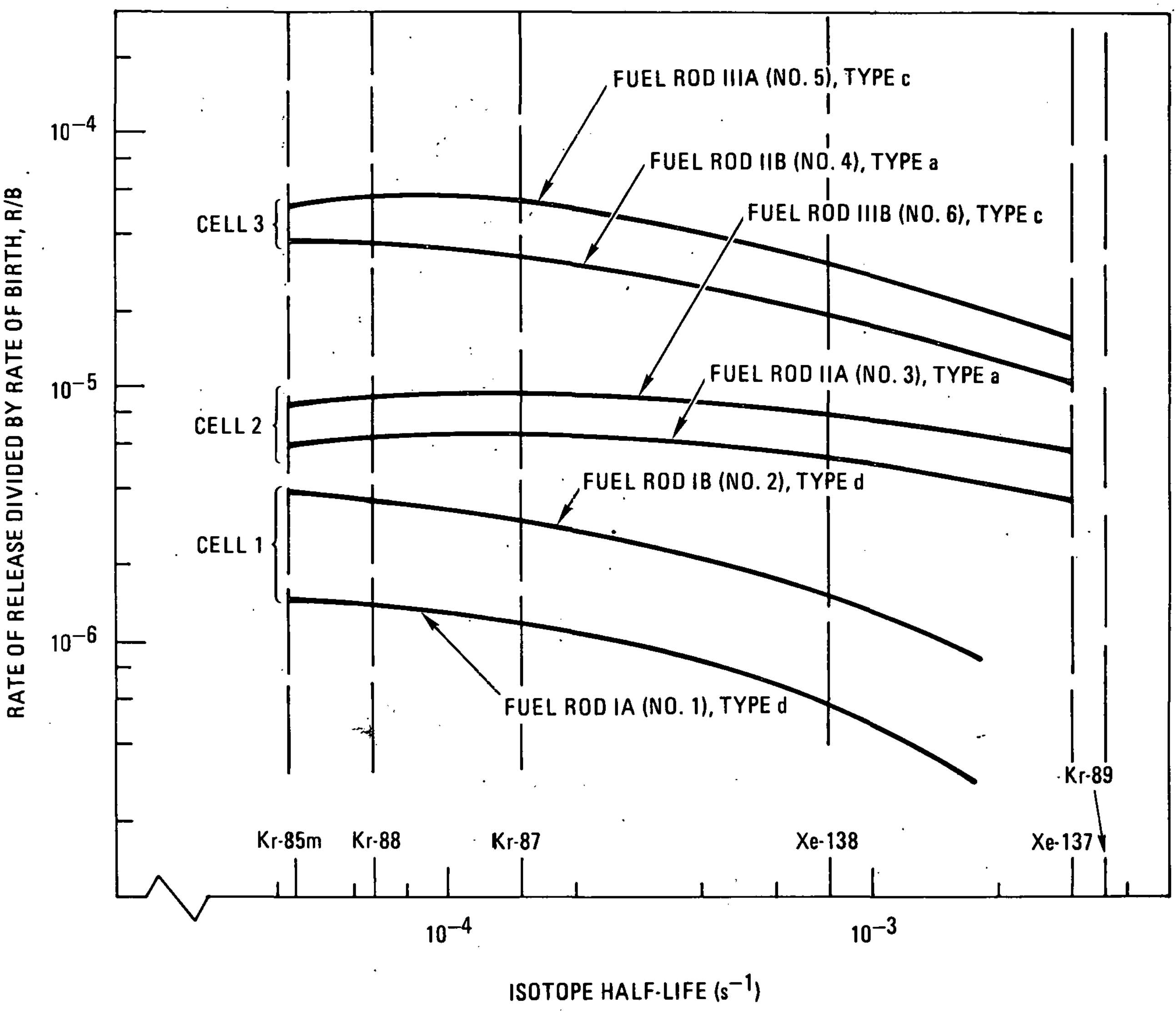

Fig. 5-30. Reirradiation and measurement of R/B gaseous release at 600°C for fuel rods in GF-2

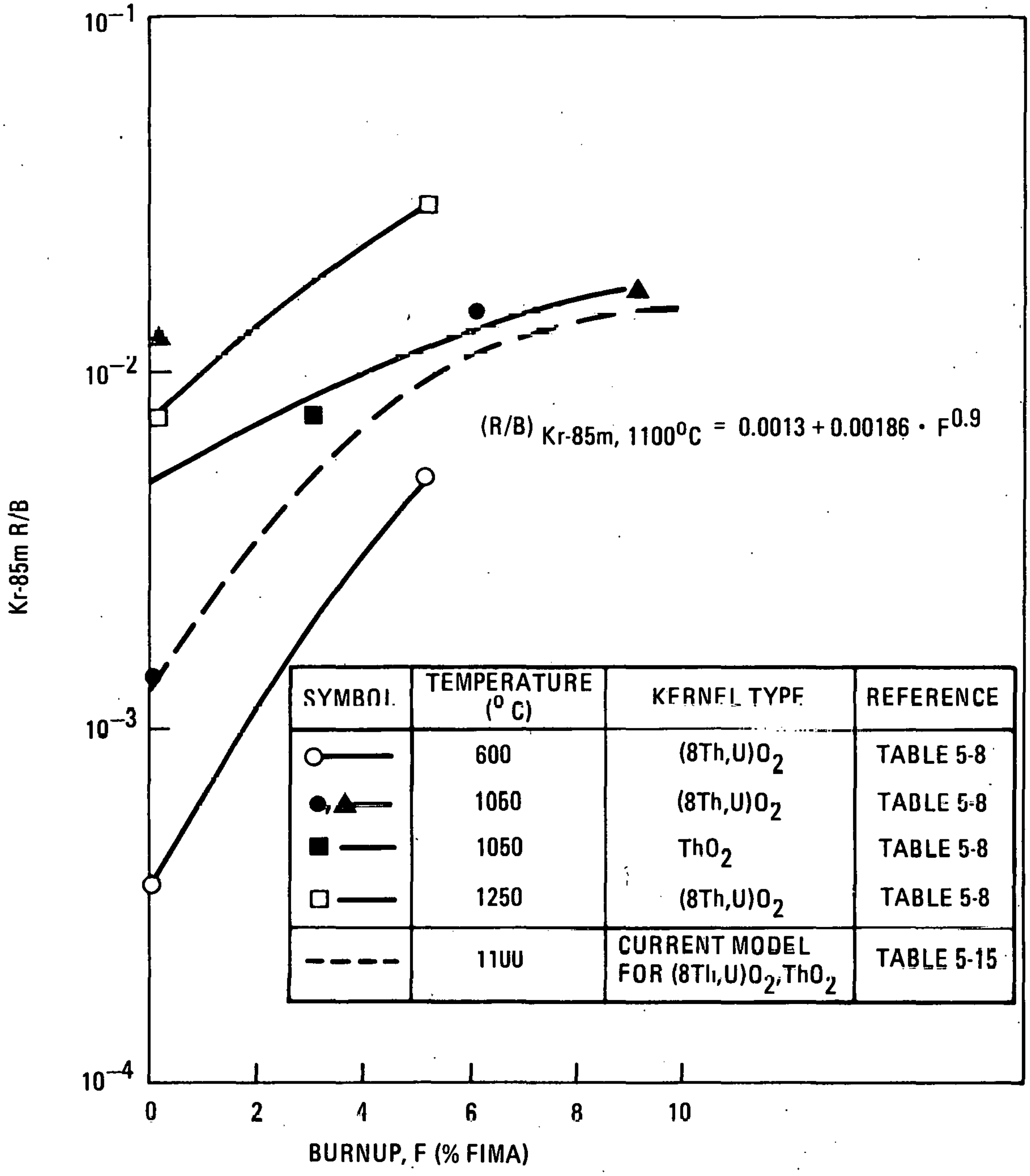

Fig. 5-31. Kr-85m R/B versus burnup for laser-failed (8Th,U)O_2 and ThO_2 fuel particles

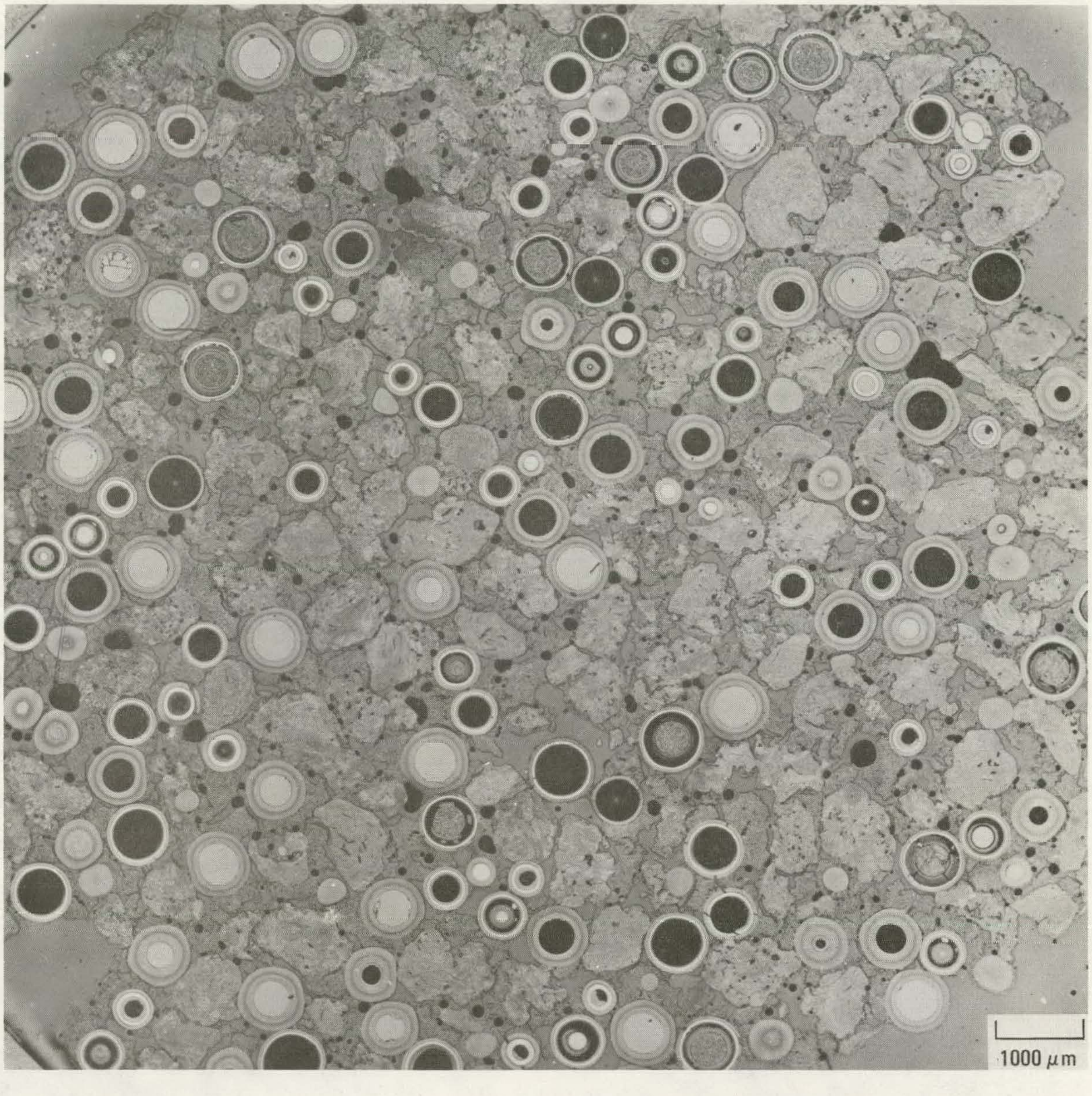

Fig. 5-32. Diametral photomicrograph of a type a fuel rod after irradiation in capsule GF-2 (location 2-3) to a fast neutron fluence of 4.9×10^{25} n/m^2 (E > 29 fJ)$_{HTGR}$ at 970°C. A macroporosity of 25% was measured.

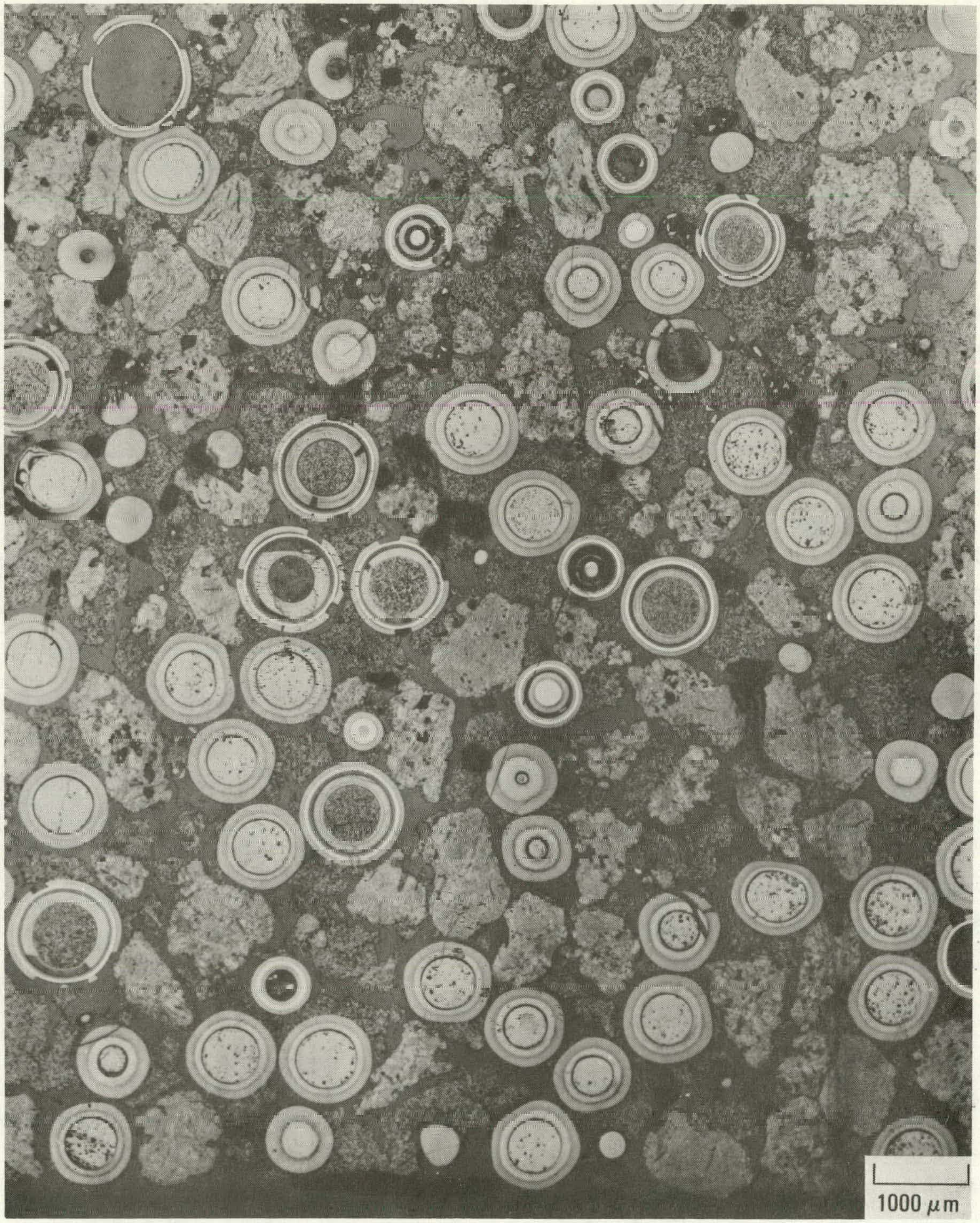

Fig. 5-33. Longitudinal photomicrograph of a type b fuel rod after irradiation in capsule GF-3 (location 2-3) to a fast neutron fluence of 9.4×10^{25} n/m^2 (E > 29 fJ)$_{HTGR}$ at 975°C. A macroporosity of 52% was measured.

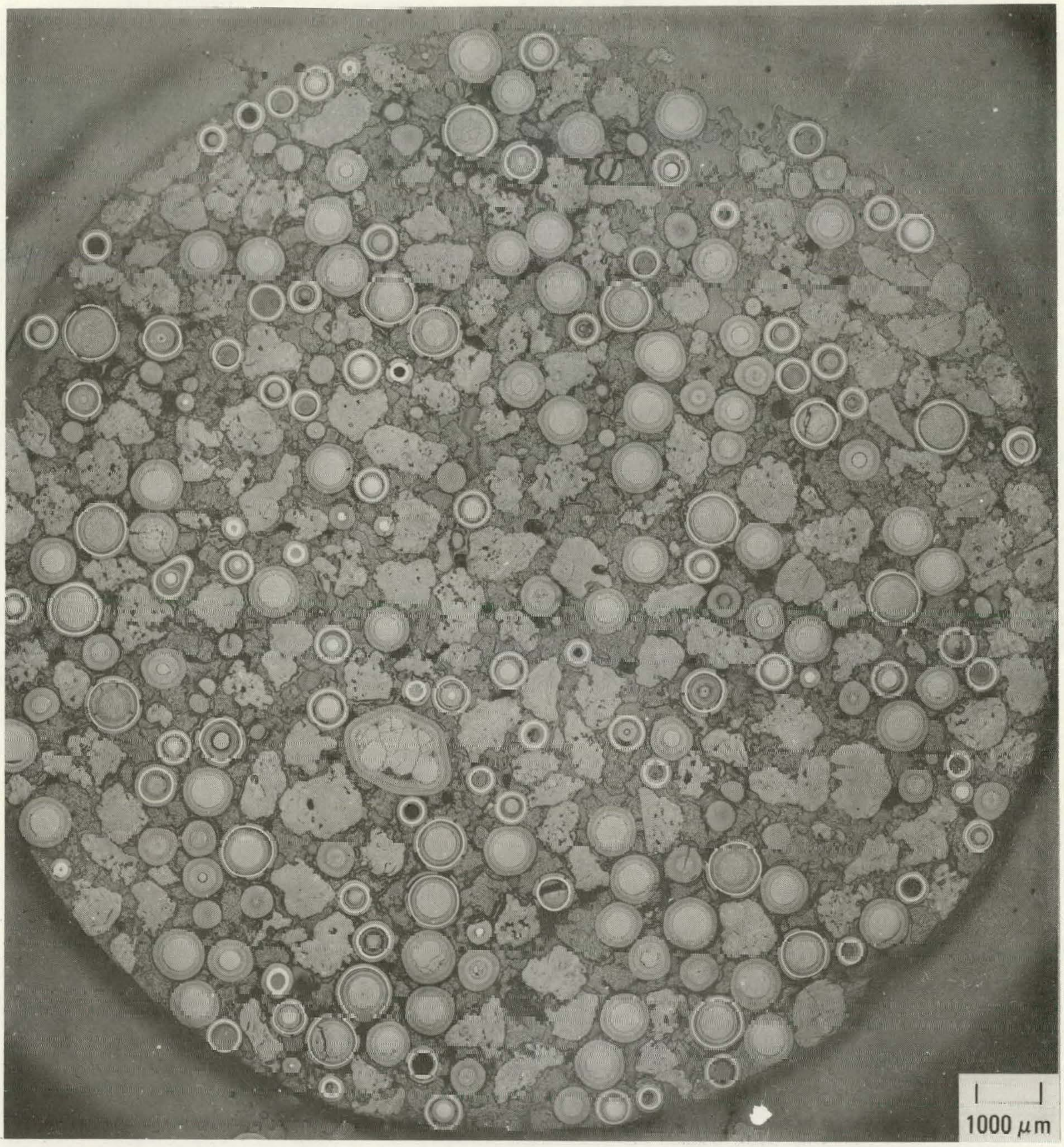

Fig. 5-34. Diametral photomicrograph of a type b' fuel rod after irradiation in capsule GF-1 (location 3-6) to a fast neutron fluence of 6.1×10^{25} n/m^2 (E > 29 fJ)$_{HTGR}$ at 1170°C. A macroporosity of 34% was measured.

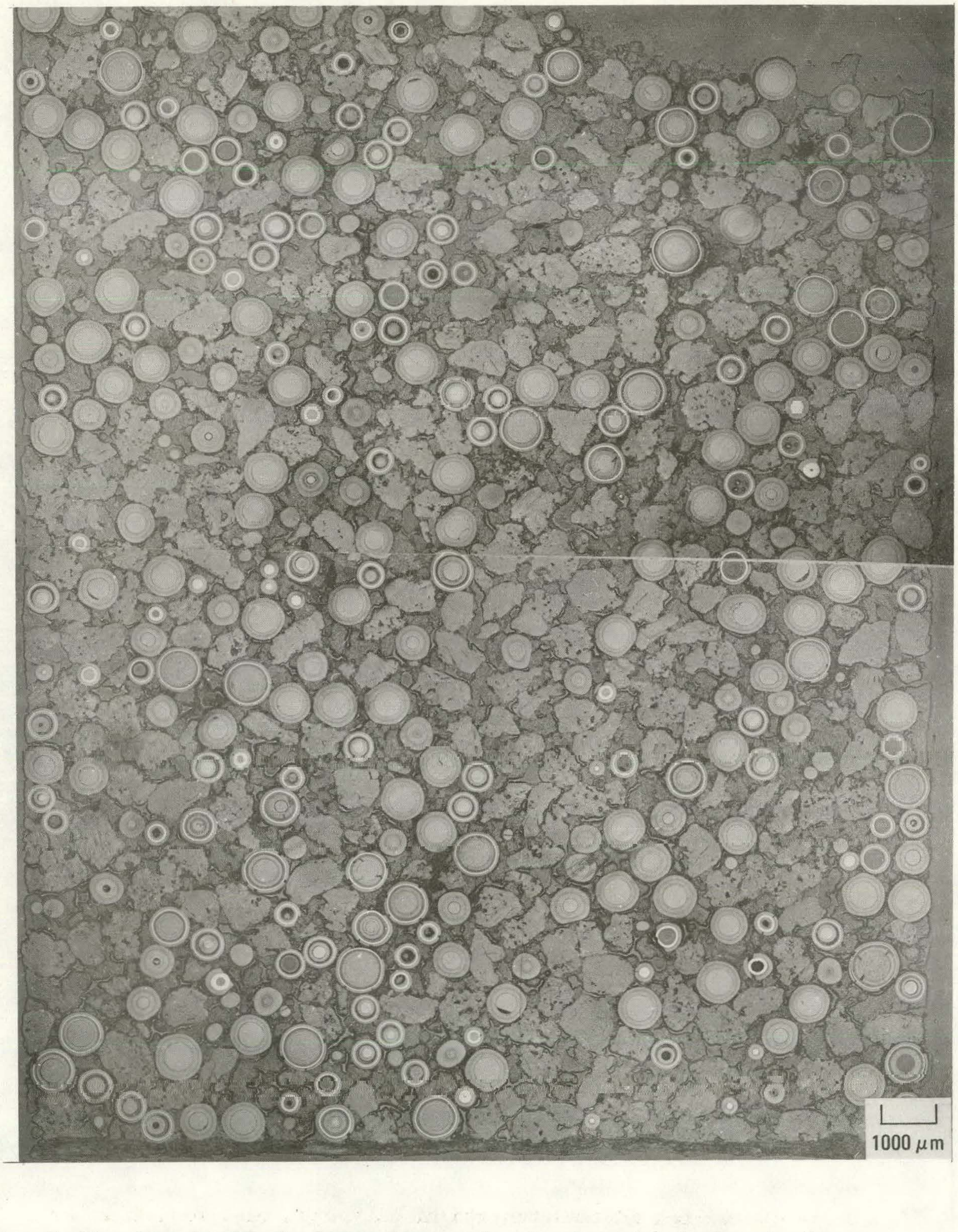

Fig. 5-35. Longitudinal photomicrograph of a type b' fuel rod after irradiation in capsule GF-1 (location 3-6) to a fast neutron fluence of 6.1 x 10^{25} n/m^2 (E > 29 fJ)$_{HTGR}$ at 1170°C. A macroporosity of 28% was measured.

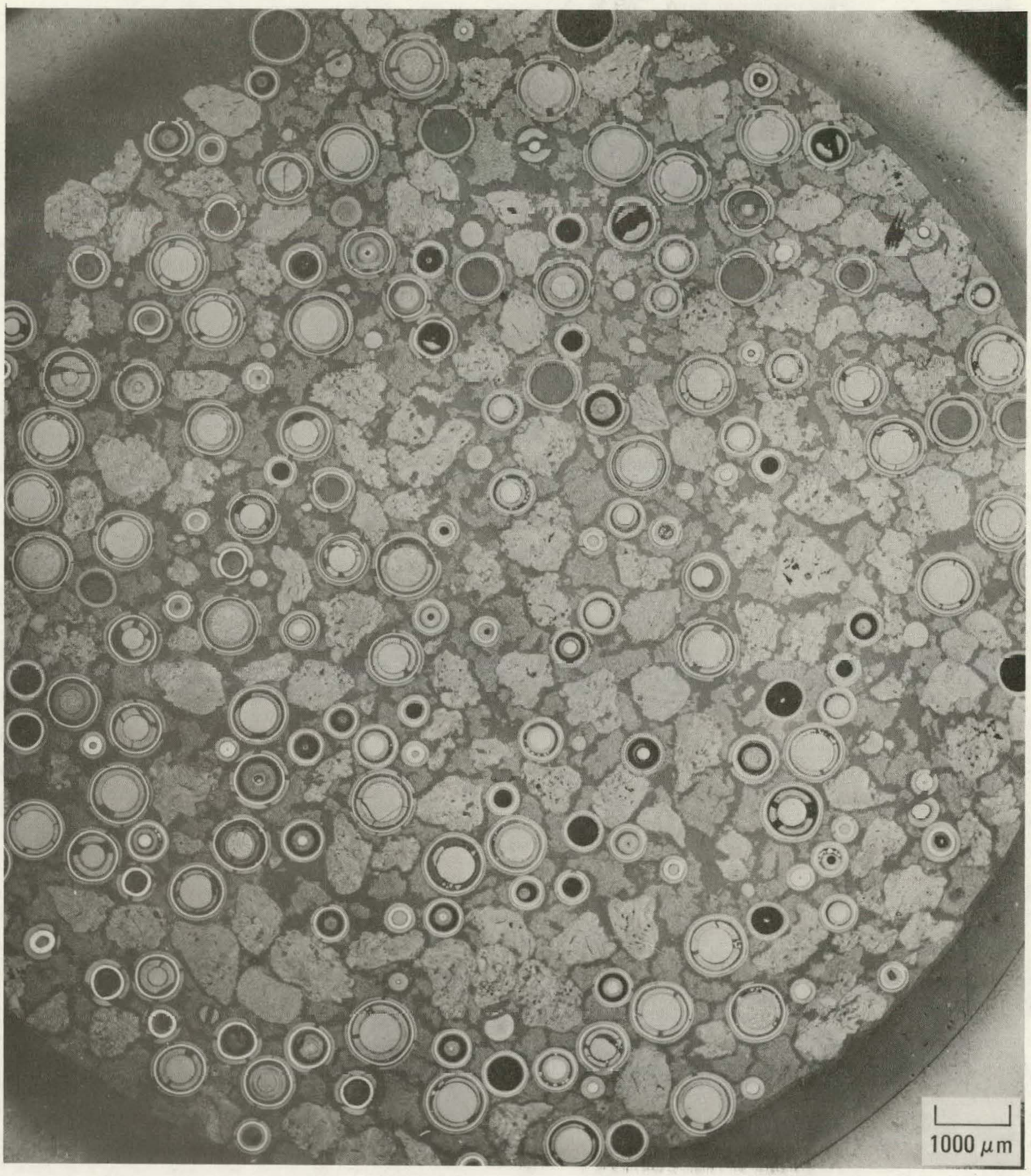

Fig. 5-36. Diametral photomicrograph of a type c fuel rod after irradiation in capsule GF-3 (location 4-6) to a fast neutron fluence of 6.0×10^{25} n/m^2 (E > 29 fJ)$_{HTCR}$ at 1120°C. A macroporosity of 52% was measured.

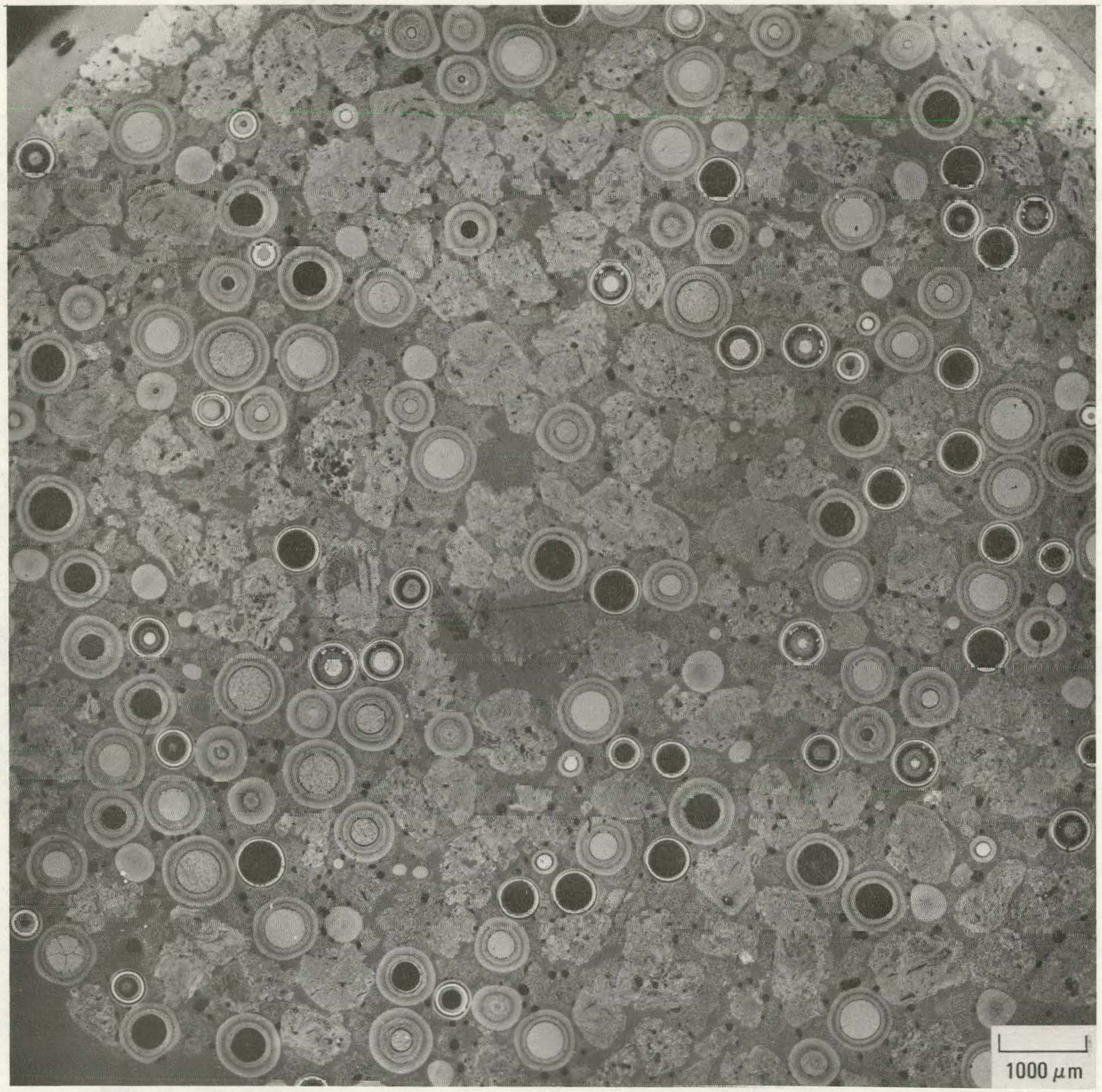

Fig. 5-37. Diametral photomicrograph of a type d fuel rod after irradiation in capsule GF-2 (location 1-1) to a fast neutron fluence of 3.4×10^{25} n/m^2 ($E > 29$ fJ)$_{HTGR}$ at 960°C. A macroporosity of 44% was measured.

Fig. 5-38. Diametral photomicrograph of a type e fuel rod after irradiation in capusle GF-1 (location 1-2) at a fast neutron fluence of 5.5 x 10^{25} n/m^2 (E > 29 fJ)$_{HTGR}$ at 1080°C. A microporosity of 0% was measured.

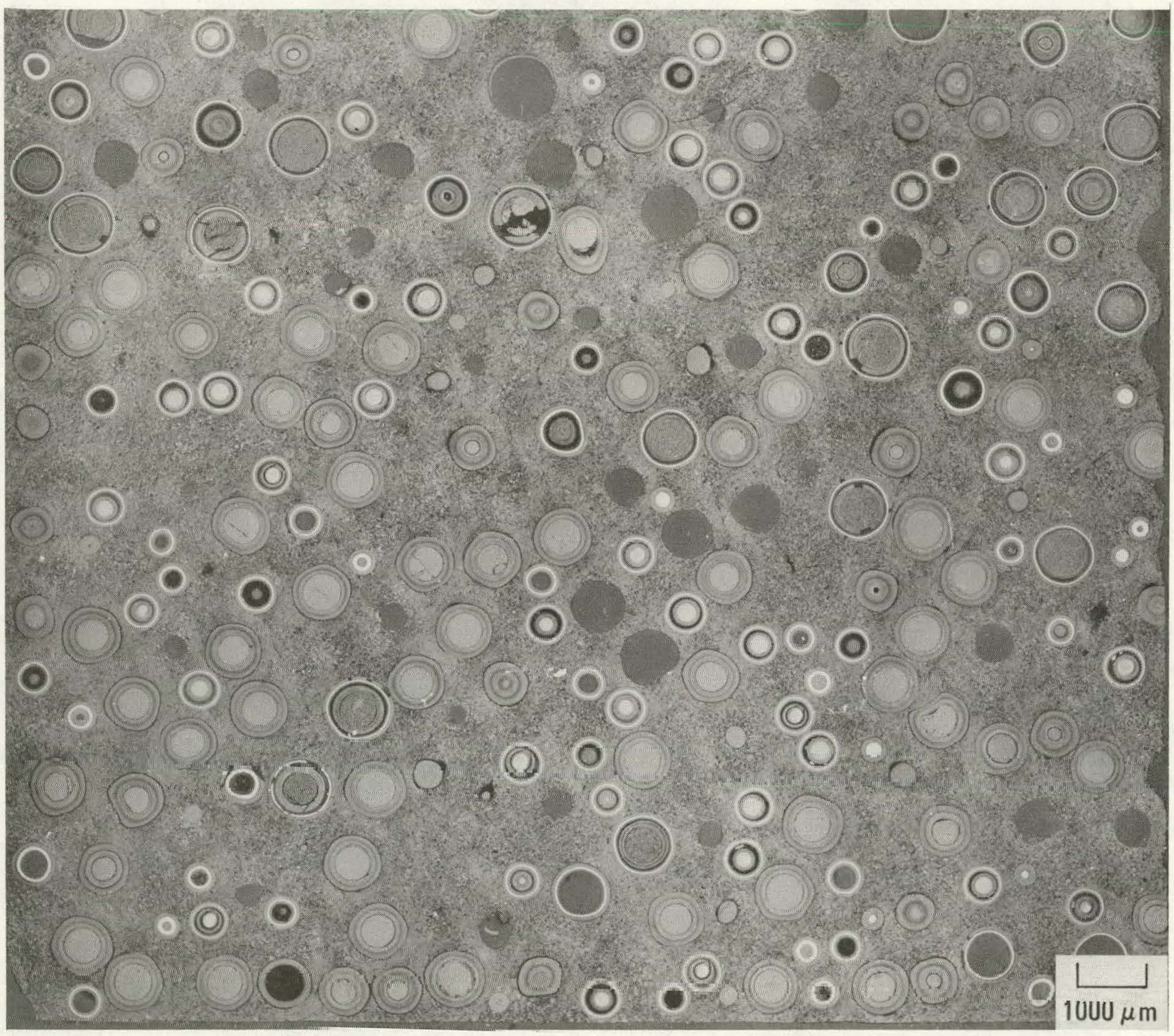

Fig. 5-39. Longitudinal photomicrograph of a type e fuel rod after irradiation in capsule GF-1 (location 1-2) to a fast neutron fluence of 5.5×10^{25} n/m^2 (E > 29 fJ)$_{HTGR}$ at 1080°C. A microporosity of 0% was measured.

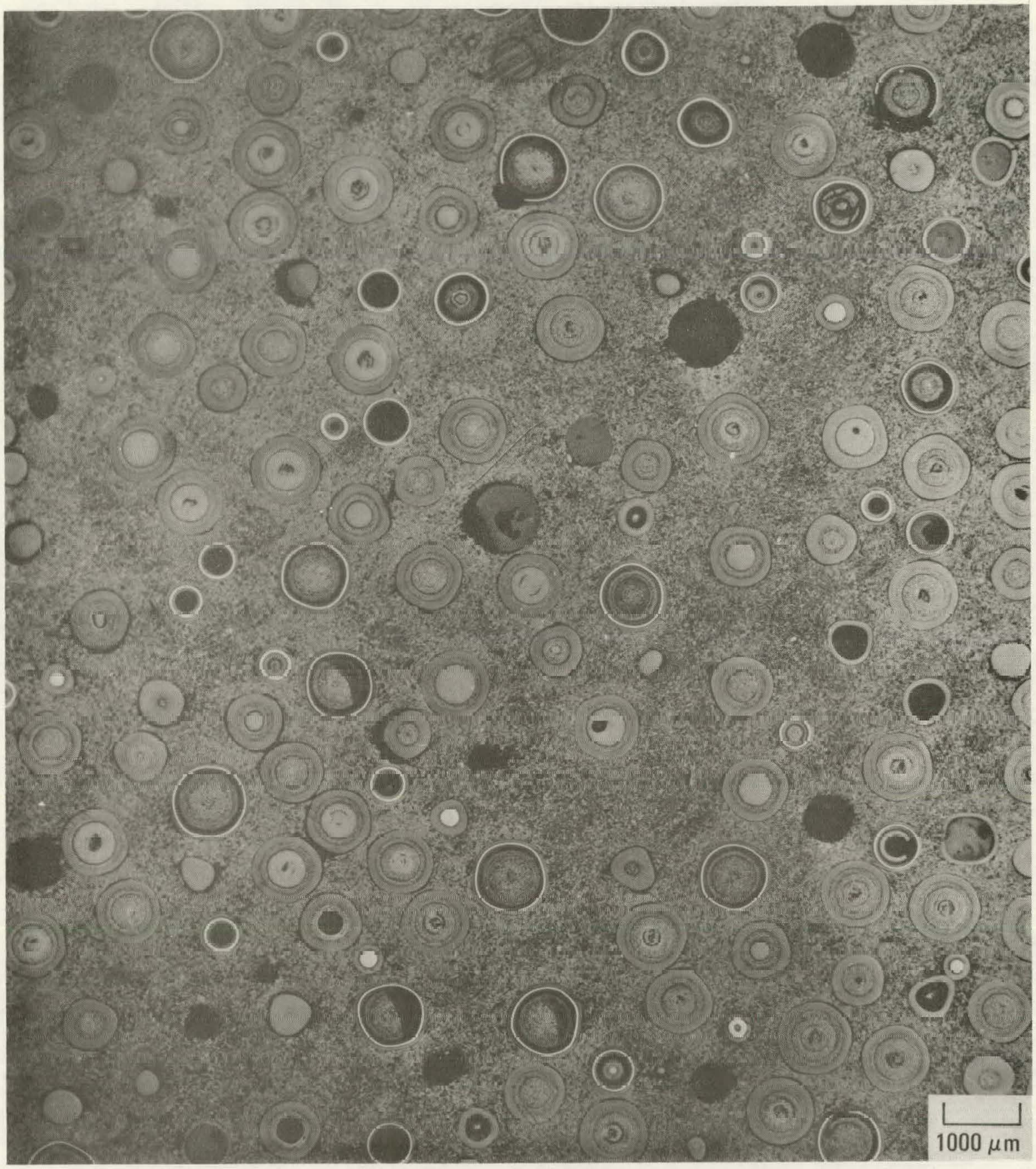

Fig. 5-40. Longitudinal photomicrograph of a type f' fuel rod after irradiation in capsule GF-3 (location 1-2) to a fast neutron fluence of 7.7×10^{25} n/m^2 $(E > 29\ fJ)_{HTGR}$ at 975°C. A macroporosity of 0% was measured.

Fig. 5-41. Representative metallographic cross section of matrix and shim material in a GA type a fuel rod. The rod was irradiated in capsule GF-1 (location 2-4) to a fast fluence of 6.7 x 10^{25} n/m^2 (E > 29 fJ)$_{HTGR}$ at 1170°C. The matrix microporosity was not measured; however, it was estimated at ∿50%.

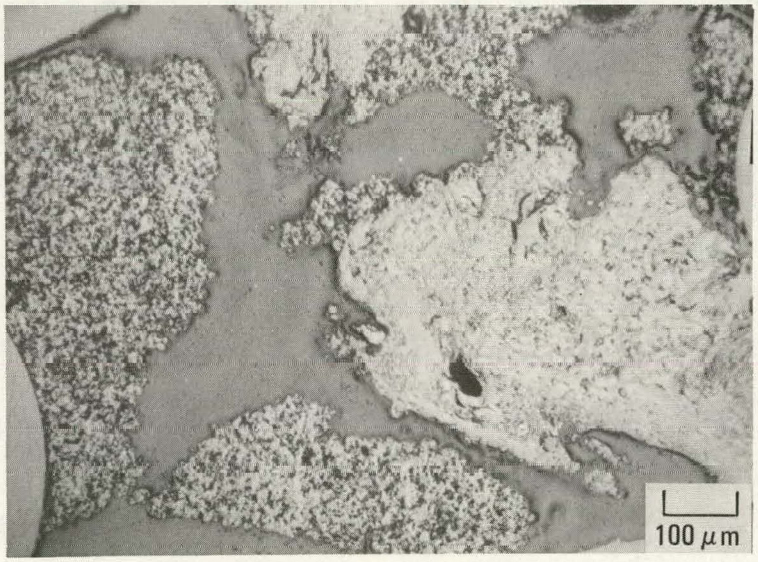

Fig. 5-42. Representative metallographic cross section of matrix and shim material in a GA type b' fuel rod. The rod was irradiated in capsule GF-1 (location 3-6) to a fast fluence of 6.1 x 10^{25} n/m^2 (E > 29 fJ)$_{HTGR}$ at 1170°C. The matrix porosity was not measured; however, it was estimated at ∿50%.

Fig. 5-43. Representative metallographic cross section of CERCA natural type matrix in CEA type e fuel rod. The rod was irradiated in capsule GF-1 (location 1-2) to a fast fluence of 5.5 x 10^{25} n/m^2 (E > 29 fJ)$_{HTGR}$ at 1080°C. A matrix microporosity of 13% was measured.

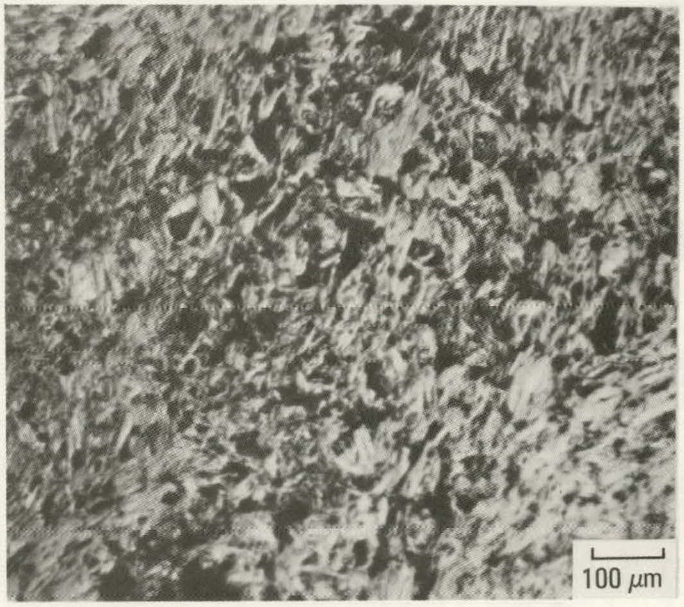

Fig. 5-44. Representative metallographic cross section of CERCA artificial type matrix in CEA type f' fuel rod. The rod was irradiated in capsule GF-3 (location 1-2) to a fast fluence of 7.7 x 10^{25} n/m^2 (E > 29 fJ)$_{HTGR}$ at 975°C. A matrix microporosity of 37% was measured.

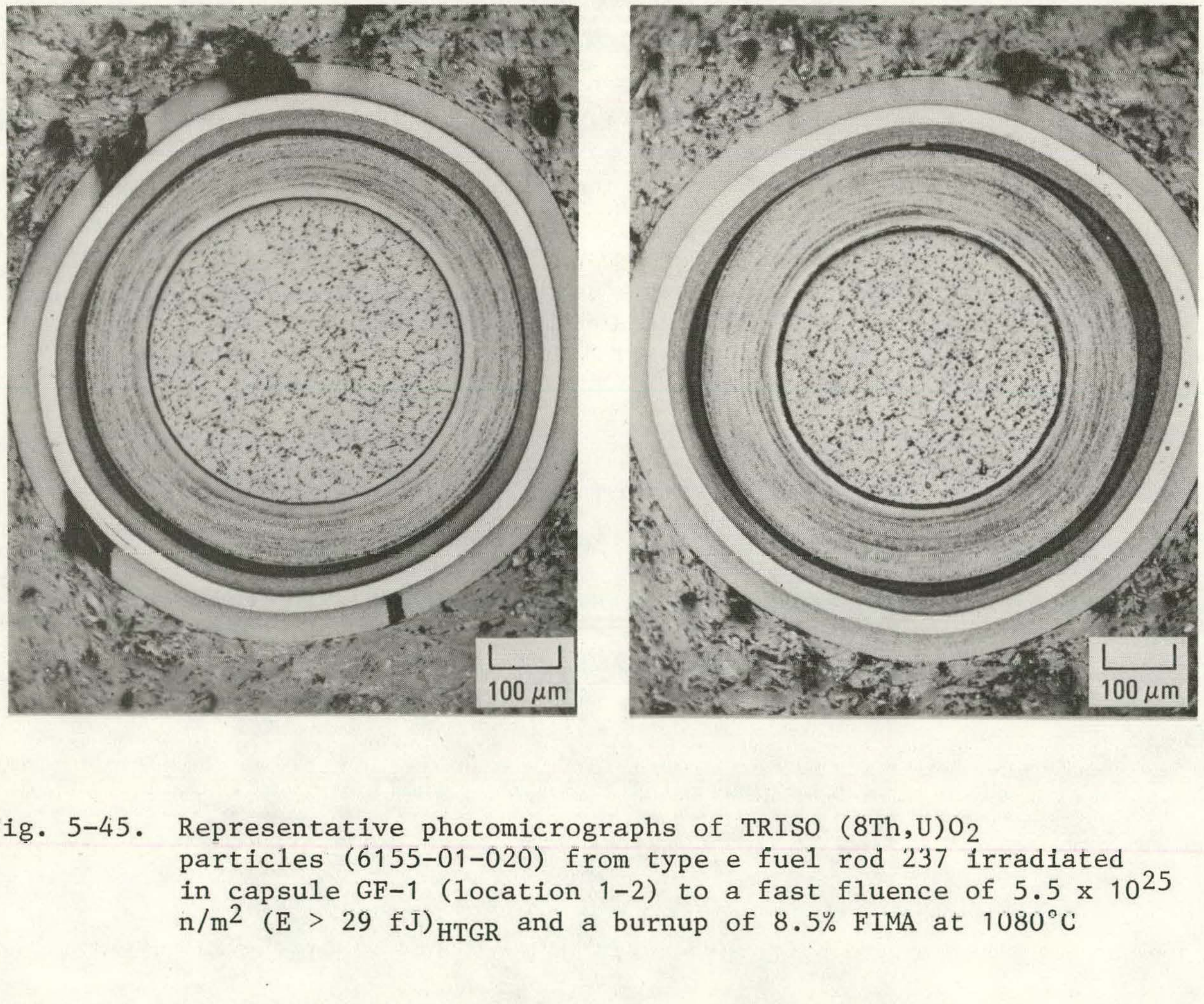

Fig. 5-45. Representative photomicrographs of TRISO $(8Th,U)O_2$ particles (6155-01-020) from type e fuel rod 237 irradiated in capsule GF-1 (location 1-2) to a fast fluence of 5.5×10^{25} n/m^2 $(E > 29\ fJ)_{HTGR}$ and a burnup of 8.5% FIMA at 1080°C

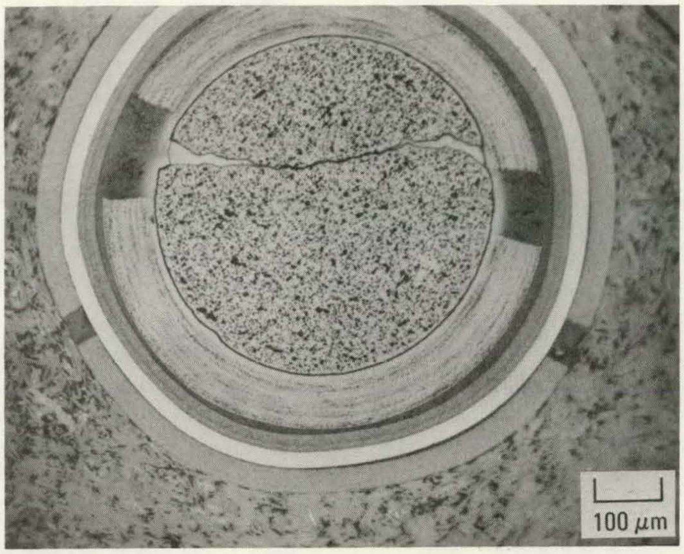

Fig. 5-46. Representative photomicrograph of TRISO $(8Th,U)O_2$ particles (6155-01-020) from type e fuel rod 237 irradiated in capsule GF-1 (location 1-2) to a fast fluence of 5.5×10^{25} n/m^2 $(E > 29\ fJ)_{HTGR}$ and a burnup of 8.5% FIMA at 1080°C

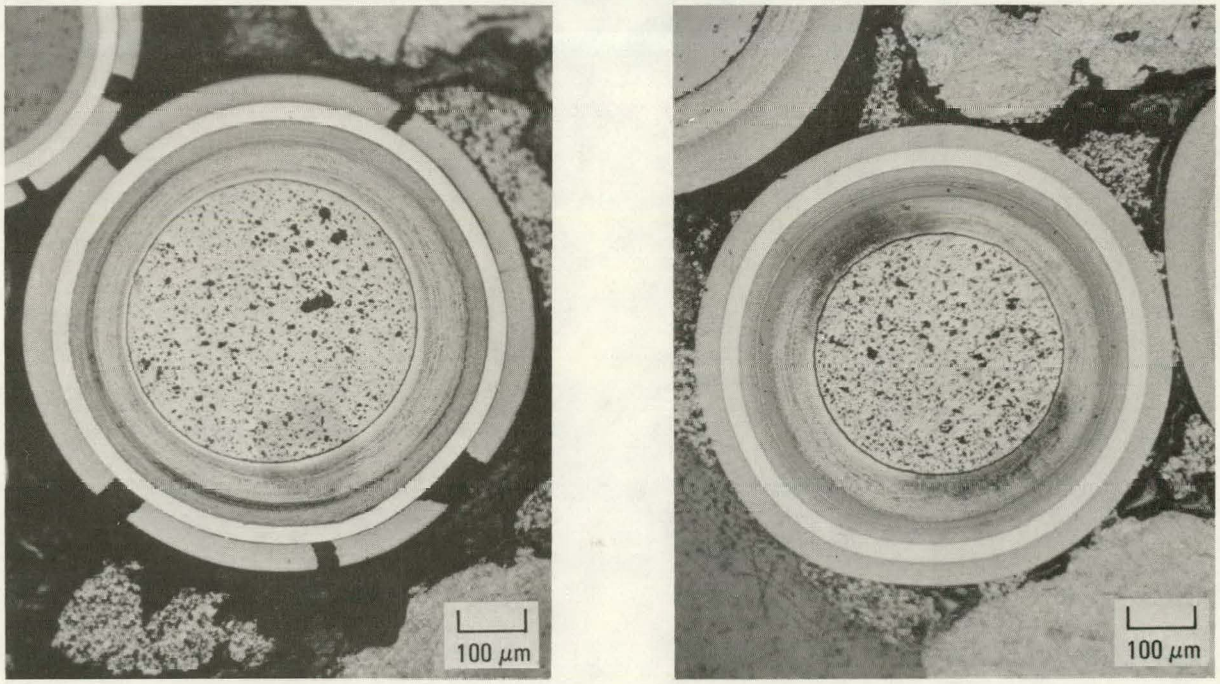

Fig. 5-47. Representative photomicrographs of TRISO $(8Th,U)O_2$ particles (6155-00-030) from type a fuel rod (7161-003-01-4) irradiated in capsule GF-1 (location 2-3) to a fast fluence of 6.4×10^{25} n/m^2 $(E > 29\ fJ)_{HTGR}$ and a burnup of 9.7% FIMA at 1170°C

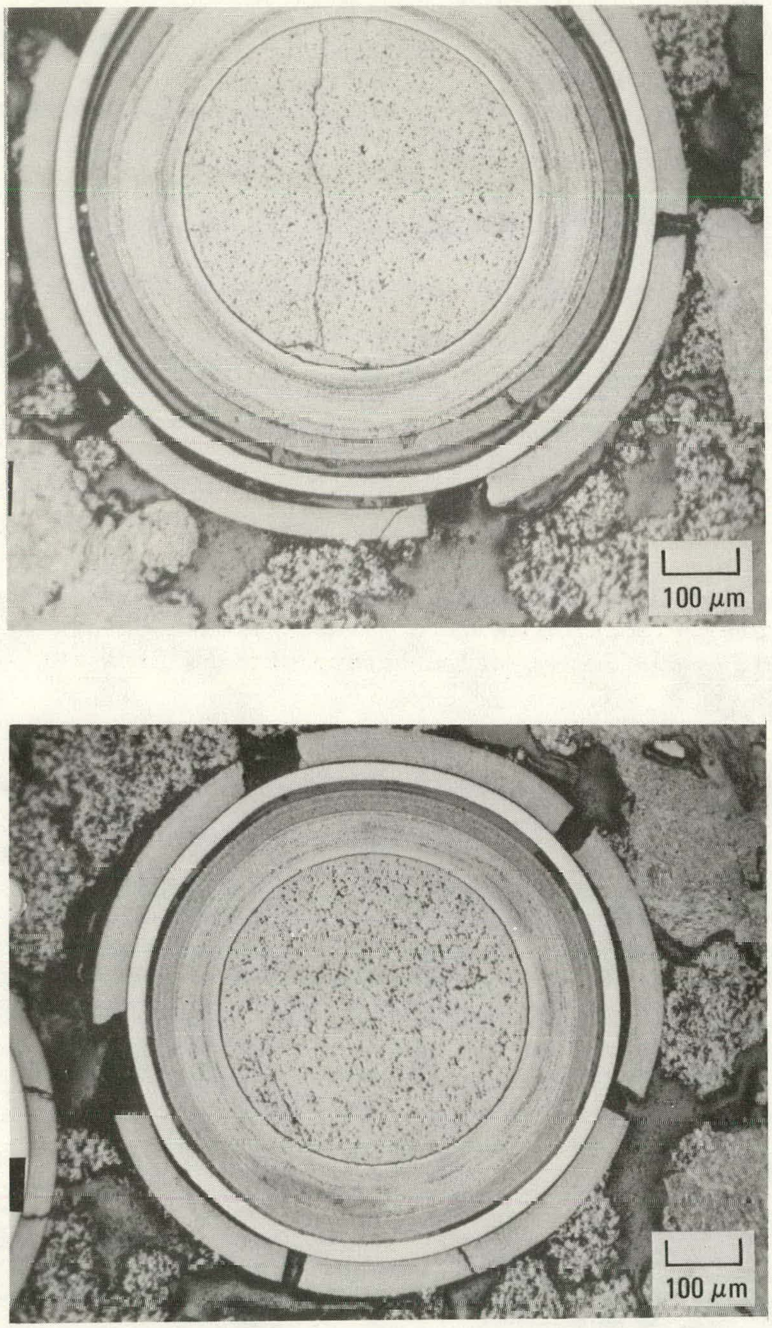

Fig. 5-48. Representative photomicrographs of TRISO $(8Th,U)O_2$ particles (6155-02-030) from type b' fuel rod (7161-003-03-5) irradiated in capsule GF-1 (location 3-6) to a fast fluence of 6.1 x 10^{25} n/m^2 $(E > 29\ fJ)_{HTGR}$ and a burnup of 9.4% FIMA at 1170°C

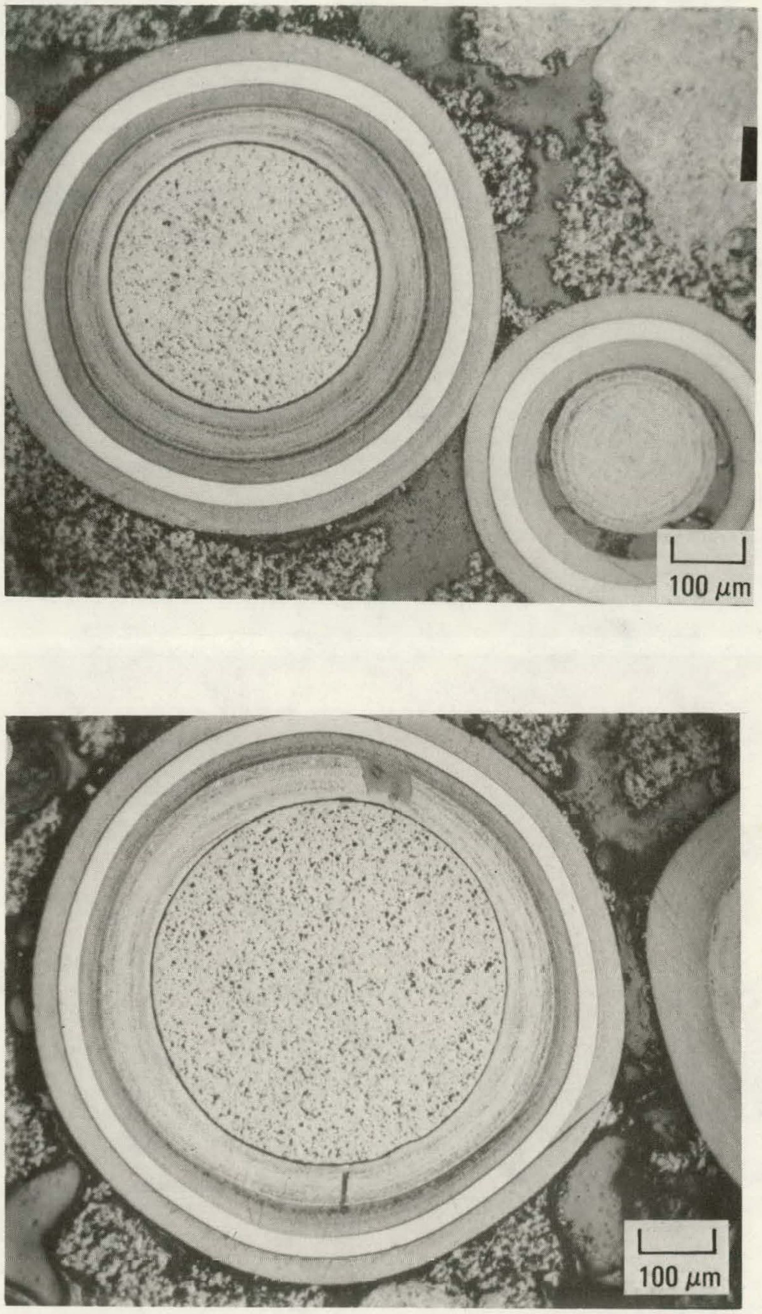

Fig. 5-49. Representative photomicrographs of TRISO $(8Th,U)O_2$ particles (6155-02-030) from a type b' fuel rod (7161-003-03-5) irradiated in capsule GF-1 (location 3-6) to a fast fluence of 6.1 x 10^{25} n/m^2 (E > 29 fJ)$_{HTGR}$ and a burnup of 9.4% FIMA at 1170°C

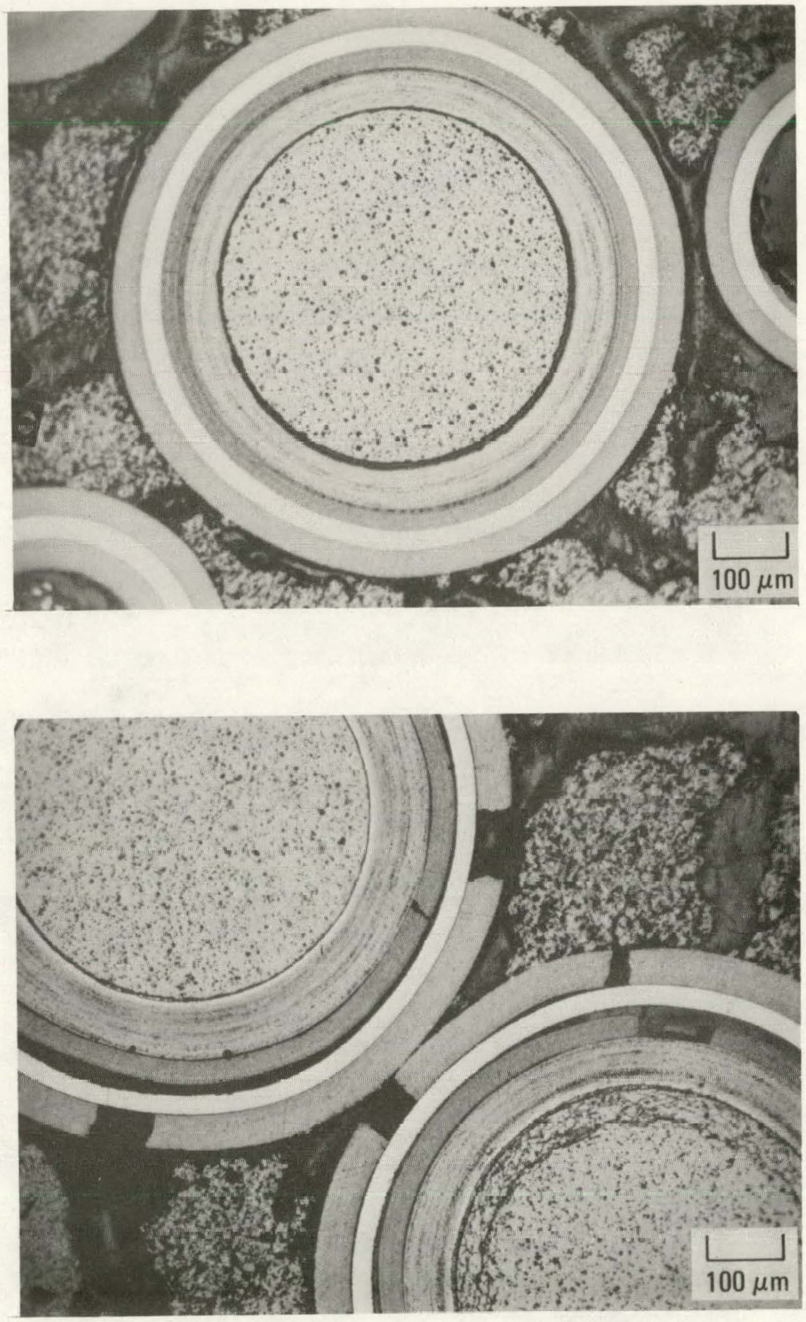

Fig. 5-50. Representative photomicrographs of TRISO $(8Th,U)O_2$ particles (6155-02-030) from a type b' fuel rod (7161-003-03-5) irradiated in capsule GF-1 (location 3-6) to a fast fluence of 6.1 x 10^{25} n/m^2 $(E > 29\ fJ)_{HTGR}$ and a burnup of 9.5% FIMA at 1170°C

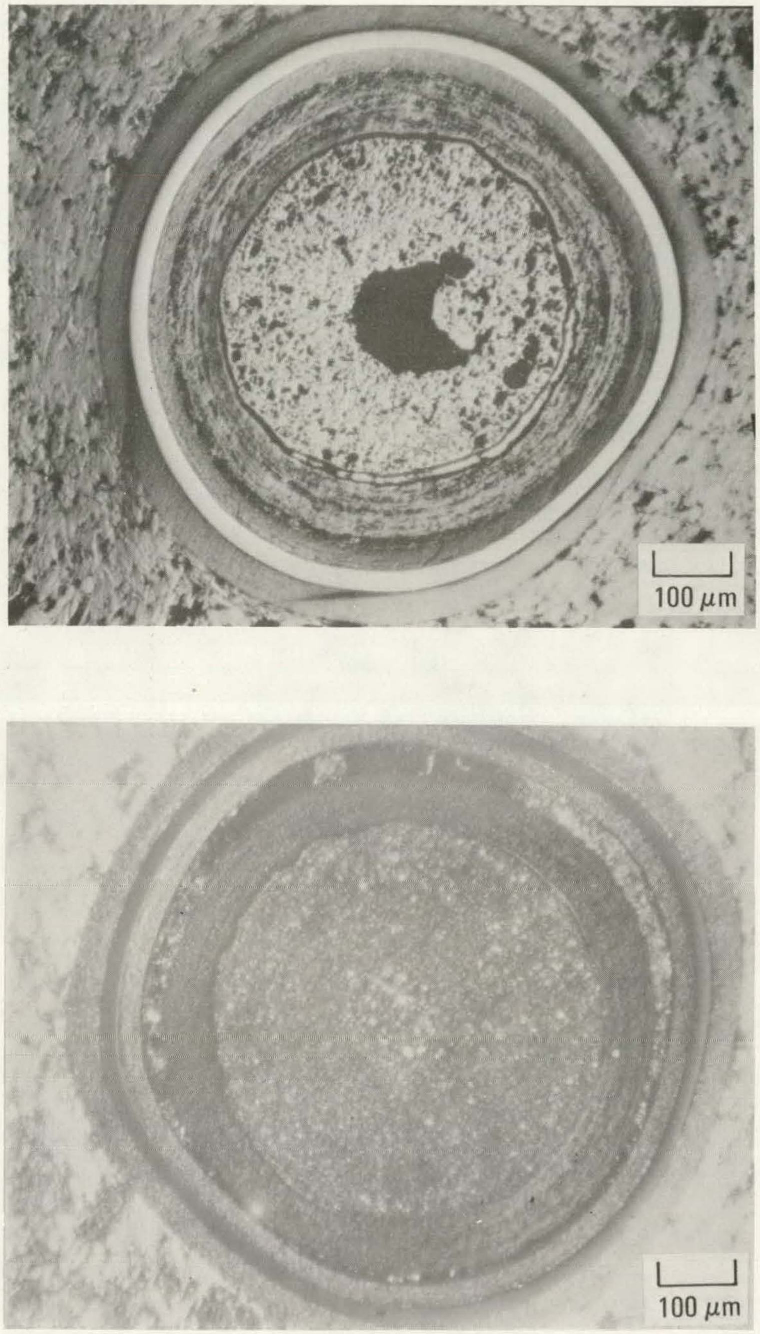

Fig. 5-51. Representative photomicrographs of TRISO $(8Th,U)O_2$ particles (MG 178) from type f' fuel rod 817 irradiated in capsule GF-3 (location 1-2) to a fast fluence of 7.7 x 10^{25} n/m^2 $(E > 29\ fJ)_{HTGR}$ and a burnup of 9.5% FIMA at 975°C

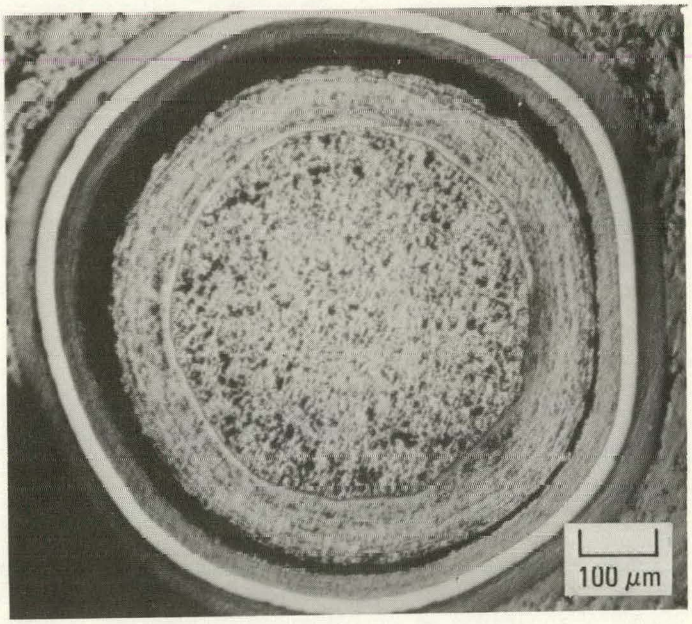

Fig. 5-52. Representative photomicrograph of TRISO $(8Th,U)O_2$ particles (MG 178) from type f' fuel rod 817 irradiated in capsule GF-3 (location 1-2) to a fast fluence of 7.7×10^{25} n/m^2 $(E > 29\ fJ)_{HTGR}$ and a burnup of 9.5% FIMA at 975°C

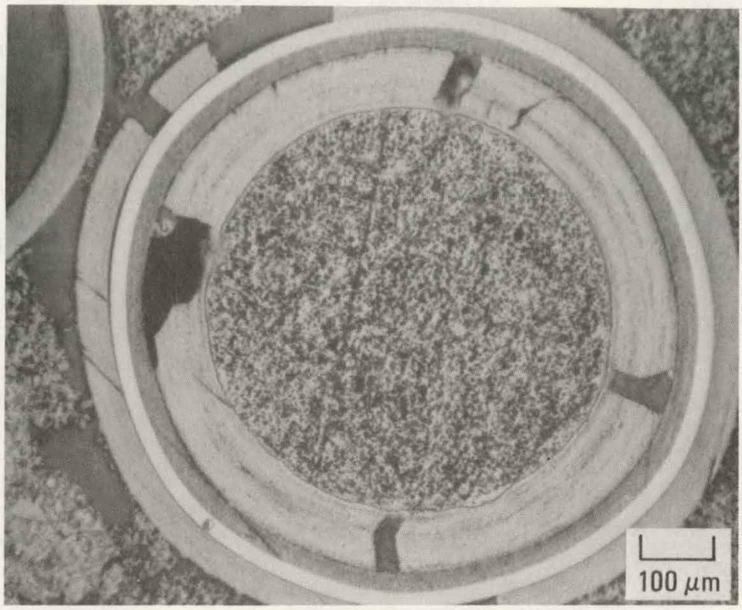

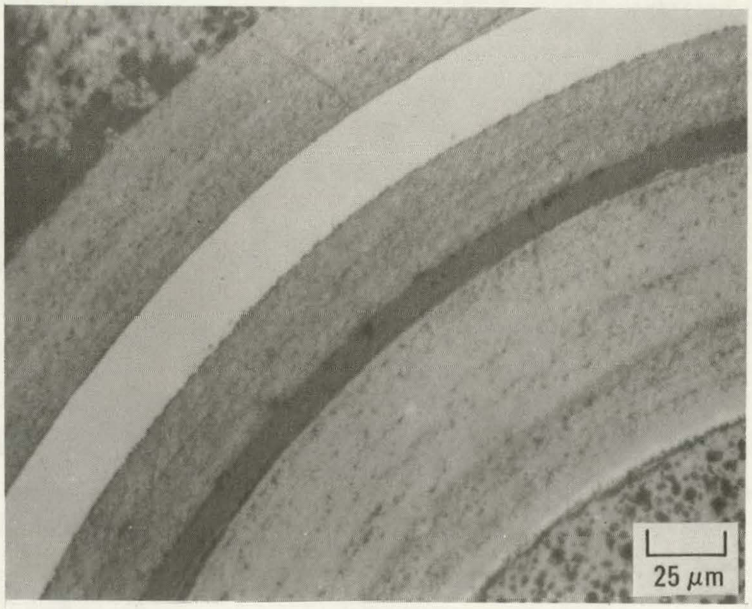

Fig. 5-53. Representative photomicrographs of TRISO $(8Th,U)O_2$ particles (6155-01-030) from type b fuel rod (7161-003-02-04) irradiated in capsule GF-3 (location 2-3) to a fast fluence of 9.4 x 10^{25} n/m^2 ($E > 29$ fJ)$_{HTGR}$ and a burnup of 11.4% FIMA at 975°C

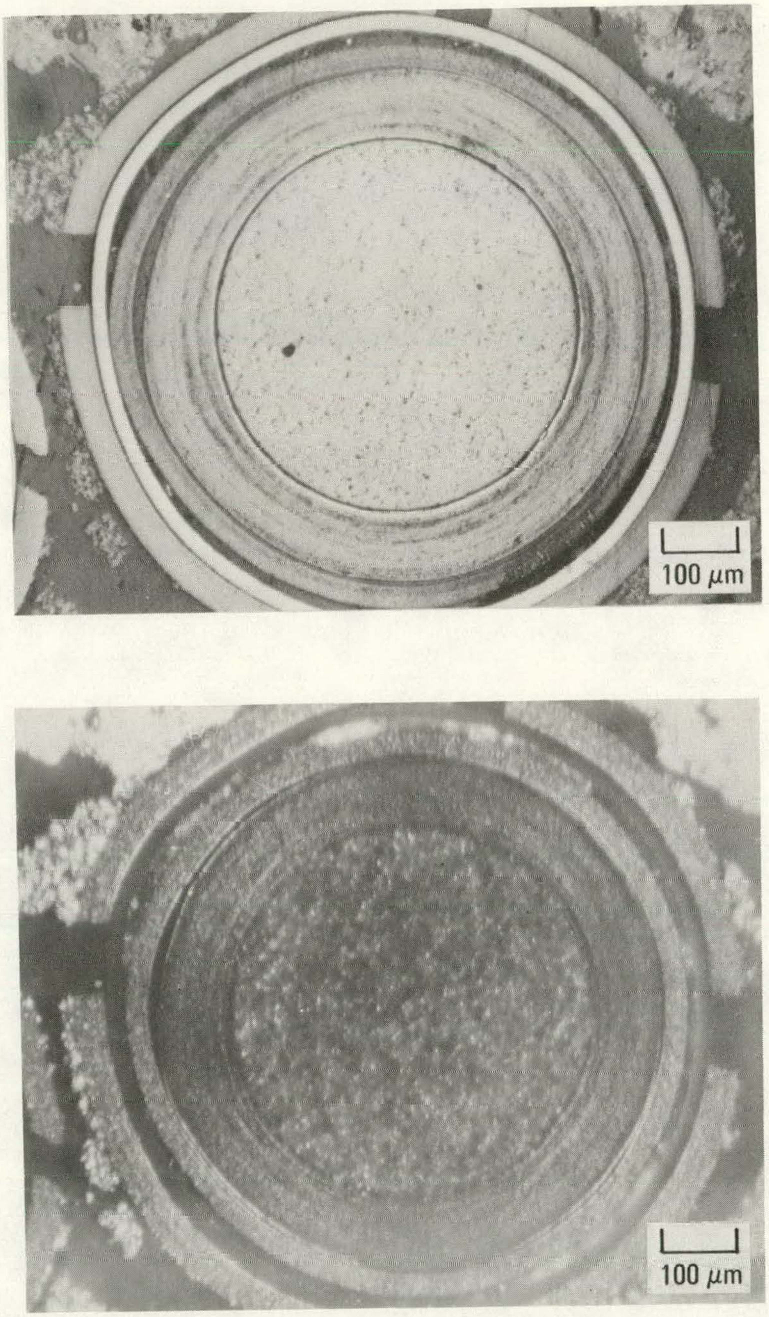

Fig. 5-54. Representative photomicrographs of TRISO $(8Th,U)O_2$ particles (6155-01-030) from type c fuel rod (7161-003-04-4) irradiated in capsule GF-3 (location 4-6) to a fast fluence of 6.0 x 10^{25} n/m^2 $(E > 29\ fJ)_{HTGR}$ and a burnup of 9.0% FIMA at 1120°C

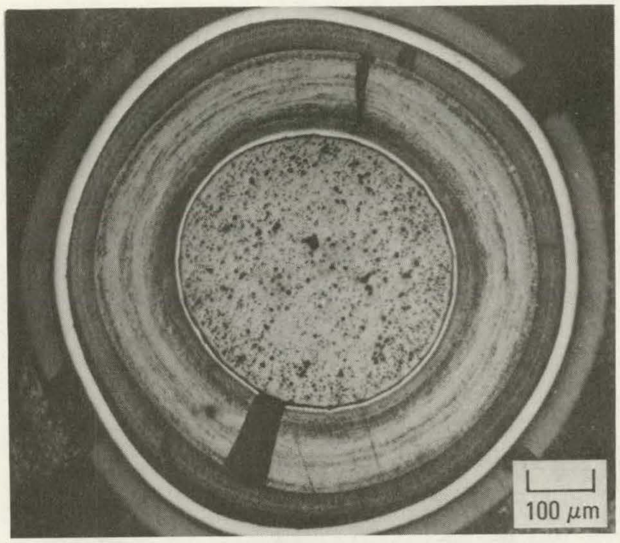

Fig. 5-55. Representative photomicrograph of TRISO (8Th,U)O_2 particles (6155-01-030) from type c fuel rod (7161-003-04-4) irradiated in capsule GF-3 (location 4-6) to a fast fluence of 6.0 x 10^{25} n/m^2 (E > 29 fJ)$_{HTGR}$ and a burnup of 9.0% FIMA at 1120°C

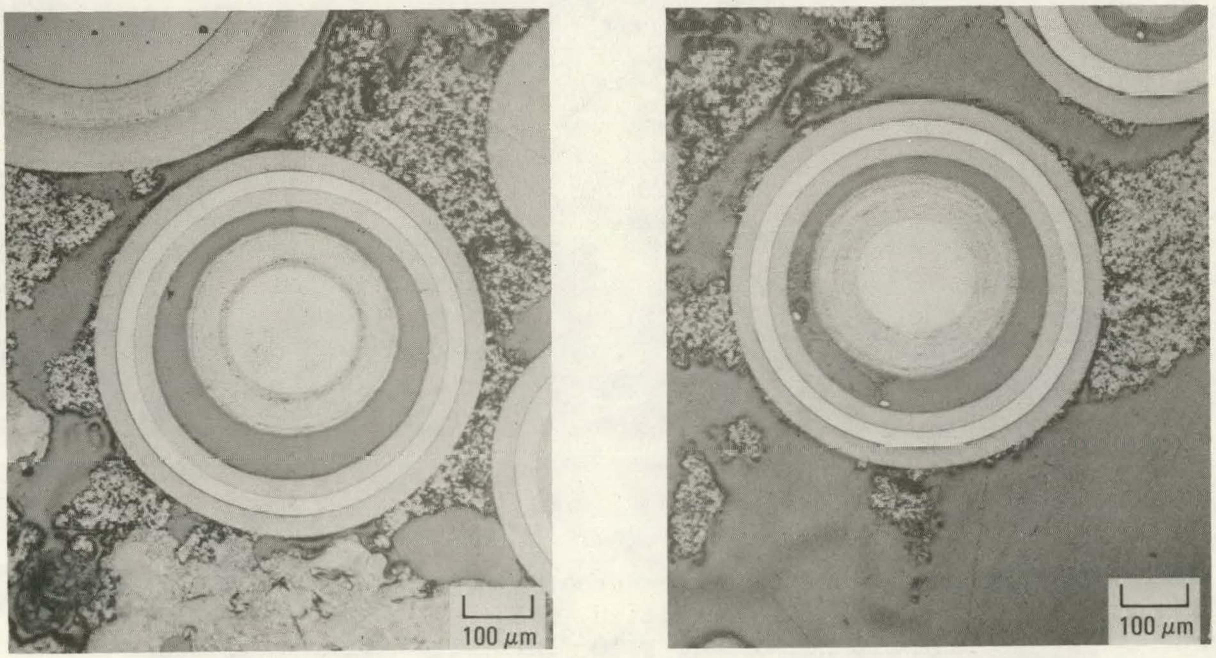

Fig. 5-56. Representative photomicrographs of TRISO inert particles (6351-01-020) from type b' fuel rod (7161-003-03-5) irradiated in capsule GF-1 (location 3-6) to a fast fluence of 6.1 x 10^{25} n/m^2 (E > 29 fJ)$_{HTGR}$ and a burnup of 9.4% FIMA at 1170°C

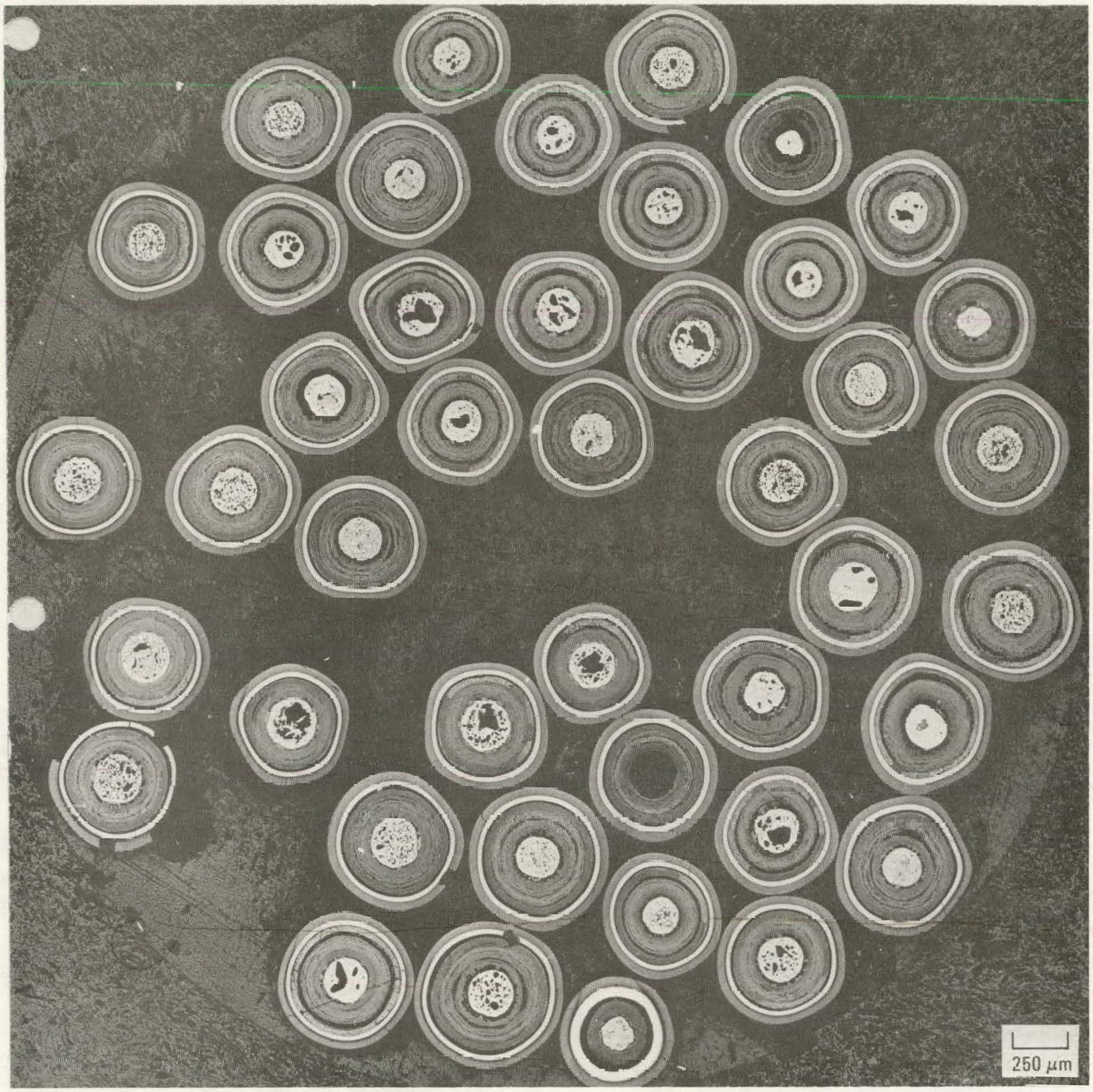

Fig. 5-57. Representative photomicrograph of unbonded TRISO UC_2 particles (6151-00-010) irradiated in capsule GF-1 (planchet 6) to a fast fluence of 2.7×10^{25} n/m^2 ($E > 29$ fJ)$_{HTGR}$ and a burnup of 50% FIMA at 1095°C

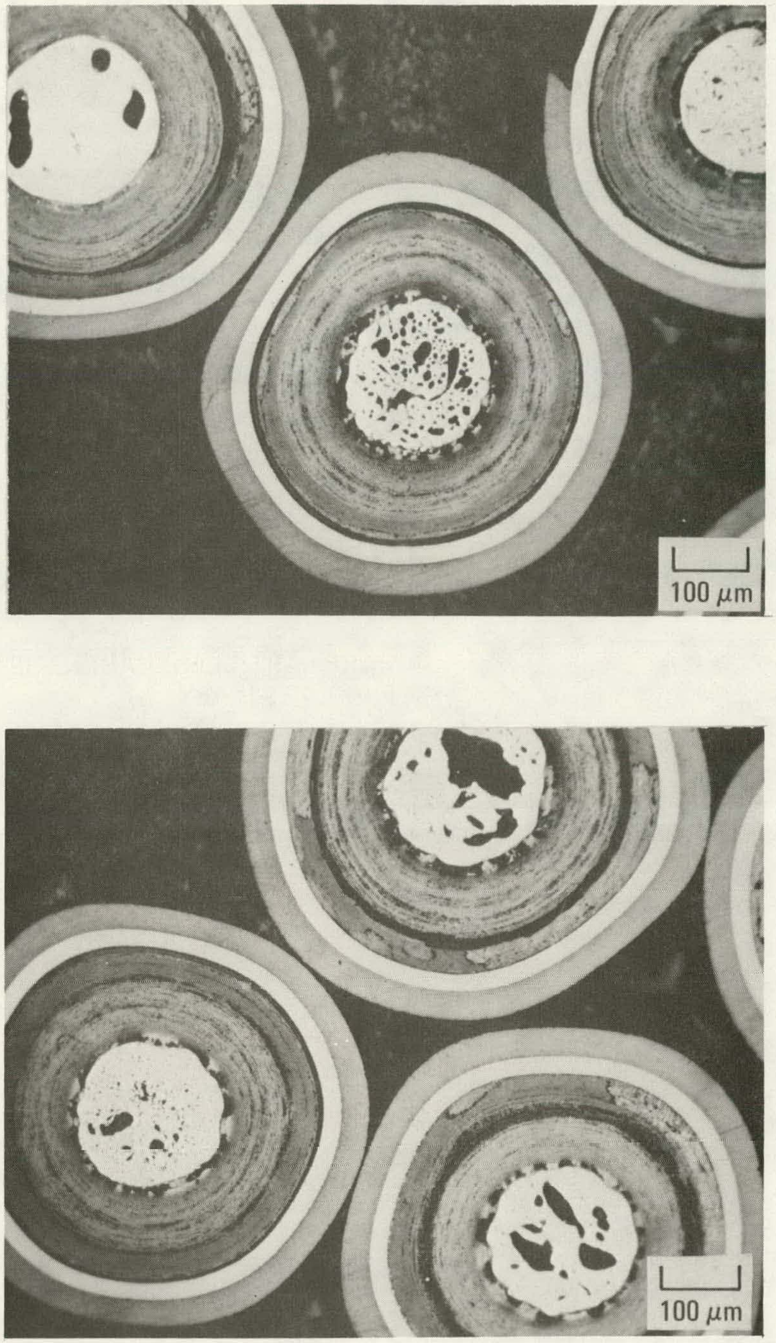

Fig. 5-58. Representative photomicrographs of unbonded TRISO UC_2 particles (6151-00-010) irradiated in capsule CF-1 (planchet 6) to a fast fluence of 2.7×10^{25} n/m^2 $(E > 29\ fJ)_{HTGR}$ and a burnup of 50% FIMA at 1095°C

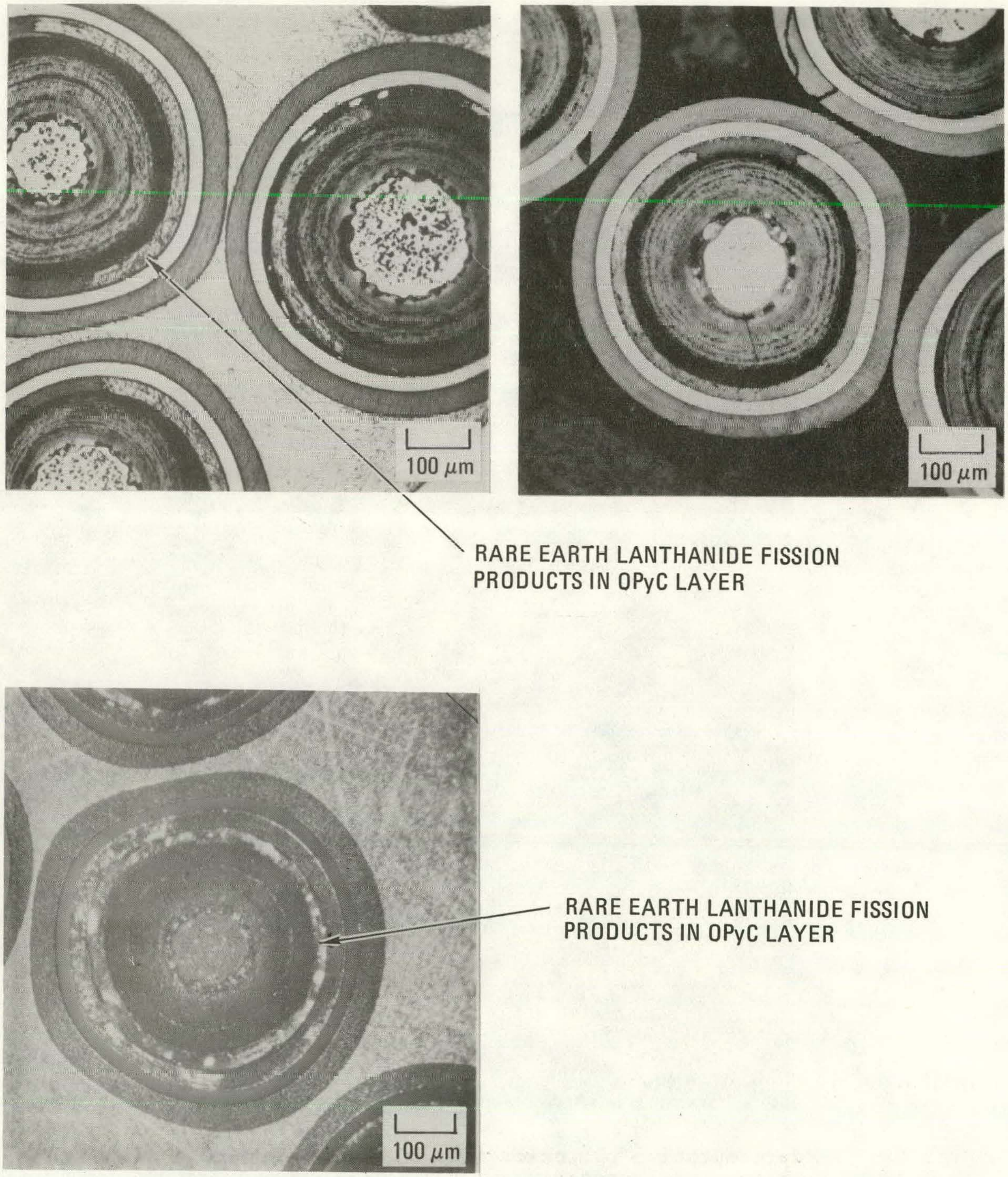

Fig. 5-59. Representative photomicrographs of unbonded TRISO UC_2 particles (6151-00-010) irradiated in capsule GF-1 (planchet 6) to a fast fluence of $2.7 \times 10^{25} \times n/m^2$ $(E > 29\ fJ)_{HTGR}$ and a burnup of 50% FIMA at 1095°C: (a) bright field and (b) polarized light

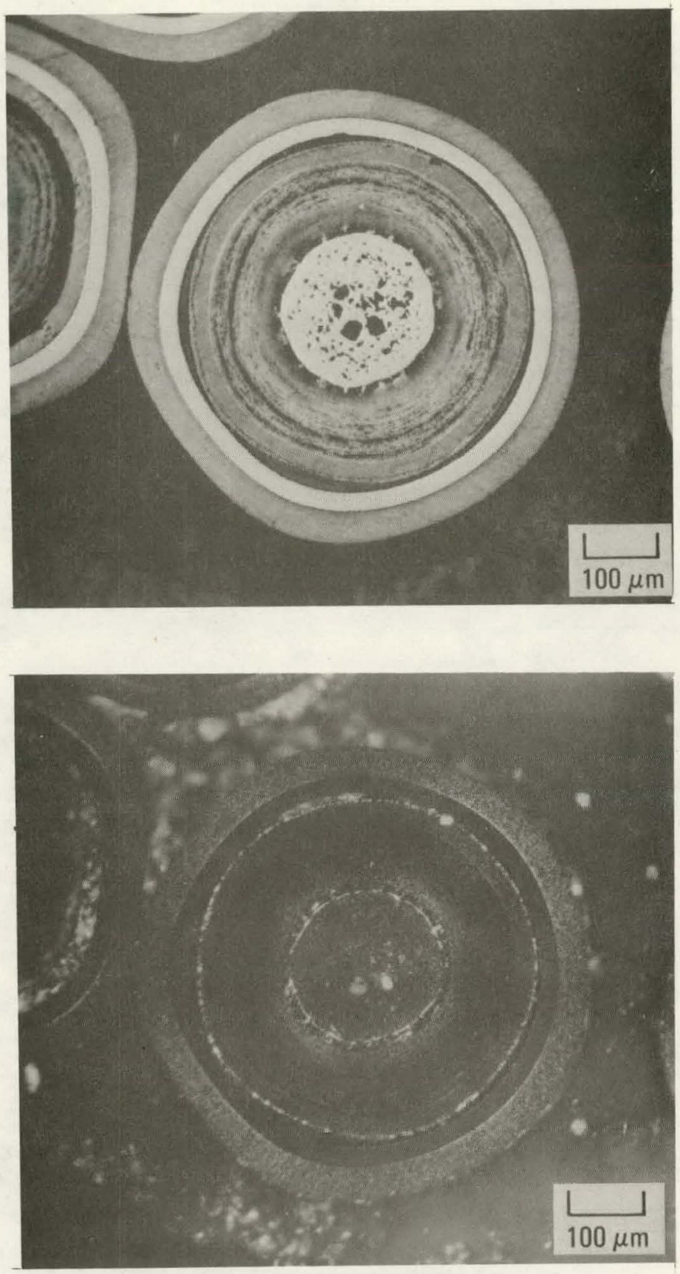

Fig. 5-60. Representative photomicrographs of unbonded TRISO UC_2 particles (6151-00-010) irradiated in capsule GF-1 (planchet 6) to a fast fluence of 2.7×10^{25} n/m^2 ($E > 29$ fJ)$_{HTGR}$ and a burnup of 50% FIMA at 1095°C

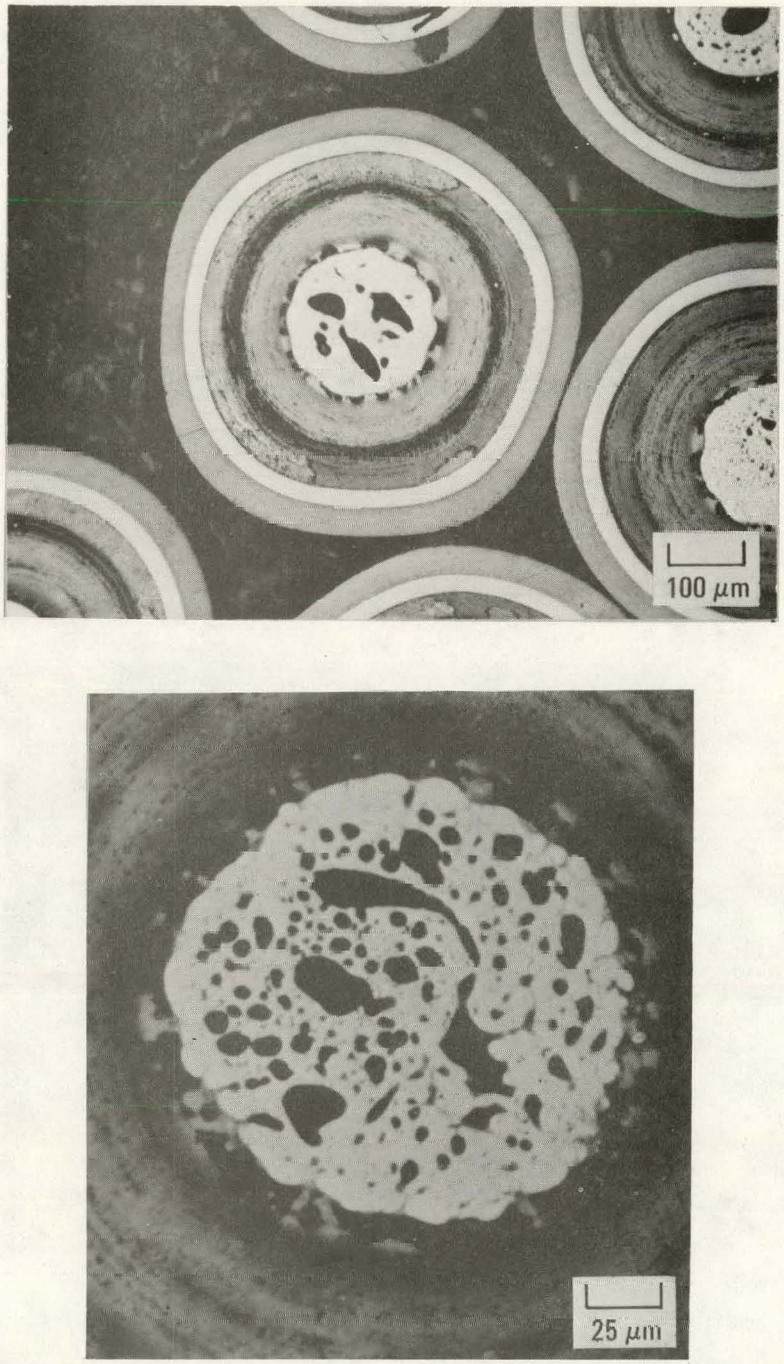

Fig. 5-61. Representative photomicrographs of unbonded TRISO UC_2 particles (6151-00-010) irradiated in capsule GF-1 (planchet 6) to a fast fluence of 2.7×10^{25} n/m^2 $(E > 29\ fJ)_{HTGR}$ and a burnup of 50% FIMA at 1095°C

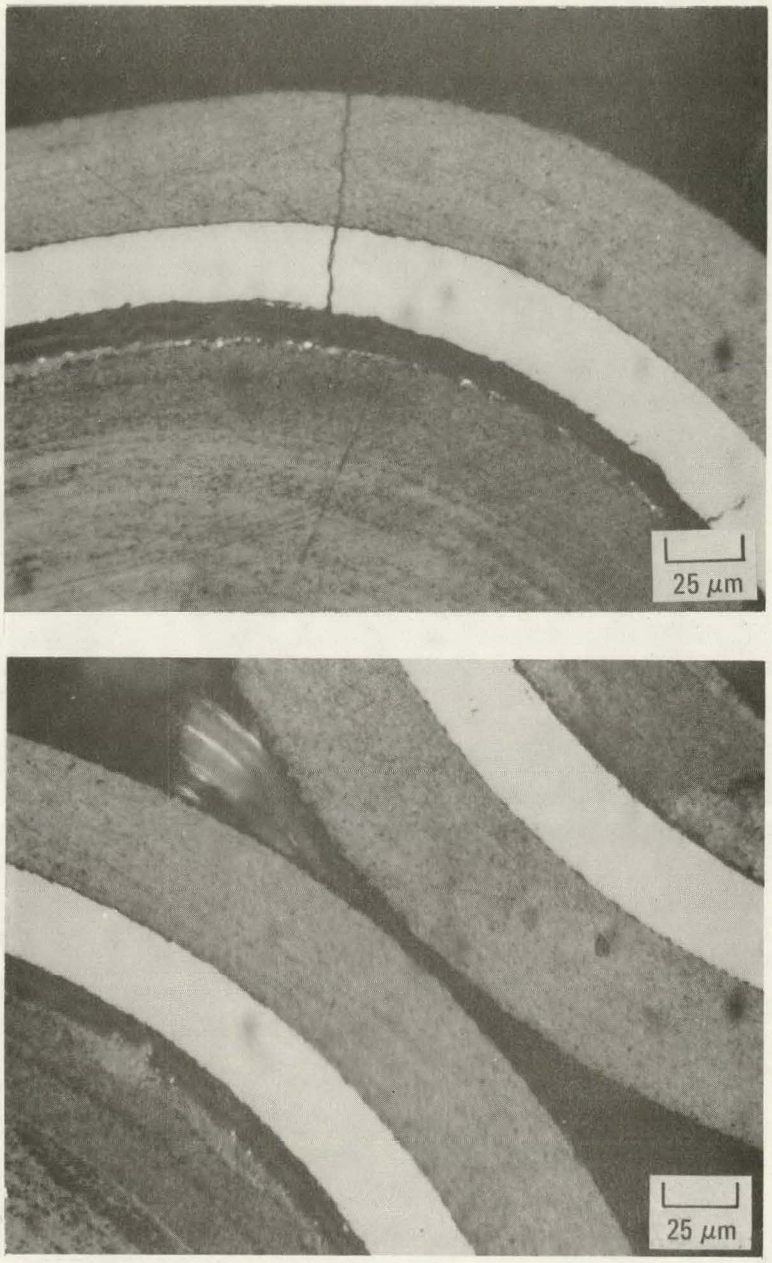

Fig. 5-62. Representative photomicrographs of unbonded TRISO UC_2 particles (6151-00-010) irradiated in capsule GF-1 (planchet 6) to a fast fluence of 2.7×10^{25} n/m^2 $(E > 29\ fJ)_{HTGR}$ and a burnup of 50% FIMA at 1095°C

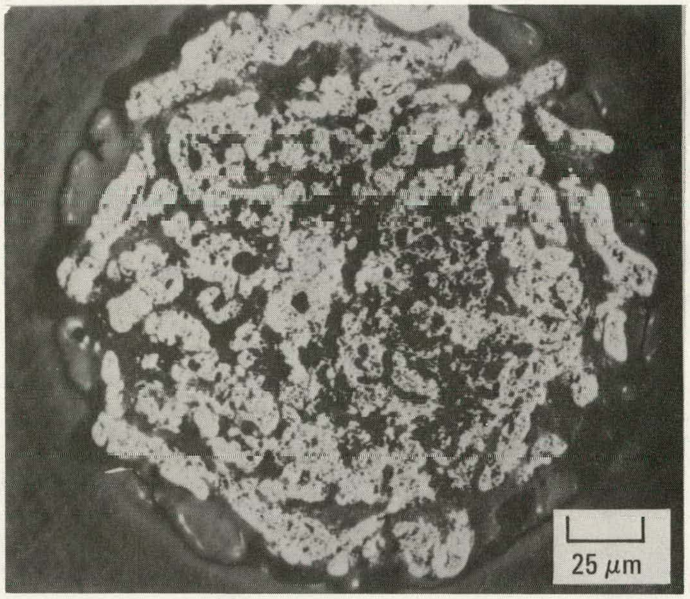

Fig. 5-63. Representative photomicrograph of unbonded TRISO UC_2 particles (6151-00-010) irradiated in capsule GF-3 (planchet 40, cell 3) at a fast fluence of 9.2×10^{25} n/m^2 (E > 29 fJ)$_{HTGR}$ and a burnup of 70% FIMA at 1000°C

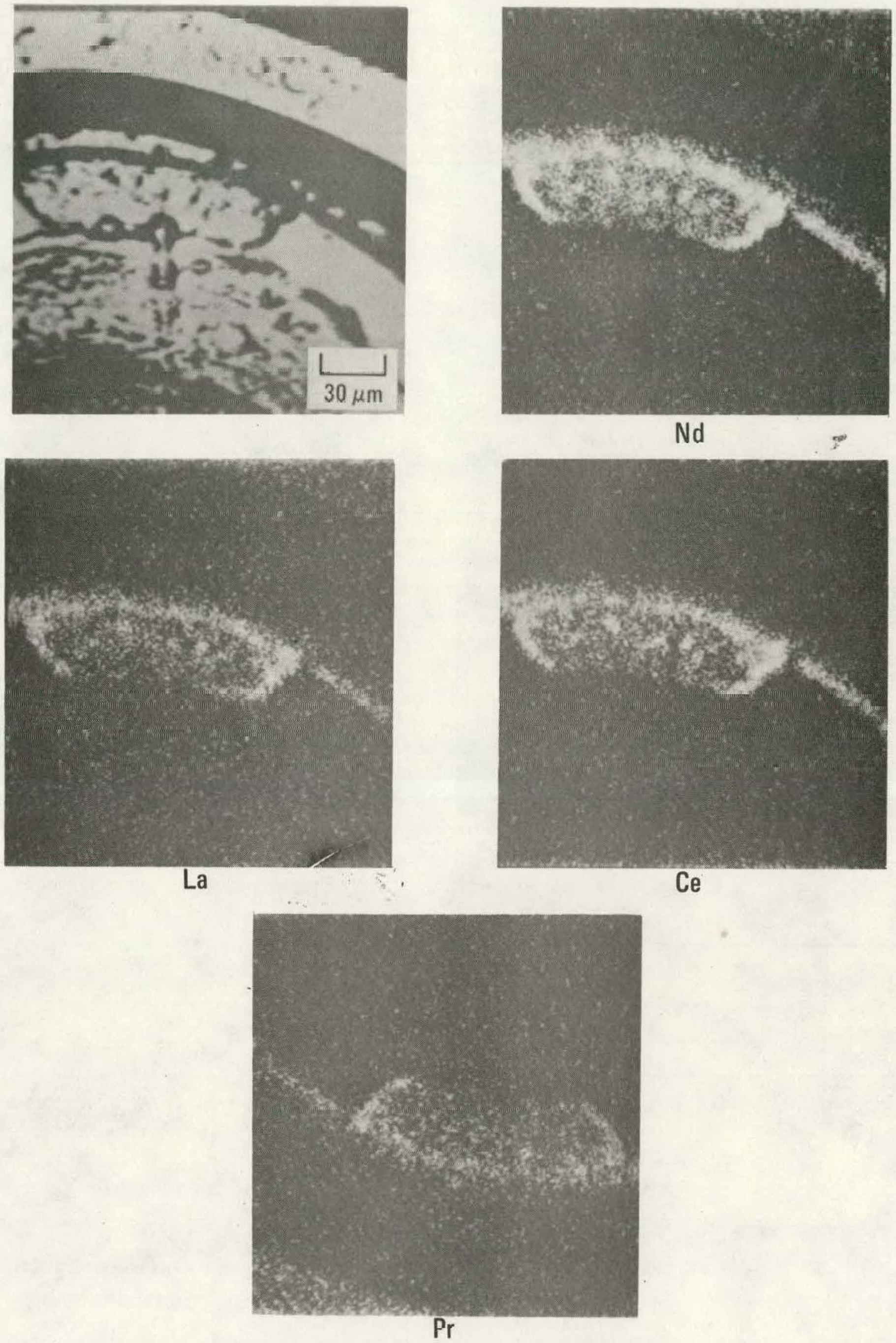

Nd

La

Ce

Pr

Fig. 5-64. Back-scattering electron image defining Nd, La, Ce, and Pr distributions in TRISO-coated UC_2 (6151-00-010) irradiated in capsule GF-1 (planchet 40) to a fast fluence of 3.6×10^{25} n/m^2 $(E > fJ)_{HTGR}$ and a burnup of 55% FIMA at 1095°C.

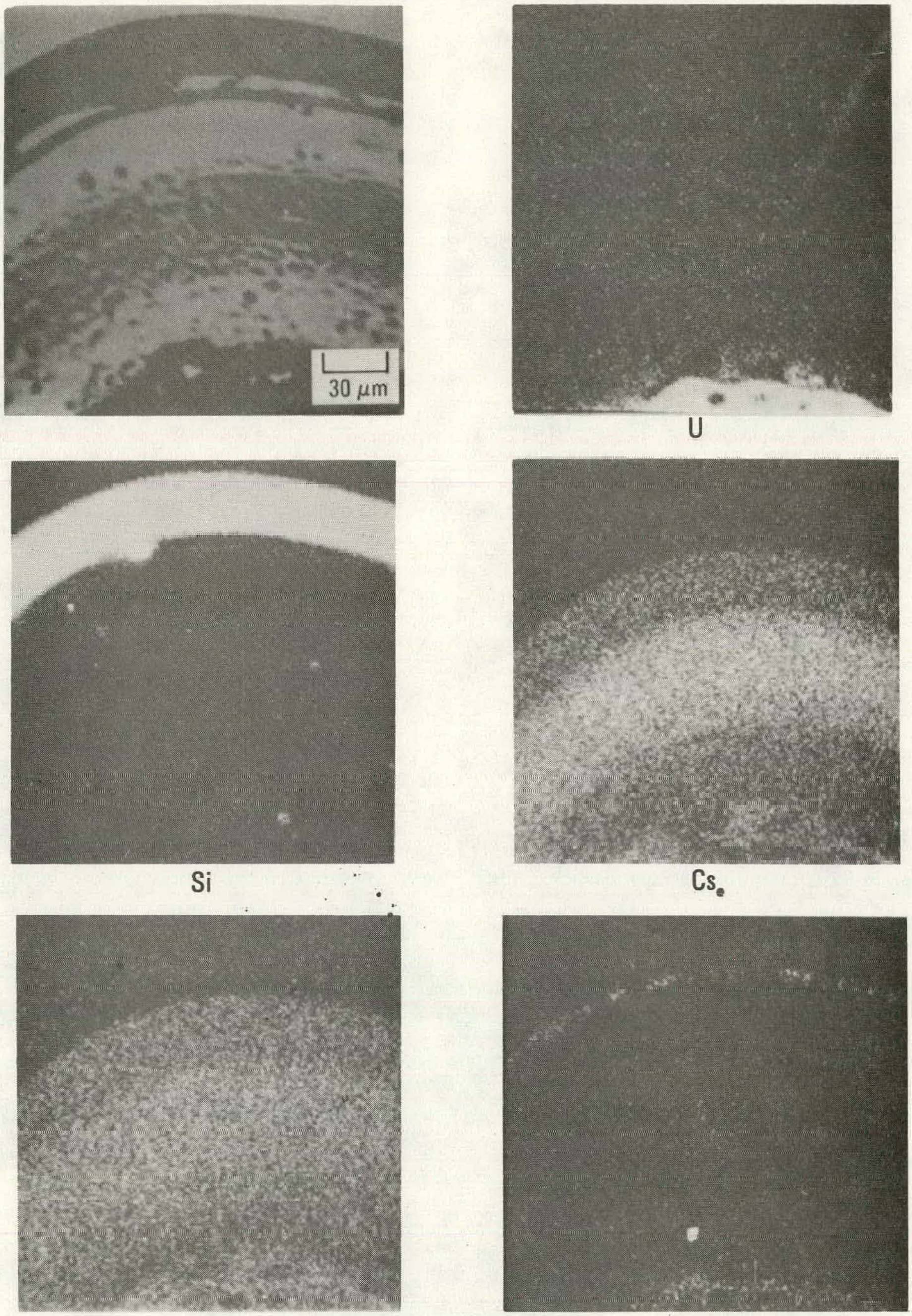

U

Si

Cs_e

Ba

Pd

Fig. 5-65. Back-scattering electron image defining U, Si, Cs, Ba, and Pd distributions in TRISO-coated UC_2 (6151-00-010) irradiated in capsule GF-1 (planchet 40) to a fast fluence of 3.6×10^{25} n/m^2 $(E > 29\ fJ)_{HTGR}$ and a burnup of 55% FIMA at 1095°C.

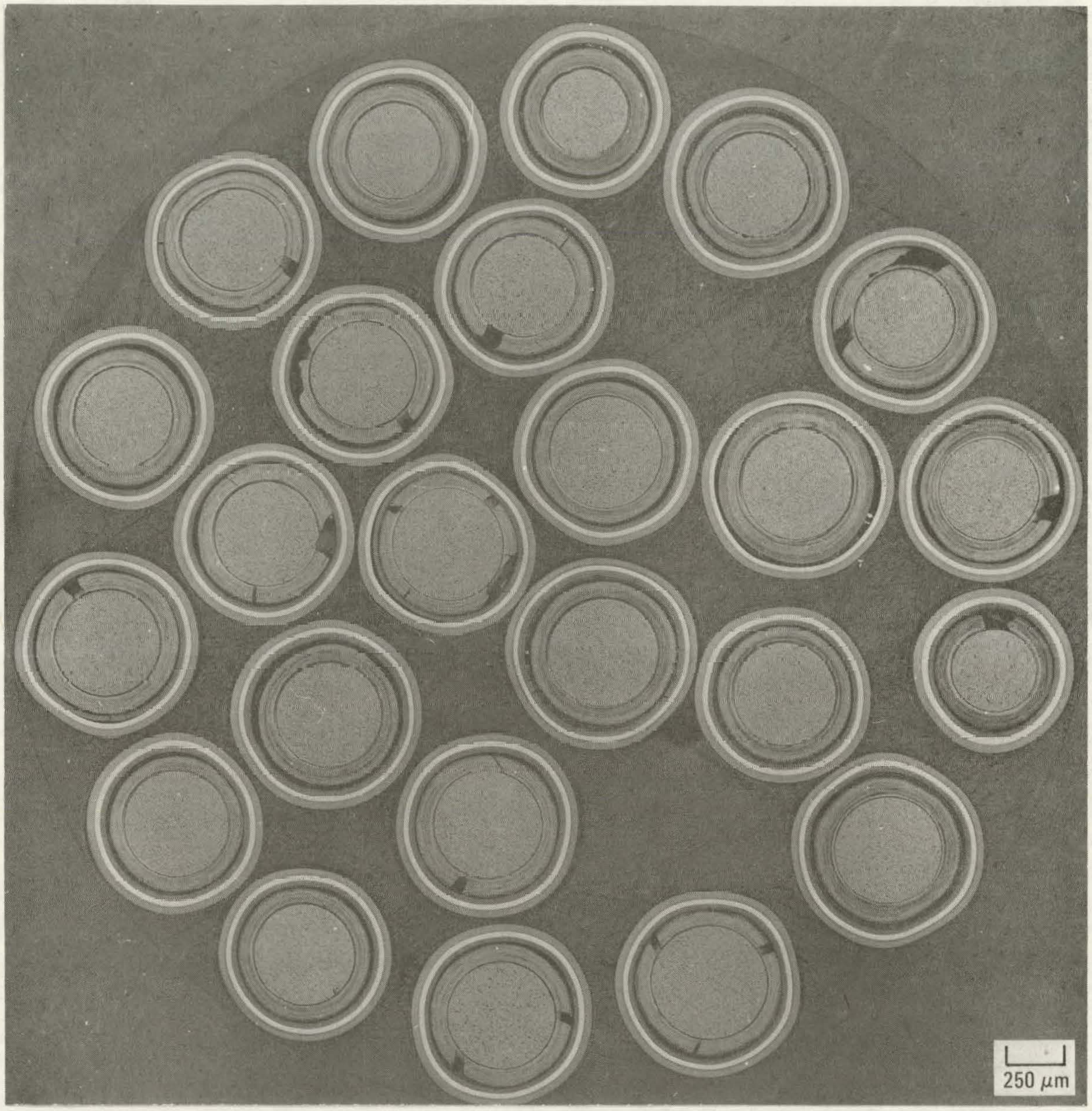

Fig. 5-66. Representative photomicrographs of unbonded TRISO $(8Th,U)O_2$ particles (6155-01-020) irradiated in capsule GF-1 (planchet 18) to a fast fluence of 3.0×10^{25} n/m^2 (E > 29 fJ)$_{HGTR}$ and a burnup of 7.1% FIMA at 1095°C

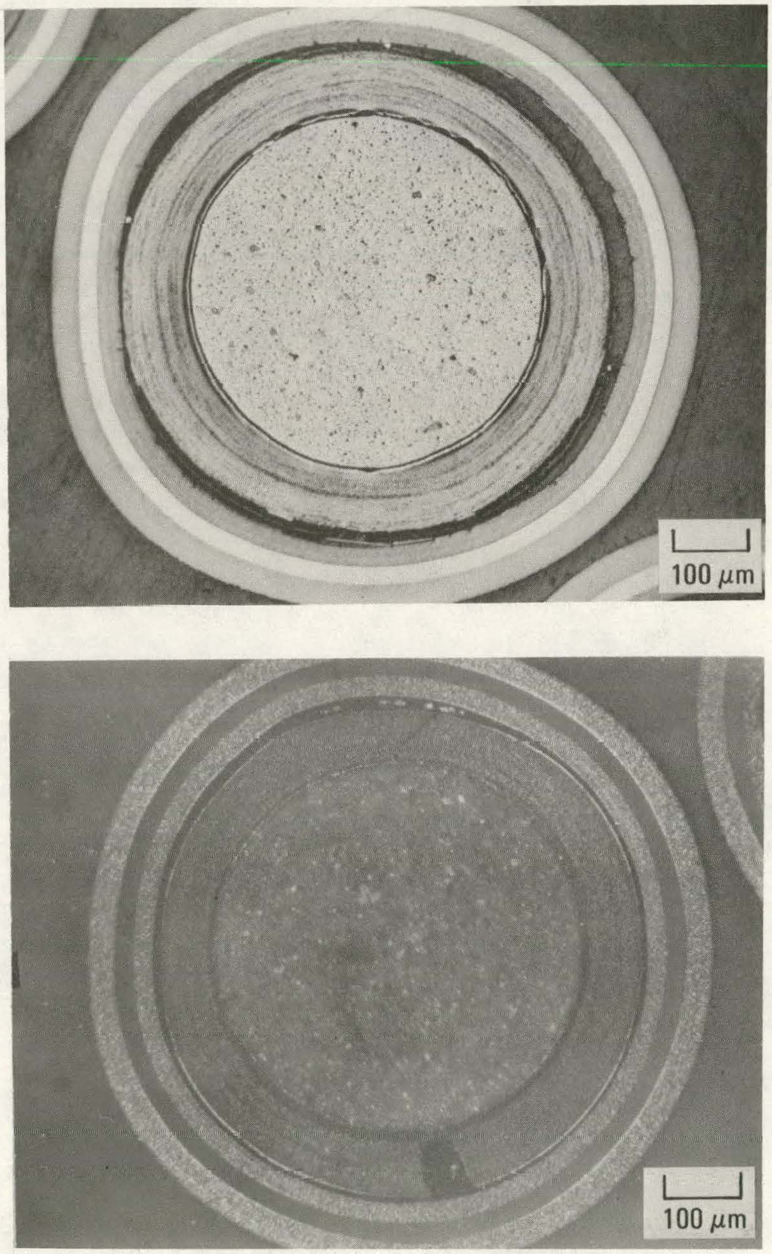

Fig. 5-67. Representative photomicrographs of unbonded TRISO $(8Th,U)O_2$ particles (6155-01-020) irradiated in capsule GF-1 (planchet 18) to a fast fluence of 3.0×10^{25} $(E > 29\ fJ)_{HTGR}$ and a burnup of 7.1% FIMA at 1095°C

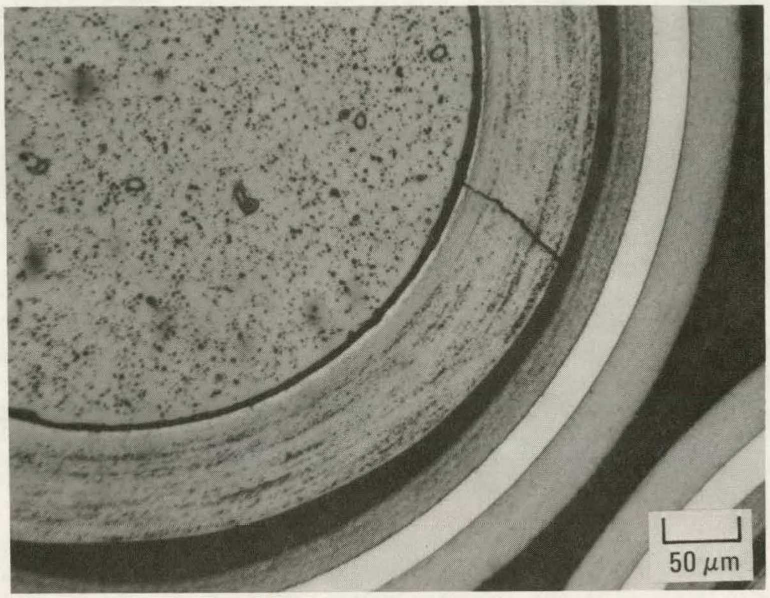

Fig. 5-68. Representative photomicrograph of unbonded TRISO $(8Th,U)O_2$ particle (6155-01-020) irradiated in capsule GF-1 (planchet 18) to a fast fluence of 3.0 x 10^{25} n/m^2 $(E > 29\ fJ)_{HTGR}$ and a burnup of 7.1% FIMA at 1095°C

Fig. 5-69. Representative photomicrograph of unbonded BISO $(8Th,U)O_2$ particles (6445-00-010) irradiated in capsule GF-3 (cell 3) to a fast fluence of 9.0×10^{25} n/m^2 $(E > 29\ fJ)_{HTGR}$ and a burnup of 11% FIMA at 1000°C

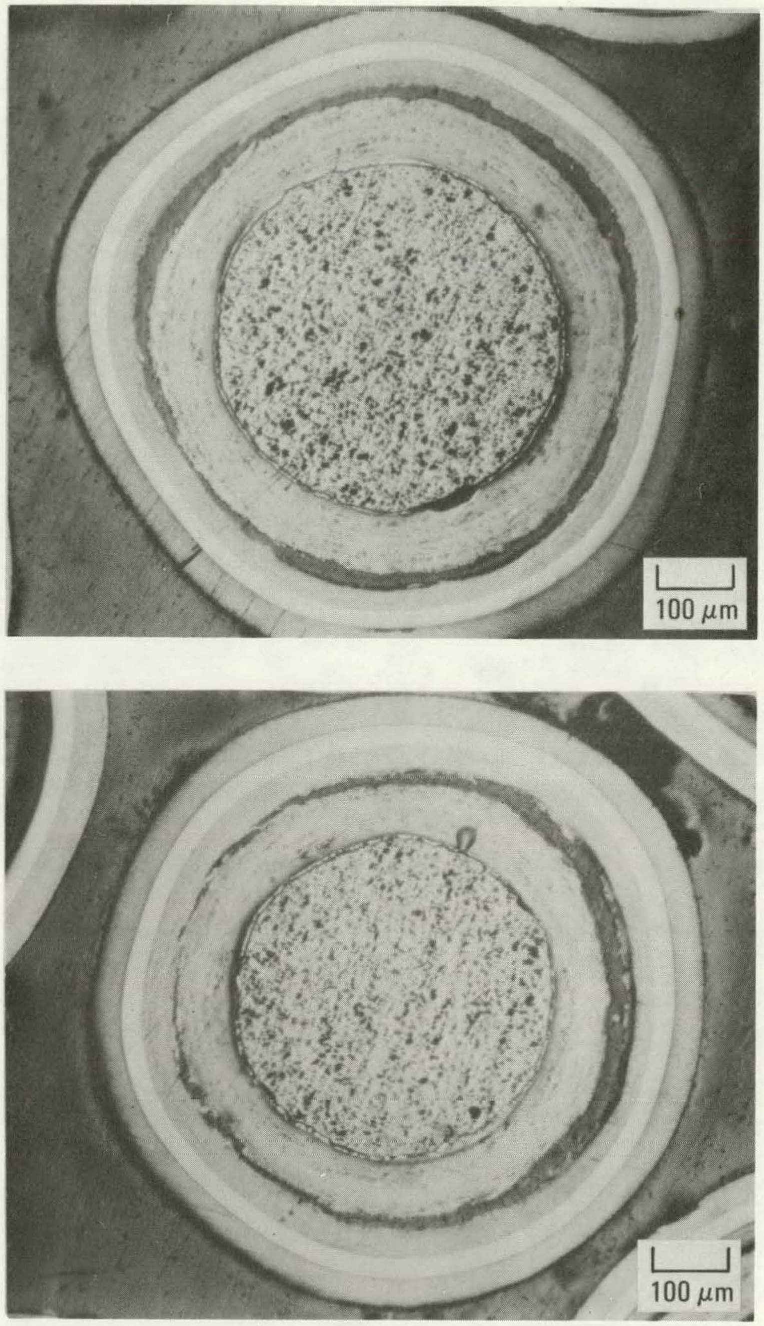

Fig. 5-70. Representative photomicrographs of unbonded TRISO (8Th,U)O_2 particles (MG 178) irradiated in capsule GF-3 (cell 3) to a fast fluence of 9.2×10^{25} n/m^2 (E > 29 fJ)$_{HTGR}$ and a burnup of 11% FIMA at 1000°C

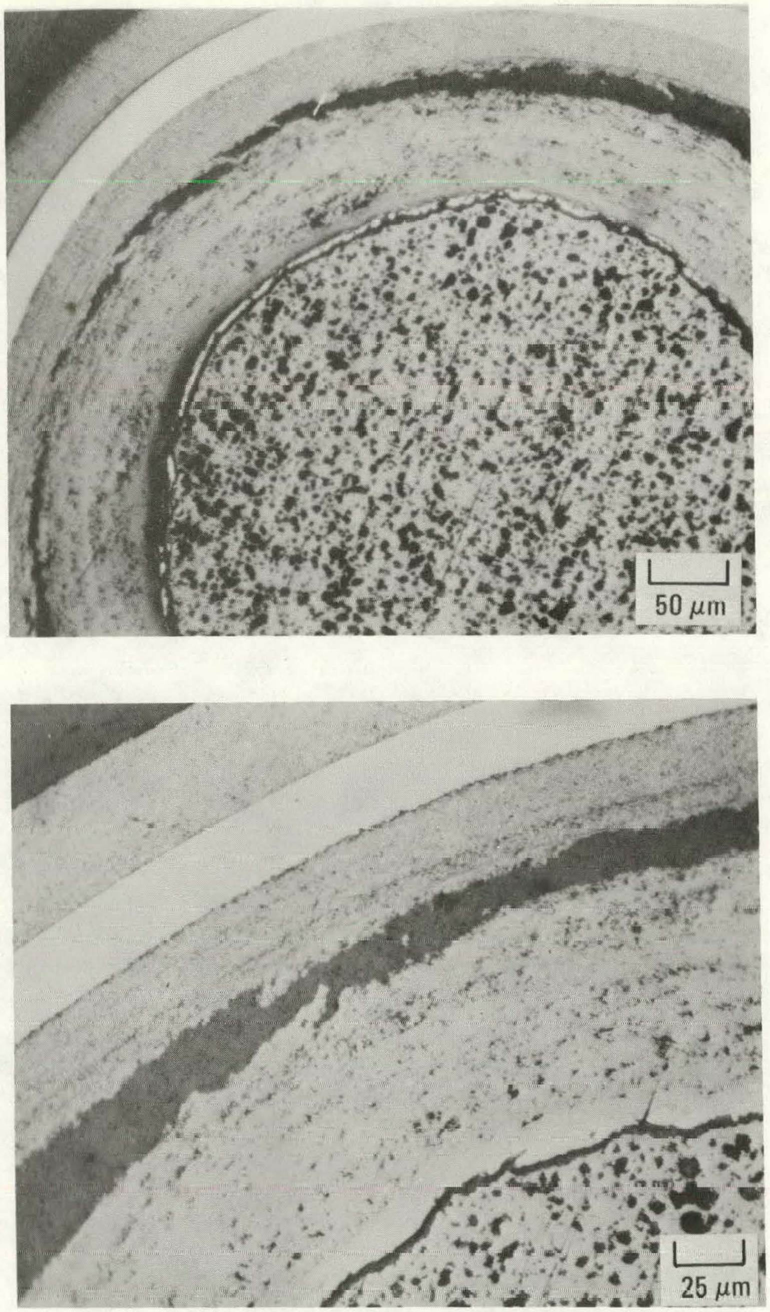

Fig. 5-71. Representative photomicrographs of unbonded TRISO $(8Th,U)O_2$ particles (MG 178) irradiated in capsule GF-3 (cell 3) to a fast fluence of 9.2×10^{25} n/m^2 $(E > 29\ fJ)_{HTGR}$ and a burnup of 11% FIMA at 1000°C

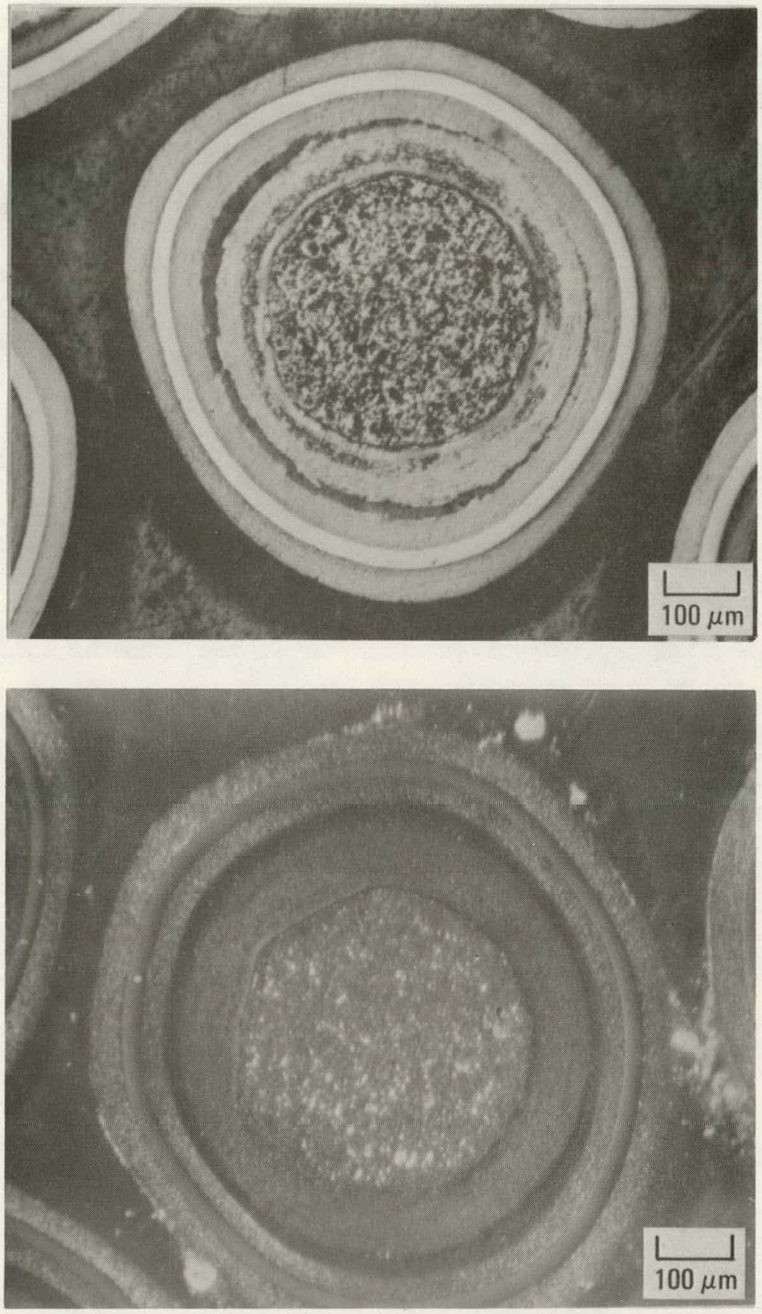

Fig. 5-72. Representative photomicrographs of unbonded TRISO $(8Th,U)O_2$ particles (MG 199) irradiated in capsule GF-3 (cell 3) to a fast fluence of 9.0×10^{25} n/m^2 $(E > 29\ fJ)_{HTGR}$ and a burnup of 11% FIMA at 1000°C

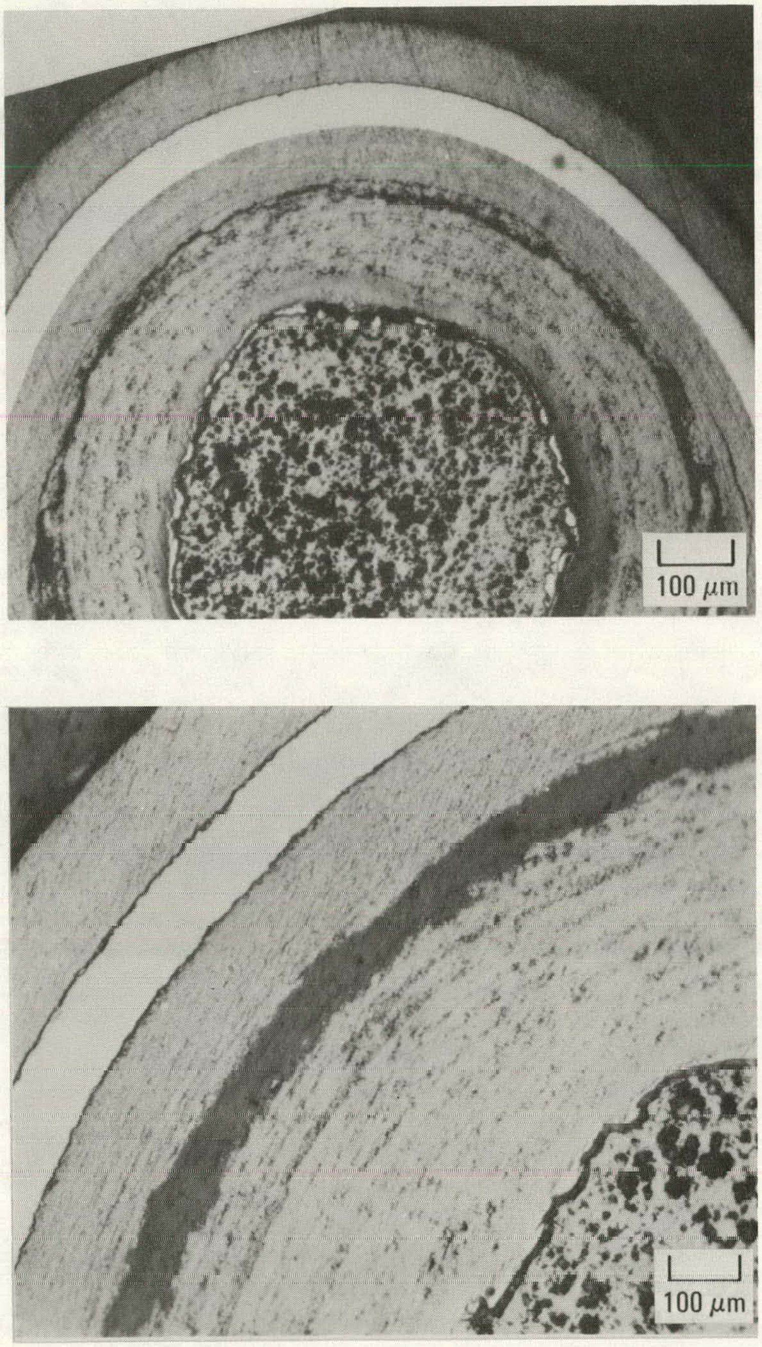

Fig. 5-73. Representative photomicrographs of unbonded TRISO (8Th,U)O_2 particles (MG 199) irradiated in capsule GF-3 (cell 3) to a fast fluence of 9.0×10^{25} n/m^2 $(E > 29\ fJ)_{HTGR}$ and a burnup of 11% FIMA at 1000°C

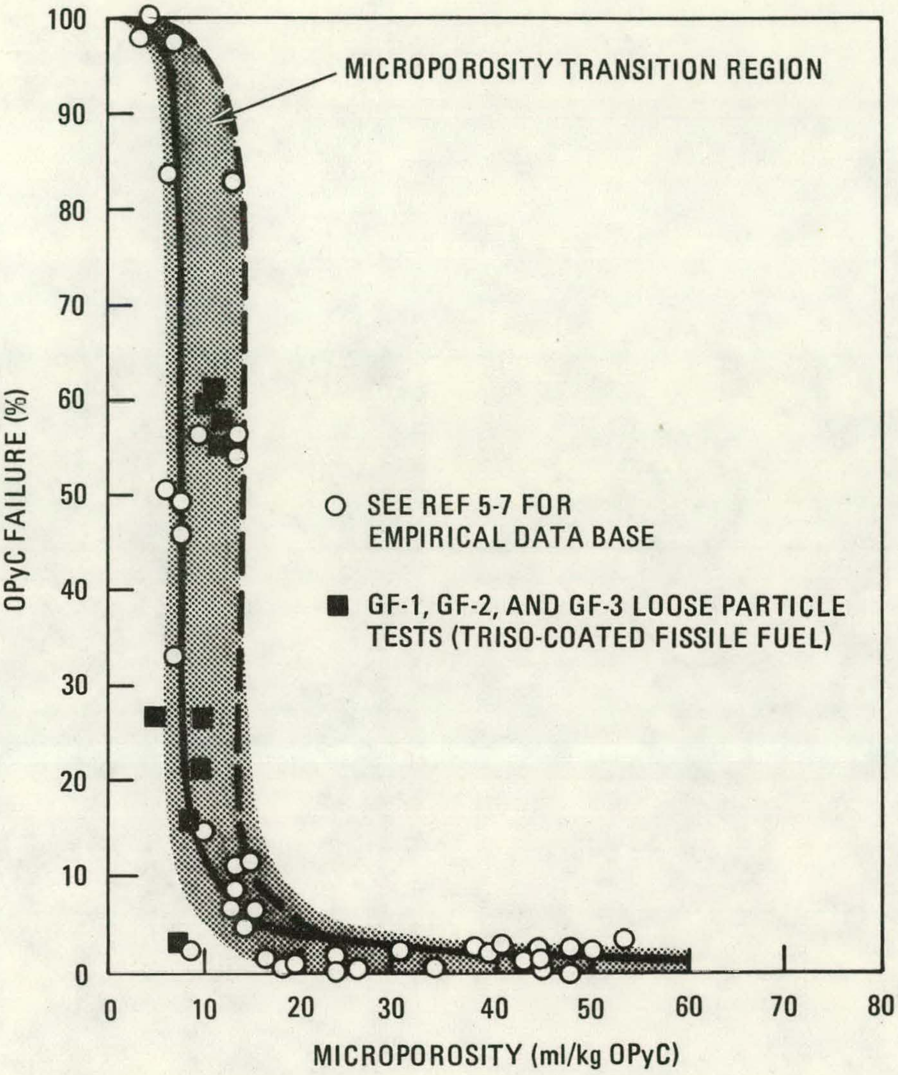

Fig. 5-74. Comparative evaluation of OPyC failure versus microporosity for GF-1, GF-2, and GF-3 loose particle tests and irradiation data base

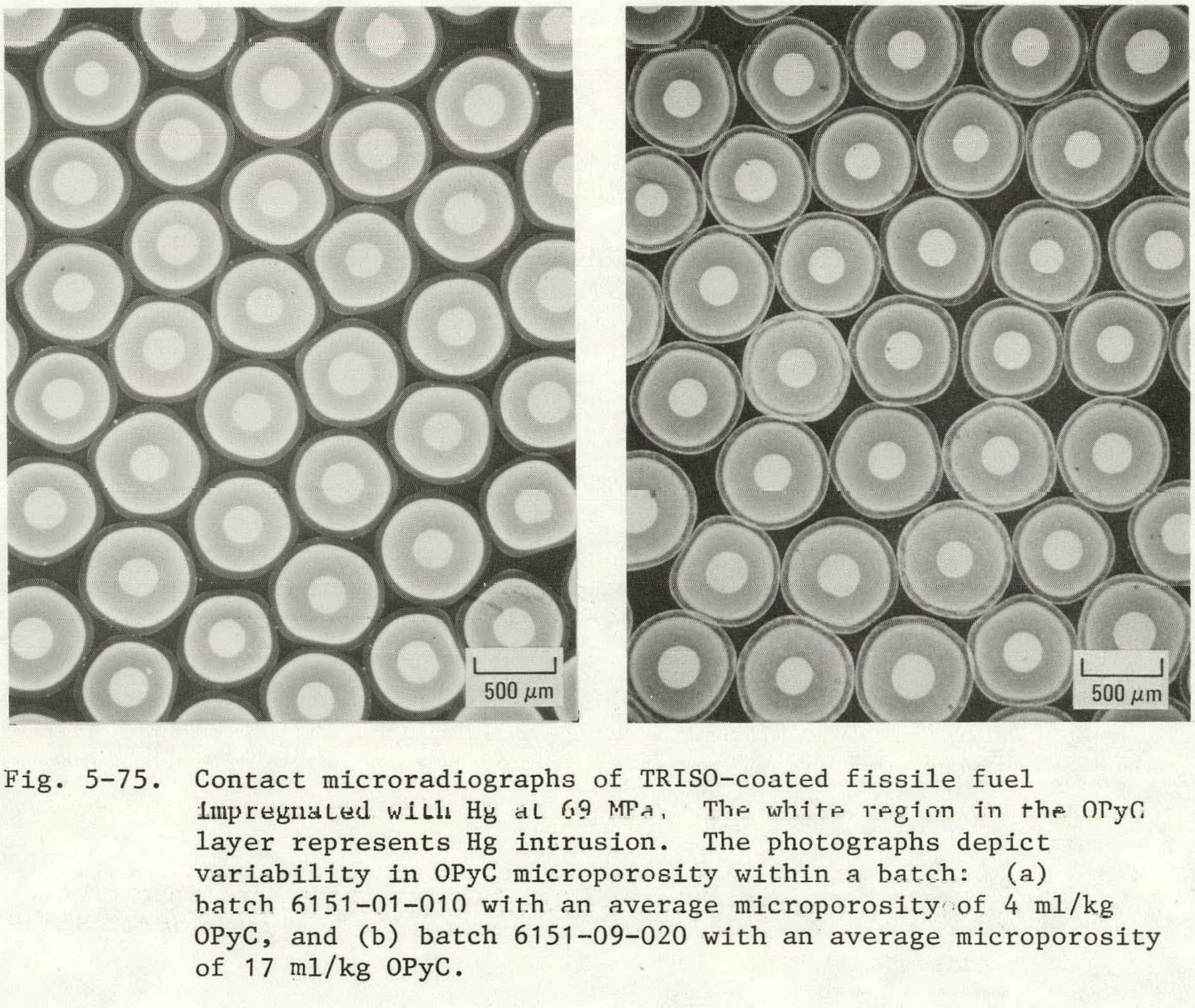

Fig. 5-75. Contact microradiographs of TRISO-coated fissile fuel impregnated with Hg at 69 MPa. The white region in the OPyC layer represents Hg intrusion. The photographs depict variability in OPyC microporosity within a batch: (a) batch 6151-01-010 with an average microporosity of 4 ml/kg OPyC, and (b) batch 6151-09-020 with an average microporosity of 17 ml/kg OPyC.

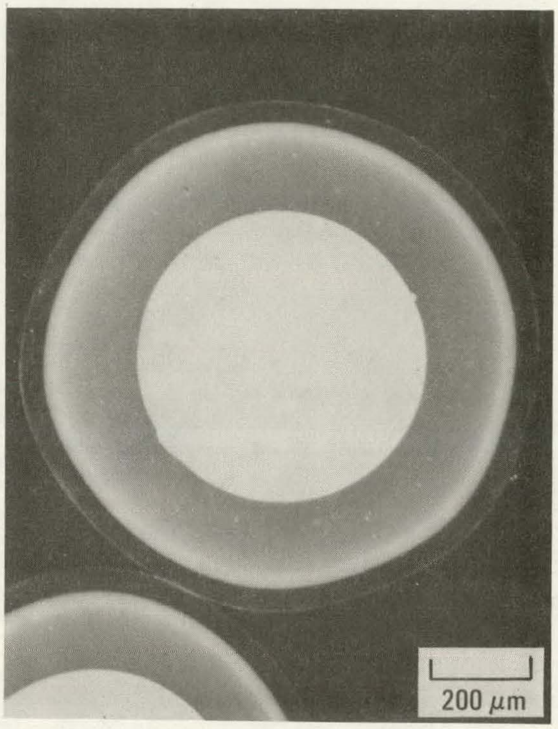

Fig. 5-76. Contact microradiograph of a TRISO-coated fissile particle from batch 6155-01-020. The particle was subjected to Hg intrusion at 69 MPa and shows the minimum degree of acceptable Hg intrusion into an OPyC layer ($\lesssim$9% of OPyC thickness). Average measured OPyC microporosity for this batch is 9.3 ml/kg OPyC.

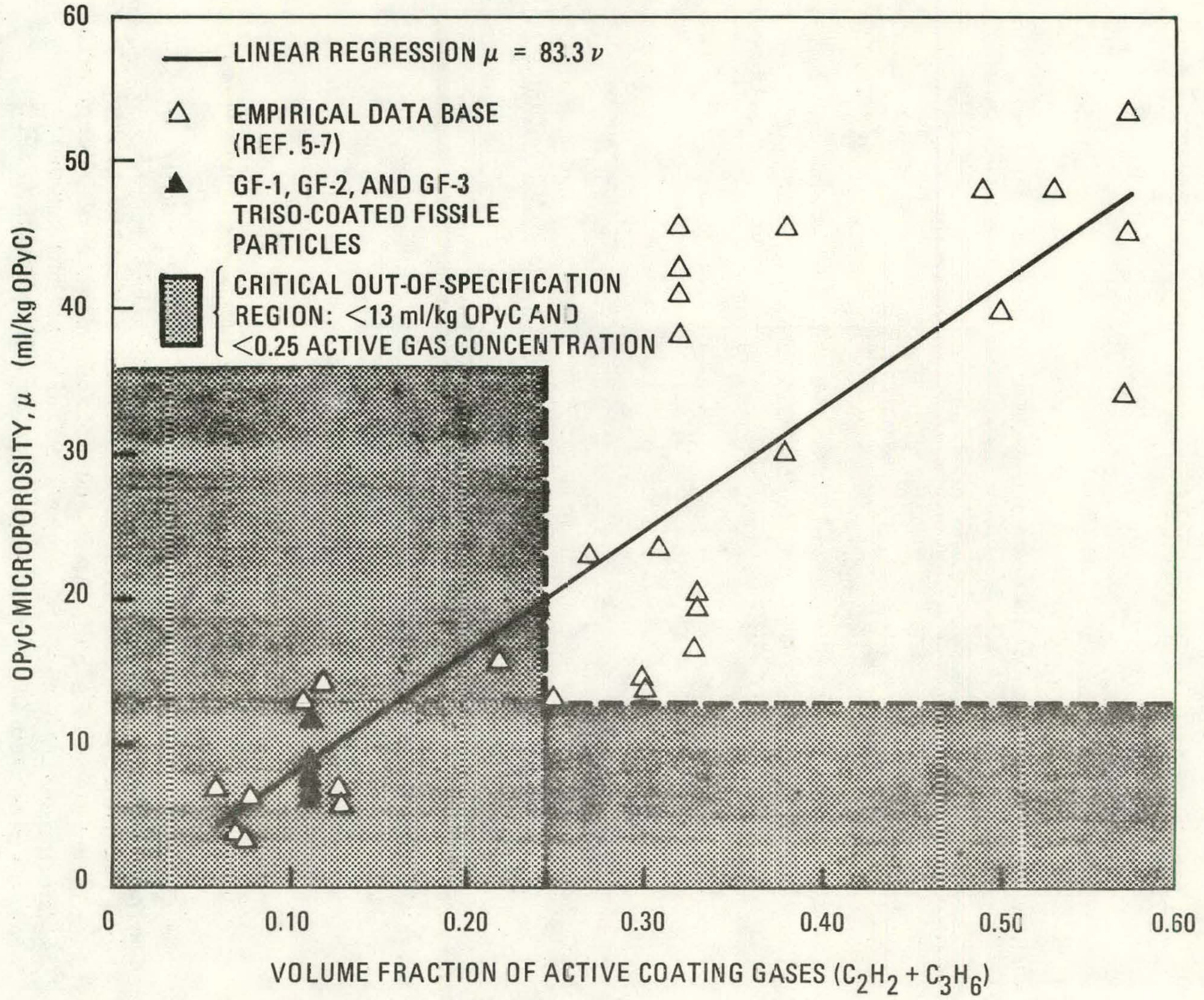

Fig. 5-77. OPyC microporosity versus the volume fraction of active coating gases

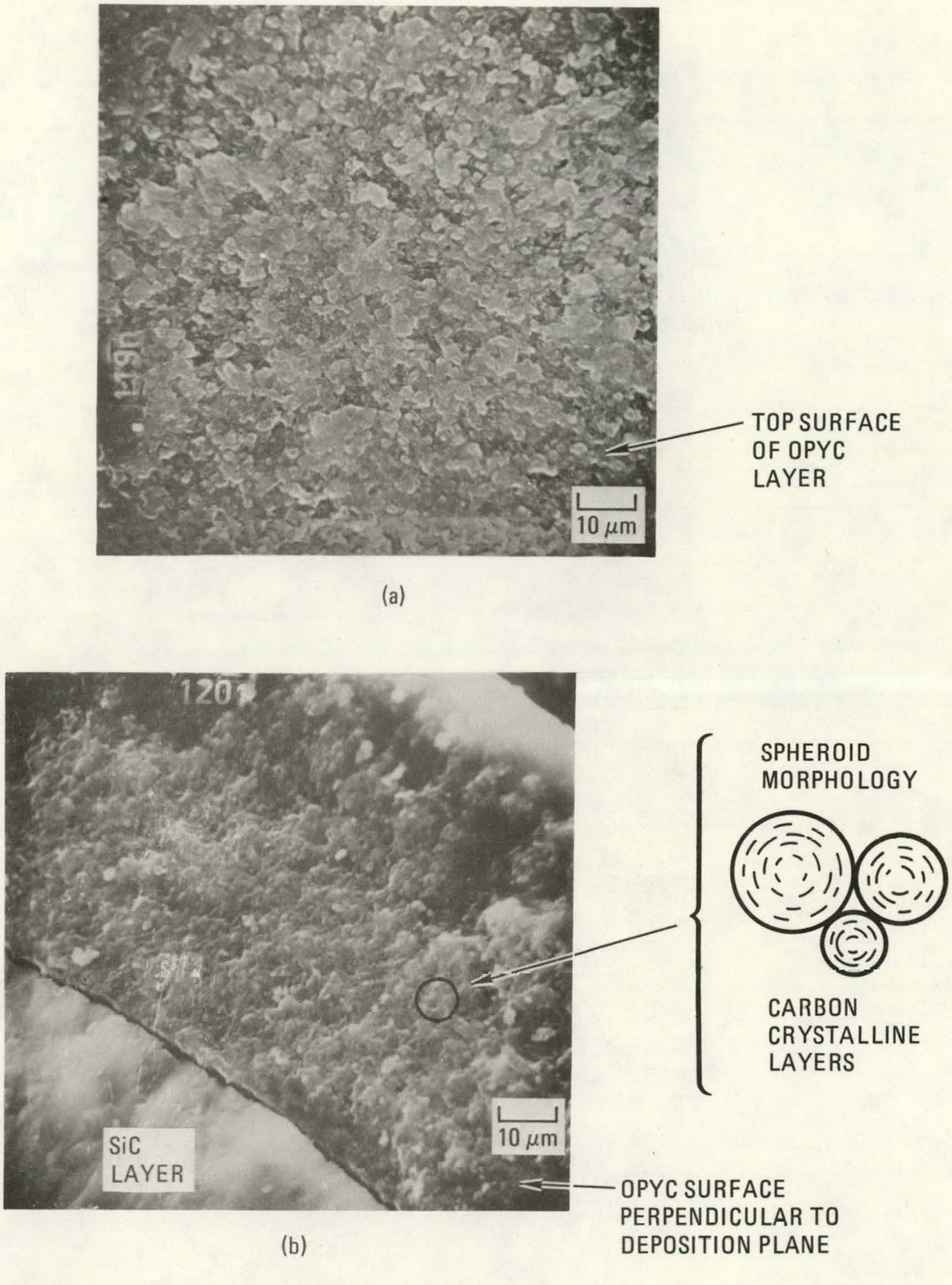

Fig. 5-78. Scanning electron microscope photographs of unirradiated OPyC layer on TRISO-coated fissile batch 6155-00-020. Structure is characterized as agglomerated spheriods with carbon crystallite layers parallel to spheriod surface.

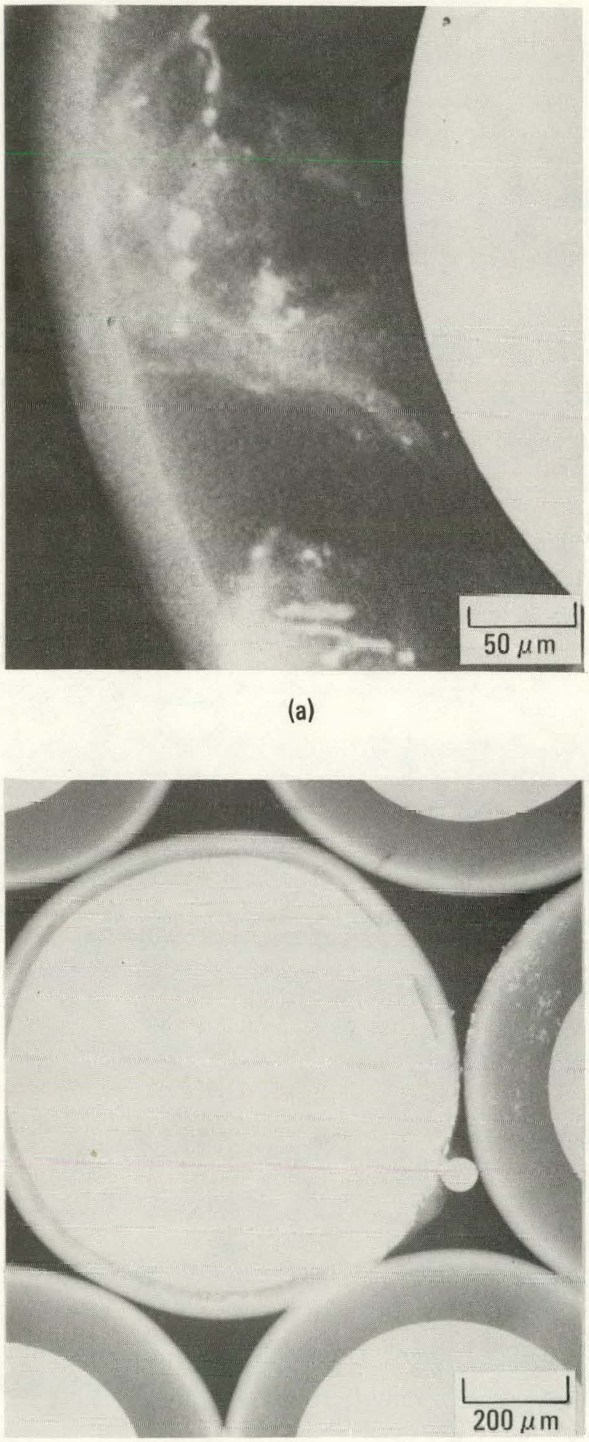

Fig. 5-79. Microradiographs of burned-back, TRISO-coated fissile particles subjected to Hg intrusion at 69 MPa: (a) particle from batch 6155-01-030 and rod type b, which shows localized Hg intrusion (white region); (b) particle from batch 6155-02-03 and rod type b, which shows complete Hg intrusion

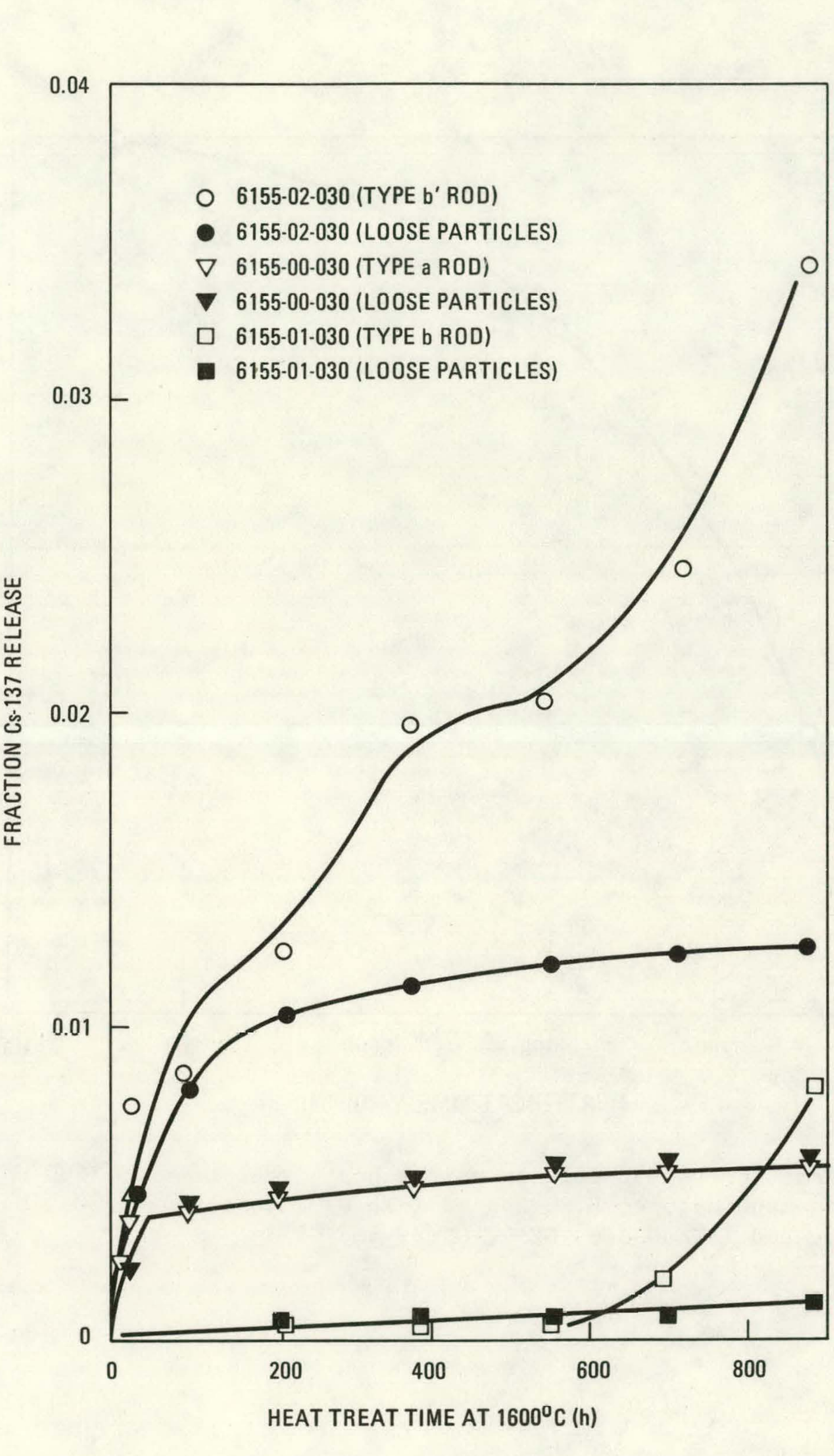

Fig. 5-80. Fraction Cs-137 release versus heat treat time at 1600°C for as-manufactured TRISO-coated (8Th,U)O_2 fuel tested in capsules GF-1, GF-2, and GF-3

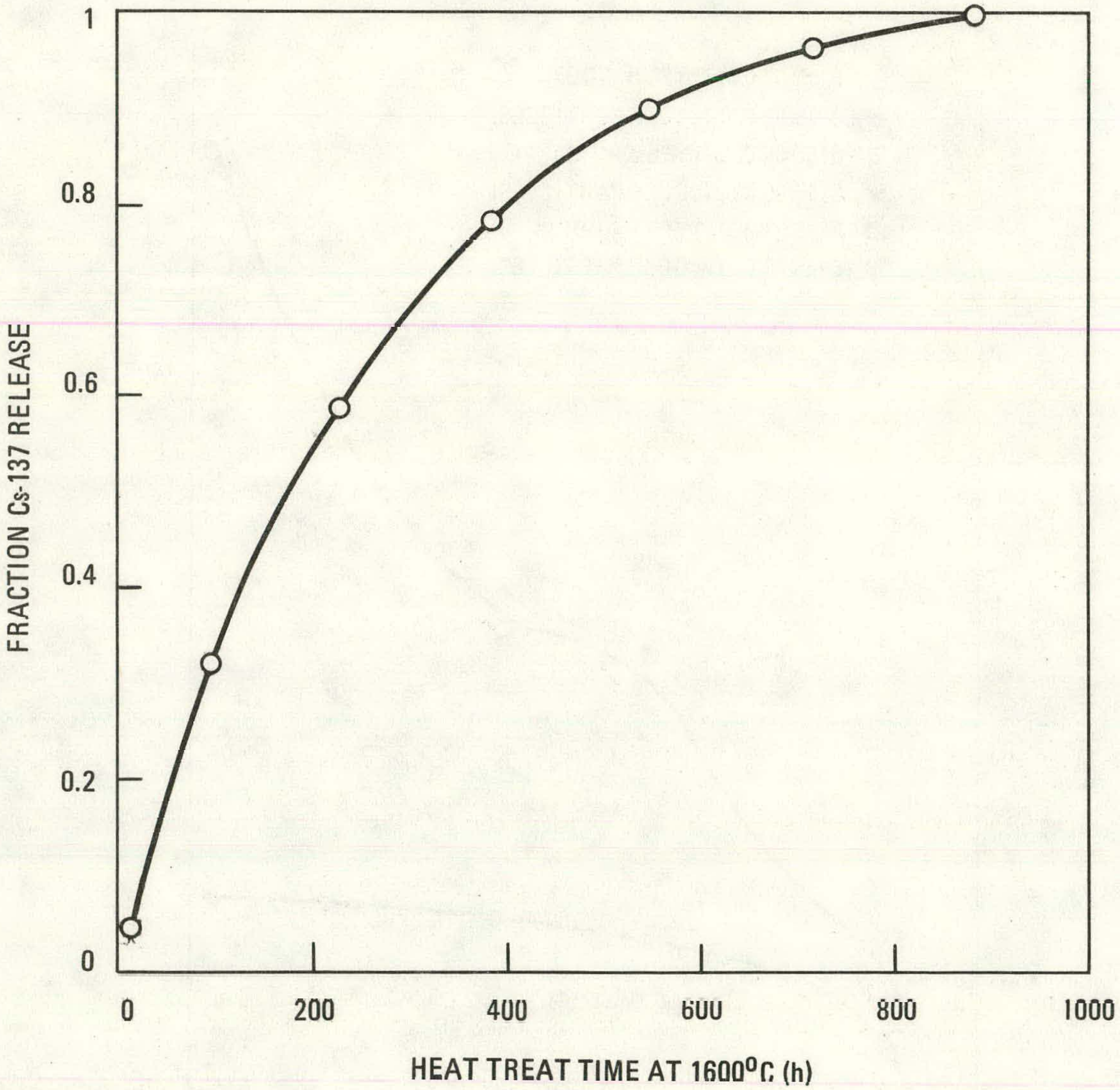

Fig. 5-81. Fraction Cs-137 release versus heat treat time at 1600°C for as-manufactured BISO-coated $(8Th,U)O_2$ (batch 6445-00-010) tested in capsules GF-1, GF-2, and GF-3

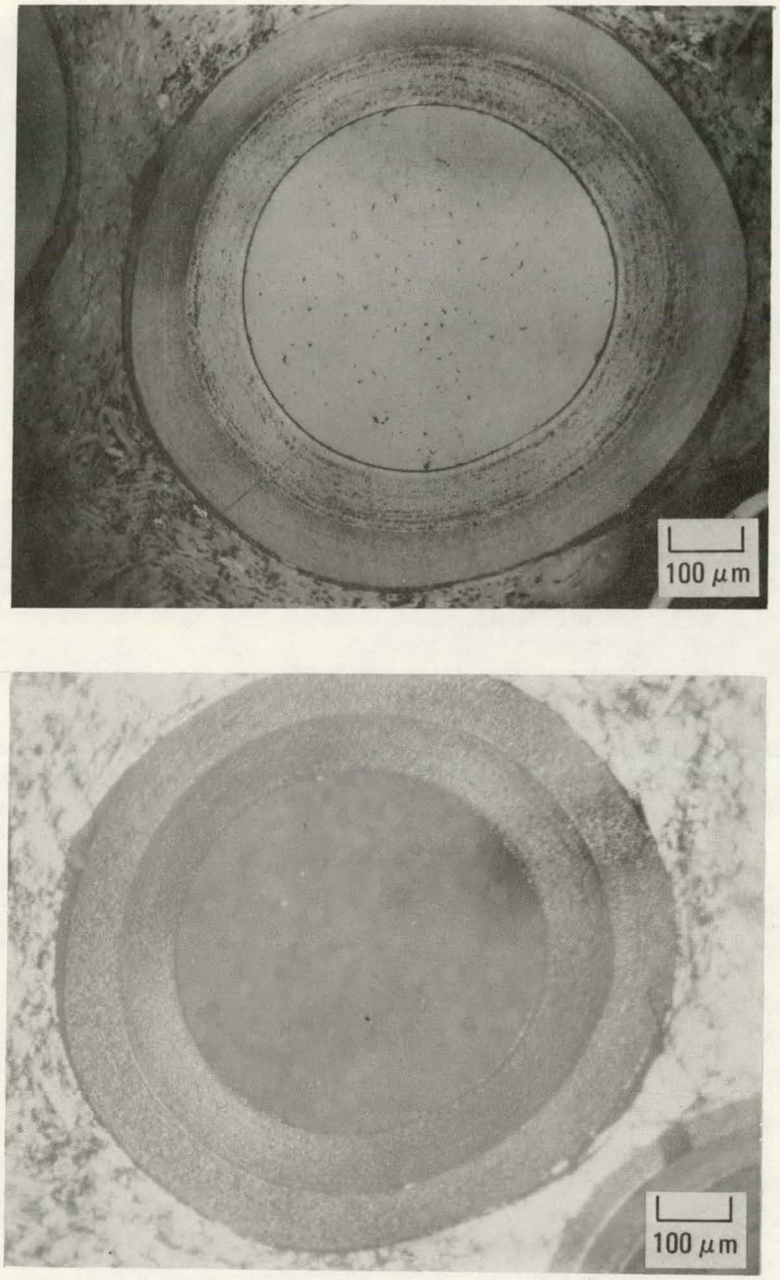

Fig. 5-82. Representative photomicrographs of BISO ThO_2 particles (6542-02-036) from type e fuel rod 237 irradiated in capsule GF-1 (location 1-2) to a fast fluence of 5.5 x 10^{25} n/m^2 (E > 29 fJ)$_{HTGR}$ and a burnup of 1.7% FIMA at 1080°C

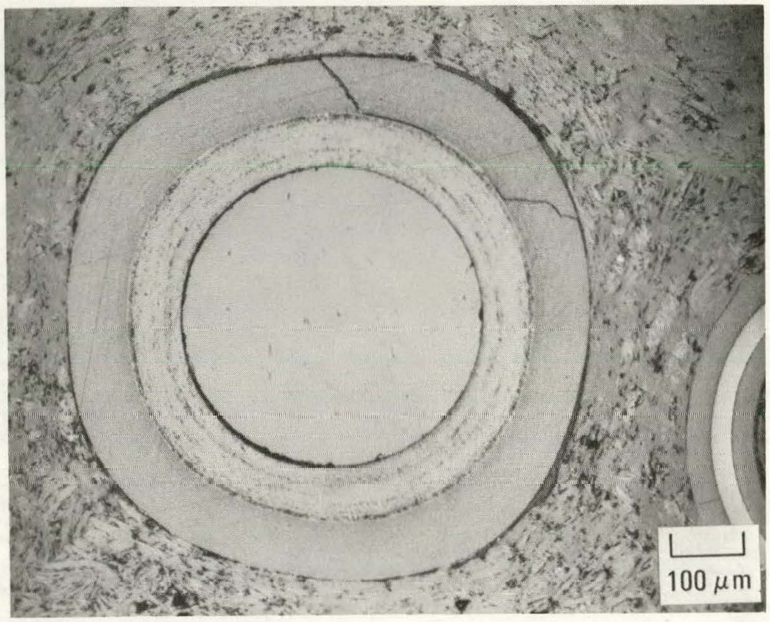

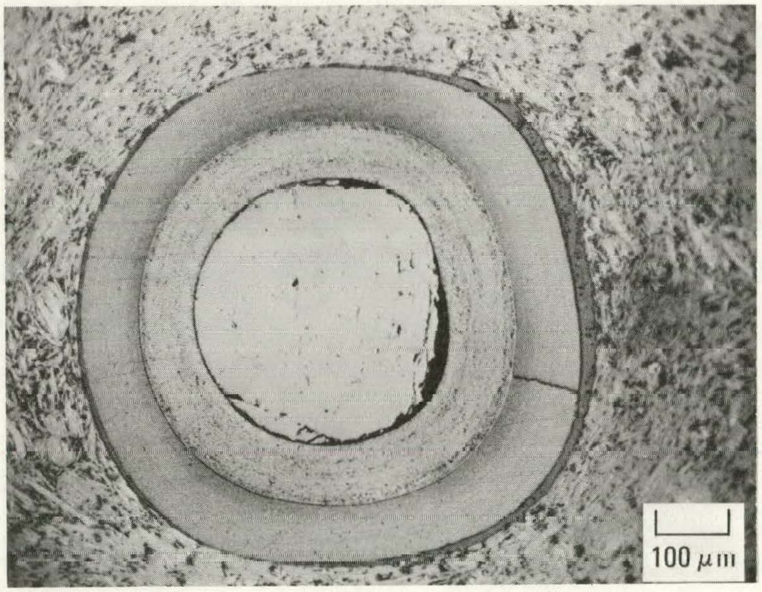

Fig. 5-83. Representative photomicrographs of BISO ThO_2 particles (6542-02-036) from type e fuel rod 237 irradiated in capsule GF-1 (location 1-2) to a fast fluence of 5.5×10^{25} n/m^2 ($E > 29$ fJ)$_{HTGR}$ and a burnup of 1.7% at 1080°C

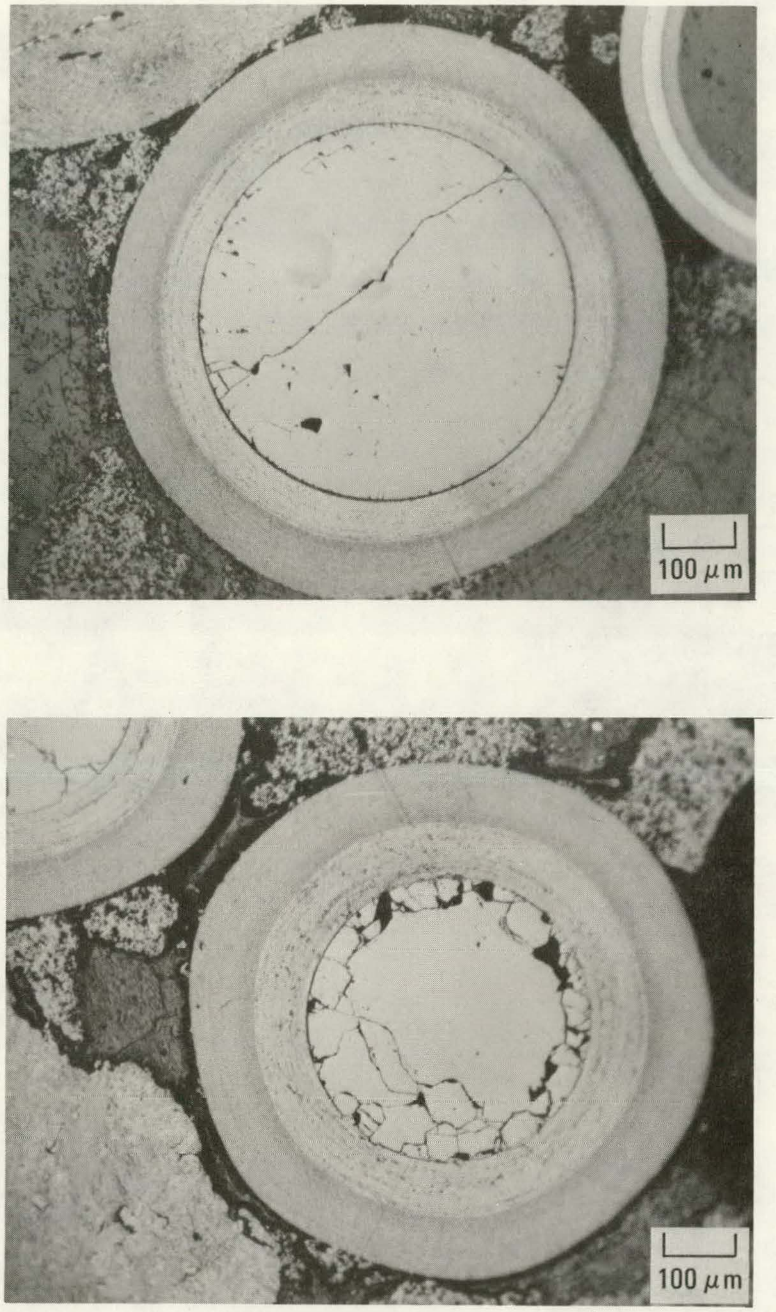

Fig. 5-84. Representative photomicrographs of BISO ThO_2 particles (6542-02-036) from type a fuel rod 7161-003-01-5 irradiated in capsule GF-1 (location 2-4) to a fast fluence of 6.7 x 10^{25} n/m^2 $(E > 29\ fJ)_{HTGR}$ and a burnup of 2.4% FIMA at 1170°C

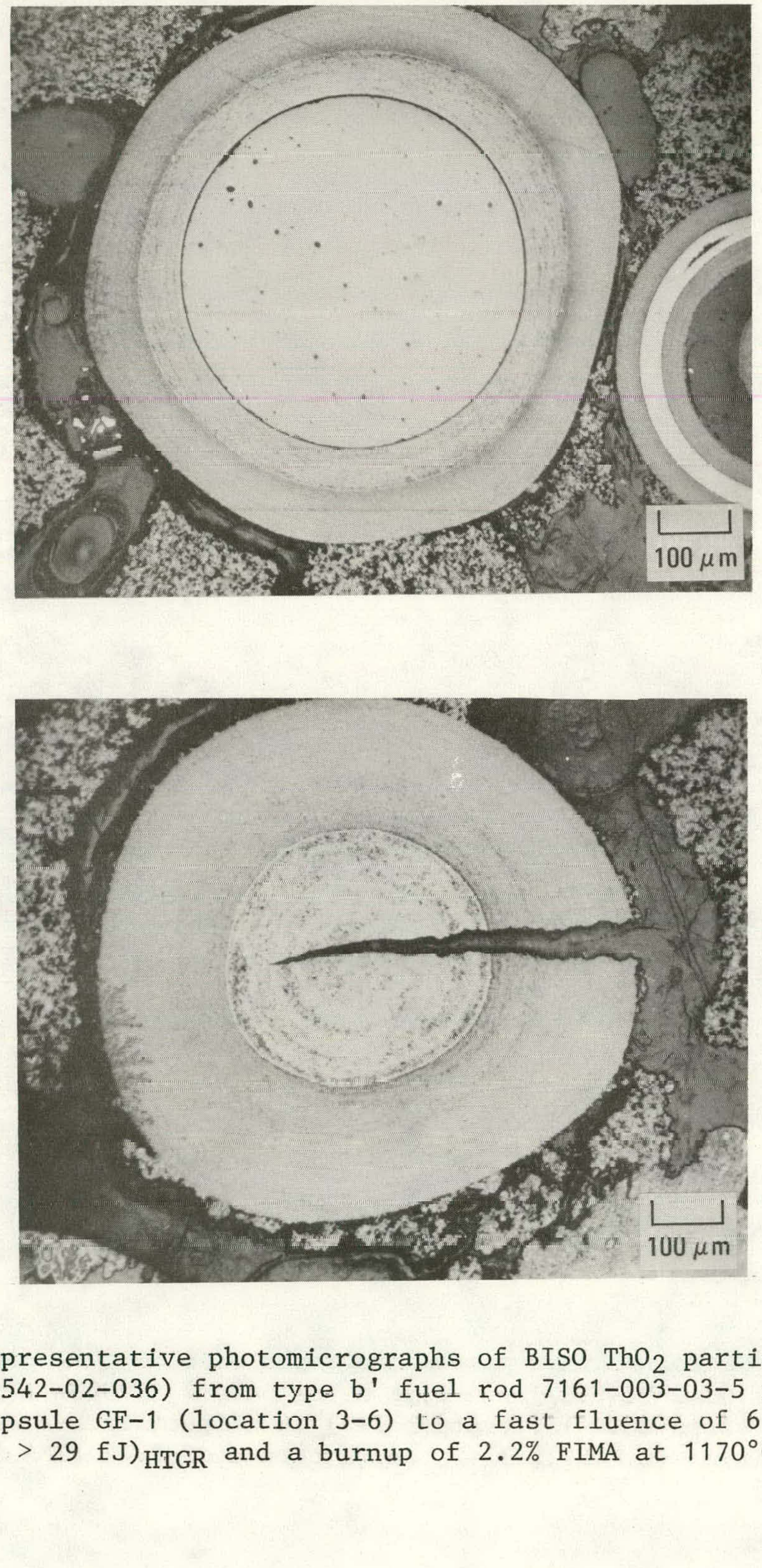

Fig. 5-85. Representative photomicrographs of BISO ThO_2 particles (6542-02-036) from type b' fuel rod 7161-003-03-5 irradiated in capsule GF-1 (location 3-6) to a fast fluence of 6.1×10^{25} n/m^2 $(E > 29\ fJ)_{HTGR}$ and a burnup of 2.2% FIMA at 1170°C

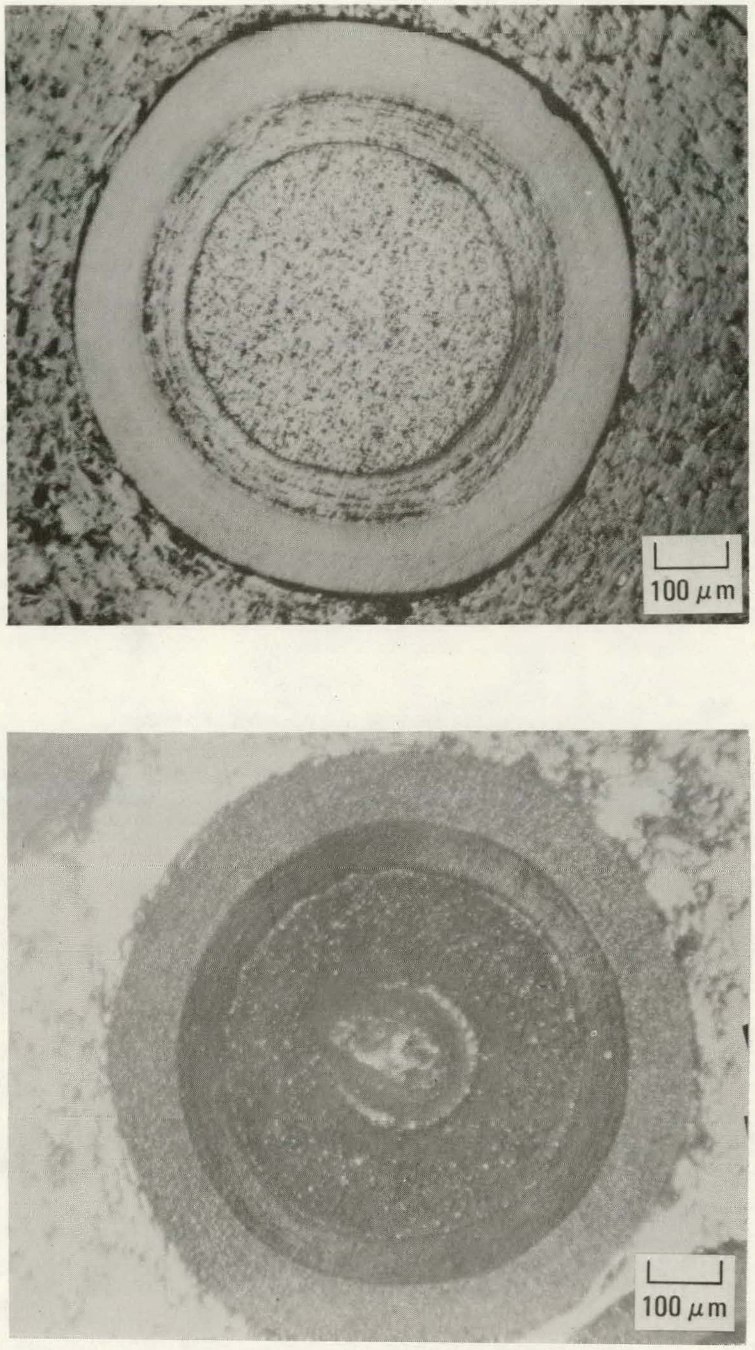

Fig. 5-86. Representative photomicrographs of BISO ThO_2 particles (MG 156) from type f' fuel rod 817 irradiated in capsule GF-3 (location 1-2) to a fast fluence of 7.7 x 10^{25} n/m^2 (E > 29 fJ)$_{HTGR}$ and a burnup of 2.2% FIMA at 975°C

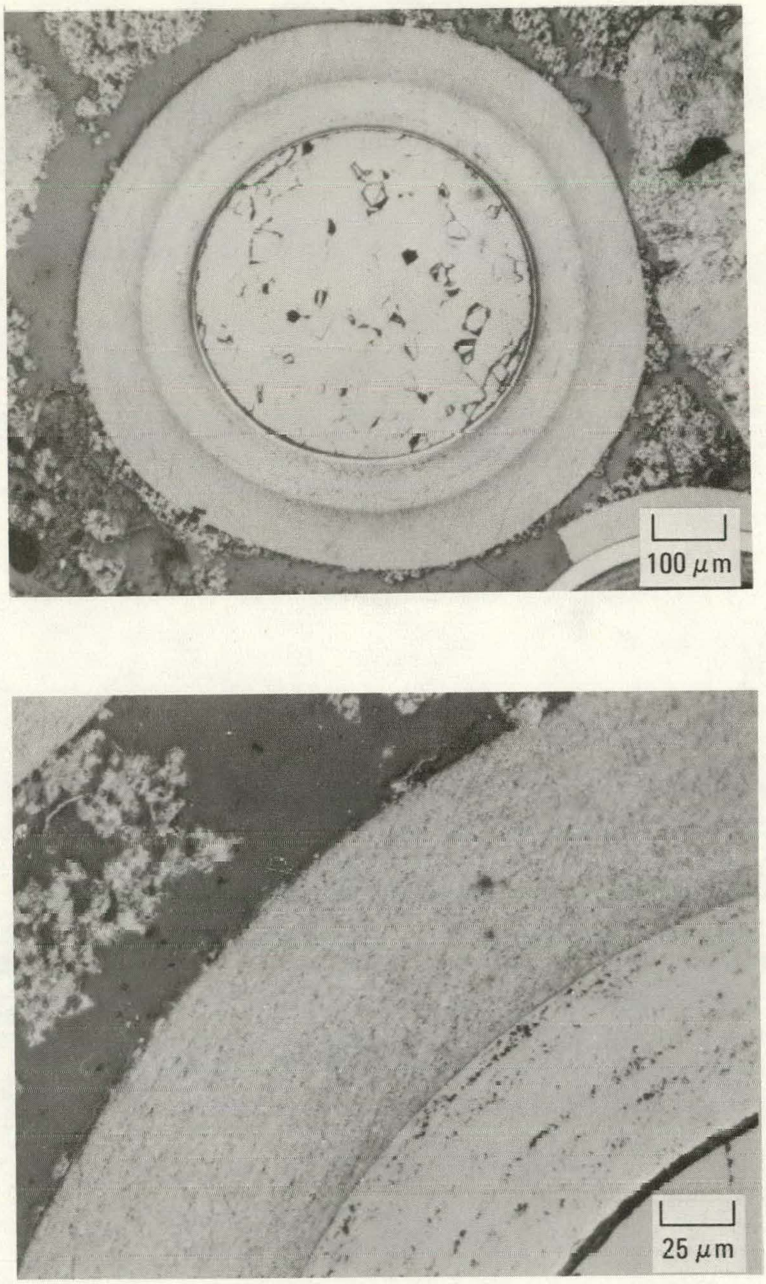

Fig. 5-87. Representative photomicrographs of BISO ThO_2 particles (6542-02-036) from type b fuel rod 7161-003-02-4 irradiated in capsule GF-3 (location 2-3) to a fast fluence of 9.4 x 10^{25} n/m^2 $(E > 29\ fJ)_{HTGR}$ and a burnup of 3.6% FIMA at 975°C

Fig. 5-88. Representative photomicrograph of unbonded BISO ThO_2 particles (6542-02-036-1) irradiated in capsule GF-1 (planchet 5) to a fast fluence of 2.6×10^{25} n/m^2 (E > 29 fJ)$_{HTGR}$ and a burnup of 1.1% FIMA at 1095°C

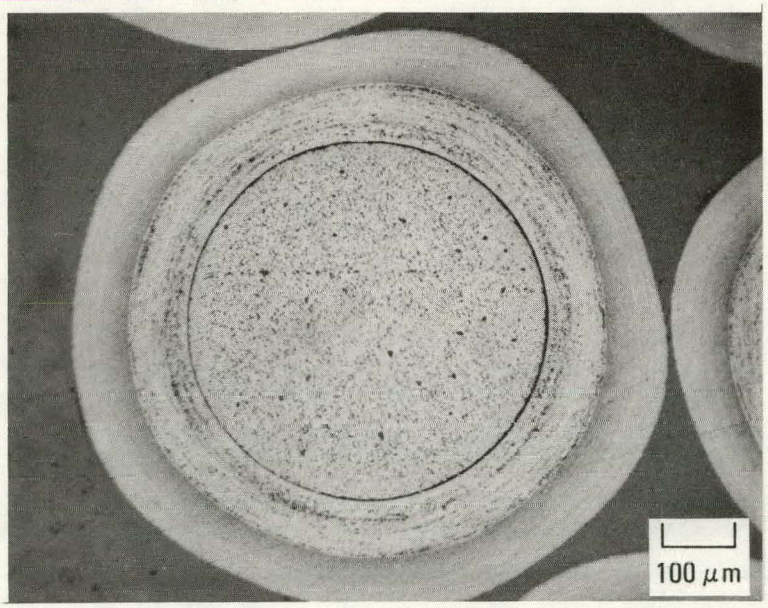

Fig. 5-89. Representative photomicrograph of unbonded BISO ThO_2 particles (6542-02-036-1) irradiated in capsule GF-1 (planchet 5) to a fast fluence of 2.6×10^{25} n/m^2 (E > 29 fJ)$_{HTGR}$ and a burnup of 1.1% FIMA at 1095°C

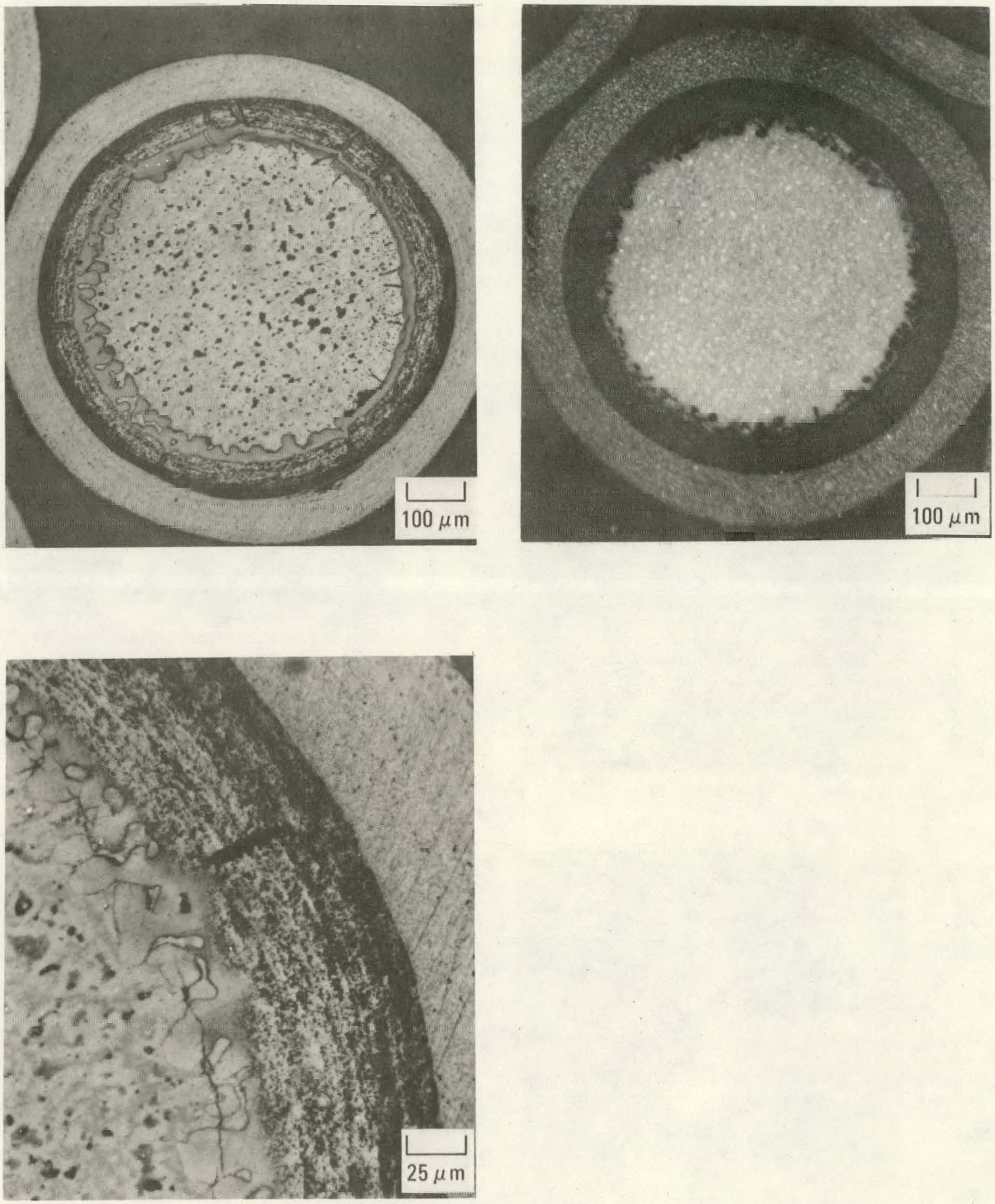

Fig. 5-90. Representative photomicrographs of unbonded BISO $(8Th,U)O_2$ particles (6111-107E) irradiated in capsule GF-1 to a fast fluence of 2.7×10^{25} n/m^2 ($E > 29$ fJ)$_{HTGR}$ and 7.1% FIMA at 1095°C. These kernels were doped with 2 Al + 4 Si

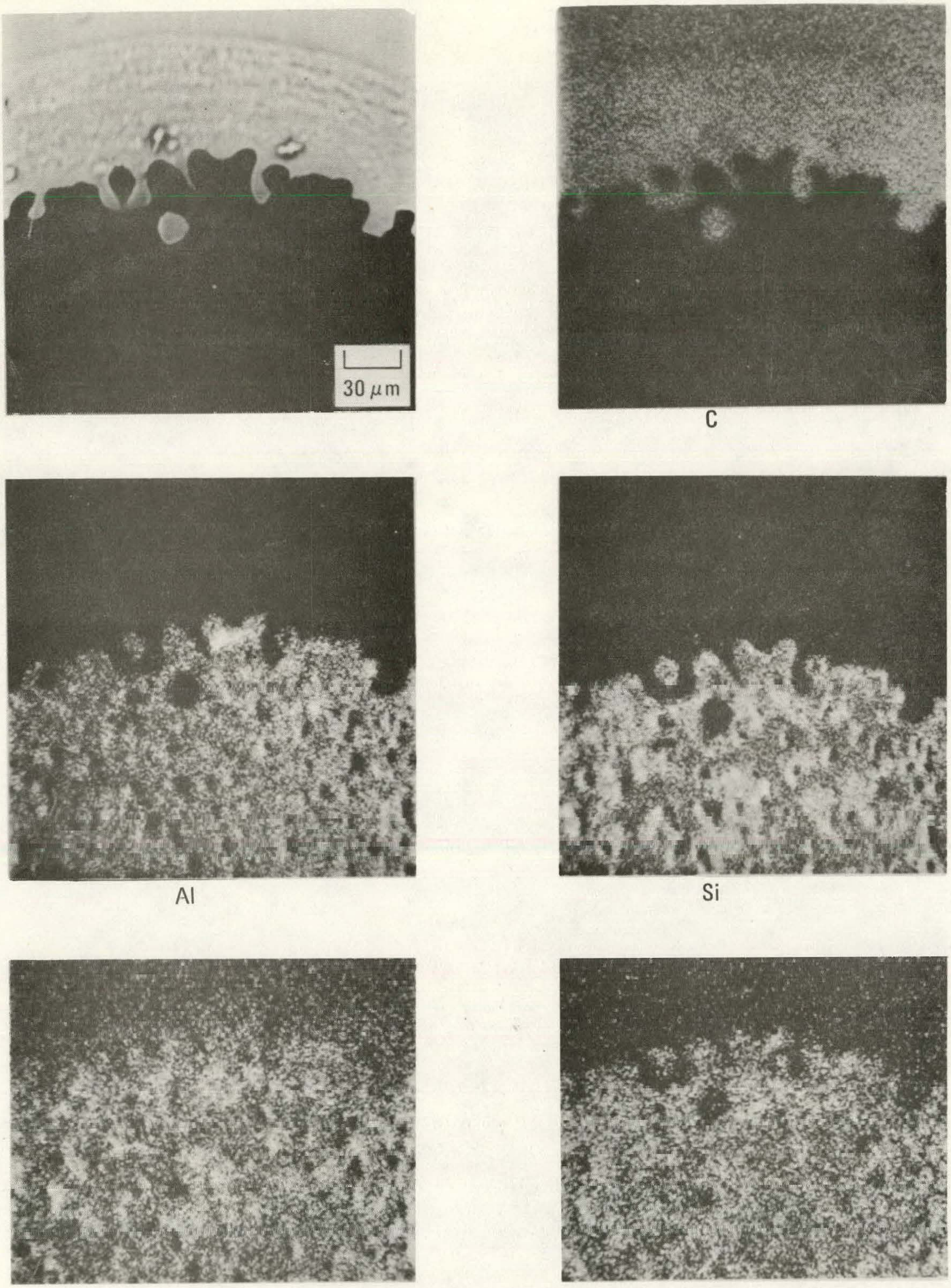

Fig. 5-91. Back-scattering electron image defining C, Al, Si, Cs, and Ba distributions in BISO-coated $(8Th,U)O_2$, batch 611-105E irradiated in GF-3 to a fast fluence of 9.0 x 10^{25} n/m^2 $(E > 29\ fJ)_{HTGR}$ and 11% FIMA at 1000°C. These kernels were doped with 2 Al + 2 Si.

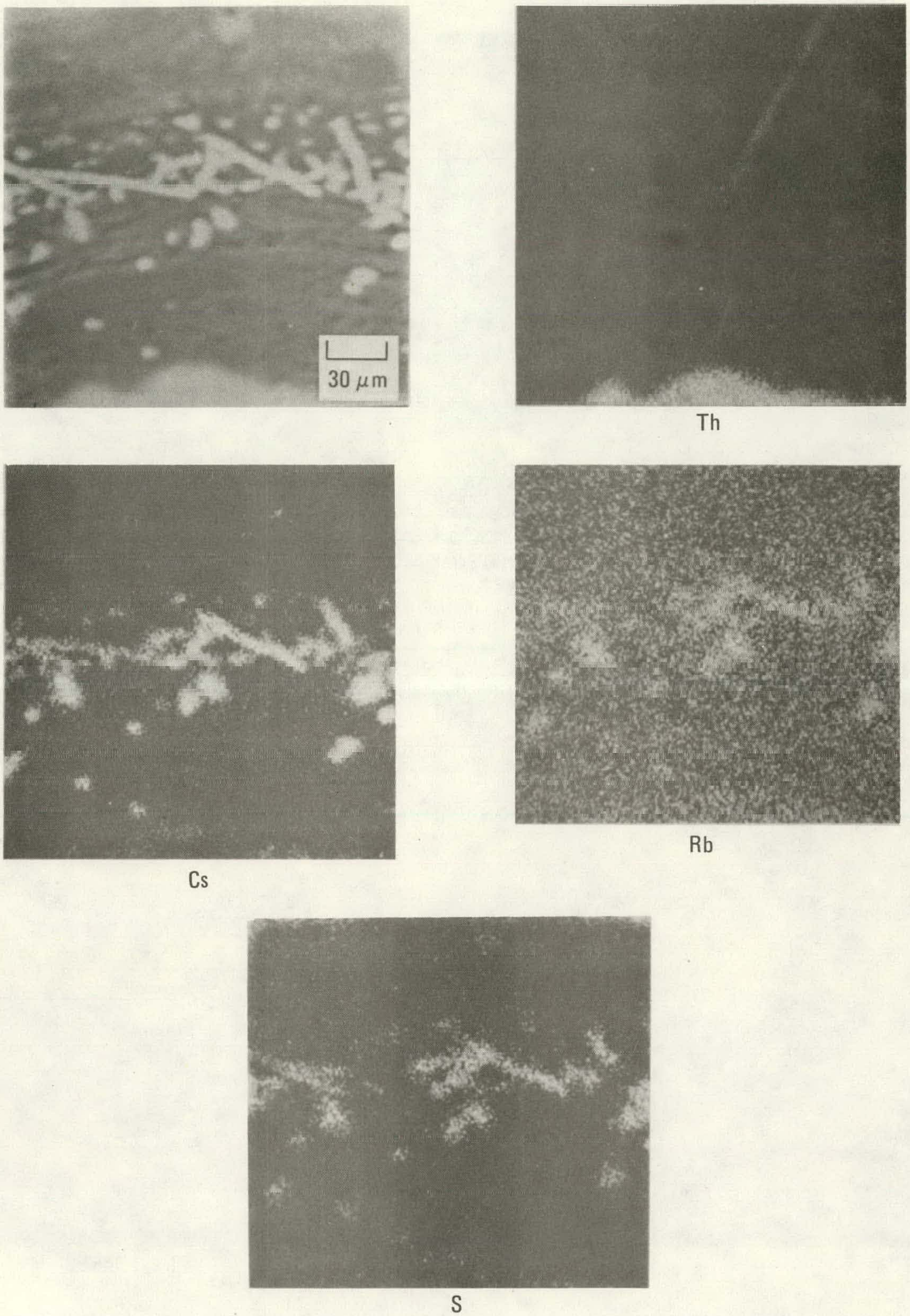

Fig. 5-92. Back-scattering electron image defining Th, Cs, Rb, and S distributions in BISO-coated (8Th,U)O_2, batch 6445-00-010 irradiated in capsule GF-1 (planchet 4) to a fast fluence of 2.7×10^{25} n/m^2 (E > 29 fJ)$_{HTGR}$ and a burnup of 7.1% FIMA at 1095°C.

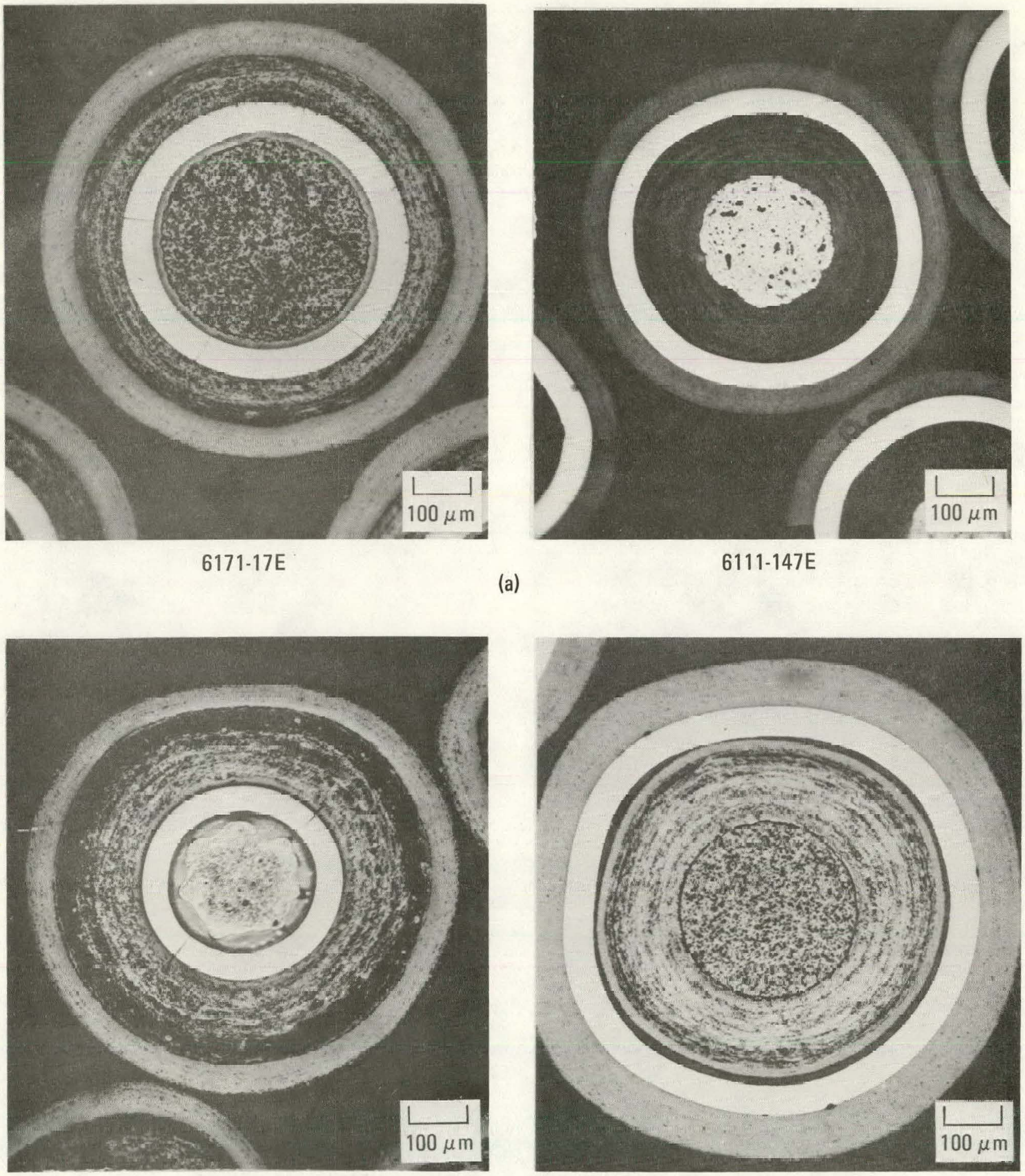

(a)

(b)

Fig. 5-93. Representative photomicrographs of unbonded ZrC-TRISO-coated $(8Th,U)O_2$ particles irradiated in capsule GF-1 at 1095°C and 53% FIMA: (a) ZrC layer deposited on kernel substrate [exposed to 3.5×10^{25} n/m^2 ($E > 29$ fJ)$_{HTGR}$], and (b) ZrC in place of SiC [exposed to 3.0×10^{25} n/m^2 ($E > 29$ fJ)$_{HTGR}$]

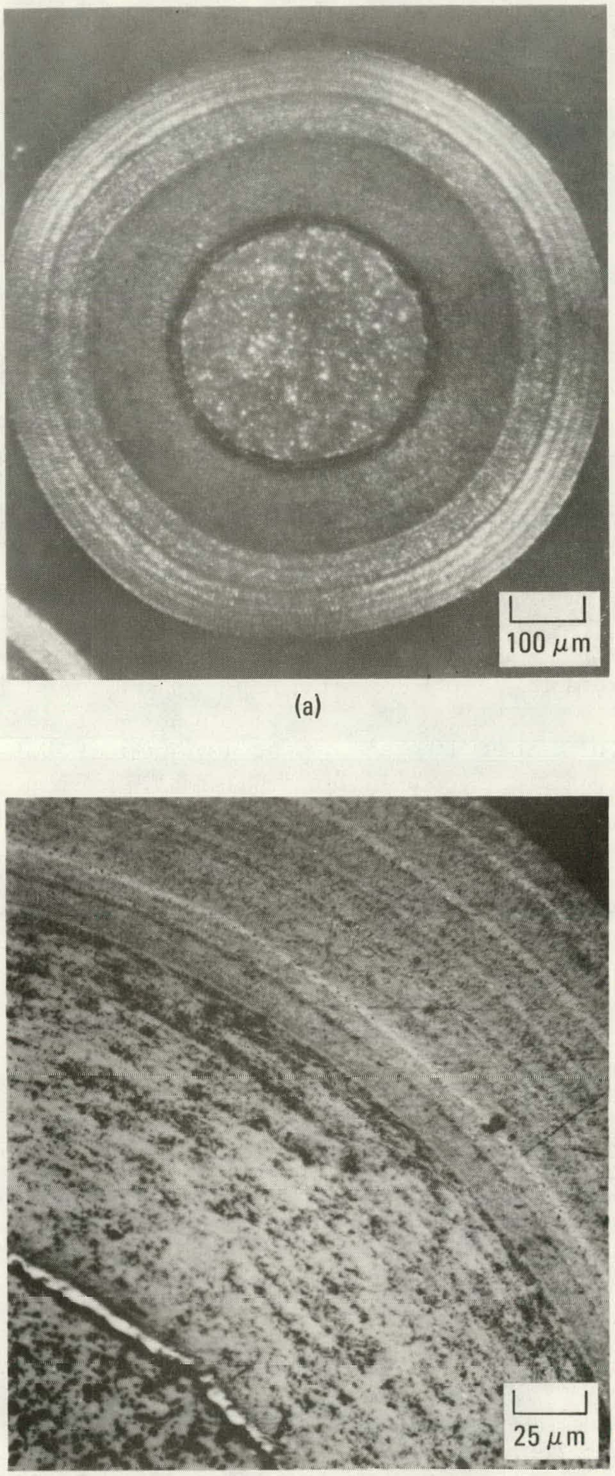

(a)

(b)

Fig. 5-94. Representative photomicrographs of unbonded BISO (8Th,U)O_2 particles (6171-115E, 30% Si dopant) irradiated in capsule GF-3 (planchet 60) to a fast fluence of 9.6×10^{25} n/m^2 $(E > 29\ fJ)_{HTGR}$ and a burnup of 11.1% FIMA at 1100°C

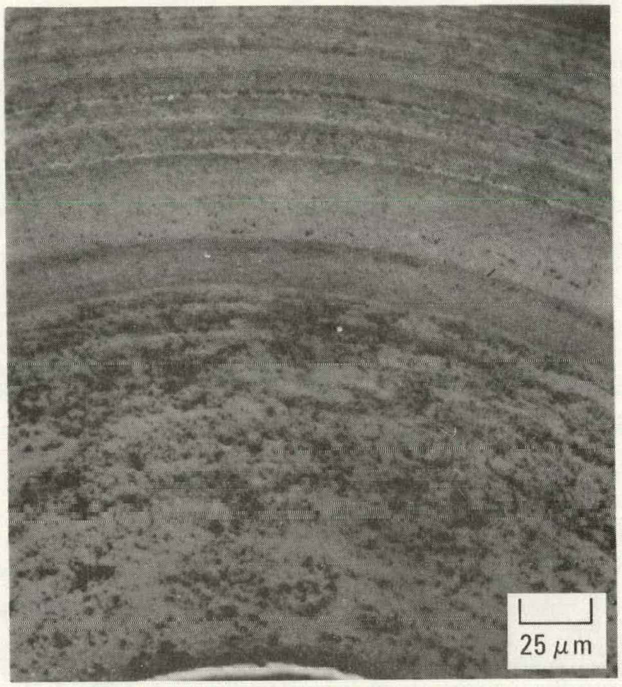

Fig. 5-95. Representative photomicrograph of unbonded BISO (8Th,U)O_2 particles (6171-107E, 25% Si dopant) irradiated in capsule GF-3 (planchet 10) to a fast fluence of 8.6 x 10^{25} n/m^2 (E > 29 fJ)$_{HTGR}$ and a burnup of 11.1% FIMA at 1000°C

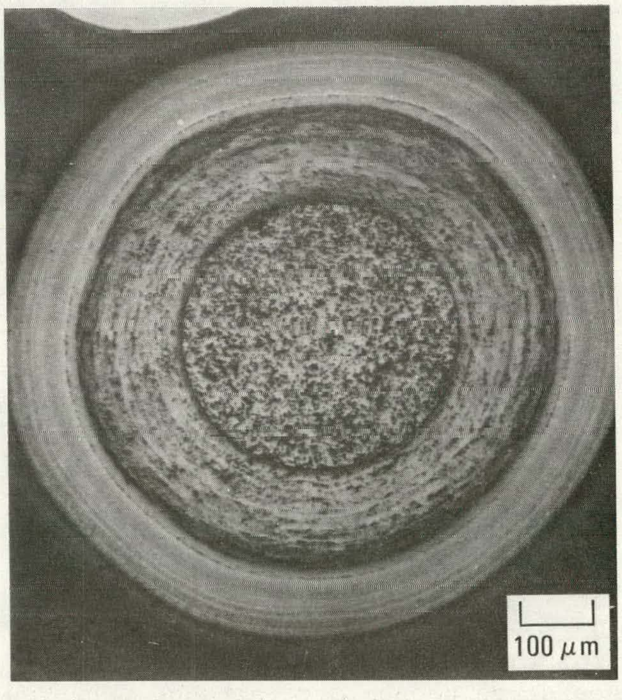

Fig. 5-96. Representative photomicrograph of unbonded BISO (8Th,U)O_2 particles (6171-105E, 19% Si-doped OPyC layer) irradiated in capsule GF-2 (plancet 62) to a fast fluence of 3.6 x 10^{25} n/m^2 (E > 29 fJ)$_{HTGR}$ and a burnup of 5.3% FIMA at 985°C

6. DISCUSSION

6.1. COATED PARTICLE IRRADIATION PERFORMANCE

6.1.1. Fissile Particles

Pressure vessel failure predictions for TRISO-coated fissile particles irradiated in GF-1, GF-2, and GF-3 were made using the TRISO*MONTE computer code. A detailed description of the calculational procedure is presented in Ref. 6-1. TRISO*MONTE calculates the maximum stress in the SiC coating layer, which is a function of dimensions and densities of individual coating components plus the temperature, burnup, and fluence to which the particle is subjected. A Monte Carlo calculational routine is then used to repeat particle stress calculations a large number of times (~1000) and define a particle stress density distribution. The predicted failure fraction is then defined as that fraction of fuel with calculated particle stresses greater than the apparent SiC failure stress (AFS). The AFS value is empirically determined from irradiation capsule data and is dependent on particle size and shape. TRISO-coated FSV fissile and fertile particles with a particle diameter in the range of GF-1, GF-2, and GF-3 fissile particles have an AFS value of -20 MPa (-2800 psi) (Ref. 6-2). In contrast, TRISO-coated UC_2 particles with a nominal diameter of 635 μm have an AFS value of 265 MPa (38,000 psi) (Ref. 6-1). Also, severely faceted TRISO-coated UC_2 particles with a 635-μm nominal diameter have an AFS value of 92 MPa (13,200 psi). The predicted pressure vessel failure levels for TRISO-coated fissile fuel tested in GF-1, GF-2, and GF-3 fuel rods was based on an AFS value of -20 MPa. This AFS value is considered most applicable to the GF-1, GF-2, and GF-3 fuel particle types. Figure 6-1 shows that no fissile particle failure was expected until fissile burnups exceeded 6% FIMA (open symbols). However, superimposed on this figure are observed failure levels for early in life ($\lesssim$4% FIMA) which are based on in-pile Kr-85m R/B results (Table 5-10). Figure 6-1 also shows that it is

5-10). Figure 6-1 also shows that it is difficult to reconcile the relatively high fissile particle failure (3% to 8.5%) early in life, based on pressure vessel stress calculations.

The explanation for the premature failure of TRISO-coated fissile particles tested in GF-1, GF-2, and GF-3 is related to the following factors:

1. Irradiation performance of OPyC layers.
2. Manufacturing defects present in the SiC layers.

6.1.1.1. OPyC Performance on TRISO-Coated Fuel. The irradiation performance of the OPyC layers is discussed in detail in Section 5.8.2.3. Briefly summarized, OPyC failure was discussed in terms of correlations with OPyC microporosity and active coating gas concentrations during OPyC deposition. These correlations were related to high crystallite anisotropy in irradiated OPyC structures with low microporosities (<13 ml/kg OPyC layer). The correlation between OPyC failure and microporosity presented in Fig. 5-74 indicates that the TRISO-coated fissile particles tested in GF-1, GF-2, and GF-3 should have a nominal OPyC failure of ~30%. This is consistent with the GF-1, GF-2, and GF-3 observations (solid data points in Fig. 5-74), which vary between 1.6% and 61.3% OPyC failure. In addition, the irradiation data on OPyC failure presented in Ref. 6-1 and obtained from GF-1, GF-2, and GF-3 support the fact that OPyC failures occur early in life at fluence exposures $\lesssim 2.5 \times 10^{25}$ n/m^2 (E > 29 fJ)$_{HTGR}$. This is attributed to peak irradiation-induced stresses that develop in the pyrocarbon layer due to rapid densification and strain anisotropy. Reference 6-3 indicates that maximum densification occurs in high-density pyrocarbons at a fluence of ~2.5×10^{25} n/m^2 (E > 29 fJ)$_{HTGR}$ and that the difference in strains perpendicular and parallel to the deposition plane increases with crystallite anisotropy. The GF-1, GF-2, and GF-3 irradiation data on TRISO-coated fissile fuel provided a basis for establishing current OPyC property and process specifications, namely, microporosity >13 ml/kg OPyC and volume fraction of active coating >0.25 (Fig. 5-77). These specification parameters have been shown to successfully control PyC microstructure, such as the degree of crystallite anisotropy, and assure acceptable OPyC performance.

6.1.1.2. TRISO-Coated SiC Performance. Adequate SiC performance in TRISO-coated fuel is assured by specification limits on the following (Ref. 6-1):

1. Range of deposition temperatures (1450° to 1700°C).
2. SiC thickness and density.
3. Defective SiC layers ($<10^{-3}$).

The first two specification requirements relate to assuring SiC performance during irradiation, while the last one controls the level of manufacturing defects. The SiC layers in GF-1, GF-2, and GF-3 particles were consistent with these specification requirements. However, further evaluation of the level of defective SiC layers in GF-1, GF-2, and GF-3 fissile fuel (refer to Section 5.8.2.4) showed that all defective SiC layers were not detected by the current QC burn-leach technique. Specifically, the level of defective SiC layers determined by radiographic evaluation after mercury intrusion at 69 MPa ranged from 2.3% to 11.8% (Table 5-17). A large fraction of these defects were SiC layers with localized microfissures (Fig. 5-79). This type of defect would not be readily discernable by the burn-leach technique since this method depends on complete burning of the IPyC and leaching of the kernel substrate. Microfissures of the type shown in Fig. 5-79 would restrict oxidation of the IPyC layer and fuel kernel leaching. Consequently, the burn-leach technique would tend to underestimate the true fraction of defective SiC layers. This result is supported further by Cs-137 diffusive release studies, which show that defective SiC layers in GF-1, GF-2, and GF-3 fissile particles ranged between 0.1% and 3.5% (Table 5-18). The fraction defective SiC layers determined radiographically was greater than that determined by Cs-137 release. However, this trend is rationalized on the basis that microfissures in the SiC such as shown in Fig. 5-79 would tend to restrict diffusive Cs-137 release, which would underestimate the true level of defective SiC layers. An important point to be noted is that as internal fission gas pressure increases during irradiation, microfissures in defective SiC layers could open up to form larger macroscopic cracks.

The above results imply that improved QC techniques need to be defined and implemented to control the level of as-manufactured defective SiC layers. This is particularly important with respect to advanced HTGR-GT plant designs, which require low metallic fission product release to achieve "hands-on" maintenance of turbines. Specifically, Ref. 6-4 shows that a defective SiC fraction of <1.2 x 10^{-4} is required to meet a 40-yr Cs-137 plateout activity of 8900 Ci for a 1530-MW(t) HTGR-GT design.

6.1.1.3. Pressure Vessel Performance. Pressure vessel failure in TRISO-coated fuel is defined as joint failure of the OPyC and SiC layers. Consequently, pressure vessel failure early in life for TRISO coated fissile fuel tested in capsules GF-1, GF-2, and GF-3 can be calculated by multiplying irradiation-induced OPyC failure by the fraction of as-manufactured defective SiC layers. Table 6-1 presents a comparative evaluation of calculated and observed pressure vessel failure early in life for TRISO-coated fissile fuel. In general, the calculated values either bracket or are consistent with observed in-pile pressure vessel failure. This agreement provides convincing experimental support that GF-1, GF-2, and GF-3 TRISO-coated fissile fuel failed early in life as a result of high OPyC failure (2.8% to 61.3%) combined with a high level of as-manufactured defective SiC layers (6.0% to 11.8%).

Figure 6-2 is a plot of observed fissile particle failures in GF-1, GF-2, and GF-3 and SSL-1 irradiation tests determined by fission gas release measurements versus calculated failure levels. Calculated failure is determined by multiplying irradiation-induced OPyC failure by the fraction of as-manufactured defective SiC layers as determined by either a burn-leach or mercury intrusion/radiographic evaluation. Figure 6-2 shows excellent agreement between observed and calculated failure based on a mercury intrusion/radiographic determination of defective SiC layers. However, a comparative evaluation shows that calculated failure levels based on burn-leach are approximately two orders of magnitude less than calculated values based on a mercury intrusion/radiographic evaluation of defective SiC layers.

6.1.2. Thermochemical Stability

6.1.2.1. Fuel Kernel Migration. During operation at high temperature, fuel kernels migrate into the surrounding pyrocarbon coatings under the influence of a temperature gradient. Kernel migration up the temperature gradient results from carbon transport and is characterized by a rejected graphite layer on the cool side of the kernel. The temperature and thermal gradient dependence of fuel kernel migration is discussed in Ref. 6-6; specifically, the kernel migration distance is calculated as follows:

$$X = \int_0^t \mathrm{KMC}(T) \, \frac{dT(\tau)/dx}{T(\tau)^2} \, d\tau \quad , \qquad (6\text{-}1)$$

where X = total migration distance (m),

$dT(\tau)/dx$ = temperature gradient (K/m) across a particle at time τ,

$T(\tau)$ = average particle temperature (K) at time τ,

t = total time (s) particles have been in core,

$\mathrm{KMC}(T)$ = kernel migration coefficient (m^2-K/s) as a function of temperature.

Reference 6-6 defines the variation in kernel migration coefficient (KMC) with 1/T for carbide and oxide fuel as

$$\begin{aligned} \mathrm{KMC} &= 0.62 \exp(-3.11 \times 10^5/RT) \text{ (carbide fuel)}, \\ \mathrm{KMC} &= 0.39 \exp(-2.96 \times 10^5/RT) \text{ (oxide fuel)}, \end{aligned} \qquad (6\text{-}2)$$

where R = natural gas constant (8.313 J/K/mol) and T = temperature (K).

Table 6-2 summarizes the thermal exposure conditions for GF-1, GF-2, and GF-3. The table shows that cells 2 and 4 in GF-1 had thermal exposure conditions that would result in the maximum fuel kernel migration in oxide and carbide fuels. Using the maximum exposure conditions in Eq. 6-1 results in predicted oxide and carbide fuel kernel migrations of <0.5 μm. This level of migration is not detectable with standard metallograhic techniques used in the GF-1, GF-2, and GF-3 PIE. Consequently, the observation of no kernel migration in oxide and carbide fuels is consistent with current performance models (Ref. 6-6) used in HTGR core design.

6.1.2.2. Metallic Fission Production Interactions. An electron microprobe evaluation of metallic fission product distributions in BISO-coated $(8Th,U)O_2$ fuel showed that only Cs and Rb migrated into the coating layers (refer to Section 5.8.2.2.). Rare earth type fission products, e.g., cerium, neodymium, lanthanum, samarium, praseodymium, and europium, were confined to the kernel substrate and were not detected in the coating layers. This is consistent with the thermodynamic stability of rare earth metals that tend to form complex oxides with the kernel material (Ref. 6-7). In turn, this reduces the mobility of these metallic fission products into coating layers. In contrast, rare earth fission products diffuse from UC_2 kernels during irradiation (refer to Section 5.8.2.2). In TRISO-coated UC_2 particles, concentrations of rare earth metallic fission products build up in the IPyC coating on the cooler side of the fuel particles and can potentially react with the SiC coating at the SiC-IPyC coating interface. The kinetics of rare earth - SiC attack in UC_2 fuel are dependent on temperature; Fig. 6-3 is a plot of the rate of change of SiC thickness versus reciprocal temperature. This figure presents a large body of data (Ref. 6-8) on SiC attack and highlights the results of UC_2 loose particle tests in GF-1 and GF-2 in comparison with the empirical data base. No rare earth - SiC attack was observed in UC_2 fuel tested in GF-1 and GF-2. However, the metallographic techniques used have a resolution limit of ~1 μm of SiC attack. A rate of attack of $\sim 1.4 \times 10^{-2}$ $\mu m/h^{1/2}$ is calculated by assuming 1 μm of rare earth - SiC attack in UC_2 fuel in GF-1 and GF-2. This rate of attack is consistent with the data base (Fig. 6-3).

6.1.3. Fertile Particles

6.1.3.1. Failure Analysis. Failure of fertile particles tested in GF-1, GF-2, and GF-3 was evaluated by:

1. Visual examination of loose particles.
2. Metallographic examination of loose particles and fuel rods.
3. In-pile Kr-85m R/B measurements.

No visually or metallographically determined pressure vessel failure was observed in fertile fuel with the exception of BISO-coated ThO_2 batch 6542-02-036. This batch was the only batch of BISO-coated fuel fabricated by GA and is discussed in detail in Sections 5.3.1 and 5.8.3.1. This batch had maximum failure percentages of 5% (determined metallographically) in batch 6542-02-036 and 2.3% (determined visually) in a "daughter" batch 6542-02-037. The "daughter" batch was density separated from the high particle density fraction of "parent" batch 6542-02-036. This results in the "daughter" batch having reduced coating thicknesses compared to the "parent" batch. Exposure conditions for the failed BISO-coated fuel were ~3.4% FIMA, $\sim 9.6 \times 10^{25}$ n/m^2 $(E > 29\ fJ)_{HTGR}$, and ~1000°C. The visually and metallographically determined failure levels for batch 6542-02-036 are generally consistent with the calculated fertile particle failures based on EOL in-pile Kr-85m R/B measurements. Table 5-11 shows calculated fertile particle failure percentages for GA-fabricated rods, which ranged from 0.24% to 7.38%. It should be emphasized that these values are based on the assumption of equal failure percentages in fertile and fissile fuel (refer to Section 5.6.1). Consequently, there is considerable uncertainty (estimated at a factor of two) in calculated fertile particle failure levels based on EOL Kr-85m R/B. The pressure vessel failure in batches 6542-02-036 and -037 is partially attributed to the low buffer thicknesses (79 and 74 μm) and OPyC thicknesses (74 and 71 μm). Currently, BISO-coated ThO_2 has reference buffer and OPyC coating thicknesses of 80 to 110 μm and 70 to 90 μm, respectively (Ref. 6-9).

One TRISO-coated batch of ThO_2 (6252-00-020) fabricated by GA was tested in type c fuel rods and as loose particles in GF-2 and GF-3. The average visually determined OPyC failure level in this batch was 13.8% (Table 5-4). The OPyC microporosity in this batch was 15 ml/kg OPyC and the OPyC layer was deposited with an active coating gas ratio of 0.13. The observed failure in this batch is consistent with the empirical correlation used to establish HTGR specification limits, namely, low microporosities (<13 ml/kg OPyC) and/or low active coating gas ratios (<0.25) are related to OPyC structures developing large crystallite anisotropy during irradiation, which results in large internal stresses and premature failure (refer to Section 5.8.2.3). No pressure vessel failure was observed metallographically in batch 6252-00-020. This is substantiated by in-pile Kr-85m R/B measurements on type c rods in capsules GF-2 and GF-3. Figures 4-23 and 4-24 show a rapid increase in Kr-85m R/B up to a fluence of 2.5 x 10^{25} m/m^2 $(E > 29\ fJ)_{HTGR}$ followed by a sharp decline and leveling off. This behavior is characteristic of fissile failure early in life (refer to Section 5.6.1) followed by a decreasing fraction of and leveling off of fissions in the fissile fuel with no additional fertile particle failure.

6.1.4. Advanced Fuel Particles

6.1.4.1. Doped Kernels. The experimental results on BISO-coated $(8Th,U)O_2$ kernels with Al and Si dopants are discussed in Section 5.8.4. In general, the results indicate that Al and Si remain in the kernel during irradiation and that Cs, Ba, and Sr have a tendency to concentrate with the dopants. Furthermore, it appears that zones rich in Si and fission products are characterized by a Si/Al ratio of ~3. This could be attributed to the thermodynamic stability of feldspar-type structures, i.e., $M(AlSi_3)O_8$, where M is a group one or two metallic fission product element. However, it should be emphasized that the presence of Al and Si dopants in $(8Th,U)O_2$ kernels did not significantly retard the migration of Cs into the coating layers (Fig. 5-91).

6.1.4.2. ZrC Coating Layers. Four experimental fuel particle designs utilizing ZrC coatings in combination with porous and dense pyrocarbon coatings were tested under high-temperature irradiation (refer to Section 5.8.4). As a fission product corrosion test for the ZrC, two particle designs employed carbide coatings applied directly over either UC_2 or $(8Th,U)O_2$ fuel kernels; the other two designs utilized ZrC outside of porous pyrocarbon coatings but without the conventional inner dense IPyC coating on either UC_2 or $(8Th,U)O_2$ fuel kernels. The particles were irradiated at 1095°C to a fast neutron fluence of 5×10^{25} n/m^2 $(E > 29\ fJ)_{HTGR}$ and burnups of ~60 and 7.1% FIMA for the UC_2 and $(8Th,U)O_2$ kernels, respectively. Metallographic and electron beam microprobe examination of the irradiated particles showed that ZrC possesses good resistance to chemical attack by fission products.

6.1.4.3. Si-Doped OPyC Layers. Five separate batches of BISO-coated $(8Th,U)O_2$ particles with Si-doped OPyC layers (19.0 to 47.5 wt % Si) were shown to exhibit excellent structural integrity during irradiation (refer to Section 5.8.4.1). These batches were tested in GF-3 to 11.1% FIMA and 9.4×10^{25} n/m^2 $(E > 29\ fJ)_{HTGR}$. One batch (6171-117E) with 47.5 wt % Si in the OPyC layer exhibited 0.3% pressure vessel failure. This may be indicative of an upper allowable limit on Si content for doped OPyC layers. The structural appearance of Si-doped OPyC layers was characterized as concentric laminated rings rich in Si content (Fig. 5-95). Also, it was shown that batch 6171-115E with 39 wt % Si in the OPyC layer possessed excellent retention of metallic fission products.

REFERENCES

6-1. Kovacs, W. J., and D. P. Harmon, "Technical Support Document for Issue C of the HTGR Fuel Product Specification," General Atomic unpublished data, August 1979.

6-2. "HTGR Fuels and Core Development Program, Quarterly Progress Report for Period Ending February 28, 1978," DOE Report GA-A14863, General Atomic Company, March 1978, pp. 9-63.

6-3. Kaae, J., "Mechanical Behavior of BISO-Coated Fuel Particles During Irradiation (Part 1)," *Nucl. Technol.* **35**, 359 (1977).

6-4. Kovacs, W. J., "Preliminary Fuel Specifications for a HTGR/Steam Cycle and GT Plant Designs," General Atomic unpublished data, April 1980.

6-5. Ballagny, A., *et al.*, "SSL-1 Spitfire Loop Experiment Postirradiation Examination and Analysis," General Atomic unpublished data, July 1978.

6-6. "Fuel Design Data Manual," General Atomic unpublished data, September 1979.

6-7. Homan, F. J., "Stoichiometric Effects on Performance of HTGR Fuels from the UCO System," *Nucl. Technol.* **35**, 428 (1977).

6-8. "HTGR Generic Technology Program Semiannual Report for the Period Ending March 31, 1980," DOE Report GA-A15842, General Atomic Company, May 1980.

6-9. "HTGR Fuel Product Specification," General Atomic unpublished, August 1979.

TABLE 6-1
COMPARATIVE EVALUATION OF CALCULATED AND OBSERVED IN-PILE PRESSURE VESSEL FAILURE EARLY-IN-LIFE FOR TRISO-COATED FISSILE FUEL

Capsule	Cell	Rod Type	Fissile Batch No.	OPyC Failure[(a)] (%)	Defective SiC Layers[(b)] (%)	Calculated Pressure Vessel Failure[(c)] (%)	Observed In-Pile Pressure Vessel Failure[(d)] (%)
GF-1	1	e, e'	6155-01-020	61.3	8.9	5.5	1.5
	2	a	6155-00-030	2.8-16.7	7.4	0.20-1.23	0.05
	3	b, b'	6144-01-030 and 6155-02-030	26.5.-61.3	6.0-6.8	1.6-4.2	3.00
GF-2	1	d	BISO fissile	--	--	--	0.07
	2	a	6155-00-030	2.8-16.7	7.4	0.20-1.2	0.13
	3	c	6155-01-030	61.3	11.8	7.2	8.57
GF-3	1	f, f'	CEA fuel (MG 178)	0.9	ND(c)	ND	0.02
	2	b,b'	6155-01-030 and 6155-02-030	26.5-61.3	6.0-6.8	1.6-4.2	5.66
	4	c	6155-01-030	61.3	11.8	7.2	5.14

(a)Determined visually (refer to Table 5-4).

(b)Determined by radiographic evaluation after mercury intrusion at 69 MPa (refer to Table 5-16).

(c)Determined by multiplying OPyC failure by defective SiC layers.

(d)Determined from in-pile Kr-85m R/B measurements (refer to Table 5-10); applied to early-in-life failure [$<2.5 \times 10^{25}$ n/m^2 (E > 29 fJ)$_{HTGR}$].

(e)ND = not determined.

TABLE 6-2
THERMAL EXPOSURE CONDITIONS FOR IRRADIATED CAPSULES GF-1, GF-2, AND GF-3

Capsule	Cell	Volume Average Temperature (°C)	Thermal Gradient (10^2 °K/m)	Irradiation Time (10^7 s)
GF-1	1	1080	135	1.85
	2[a]	1170	165	
	3	1170	160	
	4[b]	1095	35	
GF-2	1	960	105	1.72
	2	970	130	
	3	960	125	
	4	985	35	
GF-3	1	975	110	3.14
	2	975	135	
	3	1000	55	
	4	1120	85	

[a] Maximum thermal exposure conditions for kernel migration in (8Th,U)O_2 and ThO_2 fuel systems.

[b] Maximum thermal exposure conditions for kernel migration in UC_2 fuel.

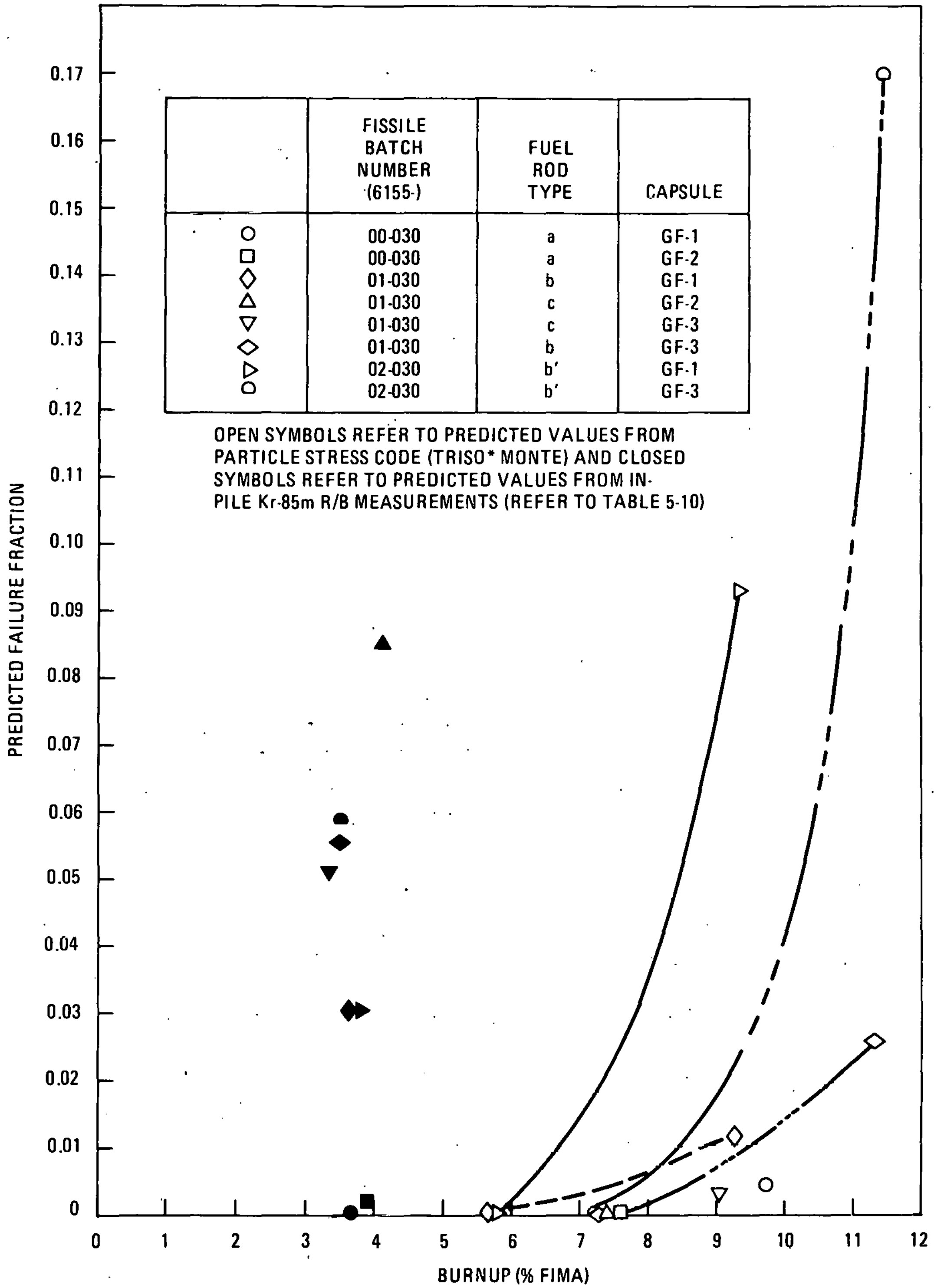

Fig. 6-1. Predicted pressure vessel failure fractions in TRISO-coated fissile fuel tested in capsules GF-1, GF-2, and GF-3

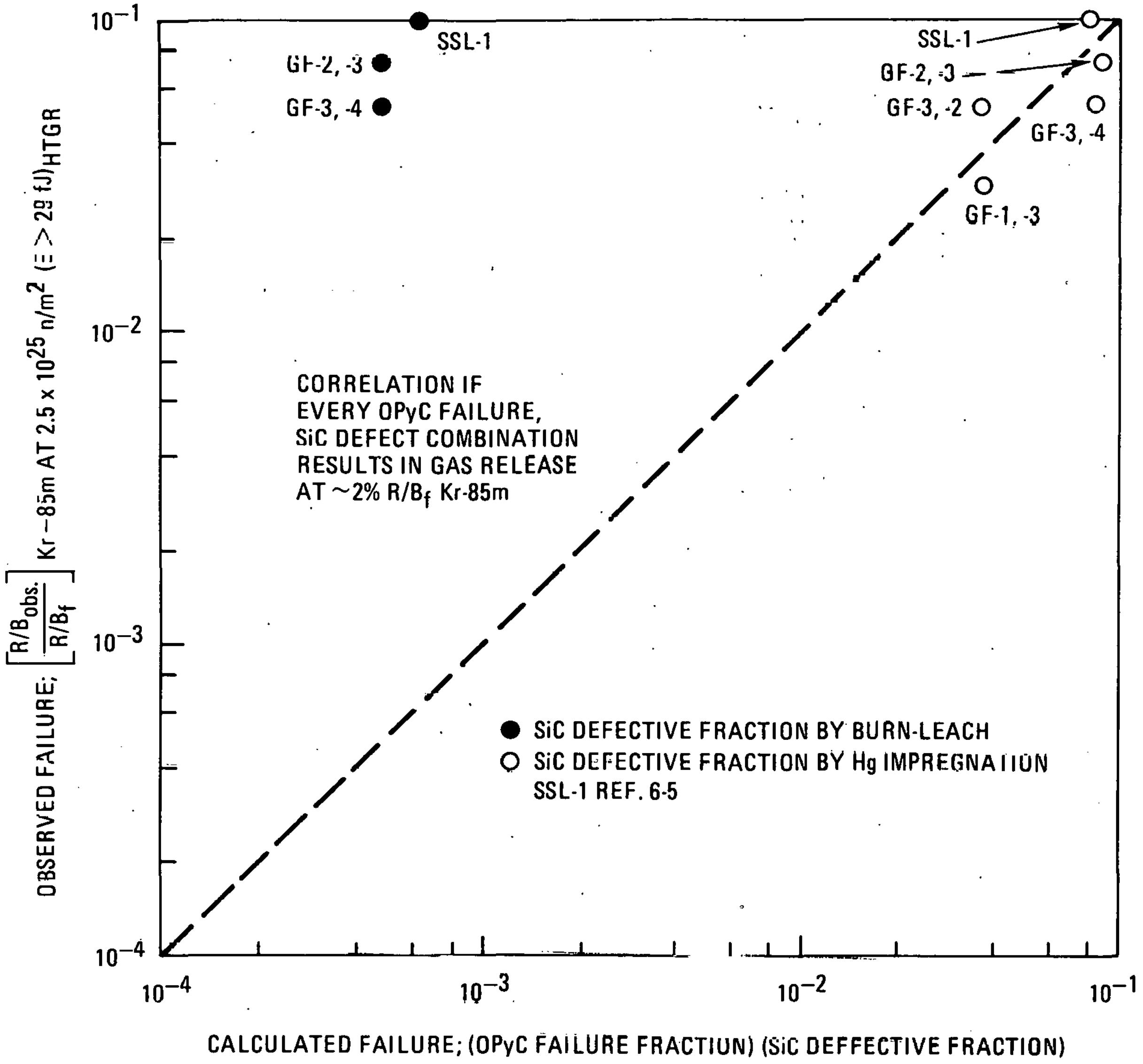

Fig. 6-2. Comparative evaluation of calculated and observed fissile particle pressure vessel failure

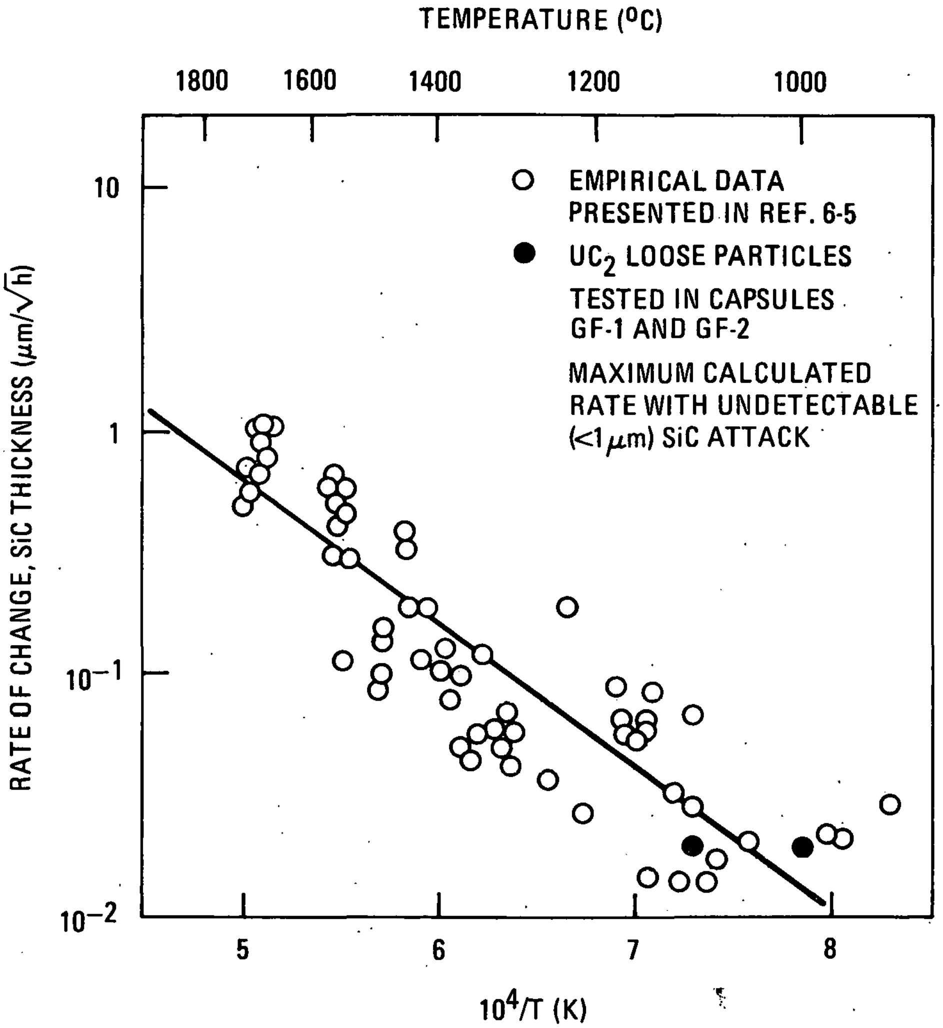

Fig. 6-3. Rate of change of SiC thickness in TRISO-coated UC_2 fuel versus reciprocal temperature. (Plot highlights GF-1 and GF-2 results with respect to empirical data base presented in Ref. 6-5.)

7. CONCLUSIONS

The GF-1, GF-2, and GF-3 PIE provided a large body of empirical data that supports a generic data base for HTGR fuel systems. Specifically, the capsules provided supporting data in the following areas:

1. Structural integrity, thermal conductivity, and irradiation-induced dimensional changes of HTGR-type fuel rods.
2. TRISO-coated particle design basis for assuring adequate irradiation performance of the OPyC and SiC layers.
3. Thermochemical stability (amoeba effect and metallic fission product - SiC attack) of (8Th,U)O_2, UC_2, and ThO_2 fuel systems.
4. Developmental fuel systems that are directed at inhibiting metallic fission product release and improving the high-temperature thermal stability of coated fuel particles.

The conclusions in each of these areas are highlighted and summarized below:

7.1. FUEL RODS

CEA rods fabricated by the CERCA process exhibited improved structural integrity compared to GA rods, which were fabricated by a matrix injection process. Irradiated GA rods were characterized by fine microcracks on the surface in contrast to the smoother apperance of CEA rods. The improved structural integrity is attributed to a combination of more coke binder and less porosity in the matrix phase. No GA rod fragmented during irradiation;

consequently, these rods demonstrate acceptable performance for HTGR-type fuel rods exposed to 975° to 1170°C and 3.8 to 9.8 x 10^{25} n/m^2 (E > 29 $fJ)_{HTGR}$.

Unirradiated fuel rods fabricated by the CEA CERCA process had thermal conductivities that were 55% to 105% greater than GA matrix-injected rods. After irradiation to fluences >5.0 x 10^{25} n/m^2 (E > 29 $fJ)_{HTGR}$ and temperatures between 960° and 1170°C, this difference was reduced to 27% to 61%. Furthermore, postirradiation fuel rod thermal conductivities ranged from 42% to 64% of the unirradiated conductivity. These data indicate that the reduction in conductivity occurs early in-ife, i.e., at fluences of ~24 x 10^{25} n/m^2 (E > 29 $fJ)_{HTGR}$. The measured reductions in thermal conductivity are subject to large uncertainties as a result of inaccuracies associated with a comparative standard measurement in the LECI thermal conductivity technique.

GF-1, GF-2, and GF-3 fuel rods fabricated with all TRISO-coated fuel particles exhibit volumetric expansions of 1% and 4% for fluences between 6 and 7 x 10^{25} n/m^2 (E > 29 $fJ)_{HTGR}$. This behavior is consistent with irradiation-induced expansion in the matrix phase. In contrast, fuel rods fabricated with TRISO- and BISO-coated fuel exhibited volumetric contractions of -6% to -1.25% for fluences between 4.5 and 7.8 x 10^{25} n/m^2 (E > 29 $fJ)_{HTGR}$. Also, GF-1, GF-2, and GF-3 fuel rods exhibited strain anisotropy that is consistent with the empirical model, showing that axial contractions are less than diametral contractions.

7.2. TRISO-COATED PARTICLE DESIGN

GA-fabricated TRISO-coated fissile particles in GF-1, GF-2, and GF-3 exhibited a nominal OPyC failure of ~30%, which ranged between 1.6% and 83.0%. The failure is attributed to structures that result in excessive strain anisotropy and high irradiation-induced stresses. These structures are produced under relatively dilute deposition conditions (volume fraction of active coating gases of ~0.1) and are characterized by low microporosities (<10 ml/kg OPyC). These results provide strong empirical support for current HTGR specification requirements on OPyC layers, namely, microporosity >13 ml/kg OPyC and volume fraction of active coating gases >0.25.

The level of as-manufactured defective SiC layers on GA-fabricated fissile fuel was between 2.3% and 11.8% as determined by mercury intrusion at 69 MPa and a radiographic evaluation. A large fraction of the defective SiC layers was characterized by localized microfissures. Furthermore, the level of defective SiC layers was substantiated by Cs-137 diffusive release measurements on as-manufactured fissile fuel. The fraction defective SiC layers determined by the mercury intrusion/radiographic technique is approximately two orders of magnitude greater than the fraction determined by the standard burn-leach technique. These results imply that the burn-leach technique is an inadequate measure of the fraction defective SiC layers over a wide range of defects, i.e., localized microfissures that breach the SiC layer or catastrophic SiC failure.

In-pile Kr-85m R/B measurements on GA-fabricated fuel rods are consistent with early-in-life [$\lesssim 2.5 \times 10^{25}$ n/m^2 (E > 29 fJ)$_{HTGR}$] fissile particle failure between 0.1% and 8.6%. This premature fissile particle failure is attributed to high OPyC failure (2.8% to 61.3%) combined with a high level of as-manufactured defective SiC layers (6.0% to 11.8%).

Pressure vessel failure levels between different TRISO-coated (8Th,U)O_2 fissile particle types indicated that the 400-μm-diameter kernel diameter was more conservative than the 500-μm-diameter designs. Specifically, early-in-life fissile particle failure in Table 5-10 shows that the 400-μm-diameter kernel tested in type a rods exhibited pressure vessel failures between 0.05% and 0.13%. This is substantially less than the 3.0% to 8.6% failure level range observed in 500-μm-diameter kernels tested in b, b', and c rods.

7.3. THERMOCHEMICAL STABILITY

No amoeba migration was observed in the $(8Th,U)O_2$, UC_2, and ThO_2 fuel systems tested in capsules GF-1, GF-2, and GF-3. These results are consistent with current performance models used in HTGR core design.

No lanthanide fission product - SiC attack was observed in the UC_2 loose particle fuel tests. Also, lanthanide fission products, e.g., cerium, neodymium, lanthanum, samarium, praseodymium, and europium, were contained within the $(8Th,U)O_2$ kernel structures. These observations are consistent with fuel performance models.

7.4. DEVELOPMENT FUELS

Aluminum and Si dopants in $(8Th,U)O_2$ kernels did not significantly retard the migration of cesium into the coating layers.

ZrC TRISO-coated UC_2 and $(8Th,U)O_2$ fuel showed good irradiation stability, and the ZrC layers possessed good resistance to chemical attack by fission products. The fuel was irradiated at 1095°C to 5×10^{25} n/m^2 $(E > 29\ fJ)_{HTGR}$ and burnups of 7.1% for $(8Th,U)O_2$ and ~60% for UC_2.

BISO-coated $(8Th,U)O_2$ with Si-doped OPyC layers in the range of 19 to 39 wt % exhibited excellent irradiation stability (no pressure vessel failure). This fuel was tested to peak exposure conditions of 11.1% FIMA, 9.4×10^{25} n/m^2 $(E > 29\ fJ)_{HTGR}$, and 1000°C.

APPENDIX

TABLE A1
FISSION GAS RELEASE RESULTS FOR ISOTOPES OF Kr AND Xe IN CAPSULE GR-1

Cell		Date Time	Fast Fluence (10^{25} n/m^2) (E > 29 fJ)$_{HTGR}$	Volume Average Temperature (°C)	R/B								
					Kr85m	Kr87	Kr88	Kr89	Xe133	Xe135m	Xe135	Xe137	Xe138
1	11	11/ 2/74 16H 0MN	1.9	1075	1.62E-04	1.10E-C4	1.24E-04	1.95E-05	1.29E-03	3.56E-05	3.95E-05	6.76E-06	1.73E-05
	12	12/ 3/74 10H 45MN	2.5	1050	1.30E-04	1.07E-04	1.12E-04	8.75E-06	9.47E-04	3.24E-05	3.80E-05	5.88E-06	1.39E-05
	13	20/ 3/74 12H 30MN	2.7	1050	1.71E-04	1.21E-04	1.57E-04	2.16E-05	4.23E-04	2.79E-05	2.96E-05	6.28E-06	1.36E-05
	14	8/ 4/74 11H 15MN	3.0	1060	1.61E-04	1.23E-04	1.21E-05	2.36E-05	3.31E-04	4.26E-05	4.31E-05	5.20E-06	1.79E-05
	15	24/ 4/74 11H 45MN	3.3	1060	1.56E-04	1.59E-04	1.42E-04		1.27E-03		3.66E-05		
	16	16/ 5/74 15H 45MN	3.8	1060	7.99E-05	7.10E-05	6.90E-05	7.40E-06	5.24E-04	2.39E-05	2.39E-05	2.94E-06	7.70E-06
	17	27/ 5/74 11H 0MN	3.9	1055	8.82E-05	6.52E-05	6.56E-05	3.91E-06	2.12E-03	2.21E-05	1.74E-05	7.81E-07	6.99E-06
	18	10/ 6/74 11H 0MN	4.1	1060	1.19E-04	8.89E-05	8.95E-05	1.15E-05	1.56E-03	3.31E-05	2.89E-05	3.41E-06	9.36E-06
	19	24/ 6/74 14H 20MN	4.4	1060	8.25E-05	6.32E-05	6.58E-05	8.95E-06	4.90E-04	2.41E-05	2.32E-05	2.45E-06	7.49E-06
	20	22/ 7/74 10H 20MN	4.7	1080	8.97E-05	4.43E-05	6.56E-05		1.26E-03	7.99E-06	2.68E-05		2.87E-06
	21	25/ 7/74 9H 20MN	4.7	1080	1.24E-04		9.64E-05		6.88E-03		3.44E-05		
	22	5/ 9/74 9H 50MN	4.8	1080	7.60E-05	5.29E-05	5.49E-05	4.46E-06	9.35E-04	9.35E-04	2.92E-05	4.63E-05	8.08E-06
	23	25/ 9/74 10H 45MN	5.2	1070	1.29E-04	7.27E-05	1.04E-04	9.56E-06	5.35E-03	3.95E-05	3.61E-05	7.20E-06	1.07E-05

TABLE A1 (Continued)

Cell		Date Time	Fast Fluence (10^{25} n/m^2) (E > 29 fJ)$_{HTGR}$	Volume Average Temperature (°C)	R/B								
					Kr85m	Kr87	Kr88	Kr89	Xe133	Xe135m	Xe135	Xe137	Xe138
2	10	5/ 2/74 11H 15MN	2.4	1170	5.20E-06	3.20E-06	3.82E-06			1.54E-06	3.55E-07		8.88E-07
	11	11/ 2/74 15H 15MN	2.5	1160	6.66E-06	4.73E-06	5.55E-06			2.1[illegible]E-06	2.99E-07		8.92E-07
	12	11/ 3/74 15H 45MN	3.3	1150	1.17E-05	8.96E-06	9.79E-06		1.01E-04	2.94E-06	3.58E-06		1.32E-06
	13	19/ 3/74 15H 30MN	3.5	1150	2.18E-05	2.09E-05	2.04E-05	1.23E-05	2.42E-04	9.94E-06	7.78E-06	5.29E-06	4.59E-06
	14	8/ 4/74 10H 0MN	4.0	1155	1.96E-05	2.04E-05	1.77E-05	4.46E-06	5.19E-05	7.67E-06	6.67E-06	1.52E-06	3.37E-06
	15	24/ 4/74 10H 25MN	4.[illegible]	1155	3.72E-05	2.32E-05	2.92E-05		7.31E-04		1.97E-05		
	16	16/ 5/74 14H 45MN	4.3	1155	4.94E-05	4.28E-05	4.05E-05	9.11E-06	1.59E-03	1.50E-05	1.17E-05	4.82E-06	6.06E-06
	17	27/ 5/74 10H 0MN	4.9	1135	9.71E-05	6.[illegible]4E-05	6.11E-05	7.31E-06	3.81E-03	1.93E-05	1.38E-05	3.76E-06	7.13E-06
	18	10/ 6/74 9H 50MN	5.4	1165	7.23E-05	6.22E-05	5.69E-05	1.63E-05	7.64E-04	2.48E-05	1.76E-05	8.38E-06	8.08E-06
	19	24/ 6/74 10H 30MN	5.7	1165	8.55E-05	7.74E-05	6.30E-05	1.37E-05	1.63E-03	3.34E-05	2.44E-05	6.05E-06	1.12E-05
	20	16/ 7/74 10H 35MN	6.0	1170	1.93E-04	1.25E-04	1.46E-04		6.05E-03	5.15E-05	5.56E-05		1.88E-05
	21	24/ 7/74 9H 20MN	6.0	1175	8.13E-05	5.73E-05	7.04E-05		9.33E-04	1.79E-05	2.43E-05		5.20E-06
	22	5/ 9/74 13H 35MN	6.1	1130	1.74E-04	1.43E-04	1.39E-04	4.27E-05	3.14E-04	7.67E-05	7.35E-05	1.65E-05	2.70E-05
	23	25/ 9/74 14H [illegible]5MN	6.5	1130	3.89E-04	2.55E-04	2.79E-04	7.63E-05	5.63E-03	1.84E-04	2.19E-04	1.47E-05	4.96E-05

TABLE A1 (Continued)

Cell		Date Time	Fast Fluence ($10^{25} n/m^2$) $(E > 29\ fJ)_{HTGR}$	Volume Average Temperature (°C)	R/B								
					Kr85m	Kr87	Kr88	Kr89	Xe133	Xe135m	Xe135	Xe137	Xe138
3	11	11/ 2/74 14H 15MN	2.3	1155	5.70E-04	3.57E-04	4.57E-04	1.06E-04	3.54E-03	1.41E-04	1.77E-04	3.97E-05	5.92E-05
	12	12/ 3/74 14H 15MN	3.1	1145	5.65E-04	3.83E-04	4.56E-04	2.34E-05	6.46E-03	1.56E-04	1.91E-04	1.64E-05	5.09E-05
	13	20/ 3/74 10H 15MN	3.2	1145	6.79E-04	3.91E-04	5.06E-04	5.06E-04	7.51E-03	1.77E-04	1.76E-04	3.38E-05	6.16E-05
	14	8/ 4/74 13H 50MN	3.8	1150	4.65E-04	3.30E-04	3.82E-04	7.26E-05	1.58E-03	1.70E-04	1.53E-04	2.24E-05	5.18E-05
	15	9/ 4/74 11H 0MN	3.8	1150	2.82E-03	1.33E-03	2.08E-03	1.25E-04		5.88E-04	2.73E-04	5.26E-05	1.59E-04
	16	24/ 4/74 14H 55MN	4.0	1155	5.93E-04	5.48E-04	4.81E-04		7.88E-03	3.50E-04	3.07E-04		6.94E-05
	17	17/ 5/74 9H 45MN	4.5	1175	3.99E-04	2.95E-04	3.17E-04	6.22E-05	7.17E-03	1.64E-04	1.37E-04	1.64E-05	4.97E-05
	18	24/ 5/74 14H 0MN	4.7	1175	2.81E-04	2.54E-04	2.43E-04	3.58E-05	1.12E-02	1.01E-04	2.88E-05	2.20E-05	3.16E-05
	19	10/ 6/74 14H 30MN	5.1	1175	2.95E-04		2.37E-04		2.10E-03		1.28E-04		
	20	21/ 6/74 9H 45MN	5.3	1175	3.20E-04	2.24E-04	2.48E-04	6.34E-05	1.10E-02	1.63E-04	1.47E-04	7.94E-06	5.32E-05
	21	16/ 7/74 13H 25MN	5.8	1160	4.26E-04	3.12E-04	3.50E-04		6.00E-03	1.40E-04	1.93E-04		4.66E-05
	22	24/ 7/74 10H 35MN	5.8	1160	4.26E-04	2.72E-04	3.28E-04		4.28E-03	1.31E-04	2.83E-04		2.99E-05
	23	5/ 9/74 15H 0MN	5.9	1150	4.13E-04	3.90E-04	3.30E-04	8.16E-05	1.30E-03	2.72E-04	2.27E-04	4.86E-05	7.30E-05
	24	25/ 9/74 16H 10MN	6.2	1140	1.13E-03	8.85E-04	7.65E-04	1.86E-04	2.16E-02	8.33E-04	7.30E-04	9.16E-05	1.74E-04

TABLE A1 (Continued)

Cell		Date Time	Fast Fluence ($10^{25} r/m^2$) $(E > 29\ fJ)_{HTGR}$	Volume Average Temperature (°C)	R/B								
					Kr85m	Kr87	Kr88	Kr89	Xe133	Xe135m	Xe135	Xe137	Xe138
4	11	6/ 2/74 9H 0MN	1.6	1100	1.15E-03	7.25E-04	8.97E-04	1.66E-04	1.07E-02	2.43E-04	3.89E-04	4.38E-05	7.90E-05
	12	11/ 2/74 10H 0MN	1.6	1095	6.41E-04	2.49E-04	3.74E-04	3.88E-05	3.55E-03	1.09E-04	2.18E-04	2.15E-05	3.05E-05
	13	14/ 3/74 10H 40MN	2.1	1140	2.50E-03	1.19E-03	1.80E-03	1.47E-04	2.66E-02	6.39E-04	6.02E-04	6.87E-05	2.12E-04
	14	11/ 4/74 14H 45MN	2.5	1[illegible]5	1.37E-03	1.01E-03	1.10E-03	2.94E-04	3.90E-03	5.52E-04	4.94E-04	1.03E-04	1.69E-04
	15	25/ 4/74 10H 10MN	2.7	1[illegible]10	1.53E-03	1.24E-03	1.21E-03	2.03E-04	1.16E-02	6.29E-04	5.86E-04	3.88E-05	1.75E-04
	16	20/ 5/74 10H 0MN	3.2	1105	3.33E-03	1.98E-03	2.69E-03	4.74E-04	4.10E-02	1.14E-03	4.36E-04	2.60E-04	3.97E-04
	17	27/ 5/74 16H 0MN	3.2	1100	6.87E-04	5.64E-04	5.38E-04	7.78E-05	8.78E-03	1.86E-04	1.84E-04	4.86E-05	7.08E-05
	18	11/ 6/74 9H 50MN	3.5	1100	1.31E-03	9.62E-04	9.57E-04	1.01E-04	7.73E-03	2.22E-04	8.11E-05	1.93E-05	8.16E-05
	19	25/ 5/74 10H 0MN	3.7	1085	2.80E-03	1.95E-03	2.87E-03	5.40E-04	1.44E-01	1.37E-03	1.00E-03	1.17E-04	4.30E-04
	20	22/ 7/74 14H 35MN	3.9	1040	1.54E-03	9.17E-04	1.07E-03		2.24E-02	2.79E-04	6.37E-04		8.93E-05
	21	25/ 7/74 11H 10MN	3.9	1045	1.72E-03	1.06E-03	1.29E-03		1.05E-02	4.42E-04	1.04E-03		1.32E-04
	22	6/ 9/74 9H 40MN	4.0	1055	2.21E-03	1.63E-03	1.60E-03	3.78E-04	4.00E-03	4.08E-04	4.56E-04	1.65E-04	1.91E-04
	23	26/ 9/74 11H 0MN	4.3	1065	9.56E-04	8.01E-04	7.92E-04	1.94E-04	5.34E-03	4.10E-04	3.90E-04	1.24E-04	1.71E-04

TABLE A2

FISSION GAS RELEASE RESULTS FOR ISOTOPES OF Kr AND Xe IN CAPSULE GF-2

Cell		Date Time	Fast Fluence (10^{25} n/m^2) (E > 29 fJ)$_{HTGR}$	Volume Average Temperature (°C)	R/B								
					Kr85m	Kr87	Kr88	Kr89	Xe133	Xe135m	Xe135	Xe137	Xe138
1	1	4/ 1/74 9H 30MN	0.1	1015	8.39E-08	5.45E-03	5.18E-08		1.03E-08	3.54E-08	4.80E-09		1.25E-08
	2	14/ 1/74 9H 30MN	0.3	1020	1.16E-07	6.22E-08	5.96E-08		6.71E-08	2.50E-08	4.26E-09		6.13E-09
	3	21/ 1/74 16H 45MN	0.4	1020	2.86E-06	2.56E-06	2.45E-06		2.83E-06	7.20E-07	8.79E-08		2.79E-07
	4	4/ 2/74 9H 15MN	0.7	1030	2.02E-06	1.74E-06	2.06E-06			1.20E-06	1.37E-07		3.80E-07
	5	18/ 2/74 15H 0MN	1.0	1030	8.17E-06	6.08E-06	6.88E-06			2.68E-06	3.16E-07		1.43E-06
	6	18/ 3/74 10H 15MN	1.2	1015					1.37E-06				
	7	3/ 4/74 16H 45MN	--	--	1.61E-06	2.45E-06	1.60E-06		5.43E-07	3.81E-05	2.52E-07		
	8	15/ 5/74 9H 15MN	1.4	990	7.34E-06	7.33E-06	7.29E-06		2.84E-06	5.24E-06	3.51E-07		2.22E-06
	9	30/ 5/74 16H 0MN	1.6	945	7.70E-06	5.15E-06	6.29E-06		7.89E-06	1.77E-04	9.49E-07		
	10	27/ 6/74 15H 25MN	1.8	940									
	11	17/ 7/74 15H 0MN	2.2	945	4.68E-06		4.58E-06		3.40E-06	9.83E-09	1.61E-06		
	12	8/ 8/74 11H 30MN	--	—					8.95E-06				
	13	26/ 9/74 16H 50MN	2.5	915	3.32E-06	2.95E-06	2.34E-06		4.49E-06		4.10E-07		

TABLE A2 (Continued)

Cell		Date Time	Fast Fluence (10^{25} n/m^2) (E > 29 fJ)$_{HTGR}$	Volume Average Temperature (°C)	R/B								
					Kr85m	Kr87	Kr88	Kr89	Xe133	Xe135m	Xe135	Xe137	Xe138
2													
	1	4/ 1/74 10H 30MN	0.1	960	1.79E-07	1.60E-07	1.50E-07		1.63E-08		6.21E-09		2.30E-08
	2	14/ 1/74 10H 30MN	0.5	960	2.51E-07	1.46E-07	1.78E-07		7.56E-08		3.35E-09		1.74E-08
	3	22/ 1/74 11H 0MN	0.7	960	2.94E-07	2.30E-07	2.45E-07		1.23E-07		4.91E-09		1.80E-08
	4	4/ 2/74 10H 5MN	1.0	960	2.76E-07	1.71E-07	2.15E-07		7.97E-08		7.38E-09		
	5	25/ 2/74 10H 45MN	1.4	965					2.16E-07				
	6	19/ 3/74 11H 0MN	1.6	985					1.14E-05				
	7	4/ 4/74 10H 30MN	--	--	5.85E-07		4.79E-07		2.09E-07		1.35E-07		
	8	30/ 5/74 14H 30MN	2.2	980	9.43E-05		7.63E-05		1.29E-04		3.80E-06		
	9	27/ 6/74 14H 35MN	2.7	960	1.11E-05	1.23E-05	1.05E-05		2.77E-05		7.22E-07		
	10	17/ 7/74 11H 0MN	3.0	955	1.24E-05		9.36E-06		1.61E-05	4.06E-08			
	11	8/ 8/74 10H 10MN	—	--					1.04E-05				
	12	26/ 9/74 15H 15MN	3.4	970	6.89E-06	9.25E-06	5.62E-06		5.08E-06		4.62E-07		

TABLE A2 (Continued)

Cell		Date Time	Fast Fluence ($10^{25} n/m^2$) $(E > 29\ fJ)_{HTGR}$	Volume Average Temperature (°C)	R/B								
					Kr85m	Kr87	Kr88	Kr89	Xe133	Xe135m	Xe135	Xe137	Xe138
3	1	4/ 1/74 11H 15MN	0.1	980	3.17E-17	2.52E-07	2.76E-07		3.56E-08	1.11E-07	1.16E-08		4.38E-08
	2	14/ 1/74 9H 30MN	0.4	975	4.27E-07	3.01E-07	3.32E-07		1.45E-07		1.42E-08		1.72E-08
	3	22/ 1/74 11H 45MN	0.6	970	3.46E-07	2.56E-07	2.74E-07		1.89E-07		9.52E-09		1.64E-08
	4	4/ 2/74 10H 45MN	0.9	965	4.31E-07	2.45E-07	2.94E-07		1.23E-07		1.22E-08		
	5	18/ 2/74 16H 15MN	1.1	965	3.39E-07	2.32E-07	2.58E-07		2.54E-07		1.35E-08		
	6	18/ 3/74 14H 15MN	1.3	975					8.92E-08				
	7	3/ 4/74 15H 30MN	--	—	4.35E-08	3.83E-08	3.52E-08		2.03E-08	1.38E-08	3.68E-09		1.19E-08
	8	15/ 5/74 15H 30MN	1.7	980	1.08E-05	8.62E-06	9.23E-06		1.15E-05	3.65E-06	8.34E-07		2.06E-06
	9	29/ 5/74 14H 30MN	1.9	970	1.89E-04	1.57E-04	1.44E-04	1.76E-05	2.30E-03	4.40E-05	5.68E-05	1.65E-05	3.59E-05
	10	18/ 6/74 14H 30MN	2.2	940	4.45E-04	3.31E-04	3.21E-04	4.48E-05	7.64E-03	1.09E-04	1.22E-04	3.56E-05	4.78E-05
	11	27/ 6/74 10H 20MN	2.5	935	5.76E-04	4.24E-04	5.09E-04	9.64E-05	2.81E-03	1.35E-04	1.43E-04	6.06E-05	6.69E-05
	12	19/ 7/74 9H 15MN	2.8	935	3.97E-04	2.69E-04	3.31E-04		1.79E-03	5.89E-05	1.37E-04		3.17E-05
	13	26/ 7/74 9H 30MN	2.9	945	4.84E-04	3.39E-04	3.94E-04	1.30E-05	2.62E-03	8.73E-05	1.77E-04	6.94E-06	5.04E-05
	14	12/ 9/74 13H 20MN	3.0	955	4.33E-04	4.19E-04	3.73E-04	5.73E-05	8.92E-04	1.44E-04	1.42E-04	3.96E-05	6.95E-05
	15	20/ 9/74 8H 50MN	3.0	960	2.70E-04	2.48E-04	2.68E-04	9.26E-05	8.71E-04	9.21E-05	1.10E-04	4.47E-05	5.65E-05

TABLE A2 (Continued)

Cell		Date Time	Fast Fluence $(10^{25} n/m^2)$ $(E > 29\ fJ)_{HTGR}$	Volume Average Temperature (°C)	R/B								
					Kr85m	Kr87	Kr88	Kr89	Xe133	Xe135m	Xe135	Xe137	Xe138
4	1	4/ 1/74 12H 0MN	0.1	1170					1.24E-05		3.92E-06		
	2	14/ 1/74 14H 30MN	0.3	1170	1.80E-04	7.25E-05	[illegible].12E-04	1.52E-06	6.88E-04	1.35E-05	2.76E-05		3.89E-06
	3	22/ 1/74 14H 40MN	0.4	1155	1.70E-04	6.99E-05	1.15E-04		8.79E-04	1.23E-05	2.63E-05		4.23E-06
	4	4/ 2/74 14H 45MN	0.7	1155	2.59E-04	1.49E-04	1.92E-04		9.96E-04	7.21E-05	9.[illegible]2E-05		1.40E-05
	5	19/ 2/74 9H 45MN	1.0	1150	3.91E-04	2.07E-04	2.85E-04	5.62E-06	1.40E-03	7.10E-15	1.13E-04	2.92E-06	1.83E-05
	6	19/ 3/74 8H 45MN	1.1	1100					2.72E-03				
	7	4/ 4/74 14H 35MN	--	--	1.13E-03		8.95E-04			6.19E-06	7.52E-04		
	8	31/ 5/74 10H 0MN	1.4	1005	4.20E-04		4.54E-04			4.06E-06	1.75E-04		
	9	28/ 6/74 9H 35MN	1.8	970	9.66E-04		8.22E-04		9.01E-04	9.92E-06	5.85E-04		
	10	26/ 7/74 14H 20MN	2.1	940					6.42E-04				
	11	27/ 9/74 9H 30MN	2.3	925					6.05E-04				

TABLE A3
FISSION GAS RELEASE RESULTS FOR ISOTOPES OF Kr AND Xe IN CAPSULE GF-3

Cell		Date Time	Fast Fluence (10^{25} n/m^2) $(E > 29\ fJ)_{HTGR}$	Volume Average Temperature (°C)	R/B								
					Kr85m	Kr87	Kr88	Kr89	Xe133	Xe135m	Xe135	Xe137	Xe138
1	1	1/ 2/74 9H 15MN	0.1	990	5.49E-06	3.26E-06	4.86E-06			3.27E-06	5.36E-07		1.19E-06
	2	12/ 2/74 11H 15MN	0.2	990	1.52E-06	1.31E-06	1.30E-06		3.83E-06	9.80E-07	1.46E-07		3.55E-07
	3	18/ 2/74 9H 15MN	0.3	995	1.44E-06	7.33E-07	9.73E-07		3.09E-06	1.06E-06	1.73E-07		3.42E-07
	4	4/ 3/74 10H 0MN	0.5	995	4.16E-06	1.51E-06	1.66E-06		4.25E-06	1.02E-06	1.64E-07		2.29E-07
	5	21/ 3/74 15H 0MN	0.8	995	1.48E-06	1.35E-06	1.28E-06		1.39E-06	9.22E-07	6.85E-08		3.22E-07
	6	10/ 4/74 10H 45MN	1.1	965	1.75E-06	1.42E-06	1.49E-06		3.71E-06	1.22E-06	2.12E-07		4.72E-07
	7	22/ 4/74 10H 0MN	1.3	965	1.34E-06	1.20E-06	1.11E-06		2.35E-06	1.01E-06	1.03E-07		3.06E-07
	8	13/ 5/74 11H 15MN	1.5	970	1.40E-06	1.46E-06	1.10E-06		2.10E-06	1.07E-06	1.63E-07		4.19E-07
	9	28/ 5/74 9H 50MN	1.8	980	8.95E-07	6.59E-07	7.46E-07		2.73E-06		1.50E-07		
	10	17/ 6/74 9H 45MN	2.0	985	9.79E-07	1.03E-06	9.43E-07		2.26E-06	7.06E-07	1.05E-07		2.25E-07
	11	25/ 6/74 14H 35MN	2.1	985	8.22E-07	2.64E-06	9.96E-07		1.99E-06	4.22E-06	9.34E-08		
	12	23/ 7/74 9H 0MN	2.4	965	1.01E-06	8.58E-07	8.89E-07		2.32E-06	5.25E-07	1.06E-07		2.66E-07
	13	9/ 9/74 10H 35MN	2.5	965	1.82E-06	1.69E-06	1.55E-06		2.06E-06	9.69E-07	1.59E-07	4.49E-07	4.25E-07
	14	19/ 9/74 14H 20MN	2.5	965	1.06E-06	1.28E-06	1.28E-06		1.96E-06	7.49E-07	1.34E-07		2.90E-07

TABLE A3 (Continued)

Cell		Date Time	Fast Fluence $(10^{25} n/m^2)$ $(E > 29\ fJ)_{HTGR}$	Volume Average Temperature (°C)	R/B								
					Kr85m	Kr87	Kr88	Kr89	Xe133	Xe135m	Xe135	Xe137	Xe138
2	1	1/ 2/74 10H 15MN	0.1	955	1.35E-07	1.13E-07	1.14E-07				5.66E-09		3.27E-08
	2	12/ 2/74 11H 50MN	0.3	955	3.30E-07	2.05E-07	2.40E-07		1.23E-07		6.98E-09		
	3	18/ 2/74 10H 5MN	0.5	955	4.11E-07	2.41E-07	3.00E-07		2.32E-07	8.84E-08	1.19E-08		3.11E-08
	4	4/ 3/74 10H 40MN	0.8	955	5.07E-07	3.44E-07	3.64E-07		1.09E-07		1.34E-08		
	5	22/ 3/74 9H 45MN	1.1	960	1.61E-06	1.49E-06	1.41E-06		1.53E-06	6.17E-07	1.10E-07		1.78E-07
	6	10/ 4/74 9H 45MN	1.5	965	1.91E-06	1.67E-06	1.59E-06		1.53E-06	6.17E-07	1.10E-07		1.78E-07
	7	22/ 4/74 11H 0MN	1.8	950	4.83E-05	4.84E-05	4.97E-05	1.13E-05	7.94E-04	1.92E-05	1.30E-05	7.23E-06	9.68E-06
	8	13/ 5/74 15H 15MN	2.1	930	1.21E-04	1.03E-04	9.32E-05	1.42E-05	3.53E-04	3.59E-05	3.31E-05	3.70E-06	1.80E-05
	9	28/ 5/74 15H 15MN	2.3	955	1.91E-04		1.62E-04		2.10E-03		6.68E-05		
	10	17/ 6/74 10H 35MN	2.8	980	3.26E-04	2.75E-04	2.47E-04	4.50E-05	8.61E-03	8.57E-05	7.83E-05		3.69E-05
	11	25/ 6/74 14H 35MN	2.9	970	3.40E-04	2.83E-04	2.65E-04	5.25E-05	5.32E-03	9.75E-05	9.90E-05	3.38E-05	4.21E-05
	12	23/ 7/74 9H 40MN	3.3	950	2.28E-04	1.30E-04	1.79E-04	4.08E-06	5.01E-03	3.08E-05	4.89E-05	3.29E-06	1.66E-05
	13	9/ 9/74 13H 50MN	3.3	970	1.29E-04	1.30E-04	1.11E-04	3.69E-05	9.83E-04	6.83E-05	5.35E-05	1.73E-05	2.13E-05
	14	19/ 9/74 9H 10MN	3.4	985	1.52E-04	1.32E-04	1.21E-04	2.75E-05	9.51E-04	5.39E-05	4.94E-05	1.65E-05	2.19E-05

TABLE A3 (Continued)

Cell		Date Time	Fast Fluence ($10^{25} n/m^2$) $(E > 29\ fJ)_{HTGR}$	Volume Average Temperature (°C)	R/B								
					Kr85m	Kr87	Kr88	Kr89	Xe133	Xe135m	Xe135	Xe137	Xe138
3	1	1/ 2/74 11H 0MN	0.1	1050	2.00E-05	1.08E-05	1.62E-05				2.08E-07		5.91E-07
	2	12/ 2/74 14H 10MN	0.3	1050	5.28E-05		2.67E-05		7.83E-05		8.64E-07		
	3	18/ 2/74 11H 5MN	0.5	1045	5.36E-05	2.15E-05	3.55E-05		1.49E-04	4.26E-06	5.94E-06		1.57E-06
	4	4/ 3/74 14H 15MN	0.8	1040	3.33E-05	1.93E-05	2.51E-05	6.54E-07	9.57E-05	3.12E-06	3.07E-06	2.73E-07	1.32E-06
	5	22/ 3/74 11H 20MN	1.1	1035	3.65E-05	2.01E-05	2.52E-05		1.34E-04	3.15E-06	4.40E-06		1.47E-06
	6	10/ 4/74 15H 0MN	1.5	1025	5.10E-05	2.59E-05	3.58E-05	9.18E-07	9.66E-05	3.49E-06	5.50E-06	3.02E-07	1.56E-06
	7	22/ 4/74 14H 15MN	1.7	1005	4.14E-05	2.57E-05	3.10E-05	1.39E-06	2.09E-04	3.68E-06	5.24E-06	3.09E-07	1.50E-06
	8	14/ 5/74 11H 30MN	2.0	980	4.06E-05	2.26E-05	2.35E-05		1.27E-04	4.08E-06	6.51E-06		1.63E-06
	9	28/ 5/74 10H 30MN	2.3	985	4.74E-05	2.51E-05	4.40E-05		1.38E-03	5.32E-06	8.87E-06	1.80E-06	2.51E-06
	10	17/ 6/74 14H 30MN	2.8	985	1.20E-04	9.79E-05	8.75E-05	2.10F-05	1.17E-03	2.93E-05	2.95E-05	1.58E-05	1.43E-05
	11	26/ 6/74 14H 45MN	2.9	970	3.99E-04	2.14E-04	2.65E-04	1.75E-05	8.03E-03	4.98E-05	6.75E-05	5.22E-06	2.46E-05
	12	23/ 7/74 14H 15MN	3.2	970	3.45E-04	1.93E-04	2.74E-04	5.65E-06	3.14E-03	5.09E-05	1.17E-04	5.66E-06	3.14E-05
	13	11/ 9.74 9H 25MN	3.3	985	2.80E-04	2.33E-04	2.17E-04	6.60E-05	5.05E-04	1.02E-04	8.01E-05	4.46E-05	5.68E-05
	14	18/ 9/74 14H 50MN	3.3	990	3.39E-04	2.85E-04	2.64E-04	4.63E-05	1.62E-03	7.59E-05	7.74E-05	2.45E-05	4.09E-05

TABLE A3 (Continued)

Cell		Date Time	Fast Fluence (10^{25} n/m^2) (E > 29 fJ)$_{HTGR}$	Volume Average Temperature (°C)	R/B								
					Kr85m	Kr87	Kr88	Kr89	Xe133	Xe135m	Xe135	Xe137	Xe138
4	1	1/ 2/74 11H 50MN	0.1	1125	7.17E-07	8.06E-07	7.35E-07				1.66E-08		7.31E-08
	2	12/ 12/74 15H 5MN	0.2	1125	1.07E-06	6.40E-07	8.03E-07		6.02E-07	2.14E-07	4.48E-08		2.69E-08
	3	18/ 2/74 12H 0MN	0.3	1125	1.11E-06	7.26E-07	9.00E-07		7.18E-07		3.02E-08		4.39E-08
	4	4/ 3/74 11H 25MN	0.5	1125	1.44E-06	1.20E-06	1.22E-06		1.07E-06	2.08E-07	6.88E-08		1.24E-07
	5	22/ 3/74 10H 25MN	0.7	1125	1.98E-05	1.41E-05	1.62E-05			5.85E-06	9.18E-07		4.90E-06
	6	10/ 4/74 11H 45MN	1.0	1130	3.25E-05	2.82E-05	2.62E-05	9.83E-06	4.53E-05	9.04E-06	9.06E-06	2.90E-06	5.60E-06
	7	22/ 4/74 15H 30MN	1.2	1120	2.84E-05	2.42E-05	2.65E-05	5.37E-06	2.28E-04	6.13E-06	6.11E-06	2.76E-06	3.71E-06
	8	14/ 5/74 14H 45MN	1.4	1115	5.52E-05	4.50E-05	4.55E-05	8.94E-06	1.40E-04	1.56E-05	1.77E-05	5.74E-06	7.41E-06
	9	28/ 5/74 12H 45MN	1.6	1145	2.79E-04	2.27E-04	2.23E-04	4.11E-05	3.18E-03	6.95E-05	7.63E-05		3.57E-05
	10	17/ 6/74 14H 30MN	1.8	1155	7.98E-04	7.57E-04	6.59E-04	1.29E-04	9.68E-03	2.20E-04	3.00E-04	7.61E-05	9.17E-05
	11	26/ 6/74 9H 45MN	1.9	1140	8.00E-04	4.99E-04	6.62E-04	1.52E-04	9.94E-03	1.29E-04	2.72E-04	5.33E-05	5.29E-05
	12	23/ 7/74 11H 20MN	2.0	1125	9.87E-04	6.55E-04	7.87E-04		4.11E-03	1.01E-04	3.94E-04		
	13	9/ 9/74 15H 45MN	2.1	1125	6.88E-04	6.74E-04	5.56E-04	1.77E-04	2.28E-03	3.01E-04	2.71E-04	8.43E-05	1.13E-04
	14	19/ 9/74 10H 45MN	2.2	1125	7.93E-04	6.77E-04	5.64E-04	9.06E-05	7.40E-03	3.05E-04	2.77E-04	5.44E-05	9.85E-05